UNIVERSITY OF CALIFORNIA, SAN DIEGO

Theoretical Studies in Spiral Edge-Flame Propagation and Particle Hydrodynamics

A dissertation submitted in partial satisfaction of the
requirements for the degree
Doctor of Philosophy

in

Engineering Sciences (Aerospace Engineering)

by

Javier Urzay

Committee in charge:

Professor Forman A. Williams, Chair
Professor Stefan G. Llewellyn Smith, Co-Chair
Professor Juan C. Lasheras
Professor Katja Lindenberg
Professor William R. Young

2010

The dissertation of Javier Urzay is approved, and it is acceptable in quality and form for publication on microfilm and electronically:

_____

_____

_____

_____
Co-Chair

_____
Chair

University of California, San Diego

2010

DEDICATION

To my parents José Ricardo and Francisca, and to my brother Ricardo.

EPIGRAPH

"All men dream, but not equally.

Those who dream by night in the dusty recesses of their minds,
wake in the day to find that it was vanity:

but the dreamers of the day are dangerous men,
for they may act on their dreams with open eyes,
to make them possible.

This I did."

"Seven Pillars of Wisdom"
by Thomas E. Lawrence.

"Caminante, son tus huellas
el camino, y nada más;
caminante, no hay camino,
se hace camino al andar.

Al andar se hace camino,
y al volver la vista atrás
se ve la senda que nunca
se ha de volver a pisar.

Caminante, no hay camino,
sino estelas en la mar."

"Campos de Castilla"
by Antonio Machado.

"Érase de un marinero
que hizo un jardín junto al mar,
y se metió a jardinero.

Estaba el jardín en flor,
y el jardinero se fue
por esos mares de Dios."

"Campos de Castilla"
by Antonio Machado.

TABLE OF CONTENTS

Signature Page . . . iii

Dedication . . . iv

Epigraph . . . v

Table of Contents . . . vi

List of Figures . . . ix

List of Tables . . . xi

Acknowledgements . . . xii

Vita and Publications . . . xv

Abstract of the Dissertation . . . xvii

I Combustion and Propagation of Spiral Edges of Diffusion Flames in Von Kármán Swirling Flows 1

Nomenclature . . . 2

Chapter 1 Introduction . . . 5

Chapter 2 Laboratory-frame formulation . . . 13
2.1 Hydrodynamic field . . . 13
2.2 Chemical kinetics model . . . 18
2.3 Mixture fraction, mass-transfer number, scalar dissipation rate and excess enthalpy . . . 19
2.4 Conserved-scalar formulation . . . 22

Chapter 3 Diffusion-flame dynamics . . . 24
3.1 The frozen regime . . . 27
3.2 The Burke-Schumann regime . . . 27
3.3 Diffusion-flame extinction . . . 30

Chapter 4 Propagation dynamics of spiral edge flames . . . 35
4.1 Frenet-frame formulation . . . 35
4.2 Influences of heat losses to the burner surface on the propagation of edge flames . . . 38
4.2.1 Order-of-magnitude analysis of the conservation equations 38
4.2.2 Adiabatic triple-flame propagation regimes . . . 40
4.2.3 Non-adiabatic triple-flame propagation regimes . . . 41
4.3 Edge dynamics . . . 44

4.3.1 The G-equation . . . 44
4.3.2 The tangential structure of a steadily rotating spiral . . . 46
4.3.3 Spiral-flame anchoring and quasi-static stability . . . 53

Chapter 5 Experimental data analysis . . . 57

Chapter 6 Conclusions . . . 66

References . . . 69

II The Elastohydrodynamic Gliding Motion and Adhesion of a Solid Particle to Soft and Sticky Substrates at Low Reynolds Numbers 73

Nomenclature . . . 74

Chapter 7 Introduction . . . 76

Chapter 8 Formulation . . . 79
8.1 Hydrodynamic equations . . . 79
8.2 The electric double-layer and van der Waals pressures. . . . 83
8.2.1 The DLVO critical ionic concentration for adhesion . . . 86
8.3 Substrate mechanics . . . 86
8.4 Nearly-rigid-wall asymptotics (NRWA) and summary of main nondimensional parameters . . . 92

Chapter 9 Particle Dynamics . . . 95
9.1 Dynamics near rigid substrates: hydrodynamic and intermolecular forces . . . 95
9.2 Statics near deformable substrates: elastomolecular forces . . . 98
9.2.1 Elastomolecular force . . . 99
9.2.2 Surface bifurcations in the substrate: elastostatic adhesion . . . 100
9.3 Dynamics near deformable substrates: elastohydromolecular forces . . . 103
9.3.1 Lift force . . . 107
9.3.2 Drag-force and drift-force first-order perturbations . . . 110
9.4 Elastohydrodynamic adhesion and lift-off . . . 114
9.4.1 Elastohydrodynamic corrections to the DLVO theory . . . 117
9.5 General influences of the substrate thickness and material incompressibility . . . 118

Chapter 10 Conclusions . . . 121

References . . . 125

III Aerodynamics and Aeroelasticity of Wind Pollination 128

Nomenclature 129

Chapter 11 Introduction 131

Chapter 12 Pollen shedding forces 136
12.1 Aerodynamic shedding forces 136
12.1.1 Steady aerodynamic forces 136
12.1.2 Unsteady aerodynamic forces. 138
12.2 Aeroelastic shedding forces 142
12.2.1 The simplified stamen model 143
12.2.2 Pollen-shedding number and probability 145

Chapter 13 Conclusions 148

References 151

LIST OF FIGURES

Figure 1.1: Direct images of triple flames and triple-flame schematics. 6
Figure 1.2: Examples of spiral patterns found in nature. 8
Figure 1.3: Schematic representation of the S-curve response of a diffusion flame. . 9
Figure 1.4: Schematic illustration of the experimental apparatus. 10
Figure 1.5: Summary of experimental flame patterns observed in the rotating porous-disk burner. 11

Figure 2.1: The model problem. 14
Figure 2.2: Hydrodynamic velocity components. 16
Figure 2.3: Mixture fraction distribution, mass-transfer number, and dimensionless scalar dissipation rate. 21

Figure 3.1: Liñán's burning regimes. 26
Figure 3.2: Equilibrium heat-loss coefficient. 28
Figure 3.3: Diffusion-flame stand-off distance. 29
Figure 3.4: Dimensionless non-adiabatic Burke-Schumann temperature. 30
Figure 3.5: Leakage parameter. 31
Figure 3.6: Outer asymptotic temperature and reactant mass fractions distributions in the diffusion-flame regime for different ranges of fuel injection mass flows. 33

Figure 4.1: The computational model problem used to study the influences of the cold porous wall on the propagation of straight edge flames. The boundary conditions indicated refer to equations in the main text. 39
Figure 4.2: Adiabatic and non-adiabatic triple-flame propagation regimes. 42
Figure 4.3: Swirl number as a function of the injection Reynolds number. 48
Figure 4.4: Spiral edges obtained by using the outer solution. 50
Figure 4.5: Spiral edges obtained by numerical integration of the G-equation. . . . 52
Figure 4.6: Stability schematics of straight edge flames in the presence of normal convective velocity gradients. 54
Figure 4.7: Quasi-static stability of spiral edges. 55
Figure 4.8: Sketch of the front propagation velocity as a function of the front tangential curvature. 56

Figure 5.1: Dimensional and nondimensional pattern maps. 59
Figure 5.2: Tip trajectories and average core radius. 60
Figure 5.3: Experimental and analytical values of the dimensionless core radius. . . 61
Figure 5.4: Comparison between the experimental images and the analytical front shapes. 63
Figure 5.5: Comparison between the experimental and analytical tail shapes. 64

Figure 7.1: Sketch of typical particle-surface interaction-energy curves in the DLVO theory. 77

Figure 8.1: The model problem. 80

Figure 8.2: Top view of the gap region showing the spatial orientation of the polar azimuth angle, phase angle and reduced angle. 82

Figure 9.1: Leading-order (rigid-wall) pressure and stress contours 97
Figure 9.2: Nondimensional static normal force on the sphere, map of static solutions, and centerline elastic displacement of the substrate. 100
Figure 9.3: Auxiliar functions for the pressure perturbation. 103
Figure 9.4: Second-order pressure and stress contours for purely translational motion. 105
Figure 9.5: Second-order pressure and stress contours for corkscrew motion. 106
Figure 9.6: Influences of rotation and azimuth angle of rotation on the lift force in the absence of intermolecular forces. 108
Figure 9.7: Dimensionless elastohydromolecular lift force on the sphere, for any rotation rate and rotation axis orientation. 109
Figure 9.8: Drag and drift coefficients of the electric force. 111
Figure 9.9: Influences of rotation and azimuth angle of rotation on the drag force disturbance. 113
Figure 9.10: Dimensionless elastohydromolecular drag force disturbance. 114
Figure 9.11: Lift-off and critical hydrodynamic compliances for elastohydrodynamic adhesion. 115

Figure 11.1: Plantago inflorescence, stamen, anther and pollen grains. 132
Figure 11.2: Insect and wind-pollinated pollens. 133
Figure 11.3: Genetic modifications performed at the University of Cambridge (UK), Department of Plant Sciences. 134

Figure 12.1: The anther boundary-layer model. 137
Figure 12.2: Sketches of the flow field around a pollen grain on an anther subject to a wind gust. 139
Figure 12.3: Unsteady boundary-layer forces. 140
Figure 12.4: Plantago inflorescence and anthers, and the mathematical model. . . . 142
Figure 12.5: Pollen-shedding probability model. 146

Figure 13.1: Zea mays anthers and inflorescence, Betula albosinensis catkin, Salix sepulchralis and Arabidopsis thaliana anthers. 149

LIST OF TABLES

Table 1.1: Representative propagator and controller variables in selected physical systems. 8

Table 5.1: Experimental data sets of spiral flames on the porous-disk burner. . . . 65

Table 8.1: Fundamental nondimensional parameters and their definition, their asymptotic ordering in the NRWA limit and numerical estimates. 93

Table 12.1: Representative measurements of anthers, filaments and pollen from a range of wind or partially wind-pollinated species. 147

ACKNOWLEDGEMENTS

When I was an undergraduate student in engineering I became aware of the beauty and power of the simplicity with which apparently very complex physical processes could be described analytically. During that period I found inspiration from a mentor, Professor Antonio L. Sánchez, who gave me an extra impulse, a motivation to follow the scientific track. He gave me examples of modesty and technical excellence, and presented the academic world to me as a joyful scenario full of opportunities. The motivations and willingness stored during my undergraduate years with him have undoubtedly been the primary fuel to propel my morale during these demanding years of graduate school. Thanks to him for his invaluable mentorship and friendship, and for his continuous moral support from the distance.

Thanks to Professor Stefan G. Llewellyn Smith, who brought me from Spain and assigned me to a research project, providing me with initial funds and resources; I am grateful to him for this once-in-a-lifetime opportunity, I gratefully acknowledge his patience with me and his initial thrust to my success in this adventure.

Thanks to Professor Forman A. Williams, who kindly offered me refuge during stormy weather, from whom I learnt a number of technical skills, and with whom I laughed and enjoyed remarkable conversations during these years, making the process of getting this degree very appealing and interesting.

During these four years I have suffered from sadness and happiness, vital cycles and instabilities that are germane to every learning process. Fortunately I found someone quite worth to be listened to and who helped me to traverse those rough terrains: I found constant shelter and moral support in Professor Juan C. Lasheras. Thanks to him for his guidance and sincere advices.

Thanks to Professor Amable Liñán, it was a true pleasure to share ideas and have conversations with him. He motivates the students and instructs them to think simpler, and thinking simpler of anything nowadays is such a great endeavor in this world full of complexities. He indirectly taught me one of the most important lessons I learnt in this place: A successful scientist must be made of an indissoluble mixture of kindness, modesty, rigor and outstanding technical skills.

I made many important friendships here. I am deeply grateful to Baldomero Alonso and Juan C. Del Álamo for their enormous support, help and friendship they have awarded to me during these years. Baldomero and I shared every thing that could have been shared, I

lived unforgettable moments and enjoyed many conversations with him that I will remember for the rest of my life. Juan Carlos offered me continuous help and sincere advice that could only be expected from a very close friend. I have learnt quite a lot from both of them. But I also met a group of other remarkable people here; I cannot help but remembering the great times lived with Gonzalo, Juliana, Andy, Javier, Vincent, Guillaume, Nicolas, Flavia, Christian, Sergi, Daniel, Marco, Zuhair, Mario, David, Vanessa, Marta, Genaro, Alberto, Gador, Laura, Rafael, Mecedes, Michael, Lourdes, Silvana, Katie, Jin, Manuel, Begoña, Francesco, Giancarlo, Carolina, Will, Pablo and Jorge. Thanks to Estévez and Jose Ramón, my two old friends from college, for keeping constantly in touch. Thanks also to Michelle and Linda for their extraordinary help from the administration floor. Thanks to Professors Paul Libby, Alison Marsden, Kal Seshadri and Glenn Ierley, with whom I enjoyed very nice philosophical and technical discussions.

My relatives have served me as a living exemplification of important life values such as integrity, consistency, honesty, endurance, perseverance and hard work. Thanks to my parents, José Ricardo and Francisca, for having tried the best that they could to give me an education that orbits around those values, which reaches far beyond any academic or technical training, and which, although yet quite incomplete at my early age, enabled me to jump some difficult hurdles and cross this finish line. It is at this very moment of my life when I truly appreciate all their efforts and I am deeply proud of being their son. Thanks to them and to my brother Ricardo for having a solid confidence on me, and for showing me that certain important subjects cannot be learnt from books or equations. Thanks to them for teaching me how needful is for a brave man not to become stuck in mediocrity, passiveness and hopelessness, but to dream and believe in a better and exciting future, to fight relentlessly for his dreams and expectations despite what others may say he can or cannot do, and to always look for new and unexplored horizons. Because the three of them are, and will always be, the grand witnesses of my life and growth, to them my entire work is dedicated.

La Jolla, California. April 9, 2010.

Chapters 1 to 5, in part, have been published in in the *Proceedings of the Combustion Institute*, "Diffusion-flame extinction on a rotating porous-disk burner," by J. Urzay, V. Nayagam and F. A. Williams (2008) **32**, 1119-1126, and have been submitted for publication in *Combustion and Flame*, "Theory of the propagation dynamics of spiral edges of diffusion flames in von Kármán swirling flows," by J. Urzay, V. Nayagam and F. A. Williams (2010). The thesis author is the primary investigator in these publications.

Chapters 7 to 10, in part, have been published in *Physics of Fluids*, "The elasto-hydrodynamic force on a sphere near a soft wall," by J. Urzay, S. G. Llewellyn Smith and B. J. Glover (2007) **19** 103106 1-7, and in the *Journal of Fluid Mechanics*, "Asymptotic theory of the elastohydrodynamic adhesion and gliding motion of a solid particle over soft substrates at low Reynolds numbers," by J. Urzay (2010) (In Press). The thesis author is the primary investigator in these publications.

Chapters 11 to 13, in part, have been published in the *Journal of Theoretical Biology*, "Wind gusts and plant aeroelasticity effects on the aerodynamics of pollen shedding: a hypothetical turbulence-initiated wind-pollination mechanism," by J. Urzay, S. G. Llewellyn Smith, E. Thompson and B. J. Glover (2009) **259** 785-792. The thesis author is the primary investigator in this publication.

Experiments in Part I were performed by Dr. V. Nayagam at the National Center for Space and Exploration Research, NASA Glenn Research Center, Cleveland (OH). This investigation was partially funded by the NASA Microgravity Combustion Science Program.

Experiments in Part III were performed by Dr. E. Thompson and Dr. B. J Glover at the Department of Plant Sciences in the University of Cambridge (UK). This investigation was funded by the Human Frontier Science Program, grant #RGY 0073/2005.

VITA

March 11, 1982	Born, Madrid, Spain.
2004-2005	Undergraduate Research Assistant, Departmento de Ingeniería Térmica y de Fluidos, Universidad Carlos III de Madrid, Spain.
Sept. 7, 2005	Ingeniero Superior Industrial, Departmento de Ingeniería Térmica y de Fluidos, Universidad Carlos III de Madrid, Spain.
2005-2007	Graduate Research Assistant, Department of Mechanical and Aerospace Engineering, University of California San Diego, USA.
Dec. 9, 2006	Master of Science in Aerospace Engineering, Department of Mechanical and Aerospace Engineering, University of California San Diego, USA.
2007-2008	Teaching Assistant, Department of Mechanical and Aerospace Engineering, University of California San Diego, USA.
2008	Outstanding Teaching Assistant Award, Department of Mechanical and Aerospace Engineering, University of California San Diego, USA.
2008-2009	Senior Teaching Assistant, Department of Mechanical and Aerospace Engineering, University of California San Diego, USA.
2009	Lecturer, Department of Mechanical and Aerospace Engineering, University of California San Diego, USA.
2010	Doctoral Dissertation Fellowship, Department of Mechanical and Aerospace Engineering, University of California San Diego, USA.
June 11, 2010	Doctor of Philosophy in Aerospace Engineering, Department of Mechanical and Aerospace Engineering and Center for Energy Research, University of California San Diego, USA.

PUBLICATIONS

Urzay J., Llewellyn Smith S. G. and Glover B. J. (2007), "The elastohydrodynamic force on a sphere near a soft wall," *Physics of Fluids* 19, 103106, 1-7.

Urzay J., Nayagam V. and Williams F. A. (2008), "Diffusion-flame extinction on a rotating porous-disk burner," *Proceedings of the Combustion Institute* 32, 1119-1126.

Urzay J., Llewellyn Smith S. G., Thompson E. and Glover B. J. (2009), "Wind gusts and plant aeroelasticity effects on the aerodynamics of pollen shedding: a hypothetical turbulence-initiated wind-pollination mechanism," *Journal of Theoretical Biology* 259, 785-792.

Urzay J. (2010), "Asymptotic theory of the elastohydrodynamic adhesion and gliding motion of a solid particle over soft substrates at low Reynolds numbers," *Journal of Fluid Mechanics* (In Press).

Urzay J., Nayagam V. and Williams F. A. (2010), "Theory of the propagation dynamics of spiral edges of diffusion flames in von Kármán swirling flows," *Combustion and Flame* (Submitted).

INVITED SEMINARS

Urzay J., "Dynamics and extinction of stretched diffusion flames in von Kármán swirling flows," (faculty search seminar) Department of Fire Protection Engineering, A. James Clark School of Engineering, University of Maryland, College Park MD, Jan. 2009.

Urzay J., "Fundamental studies in combustion and fluid dynamics," (faculty search seminar) Departamento de Ingeniería Aeroespacial, Escuela Politécnica Superior, Universidad Carlos III de Madrid, Spain, March 2010.

FIELDS OF STUDY

Major Field: **Aerospace Engineering**

Studies in Combustion
Professor Forman A. Williams.

Studies in Fluid Mechanics
Professors Stefan G. Llewellyn Smith and Kraig Winters.

Studies in Turbulence
Professors Sutanu Sarkar and Laurence Armi.

Studies in Environmental Fluid Dynamics
Professor James Rottman.

Studies in Gasdynamics
Professors Forman A. Williams and Yousef M. Bahadori.

Studies in Applied Mathematics
Professors Glenn Ierley, William R. Young and Daniel Tartakovsky.

Studies in Numerical Analysis
Professor Thomas R. Bewley.

ABSTRACT OF THE DISSERTATION

Theoretical Studies in Spiral Edge-Flame Propagation and Particle Hydrodynamics

by

Javier Urzay

Doctor of Philosophy in Engineering Sciences (Aerospace Engineering)

University of California, San Diego, 2010

Professor Forman A. Williams, Chair
Professor Stefan G. Llewellyn Smith, Co-Chair

Applied mathematics techniques are used in this investigation to gain insight into three different physical processes of current interest in combustion and fluid dynamics.

The first problem addresses the propagation of spiral edge flames found in von Kármán swirling flows induced in rotating porous-disk burners. In this configuration, a porous disk is spun at a constant angular velocity in an otherwise quiescent oxidizing atmosphere. Gaseous methane is injected through the disk pores and burns in a flat diffusion flame adjacent to the disk. Among other flame patterns experimentally found, a stable, rotating spiral flame is observed for sufficiently large rotation velocities and small fuel flow rates as a result of partial extinction of the underlying diffusion flame. The tip of the spiral can undergo a steady rotation for sufficiently large rotational velocities or small fuel flow rates, whereas a meandering tip in an epicycloidal trajectory is observed for smaller rotational velocities and larger fuel flow rates. A formulation of this problem is presented in the equidiffusional and thermodiffusive limits within the framework of one-step chemistry with large activation energies. Conditions for extinction of the underlying uniform diffusion flame are obtained by using activation energy asymptotics. Edge-flame propagation regimes are obtained by scaling analyses of the conservation equations and exemplified by numerical simulations of nearly straight two-dimensional edge flames near a cold porous wall in a von Kármán boundary layer, for which lateral heat losses to the disk induce extinction of the

trailing diffusion flame but are relatively unimportant in the front region, consistent with the existence of the cooling tail found in the experiments. The propagation dynamics of a steadily rotating spiral edge is studied in the large-core limit, for which the characteristic Markstein length is much smaller than the distance from the center at which the spiral tip is anchored. An asymptotic description of the edge tangential structure is obtained, spiral edge shapes are calculated, and an expression is found that relates the spiral rotational velocity with the rest of the parameters. A quasistatic stability analysis of the edge shows that the edge curvature at extinction in the tip region is responsible for the stable tip anchoring at the core radius. Finally, experimental results are analyzed, and theoretical predictions are tested.

The second problem analyzes, in the limit of small Reynolds and ionic Péclet numbers and small clearances, the canonical problem of the forces exerted on a small solid spherical particle undergoing slow translation and rotation in an incompressible fluid moving parallel to an elastic substrate, subject to electric double-layer and van der Waals intermolecular forces, as a representative example of particle gliding and of the idealized swimming dynamics of more complex bodies near soft and sticky surfaces in a physiological solvent. The competition of the hydrodynamic, intermolecular and surface-deformation effects, induces a lift force, and drag-force and drift-force perturbations, which do not scale linearly with the velocities, and produces a non-additivity of the intermolecular effects by reducing the intensity of the repulsive forces and by increasing the intensity of the attractive forces. Reversible and irreversible elastohydrodynamic adhesion regimes are found, and elastohydrodynamic corrections are derived for the critical coagulation concentration of electrolyte predicted by the the Derjaguin-Landau Verwey-Overbeek (DLVO) standard theory of colloid stabilization.

The third problem addresses the dynamics of pollen shedding from wind-pollinated plants, and establishes a fluid-dynamical framework for future refinements. A simple scaling analysis, supported by experimental measurements on typical wind-pollinated plant species, is used to estimate the suitability of previous resolutions of this process based on wind-gust aerodynamic models of fungal-spore liberation. According to this scaling analysis, unsteady boundary-layer forces produced by wind gusts are found to be mostly ineffective since the Stokes-Reynolds number is a small parameter for typical anemophilous species and wind streams. A hypothetical model of a stochastic aeroelastic mechanism, initiated by the atmospheric turbulence typical of the micrometeorological conditions in the vicinity of the plant, is proposed to contribute to wind pollination.

Part I

Combustion and Propagation of Spiral Edges of Diffusion Flames in Von Kármán Swirling Flows

NOMENCLATURE

a	Disk radius (m)
A	Pseudo-collision frequency of the global step (1/s)
α	Mass of fuel feed stream needed to burn a unit mass of air in stoichiometric proportions (-)
$\mathcal{B}$	Mass-transfer number (-)
β	Dimensionless heat loss coefficient (-)
β_{fl}	Dimensionless heat loss coefficient in the diffusion flame (-)
β_{fr}	Dimensionless heat loss coefficient in the frozen mixture (-)
χ	Scalar dissipation rate (1/s)
$\widetilde{\chi}$	Normalized scalar dissipation rate (-)
$\widetilde{\chi}_{fl}$	Normalized scalar dissipation rate in the flame (-)
$\widetilde{\chi}_S$	Normalized scalar dissipation rate on the disk surface (-)
c_p	Average specific heat (J/kgK)
Da	Pseudo-collision Damköhler number (-)
Δ	Reduced Damköhler number (-)
Δ_E	Reduced Damköhler number at extinction (-)
Δ_f	Reduced Damköhler number of the front (-)
Δ_{fl}	Reduced Damköhler number of the diffusion flame (-)
δ_f	Front thickness (m)
δ_{fl}	Diffusion-flame thickness (m)
δ_L^0	Planar premixed-flame thickness (m)
δ_M	Mixing-layer thickness (m)
ΔT	Difference between the atmosphere and disk temperatures (K)
D_T	Average thermal diffusivity (m^2/s)
η	Inner coordinate in the diffusion-flame reaction region (-)
ϵ	inverse of the Zel'dovich number (-)
F	Auxiliar indicator function (-)
G	Indicator function (-)
γ	Leakage parameter (-)
Γ	Edge-flame propagation parameter (-)
H	Excess enthalpy (J)
H_f	Excess enhalpy in the front (J)

H_{fl}	Excess enthalpy in the diffusion flame (J)
H_{fr}	Excess enhalpy in the frozen mixture (J)
H_S	Excess enthalpy on the disk surface (J)
$\mathcal{K}_s$	Tangential curvature (1/m)
ℓ	Characteristic radial distance of tip anchoring (m)
λ	Dimensionless Markstein diffusivity (-)
$\dot{m}''$	Fuel mass flow rate p.u. surface (kg/m^{2}s)
Ma	Markstein number (-)
n	Normal intrinsic coordinate (m)
n_E	Cooling-tail length (m)
ω	Spiral rotational velocity (rad/s)
Ω	Disk rotational velocity (rad/s)
P_∞	Ambient pressure (Pa)
ϕ	Dimensionless self-similar stream function (-)
ϕ_∞	Dimensionless air entrainment (-)
$\lvert\phi'_{fl}\rvert$	Dimensionless radial velocity gradient in the flame (-)
Pr	Average Prandtl number
Q	Chemical heat release p.u. mass of fuel (J/kg)
r	Radial distance (m)
$r^\bigstar$	Core radius (m)
Re_j	Injection Reynolds number or injection parameter (-)
ρ	Average density (kg/m^3)
s	Tangential intrinsic coordinate (m)
S	Mass of oxidizer burnt p.u. mass of fuel in stoichiometric proportions (-)
$\mathcal{S}$	Swirl number (-)
$\mathrm{S}^0_{L,st}$	Planar premixed-flame speed in stoichiometric proportions (m/s)
σ	Intermediate coordinate in the tip region (-)
t	Time coordinate (s)
t_E	Time for extinction of the diffusion flame (s)
T	Temperature (K)
T_a	Activation temperature of the global step (K)

T_∞	Atmosphere temperature (K)
T_f	Dimensionless front temperature (K)
T_{fl}	Dimensionless diffusion-flame temperature (K)
T_{fl}^∞	Adiabatic flame temperature (K)
T_S	Disk surface temperature (K)
$\mathrm{U_{LF}}$	Laboratory-frame velocity of the front (m/s)
$\mathrm{U_n}$	Edge-flame propagation velocity (m/s)
$\mathrm{U_n^0}$	Straight edge-flame propagation velocity (m/s)
Υ	Quasi-static stability parameter (-)
$\mathbf{v}$	Hydrodynamic velocity (m/s)
$\mathbf{v}_\perp$	Two-dimensional hydrodynamic velocity field (m/s)
$\mathbf{v}_{\mathrm{n,rel}}$	Hydrodynamic velocity relative to the edge flame (m/s)
φ	Tangent of the slope angle of the front (-)
V_{fl}	Dimensionless azimuth velocity gradient in the flame (-)
W_F	Fuel molecular weight (kg/mol)
W_{O_2}	Oxidizer molecular weight (kg/mol)
ξ	Inner coordinate in the tip region (-)
Y_{iS}	Mass fraction on the disk surface (-)
$Y_{F,F}$	Fuel mass fraction in the fuel feed stream (-)
$Y_{F,st}$	Fuel mass fraction at stoichiometric proportions (-)
$Y_{O_2,A}$	Atmospheric oxidizer mass fraction (-)
$Y_{O_2,st}$	Oxidizer mass fraction at stoichiometric proportions (-)
$\hat{Y}_i$	Mass fraction normalized with the corresponding stoichiometric mass fraction
Z	Mixture fraction (-)
z_{fl}	Dimensionless flame stand-off distance (-)
$\widetilde{Z}$	Mixture fraction normalized with that on the disk surface (-)
$\widetilde{Z}_{fl}$	Normalized stoichiometric mixture fraction
Z_S	Mixture fraction on the disk surface (-)
$\widetilde{Z}^\star$	Stretched, normalized mixture fraction (-)
Z_{st}	Stoichiometric mixture fraction (-)

Chapter 1

Introduction

Premixed combustion, where the fuel and oxidizer are completely mixed before entering into the combustion chamber, and non-premixed combustion, where the fuel and oxidizer are injected separately, are the two fundamental modes of combustion upon which the basis of the combustion theory was first formulated [1]. However, in aerospace and automotive propulsion applications such as gas turbines, direct-injection gasoline engines and diesel engines, combustion occurs in neither of these two pure modes. In such systems, fuel and oxidizer enter separately in the combustion chamber, they become partially mixed by turbulence, and flame propagation occurs in the stratified mixture once it has been ignited. This combustion mode is often referred to as partially premixed [2]. Similar to the premixed and diffusion flames in premixed and non-premixed combustion respectively, the corresponding canonical problem in partially premixed combustion is the propagation of triple flames in strained mixing layers [3-8]. A triple flame is a tri-brachial structure composed of a fuel-lean premixed front, an oxidizer-lean premixed front, and a trailing diffusion flame where the excess reactants burn in a diffusion-controlled regime. The two premixed wings are curved since the premixed-flame speed decreases with departures from stoichiometric proportions. The propagation dynamics of triple flames is mainly dominated by the composition gradient of the mixture, or, equivalently, by the characteristic diffusion time of the reactants through the flame thickness. Long diffusion times (small composition gradients) produce strong and advancing quasi-planar premixed fronts within which reactant depletion occurs in a much shorter chemical time scale, followed by a strong diffusion flame that burns at a much slower rate. Short diffusion times (large composition gradients) produce highly curved wings and, sometimes, the absence of the tri-brachial structure, resulting in a slender edge flame followed by a weak diffusion flame, where the

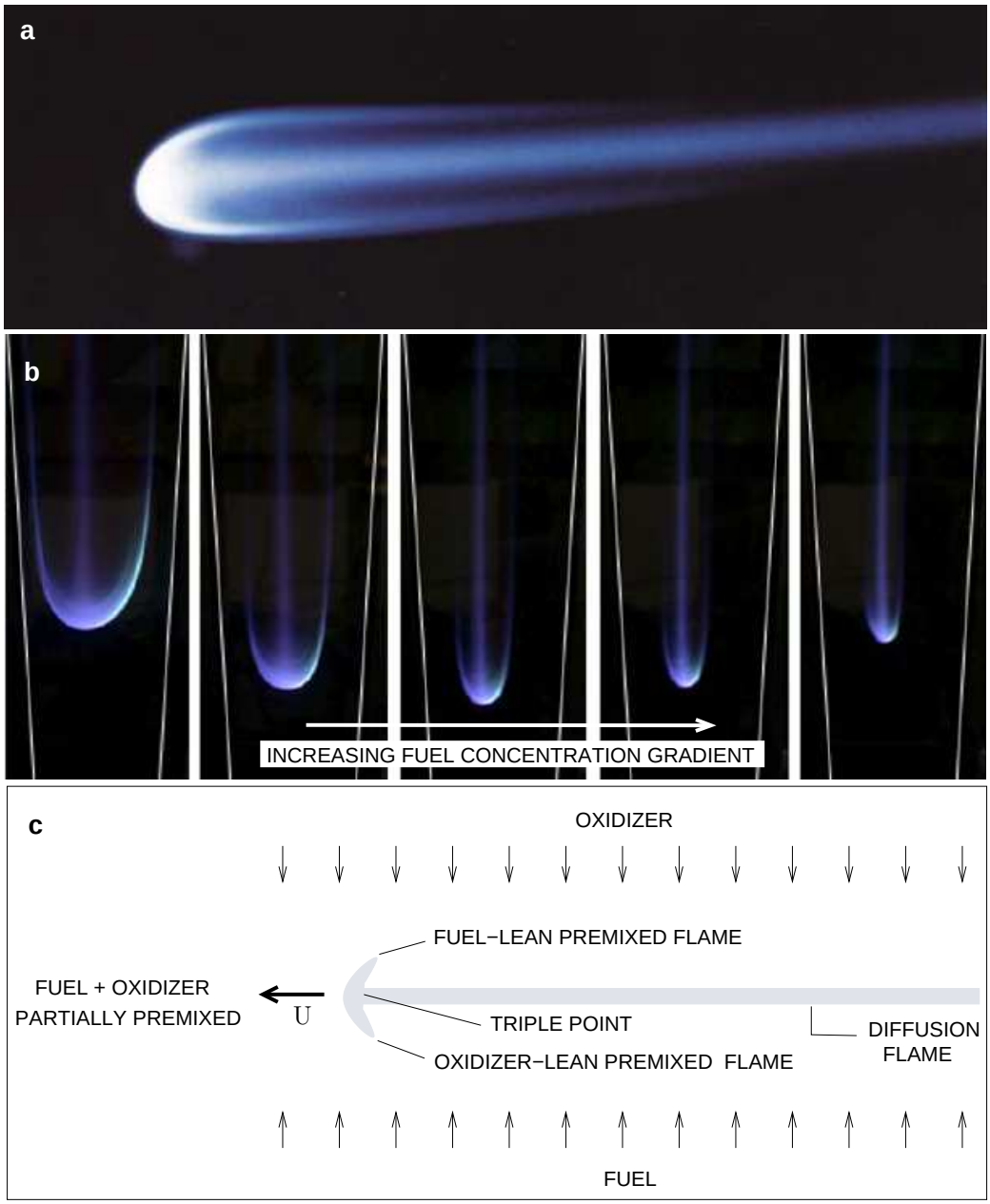

Figure 1.1: (a) Direct image of a CH_4-air triple flame (adapted from [6]), (b) Direct images and effects of fuel concentration gradient on CH_4-air triple flames (adapted from [9]), (c) Schematics of a triple flame propagating from right to left in a strained mixing layer.

chemical depletion process is slowed down by the short residence time of the reactants in the flame. In both limits, the resulting imbalance between the streamwise heat diffusion and chemical heat release produce advancing or retreating motions of the entire flame kernel at velocities that correspond to eigenvalues of the problem. The resolution of triple flames

in general flows constitutes a formidable challenge from the analytical and computational standpoints because of the intrinsic eigenvalue character of the problem and the associated flame stabilization difficulties. Figure 1.1 shows experimental visualizations of triple flames and their schematics.

Swirling flows enhance fuel and oxidizer mixing at the molecular level, promote combustion and flame propagation [1, 2], and reduce emissions [10]. Examples of combustion enhancement by increased mixing occur naturally in fire whirls, or in specific engineering designs such as swirl combustors in gas turbines, swirl-generating inlet ports and swirl piston bowls in internal combustion engines. The interaction of flames with swirling air flows in combustion chambers can enhance local extinction for sufficiently large strain rates or heat losses. The boundaries produced by these local extinction phenomena are edge flames, which propagate through the mixture with characteristics similar to those of deflagrations [3]. In swirling boundary layers, local quenching can produce a number of flame patterns and flame fronts, such as straight edge flames, single spiral edge flames, multiple spiral edge flames, flame rings and flame holes, that propagate in the mixture in a nontrivial manner [11-14].

From a broader physical standpoint, spiral patterns are ubiquitous in nature. The Belousov-Zabothinsky reaction and the catalytic surface oxidation of CO are examples of spiral pattern formation found in physical chemistry. Cell aggregation and calcium waves are examples of spiral patterning in cell signaling. Similarly, cardiac fibrillation waves take the form of meandering spirals, and whirlpool galaxies also display spiral-shaped arms. Some of these patterns are shown in figure 1.2. Excitability is a common characteristic shared by all these systems. The concept of excitability of a system regards its ability to trigger abrupt and substantial responses -by means of the autocatalytic production of a propagator or trigger variable- to disturbances from a rest state that cross certain characteristic thresholds [15]. After such a response the system momentarily shows a refractory behavior moderated by a controller or refractory variable, in that the system is immune to further stimulation and eventually recovers full excitability. The first four rows in table 1.1 identify the different propagator and controller variables found in four common physical systems [16, 17].

In the context of flame propagation in stratified mixtures, excitability is related to the reactivity of the mixture and the high sensitivity to temperature because of the effectively high overall activation energy involved in typical combustion chemical reactions. Although the trajectory of a fluid particle occurs generally in a multidimensional space, its initial and final states can be placed on a S-curve response of a diffusion flame [23] as shown

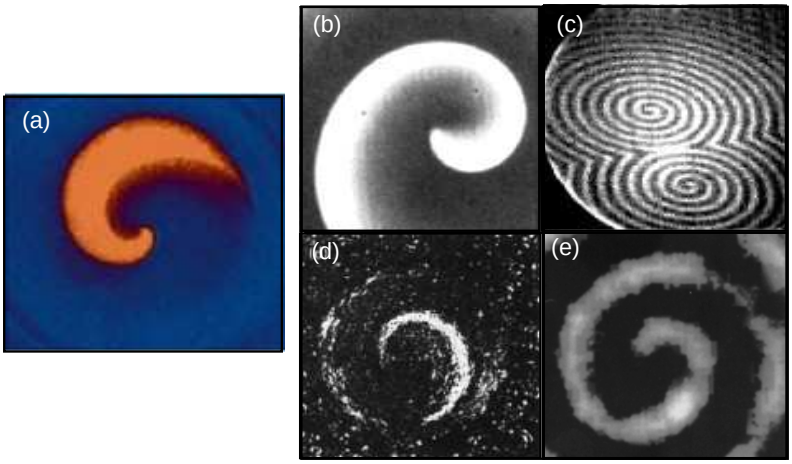

Figure 1.2: Examples of spiral patterns found in nature, (a) spiral diffusion flames (adapted from [18]), (b) Belousov-Zhabotinsky reaction (adapted from [19]), (c) catalytic CO-Pt surface reaction (adapted from [20]), (d) multicellular aggregation (adapted from [21]), (e) calcium waves (adapted from [22]).

Table 1.1: Representative propagator and controller variables corresponding to the systems of figure 1.2.

System	Propagator	Controller
BZ reaction	bromous acid	ferroin
Surface catalysis	temperature	catalytic activity
Cell aggregation	cyclic adenosine monophosphate	membrane receptor
Calcium waves	membrane potential	ionic conductance
Spiral edge flames	temperature	lateral heat loss

in figure 1.3(a), which represents the maximum temperature as a function of the reduced Damköhler number Δ, which is defined as

$$\Delta = \frac{t_d}{t_c}, \tag{1.1}$$

where t_d is the diffusion time through the flame or flame-transit time, and t_c is the local chemical time in the flame. Spatial regions of sufficiently low temperature, in which the mixture remains chemically frozen, may be thought of as a rest state, from which an appreciable excursion may occur when Δ is sufficiently large to trigger thermal runaway and ignite the mixture. Flame propagation and diffusion of heat into neighboring regions occur

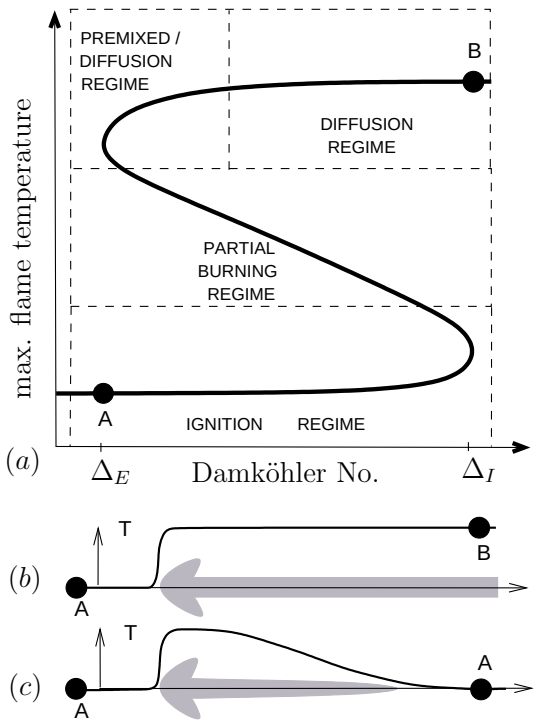

Figure 1.3: (a) Schematic representation of the S-curve response of a diffusion flame. The frozen and Burke-Schumann rest states are denoted by A and B, respectively. (b) Temperature profile along the stoichiometric line of a vigorously burning edge flame. (c) Temperature profile along the stoichiometric line of an edge whose diffusion flame has undergone extinction.

once the mixture has been ignited, causing the excitation process to spread spatially into zones initially frozen. For large activation energies and adiabatic systems, the region downstream from the front is close to a Burke-Schumann or equilibrium rest state, involving a reaction zone into which each reactant diffuses and reacts producing a diffusion flame, as in figure 1.3(b). This trailing flame extends infinitely far downstream from the front as in an adiabatic, equidiffusive edge flame or triple flame [3-8].

For a spiral edge flame, the system achieves the rest state again by means of an extinction tail, as in figure 1.3(c). As shown further below, lateral heat losses to the burner surface extinguish the flame when the flame temperature is sufficiently small for the local Δ to be small, such that the local chemical time becomes large and of the same order as the diffusion time, which produces leakage of unburnt reactants, an associated flame-temperature drop and flame extinction. After extinction, the gaseous mixture is at first refractory to another disturbance, but it finally recovers full ignitability when the reactants are replenished by advection, reproducing the same edge-flame pulse after one revolution

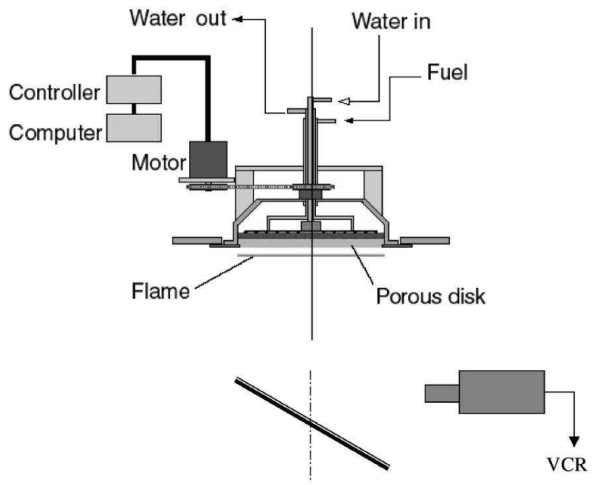

Figure 1.4: Schematic illustration of the experimental apparatus.

provided that no mixing histeresis has taken place. While this discussion describes how spiral-flame phenomena may be related in general to spiral waves in excitable media, it will be seen later that figure 1.3(a) does not precisely describe the specific experiments of figure 1.2(a), in that the indicated ignition event, in fact, is not involved in the physics of the actual process.

However similar at first sight, pattern formation in diffusion flames is a qualitatively and quantitavely different problem than those shown in figure 1.2(b-e), which mainly correspond to reactive-diffusive systems; contrary to the intrinsic two-dimensional diffusive dynamics of the processes of figure 1.2(b-e), three-dimensional diffusion and advection effects make the analytical and numerical tractability of the spiral flames quite more challenging. Additionally, the strong non-linearities associated with the reaction term in flames are typically exponential in the temperature as in the Zeldovich-Frank-Kamenetskii theory [24], which produces sharp interfaces and singular behaviors, whereas classical developments in reactive-diffusive systems have typically used smoother polynomial non-linearities to account for the propagator source as in the Kolmogorov-Petrovskii-Piskunov theory [25]. Finally, unlike earlier analyses performed on the modelling of the processes shown in figure 1.2(b-e), the conservation equations and chemical reaction rates used in combustion systems stem from fundamental principles of the kinetic theory of gases, which confers more rigor on the present investigation.

A set of controlled experiments performed with the porous-disk burner demonstrated the existence of a map of flame patterns [12]. The experiments used a sintered bronze,

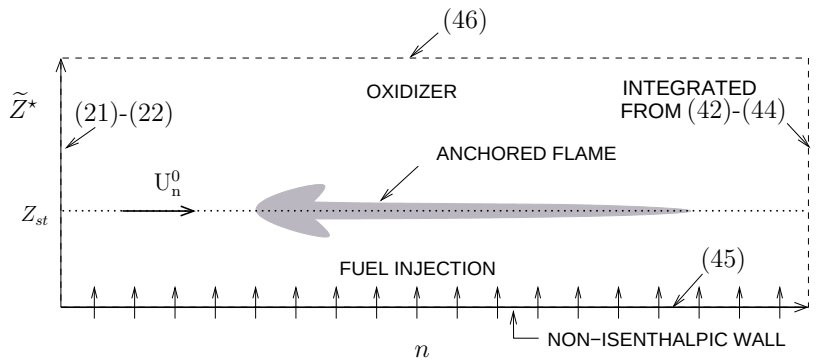

Figure 1.5: Summary of experimental flame patterns in the rotating porous-disk burner [12].

water-cooled porous disk of radius $a = 10$ cm. Gaseous methane was fed to the disk with uniform and constant fuel flow rate $\dot{m}'' = 0.2 - 2.0$ g/m^{2}s from a compressed-gas bottle of fuel mass fraction $Y_{F,F} \approx 1.0$, and injection temperature $T_S \approx 300$ K equal to the disk cooling temperature. The exposed disk porous surface was oriented facing downwards to avoid buoyant instabilities, in an otherwise quiescent oxidizing atmosphere of oxidizer mass fraction $Y_{O_2,A} \approx 0.24$, and temperature $T_\infty \approx 300$ K, and it was spun at a constant angular velocity $\Omega = 2 - 50$ rad/s. The experimental arrangement is depicted in figure 1.4. Further details of the experimental results are given in Chapter 5. The experimental flame patterns studied in this investigation are shown in figure 1.5. At moderate fuel injection rates, as Ω was increased the axisymmetric diffusion flame developed a pulsating flame hole. This mode has been studied in earlier works [26-28] for both the rotating disk and counterflow flames by using simplified algebraic models of the underlying diffusion flame [29]. An increase in the disk rotational velocity caused transition to a single-armed, counter-rotating spiral flame, with characteristics similar to those of the spiral flames observed in burning solid fuels as described elsewhere [18]. Further increase in Ω caused transition to flame modes such as multi-armed spirals and flame rings, which probably were influenced by edge effects. The flame was finally blown off the disk at higher Ω. Total flame extinction was achieved for sufficiently small $\dot{m}''$ or high Ω. Disk water-cooling ensured that the observed patterns were not caused or stabilized by thermal inertial effects of the disk. The downward-facing arrangement favored a flat flame, buoyant instabilities being suppressed by the closeness of the flame to the disk.

This part of the thesis is organized into five additional chapters. Chapter 2 is dedicated to a general formulation of the problem in the laboratory frame within the framework

of a thermodiffusive, equidiffusional model using a single-step chemical reaction of large activation energy. Chapter 3 addresses the dynamics of a diffusion flame enveloping the entire disk. Chapter 4 is dedicated to the analysis of the propagating dynamics of spiral edge flames. Finally, experimental results are analyzed and theoretical predictions are tested in Chapter 5, and conclusions are drawn in Chapter 6.

Chapter 2

Laboratory-frame formulation

A schematic diagram of the problem is shown in figure 2.1, which follows the experimental set-up introduced in the preceding Chapter and contains the most relevant variables. A formulation based on the thermodiffusive and equidiffusional description of the underlying one-dimensional diffusion flame, using a single-step chemical reaction of large activation energy, is developed in what follows. Thus, the density ρ, viscosity ν, specific heat c_p, thermal diffusivity D_T and Prandtl number $\mathrm{Pr} = \nu/D_T$ are taken to be those of the air at normal conditions. These approximations are reasonable for not-too-large rotation rates, small heat-release parameters and near-extinction flames [30], and for near-unity Lewis numbers as in methane-air non-premixed combustion systems [31], for which the fuel and oxidizer Lewis numbers $\mathrm{Le}_F = D_T/D_F = 0.97$ and $\mathrm{Le}_{O_2} = D_T/D_{O_2} = 1.11$ are sufficiently close to unity.

2.1 Hydrodynamic field

In the conditions relevant to these experiments, that is at moderately high bulk Reynolds numbers $\mathrm{Re}_a = \Omega a^2/\nu \sim 10^4$, as the burner rotates the viscous effects are confined to a thin boundary layer of approximate thickness $\delta_M = \sqrt{\nu/\Omega}$ [32], which is obtained by a balance of centrifugal pressure, of $O(\rho\delta_M^2\Omega^2)$ and shear stress, of $O(\nu\rho\Omega)$, with $\delta_M/a \ll 1$. The rotation of the disk induces an entrainment of the ambient fluid with a characteristic velocity $\Omega\delta_M$. This fluid is carried by the disk surface through friction and is ejected centrifugally with a characteristic velocity $\Omega\delta_M r$, where r is the ratio of the radial coordinate to δ_M. This velocity is much larger than the entrainment velocity at sufficiently large radial distances from the center, $r \gg 1$.

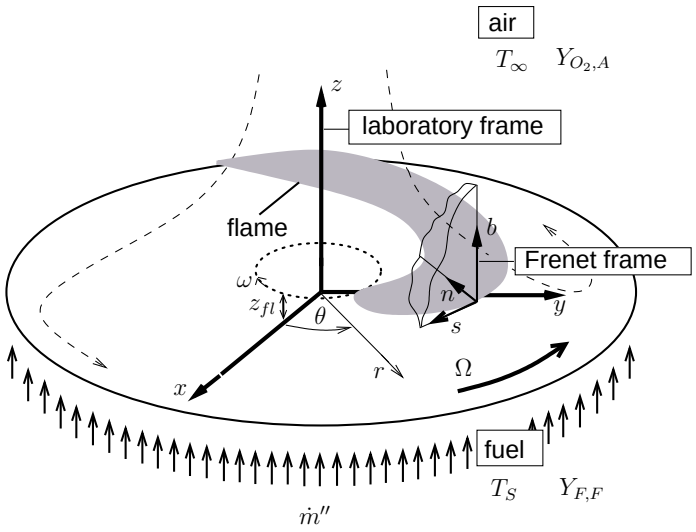

Figure 2.1: The model problem.

A derivation of the von Kármán flow is summarized below for illustrative purposes. The conservation equations are written in nondimensional variables, with δ_M the unit of length, $\delta_M\Omega$ the unit of velocity and $\rho\delta_M^2\Omega^2$ the unit of pressure. In these variables, a cylindrical coordinate system $\{r, \theta, z\}$ is introduced, and the mass and momentum conservation equations for the velocity vector $\mathbf{v} = (\mathrm{v}_r, \mathrm{v}_\theta, \mathrm{v}_z)$ and pressure P become

$$\frac{1}{r}\frac{\partial}{\partial r}(r\mathrm{v}_r) + \frac{\partial \mathrm{v}_z}{\partial z} = 0, \tag{2.1}$$

$$\mathrm{v}_r\frac{\partial \mathrm{v}_r}{\partial r} - \frac{\mathrm{v}_r^2}{r} + \mathrm{v}_z\frac{\partial \mathrm{v}_r}{\partial z} = -\frac{\partial P}{\partial r} + \frac{\partial}{\partial r}\left[\frac{1}{r}\frac{\partial}{\partial r}(r\mathrm{v}_r)\right] + \frac{\partial^2 \mathrm{v}_r}{\partial z^2}, \tag{2.2}$$

$$\mathrm{v}_r\frac{\partial \mathrm{v}_\theta}{\partial r} + \frac{\mathrm{v}_r\mathrm{v}_\theta}{r} + \mathrm{v}_z\frac{\partial \mathrm{v}_\theta}{\partial z} = \frac{\partial}{\partial r}\left[\frac{1}{r}\frac{\partial}{\partial r}(r\mathrm{v}_\theta)\right] + \frac{\partial^2 \mathrm{v}_\theta}{\partial z^2}, \tag{2.3}$$

$$v_r\frac{\partial \mathrm{v}_z}{\partial r} + v_z\frac{\partial \mathrm{v}_z}{\partial z} = -\frac{\partial P}{\partial z} + \frac{1}{r}\frac{\partial}{\partial r}\left(r\frac{\partial \mathrm{v}_z}{\partial r}\right) + \frac{\partial^2 \mathrm{v}_z}{\partial z^2}, \tag{2.4}$$

where azimuth transport terms have been dropped because of the rotational symmetry of the flow. Equations (4.15)-(2.4) are subject to non-slip and far-field boundary conditions,

$$z = 0, \qquad \mathrm{v}_r = 0, \quad \mathrm{v}_\theta = r, \quad \mathrm{v}_z = \mathrm{Re}_j, \tag{2.5}$$

$$z \to \infty, \qquad \mathrm{v}_r \to 0, \quad \mathrm{v}_\theta \to 0, \quad v_z \to \phi_\infty(\mathrm{Re}_j), \quad P \to P_\infty, \tag{2.6}$$

In this formulation, $\phi_\infty = O(1)$ is the dimensionless air entrainment far from the disk and is calculated as part of the hydrodynamic solution, and

$$\mathrm{Re}_j = \frac{\dot{m}''}{\rho\sqrt{\nu\Omega}} \tag{2.7}$$

is the injection Reynolds number or dimensionless fuel injection rate Re_j, defined as the ratio of the injection velocity $\dot{m}''/\rho$ to the characteristic entrainment normal to the disk $\delta_M\Omega$. The typical values of Re_j encountered in the experiments are found to be much smaller than unity for most of the studied data range as shown in Chapter 5, which involves small injection velocities. Substituting the von Kármán transform

$$\mathbf{v} = -\frac{\phi'(z)r}{2}\mathbf{e_r} + V(z)r\mathbf{e}_\theta + \phi(z)\mathbf{e_z}, \tag{2.8}$$

into (2.2) and (2.3), the equations

$$\phi''' = \phi''\phi - \phi'^2/2 + 2V^2, \tag{2.9}$$

$$V'' = \phi V' - \phi' V, \tag{2.10}$$

are obtained, which are subject to

$$z = 0, \qquad \phi = \mathrm{Re}_j, \quad \phi' = 0, \quad V = 1, \tag{2.11}$$

$$z \to \infty, \qquad \phi \to \phi_\infty(\mathrm{Re}_j), \quad \phi' \to 0, \quad V \to 0. \tag{2.12}$$

In this formulation, $\phi(z)$ is a self-similar stream function given by

$$\phi = 2\psi/r^2 \tag{2.13}$$

in terms of the two-dimensional stream function ψ, which can be related to the velocity components by

$$v_r = -\frac{1}{r}\frac{\partial\psi}{\partial z} \quad \text{and} \quad v_z = \frac{1}{r}\frac{\partial\psi}{\partial r}. \tag{2.14}$$

The strain rate, vorticity and static pressure depend solely on z as a consequence of the radial uniformity of the entrainment. Equation (2.4) can be used to obtain an expression for the normal distribution of static pressure, which is an irrelevant variable that can be eliminated in this thermodiffusive framework. These considerations are not accurate near the disk edge, where the self-similarity imposed by (2.8) is lost and the velocity normal to the disk and the normal strain rate do not depend solely on the normal coordinate z, so that the present calculation implicitly assumes a flow over an infinite disk with uniform air entrainment.

Figure 2.2 shows the velocity components v_r, v_θ and v_z given by (2.8) and the numerical solutions to (2.9)-(2.12)

For $\mathrm{Re}_j \ll 1$, the asymptotic expansions

$$\begin{aligned} \phi &= \phi_0 + \mathrm{Re}_j\phi_1 + O(\mathrm{Re}_j^2), \\ V &= V_0 + \mathrm{Re}_j V_1 + O(\mathrm{Re}_j^2). \end{aligned} \tag{2.15}$$

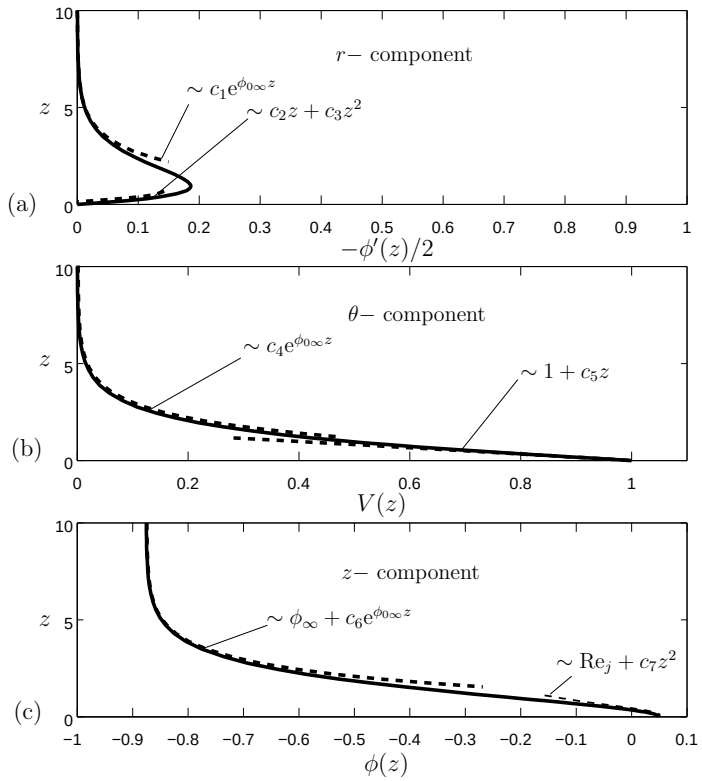

Figure 2.2: Numerical (solid line) and asymptotic (dashed line) profiles for the (a) radial velocity, (b) azimuth component, and (c) vertical component of the flow velocity, for $\mathrm{Re}_j = 0.05$. In this figure, $\phi_{0\infty} = -0.884$, $c_1 = 0.924 + 2.620\mathrm{Re}_j$, $c_2 = 0.510 + 0.046\mathrm{Re}_j$, $c_3 = -0.500 + 0.510\mathrm{Re}_j$, $c_4 = 1.202 + 2.425\mathrm{Re}_j$, $c_5 = -0.616 + 0.412\mathrm{Re}_j$, $\phi_\infty = -0.884 + 0.202\mathrm{Re}_j$, $c_6 = 2.091 + 5.926\mathrm{Re}_j$, $c_7 = \mathrm{Re}_j$ and $c_8 = -c_2$ are constants calculated numerically.

are introduced into (2.9)-2.12). To leading order in Re_j, the conservation equations (2.9) and (2.10) correspond to a von Kármán swirling flow with zero fuel injection [32],

$$\phi_0''' = \phi_0\phi_0'' + 2V_0^2 - \frac{\phi_0'^2}{2}, \tag{2.16}$$

$$V_0'' = \phi_0 V_0' - \phi_0' V_0, \tag{2.17}$$

subject to

$$z = 0, \qquad \phi_0 = 0, \quad \phi_0' = 0, \quad V_0 = 1, \tag{2.18}$$

$$z \to \infty, \qquad \phi_0 \to \phi_{0\infty}, \quad \phi_0' \to 0, \quad V_0 \to 0. \tag{2.19}$$

For small z, equations (2.16) and (2.17) can be reduced to $\phi_0''' \sim 2$, and $V_0' \sim a_2$ in the first approximation, so that $\phi_0 \sim z^3/3 + a_1 z^2$ and $V_0 \sim 1 + a_2 z$, For large z, $\phi_0''' \sim \phi_{0\infty}\phi_0''$, and $V_0'' \sim \phi_{0\infty} V_0'$, which gives the asymptotic behaviors $\phi_0 \sim \phi_{0\infty} + (b_1/\phi_{0\infty}^2)e^{\phi_{0\infty} z}$ and

$V_0 \sim (b_2/\phi_{0\infty})e^{\phi_{0\infty} z}$. In this formulation

$$a_1 = -0.510, \quad a_2 = -0.616, \quad \phi_{0\infty} = -0.884,$$

$$b_1 = 1.634, \quad \text{and} \quad b_2 = -1.063, \tag{2.20}$$

are constants obtained from solving (2.16)-(2.19) numerically using a nonlinear shooting method with a generalized Newton-Raphson method for achieving convergence.

To second order in Re_j, the conservation equations (2.9) and (2.10)

$$\phi_1''' = \phi_0\phi_1'' + \phi_0''\phi_1 + 4V_0V_1 - \phi_0'\phi_1', \tag{2.21}$$

$$V_1'' = V_1'\phi_0 + V_0'\phi_1 - \phi_0'V_1 - \phi_1'V_0, \tag{2.22}$$

subject to

$$z = 0, \qquad \phi_1 = 1, \quad \phi_1' = 0, \quad V_1 = 0, \tag{2.23}$$

$$z \to \infty, \qquad \phi_1 \to \phi_{1\infty}, \quad \phi_1' \to 0, \quad V_1 \to 0. \tag{2.24}$$

For $z \ll 1$ equations (2.21) and (2.22) reduce to $\phi_1''' \sim 2a_1$ and $V_1'' \sim a_2$, from where $\phi_1 \sim a_1 z^3/3 + a_1' z^2 + 1$ and $V_1 \sim a_2 z^2/2 + a_2' z$. For large z, $\phi_1''' \sim \phi_{0\infty}\phi_1$ and $V_1'' \sim \phi_{0\infty}V_1'$, which gives $\phi_1 \sim \phi_{1\infty} + (b_1'/\phi_{0\infty}^2)e^{\phi_{0\infty} z}$ and $V_1 \sim (b_2'/\phi_{0\infty})e^{\phi_{0\infty} z}$, where the constants

$$a_1' = -0.046, \quad a_2' = 0.412, \quad b_1' = 4.361,$$

$$b_2' = -2.144, \quad \text{and} \quad \phi_{1\infty} = 0.202, \tag{2.25}$$

are numerically evaluated following a similar numerical scheme as before. The entrainment first perturbation $\phi_{1\infty}$ is a positive number, which indicates that the total entrainment is reduced because of the fuel injection.

To summarize, the asymptotic solutions in regions near and far from the disk

$$\begin{aligned}
z \ll 1, \qquad & \phi = a_1 z^2 + z^3/3 + \mathrm{Re}_j(1 + a_1' z^2 + a_1 z^3/3) + O(\mathrm{Re}_j^2), \\
& V = 1 + a_2 z + \mathrm{Re}_j(a_2' z + a_2 z^2/2) + O(\mathrm{Re}_j^2), \\
z \gg 1, \qquad & \phi = \phi_{0\infty} + (b_1/\phi_{0\infty}^2)e^{\phi_{0\infty} z} + \mathrm{Re}_j[\phi_{1\infty} + (b_1'/\phi_{0\infty}^2)e^{\phi_{0\infty} z}] + O(\mathrm{Re}_j^2), \\
& V = (b_2/\phi_{0\infty})e^{\phi_{0\infty} z} + \mathrm{Re}_j(b_2'/\phi_{0\infty})e^{\phi_{0\infty} z} + O(\mathrm{Re}_j^2).
\end{aligned} \tag{2.26}$$

are found, with the constants of integration given by (2.20) and (2.26). A comparison with the numerical solution to (2.9)-(2.12) is shown in figure 2.2.

2.2 Chemical kinetics model

The chemical reaction is considered to be a single-step, second-order irreversible reaction between methane and the oxygen of the air,

$$CH_4 + 2O_2 \rightarrow CO_2 + 2H_2O,$$

with a dimensionless global rate of reaction

$$\hat{\omega} = \mathrm{Da}\hat{Y}_F\hat{Y}_{O_2}\mathrm{e}^{-T_a/T}. \tag{2.27}$$

In this formulation, $\hat{Y}_F$ and $\hat{Y}_{O_2}$ are the fuel and oxidizer mass fractions nondimensionalized with their stoichiometric values $Y_{F,st} = \alpha Y_{F,F}/(1+\alpha)$ and $Y_{O_2,st} = Y_{O_2,A}/(1+\alpha)$, where $\alpha = Y_{O_2,A}/SY_{F,F}$ is the mass of the fuel feed stream that is needed to mix with a unit mass of air to generate a stochiometric mixture, and S is the mass of oxidizer burnt per unit mass of fuel consumed in stoichiometric proportions. For methane-air systems and undiluted fuel streams, typical values of α and S are 0.06 and 4 respectively. Similarly, T denotes the temperature nondimensionalized with the adiabatic temperature increment $QY_{F,st}/c_p$, where Q is the heat release per unit mass of fuel, and T_a represents the dimensionless activation temperature of the chemical reaction. In this formulation, the parameter Da is a pseudo-collision Damköhler number given by

$$\mathrm{Da} = \frac{Y_{O_2,st}A}{\Omega}, \tag{2.28}$$

which represents the ratio of a pseudo-collision time $(Y_{O_2,st}A)^{-1}$ to the flow time Ω^{-1}, with $A = \rho B/W_{O_2}$ the frequency factor of the global step, and W_{O_2} the oxidizer molecular weight.

Since usual hydrocarbon overall activation temperatures T_a are large, the chemical time shows an extraordinary dependence on the temperature. For large activation energies, $T \sim T_\infty$ in regions far from the flame, and the chemical time reaches its largest value $t_{c\infty}$ there. The chemical reaction is negligible in these regions and the mixture is chemically frozen. In regions close to the flame, the temperature reaches a flame temperature, $T \sim T_{fl}$, and the chemical time attains its smallest value t_{cfl}. The ratio of both chemical times is $t_{c\infty}/t_{cfl} \sim \mathrm{e}^{1/\epsilon}$, where

$$\epsilon = \frac{T_{fl}^2}{T_a} \tag{2.29}$$

is the inverse of a Zel'dovich number when T_{fl} and T_a are nondimensionalized with the adiabatic temperature increment. If T_{fl} and T_a are dimensional, an equivalent definition of ϵ

is $\epsilon = T_{fl}^2/[T_a(T_{fl}-T_{st})]$, where T_{st} is the temperature of the frozen mixture in stoichiometric proportions. The value of ϵ is usually much smaller than unity in combustion applications. When (2.29) is used in (2.27), the Arrhenius exponential term becomes

$$\mathrm{e}^{-T_a/T} = \mathrm{e}^{-T_a/T_{fl}} \cdot \exp\left[-\frac{1}{\epsilon}\left(\frac{T_{fl}-T}{T/T_{fl}}\right)\right], \tag{2.30}$$

which, in the large-activation energy limit vanishes except in regions of the combustion field where the temperature is close to that of the flame, $T_{fl} - T = O(\epsilon)$, with $\hat{\omega}$ similar to a Dirac-delta function centered at the flame location in the first approximation.

This simple chemical-kinetic model leaves three parameters in the formulation, namely, the preeexponential factor B, the activation temperature T_a and the heat released per unit mol of fuel Q. The values $B = 6.9 \times 10^{14}\mathrm{cm}^3/(\mathrm{mol\ s})$, $Q = 802.4\mathrm{KJ/mol}$ and $T_a = 15,900$ K are used as a reference in stoichiometric proportions [33]. Adjustments of the activation temperature are needed in Chapter 5 to reproduce the experimental data for extinction of the uniform diffusion flame. A model based on variable activation energy and heat release, which has been shown to compare favorably with experiments and detailed-chemistry numerical simulations in earlier work [33], is used in the numerical simulations of Chapter 5 to avoid unrealistic super-adiabatic flame speeds on fuel-rich regions that are artifacts of hydrocarbon-air single-step reactions with constant activation energy. More involved analyses would need to consider the full CH_4-air chemical kinetics [31, 34] or reduced mechanisms for flame extinction [35, 34].

2.3 Mixture fraction, mass-transfer number, scalar dissipation rate and excess enthalpy

The mixture fraction Z is defined here as

$$Z = \frac{SY_F - Y_{O_2} + Y_{O_2,A}}{SY_{F,F} + Y_{O_2,A}}, \tag{2.31}$$

with $Z = 1$ indicating fuel-only regions, $Y_{O_2} = 0$ and $Y_F = Y_{FF}$, and $Z = 0$ indicating oxidizer-only regions, $Y_F = 0$ and $Y_{O_2} = Y_{O_2,A}$. When (2.31) is normalized with the mixture fraction Z_S on the disk surface, the normalized mixture fraction

$$\widetilde{Z} = \widetilde{Z}_{fl}\left(\frac{\hat{Y}_F - \hat{Y}_{O_2}}{1+\alpha} + 1\right), \qquad 0 \leqslant \widetilde{Z} \leqslant 1, \tag{2.32}$$

is obtained, with $\widetilde{Z} = 0$ far from the disk and $\widetilde{Z} = 1$ on the disk surface. Here

$$\widetilde{Z}_{fl} = Z_{st}/Z_S, \tag{2.33}$$

represents the normalized stochiometric coordinate location with respect to Z_S, with

$$Z_{st} = \frac{\alpha}{1+\alpha} \sim 0.056 \tag{2.34}$$

the stoichiometric mixture fraction, which coincides with the diffusion flame location in this equidiffusive analysis. The mixing and hydrodynamic fields can be easily related in the present thermodiffusive approximation by making use of (2.32) in the species conservation equations to integrate a second-order homogeneous differential equation for $\widetilde{Z}(z)$ with appropriate porous-disk boundary conditions, which gives [36]

$$\widetilde{Z}(z) = \frac{\mathrm{Re}_j \mathrm{Pr}}{\mathcal{B}} \int_z^\infty \left\{ \exp\left[\int_0^\xi \mathrm{Pr}\phi(z)dz \right] \right\} d\xi, \tag{2.35}$$

where $\mathcal{B}$ is an effective mass-transfer number defined by

$$\mathcal{B} = \frac{Z_{st}}{\widetilde{Z}_{fl} - Z_{st}} = \frac{\alpha(1+\alpha+\hat{Y}_{F,S} - \hat{Y}_{O_2,S})}{1+\alpha+\alpha(\hat{Y}_{O_2,S} - \hat{Y}_{F,S})}, \tag{2.36}$$

and the subindex $_S$ refers to the fuel and oxidizer mass fractions on the disk surface. The effective mass-transfer number increases monotonically with Re_j. If there is no fuel injected, $\mathrm{Re}_j = 0$, $\widetilde{Z}_{fl} \to \infty$, $Z_S = 0$, $Y_{F,S} = 0$, $Y_{O_2,S} = Y_{O_2,A}$ and $\mathcal{B} = 0$. Similarly, for large injection rates, $\mathrm{Re}_j \to \infty$, $\widetilde{Z}_{fl} \to Z_{st}$, $Z_S \to 1$, $Y_{F,S} \to Y_{F,F}$, $Y_{O_2,S} \to 0$ and $\mathcal{B} \to \infty$. Using (2.32), (2.35) and (2.36), an equivalent definition

$$\mathcal{B} = \mathrm{Re}_j \mathrm{Pr} \int_0^\infty \left\{ \exp\left[\int_0^\xi \mathrm{Pr}\phi(z)dz \right] \right\} d\xi, \tag{2.37}$$

is found. Substituting the expansion for ϕ (2.15) into (2.37), the asymptotic series

$$\begin{aligned} \mathcal{B} = \mathrm{Re}_j \mathrm{Pr} \int_0^\infty \exp\left[\int_0^\xi \mathrm{Pr}\phi_0(z)dz \right] \left[1 + \mathrm{Re}_j \int_0^\xi \phi_1(z)dz \right] d\xi \\ = \mathcal{B}_0 \mathrm{Re}_j + \mathcal{B}_1 \mathrm{Re}_j^2 + O(\mathrm{Re}_j^3), \end{aligned} \tag{2.38}$$

is obtained for $\mathrm{Re}_j \ll 1$, with

$$\mathcal{B}_0 = \mathrm{Pr} \int_0^\infty \exp\left[\int_0^\xi \mathrm{Pr}\phi_0(z)dz \right] = 2.180, \tag{2.39}$$

and

$$\mathcal{B}_1 = \mathrm{Pr} \int_0^\infty \exp\left[\int_0^\xi \mathrm{Pr}\phi_0(z)dz \right] \left[\int_0^\xi \phi_1(z)dz \right] d\xi = 2.349, \tag{2.40}$$

which are calculated by numerical integration of the leading-order (2.16)-(2.19) and second-order (2.21)-(2.24) problems of the hydrodynamic flow field and evaluated for $\mathrm{Pr} = 0.71$. These results for $\widetilde{Z}$ and $\mathcal{B}$ are shown in figure 2.3(a,b).

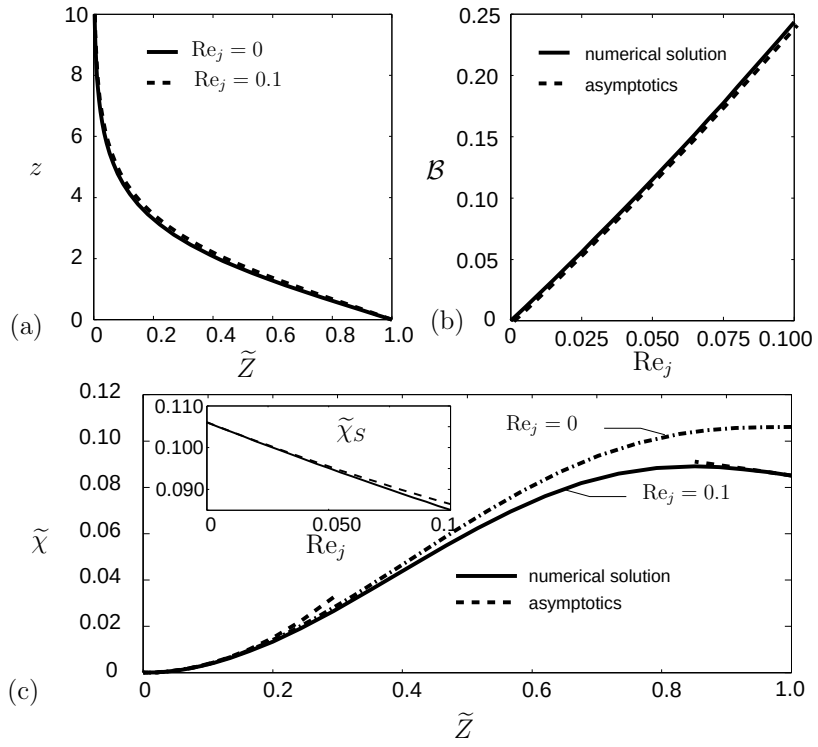

Figure 2.3: (a) Mixture fraction distribution (2.35), (b) mass-transfer number (2.37), and (c) dimensionless scalar dissipation rate (2.42). The inset shows the dimensionless scalar dissipation rate on the disk surface.

The value of the mixture fraction on the disk surface increases with the fuel injection rate, and can be expressed as

$$Z_S = \frac{\mathcal{B}}{1+\mathcal{B}}, \tag{2.41}$$

where use has been made of expressions (2.33) and (2.36), which gives $Z_S \sim \mathcal{B}_0 \mathrm{Re}_j + (\mathcal{B}_1 - \mathcal{B}_0^2)\mathrm{Re}_j^2 + O(\mathrm{Re}_j^3)$ using (2.39) and (2.40).

The squared gradient of the mixture fraction multiplied by the thermal diffusivity is commonly referred to as the scalar dissipation rate χ in turbulent combustion [2], and it represents the inverse of a characteristic diffusion time. When the diffusion time is evaluated in the burning diffusion flame, $\widetilde{Z} = \widetilde{Z}_{fl}$, a characteristic flame-transit time or reactant diffusion time through the flame $t_d \sim 1/\chi_{fl}$ is obtained, which is usually large compared to the local chemical time $t_c \sim (AY_{O_2,st})^{-1} \exp(T_a/T)$ to ensure complete reactant depletion. Here the same nomenclature is used, and the expression for the nondimensional scalar dissipation rate

$$\widetilde{\chi}(z) = \left(\frac{d\widetilde{Z}}{dz}\right)^2 = \left(\frac{\mathrm{PrRe}_j}{\mathcal{B}}\right)^2 \exp\left[2\int_0^z \mathrm{Pr}\phi(\xi)d\xi\right], \tag{2.42}$$

is found, where use has been made of (2.35). The value of $\widetilde{\chi}$ on the disk surface is given by $\widetilde{\chi}_S = (\mathrm{PrRe}_j/\mathcal{B})^2$. For small mixture fractions $\widetilde{Z} \to 0$ ($z \to \infty$), the approximation $\phi \sim \phi_\infty$ in (2.35) yields $\widetilde{\chi}(\widetilde{Z}) \sim (\phi_\infty \mathrm{Pr}\widetilde{Z})^2$. Similarly, for $\widetilde{Z} \sim 1$ ($z \to 0$), the approximation $\phi \sim \mathrm{Re}_j$ gives $\widetilde{\chi}(\widetilde{Z}) \sim \widetilde{\chi}_S[1-3(\widetilde{Z}-1)\mathrm{PrRe}_j/\widetilde{\chi}_S^{1/2}]^{2/3}$. The distribution of $\widetilde{\chi}$ is shown in figure 2.3(c). In this notation, the dimensional flame-transit time is given by $t_d \sim \delta_M^2/(D_T Z_S^2 \widetilde{\chi}_{fl})$, which decreases with increasing mass flow rate and angular velocity.

An excess enthalpy H, nondimensionalized with the chemical heat release $QY_{F,st}/W_F$, can be defined as

$$H = \frac{\alpha \hat{Y}_F + \hat{Y}_{O_2}}{1+\alpha} - 1 + T - T_\infty, \tag{2.43}$$

with $H = 0$ in the oxidizer feed stream, and $H = H_S$ on the disk surface, where H_S, in the most general case, varies with time and position on the disk surface in a manner that is calculated as part of the solution. The excess enthalpy is zero everywhere for an equidiffusive counterflow diffusion flame with equal thermal enthalpies of oxidizer and fuel feed streams [23]. The excess enthalpy in the present analysis is, however, non-zero even in the case of equal feed-stream temperatures, $T_S = T_\infty$, because of heat losses to the disk.

2.4 Conserved-scalar formulation

In these variables and in the laboratory reference frame, the species and energy conservation equations become

$$\frac{\partial H}{\partial t} + \mathbf{v}_\perp \cdot \nabla_\perp H = \frac{\nabla_\perp^2 H}{\mathrm{Pr}} + \frac{\widetilde{\chi}(\widetilde{Z})}{\mathrm{Pr}} \frac{\partial^2 H}{\partial \widetilde{Z}^2}, \tag{2.44}$$

$$\frac{\partial T}{\partial t} + \mathbf{v}_\perp \cdot \nabla_\perp T = \frac{\nabla_\perp^2 T}{\mathrm{Pr}} + \frac{\widetilde{\chi}(\widetilde{Z})}{\mathrm{Pr}} \frac{\partial^2 T}{\partial \widetilde{Z}^2} + \mathrm{Da}\hat{Y}_F \hat{Y}_{O_2} \mathrm{e}^{-T_a/T}, \tag{2.45}$$

$$\hat{Y}_F = H + \widetilde{Z}/\widetilde{Z}_{fl} + T_\infty - T, \tag{2.46}$$

$$\hat{Y}_{O_2} = 1 + \alpha\left(1 - \widetilde{Z}/\widetilde{Z}_{fl}\right) + H + T_\infty - T, \tag{2.47}$$

subject to

$$H + \frac{\beta}{Z_{st}} + \frac{1}{\mathcal{B}} \frac{\partial H}{\partial \widetilde{Z}} = 0, \quad T = T_S, \tag{2.48}$$

at $\widetilde{Z} = 1$,

$$H \to 0, \qquad T \to T_\infty \tag{2.49}$$

at $\widetilde{Z} = 0$,

$$\frac{\partial H}{\partial r} \to 0, \qquad \frac{\partial T}{\partial r} \to 0, \tag{2.50}$$

for $r \to \infty$, and

$$\frac{\partial H}{\partial \theta}\Big|_{\theta=0} = \frac{\partial H}{\partial \theta}\Big|_{\theta=2\pi}, \qquad \frac{\partial T}{\partial \theta}\Big|_{\theta=0} = \frac{\partial T}{\partial \theta}\Big|_{\theta=2\pi}, \tag{2.51}$$

for $0 \leqslant r < \infty$ and $0 \leqslant \widetilde{Z} \leqslant 1$. In this formulation, the time coordinate t is nondimensionalized with the flow time Ω^{-1}, and $\nabla_\perp$ and $\mathrm{v}_\perp$ are the two-dimensional gradient operator and two-dimensional hydrodynamic velocity field in r and θ. The first of the boundary conditions appearing in (2.48) is obtained by combining the thermal-contact condition $T = T_S$ along the disk surface with (2.43), and with fuel and oxidizer mass conservation equations on the disk surface, which in dimensional variables correspond to $\dot{m}'' Y_F - \rho D_F \partial Y_F/\partial z = \dot{m}'' Y_{F,F}$ and $\dot{m}'' Y_{O_2} = \rho D_{O_2} \partial Y_{O_2}/\partial z$. Additionally,

$$\beta = Z_{st} \left\{ (T_\infty - T_S) - \frac{1}{\mathcal{B}} \frac{\partial T}{\partial \widetilde{Z}}\bigg|_{\widetilde{Z}=1} \right\} \tag{2.52}$$

is a heat-loss coefficient that accounts for feed-stream enthalpy differences and heat losses to the disk surface, the behavior of which is analyzed in Chapter 3. The coefficient β generally decreases with increasing Re_j for subadiabatic disk temperatures as it will be seen in Chpater 3, figure 3.2.

Equations (2.8), (2.35), (2.37), (2.42) and (2.44)-(2.52) give rise to the three-dimensional solution of the temperature and excess enthalpy distributions in the physical space and in the laboratory reference frame. The numerical integration of an equivalent set of conservation equations in a non-conserved scalar form was performed in earlier work [14] to capture spiral flames with reasonable success given the difficulty of such three-dimensional and intensive calculation, although spiral meandering and solid-rigid rotation around a central hole were not obtained, thus contradicting existing experiments (perhaps due to an inaccurate resolution of the vicinity of the burner axis), and analyses of the front and trailing diffusion-flame structures and their propagation dynamics were not performed. Nonetheless, that study is valuable in that it confirms that all the essential physics is contained within the set of equations outlined above.

Chapter 3

Diffusion-flame dynamics

The problem (2.44)-(2.52) can be solved analytically in the uniform diffusion-flame regime, in which a diffusion flame envelops the entire disk, and the length scale of the temperature and composition variations in the normal direction to the flame is much smaller than the radial and azimuthal length scales. As observed in figure 1.5, this regime occurs for sufficiently large fuel flow rates and small rotational velocities, or equivalently, for sufficiently large Re_j although still small compared with unity. Under these approximations, equations (2.44)-(2.47) become

$$\frac{d^2H}{d\widetilde{Z}^2} = 0, \tag{3.1}$$

$$\frac{\widetilde{\chi}}{\mathrm{Pr}}\frac{d^2T}{d\widetilde{Z}^2} = -\mathrm{Da}\hat{Y}_F\hat{Y}_{O_2}\mathrm{e}^{-T_a/T}, \tag{3.2}$$

$$\hat{Y}_F = H + \widetilde{Z}/\widetilde{Z}_{fl} + T_\infty - T, \tag{3.3}$$

$$\hat{Y}_{O_2} = 1 + \alpha\left(1 - \widetilde{Z}/\widetilde{Z}_{fl}\right) + H + T_\infty - T, \tag{3.4}$$

subject to the boundary conditions (2.48) and (2.49) respectively on the disk surface and in the far field. In this limit, the heat flux to the disk is a uniform constant that generally depends on the injection fuel rate Re_j, so that the heat-loss coefficient β given by equation (2.52) is uniform on the entire disk surface.

Integrating the enthalpy equation (3.1), the excess enthalpy

$$H = -\beta\widetilde{Z}/\widetilde{Z}_{fl}, \tag{3.5}$$

is obtained. The excess enthalpy is produced by enthalpy differences between the fuel and oxidizer feed streams and the heat losses to the nearby disk surface. Substituting the excess

enthalpy (3.5) into equations (3.3) and (3.4), the equations

$$\frac{\widetilde{\chi}}{\mathrm{Pr}}\frac{d^2T}{d\widetilde{Z}^2} = -\mathrm{Da}\hat{Y}_F\hat{Y}_{O_2}\mathrm{e}^{-T_a/T}, \tag{3.6}$$

$$\hat{Y}_F = (1-\beta)\widetilde{Z}/\widetilde{Z}_{fl} + T_\infty - T, \tag{3.7}$$

$$\hat{Y}_{O_2} = 1 + \alpha - (\alpha+\beta)\widetilde{Z}/\widetilde{Z}_{fl} + T_\infty - T, \tag{3.8}$$

are obtained. Equation (3.6) is subject to the boundary conditions

$$T = T_S \tag{3.9}$$

at $\widetilde{Z} = 1$, and

$$T \to T_\infty \tag{3.10}$$

at $\widetilde{Z} = 0$.

A similar problem to (3.6)-(3.10) was found by Liñán in his seminal paper [23] on the asymptotic structure of counterflow diffusion flames for large activation energies. Liñán identified four distinguished burning regimes: (i) an ignition regime, in which ignition is produced by an increase in the Damköhler number sufficient to cause temperature variations of $O(\epsilon)$, where ϵ is given by (2.29), in a initially frozen mixture of fuel and oxidizer; (ii) a partial-burning (unstable) regime, in which $O(1)$ leakage of fuel and oxidizer occurs through the flame; (iii) a premixed-flame regime, in which extinction occurs with $O(1)$ leakage of one of the reactants through the flame resembling an inner premixed-flame structure; (iv) a diffusion-flame regime in which no reactant leakage occurs in the first approximation (the vigorous-burning, fast-burning or Burke-Schumann solution) and extinction occurs with $O(\epsilon)$ leakage of both reactants through the flame. Figure 3.1 shows the asymptotic ordering of the different extinction regimes and the characteristic S-curve from Liñán's analysis [23] in terms of the reduced Damköhler number Δ given by (1.1).

Large reduced Damköhler numbers Δ represent short chemical times and small reaction-layer thicknesses compared with typical diffusion times through the flame and typical diffusion lengths, which corresponds to a fast-burning regime. Ignition occurs at large Δ when the diffusion time is sufficiently large or the strain rate is sufficiently low to allow thermal runaway after small temperature variations of order ϵ in the initially frozen mixture. Sufficiently small Δ can cause flame extinction when the chemical time becomes of the same order as the typical flame-transit time and the chemical process is not fast enough to deplete the reactants, which produces a temperature drop in the flame and reactant leakage through the reaction region.

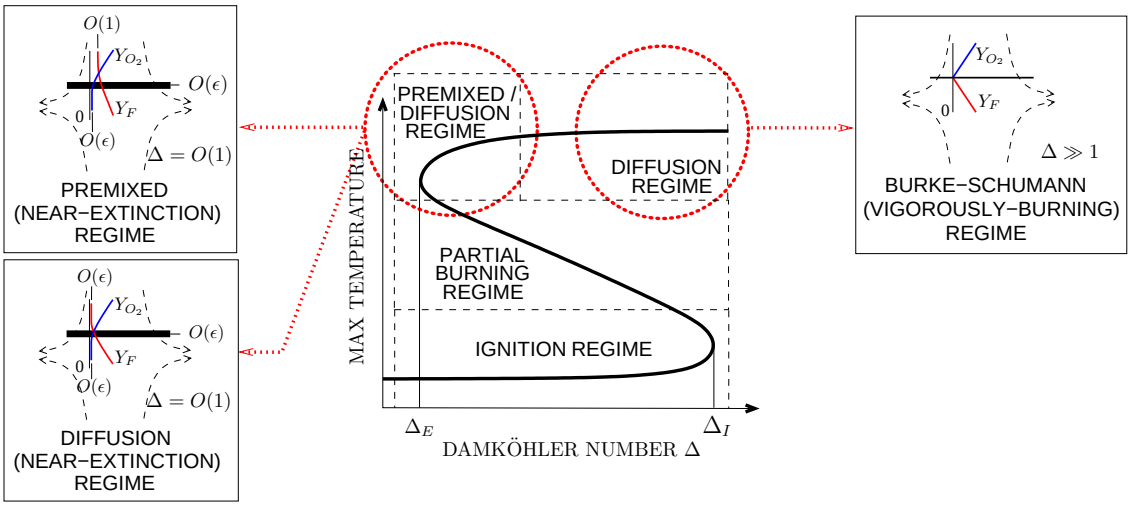

Figure 3.1: Liñán [23] S-curve, asymptotic orderings and burning regimes schematics.

In the large activation energy limit, the extinction of a diffusion flame can occur in either the premixed or diffusion-flame regimes. Activation-energy asymptotic analyses (AEA) applied to extinction in hydrocarbon-air nonpremixed combustion systems typically yield extinction in the premixed regime with a premixed structure on the oxidizer side. This erroneous tendency of AEA, namely predicting dominant fuel leakage instead of the inherent oxidizer leakage produced by chemical kinetics effects [34], has been solved by using rate-ratio asymptotic analysis (RRA) [35], and more recently, by conveniently modifying the activation temperature through the flame in a single-step methane-air chemical kinetic mechanism [33], in which the activation temperature is increased in flame regions of large mixture fraction to increase the chemical time and freeze the reaction on the fuel side of the flame, which enhances oxidizer leakage. In the present analysis, the proximity of the flame to the disk surface increases the leakage of oxidizer and overcomes the tendency of AEA of giving unrealistic extinction conditions in comparison to pure counterflow configurations. As a consequence, both fuel and oxidizer leak in similar amounts through the flame, and, as detailed in Section 3.3, the extinction process can be described in the diffusion flame regime for not too small or too large injection Reynolds numbers, since both extremes yield premixed-flame structures on the fuel and oxidizer sides of the flame respectively.

3.1 The frozen regime

In the frozen limit, the diffusion time is much smaller than the local chemical time, $\Delta \ll 1$, the reaction term is negligible in the first approximation, and (3.6) reduces to $d^2T/d\widetilde{Z}^2 = 0$ subject to (3.9) and (3.10), which gives

$$T = T_\infty - \beta_{fr}\widetilde{Z}/\widetilde{Z}_{fl}, \tag{3.11}$$

$$H = -\beta_{fr}\widetilde{Z}/\widetilde{Z}_{fl}, \tag{3.12}$$

$$\hat{Y}_F = \widetilde{Z}/\widetilde{Z}_{fl}, \tag{3.13}$$

$$\hat{Y}_{O_2} = 1 + \alpha\left(1 - \widetilde{Z}/\widetilde{Z}_{fl}\right), \tag{3.14}$$

where β_{fr} denotes the heat loss coefficient (2.52) in the frozen regime based on the frozen temperature profile,

$$\beta_{fr} = \widetilde{Z}_{fl}(T_\infty - T_S). \tag{3.15}$$

The value $H_{fr} = -\beta_{fr}$ represents the excess enthalpy evaluated at the stoichiometric coordinate. Because of the boundary condition at the disk surface, this excess enthalpy is negative if the plate temperature is less than that of the air and positive if it is greater. For zero fuel injection, $\mathrm{Re}_j = 0$, the excess enthalpy of the inert swirling air flow is zero everywhere if the ambient temperature equals the disk surface temperature, $T_S = T_\infty$, as expected for the non-reacting isothermal flow regime. The local equivalence ratio $\Phi = (Y_F/Y_{O_2})/(Y_{F,st}/Y_{O_2,st}) = \hat{Y}_F/\hat{Y}_{O_2}$ can be expressed in terms of the mixture fraction as

$$\Phi = \left(\frac{1}{\alpha}\right)\frac{Z}{1-Z} = \left(\frac{\widetilde{Z}}{\widetilde{Z}_{fl}}\right)\frac{1 - Z_{st}}{1 - Z_{st}\widetilde{Z}/\widetilde{Z}_{fl}}. \tag{3.16}$$

Further increase in Δ to a critical Δ_I by, for instance, decreasing the angular velocity or increasing the disk temperature, gives rise to higher-order corrections to (3.11)-(3.14), which are representative of flame autoignition as depicted in figure 3.1.

3.2 The Burke-Schumann regime

A diffusion-controlled combustion regime exists for large Damköhler numbers, in which the temperature and composition fields do not depend on the chemical kinetics in the first approximation. In this regime, the local chemical time is much shorter than the diffusion time through the flame, $\Delta \gg 1$, so that the flow remains in chemical equilibrium on both sides of a thin reaction sheet of infinitesimal thickness, which is much smaller than

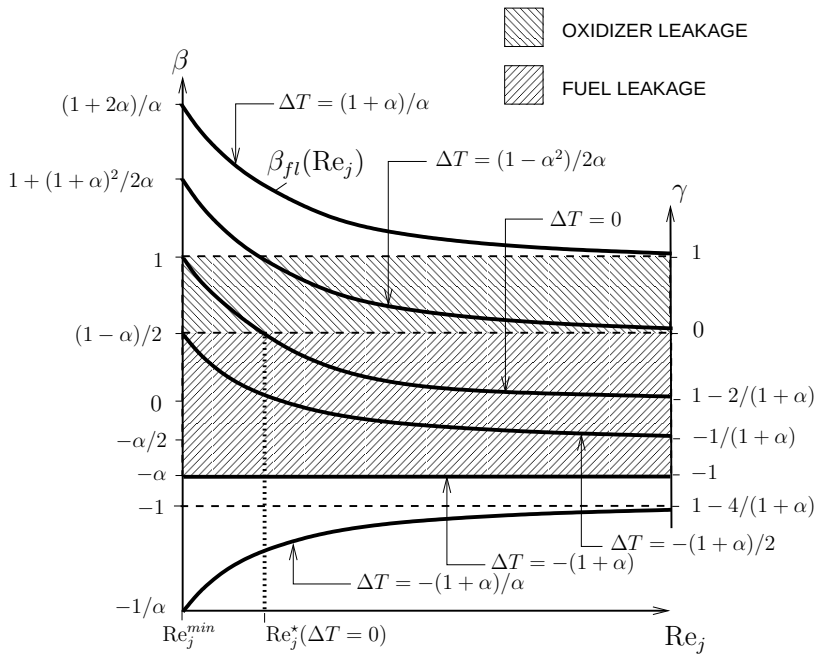

Figure 3.2: Sketch of the equilibrium heat-loss coefficient β_{fl} as a function of Re_j given by (3.22) for different $\Delta T = T_\infty - T_S$ (solid line). The right axis represents the value of γ given by (3.36) for each particular value of β_{fl}. In the hatched region $|\gamma| \leqslant 1$ there is abrupt extinction obeying (3.39).

the hydrodynamic length scale, and no reactant leakage occurs in the first approximation. For large activation energies, temperature variations in the flame are expected to be of order $\epsilon = T_{fl}^2/T_a \ll 1$. In this formulation, T_{fl} is the equilibrium flame temperature in the Burke-Schumann limit. Thus, (3.6) reduces to $d^2T/d\widetilde{Z}^2 = -\mathrm{Pr}\hat{\omega}/\widetilde{\chi}$, with $\hat{\omega}$ approximated as a Dirac-delta function. The solution to these equations is

$$T = T_\infty + 1 + \alpha - (\alpha + \beta_{fl})\,\widetilde{Z}/\widetilde{Z}_{fl}, \tag{3.17}$$

$$\hat{Y}_F = (1+\alpha)(\widetilde{Z}/\widetilde{Z}_{fl} - 1), \quad \hat{Y}_{O_2} = 0, \tag{3.18}$$

in the fuel region $\widetilde{Z}_{fl} \leqslant \widetilde{Z} \leqslant 1$,

$$T = T_\infty + (1-\beta_{fl})\widetilde{Z}/\widetilde{Z}_{fl}, \tag{3.19}$$

$$\hat{Y}_{O_2} = (1+\alpha)(1 - \widetilde{Z}/\widetilde{Z}_{fl}), \quad \hat{Y}_F = 0, \tag{3.20}$$

in the oxidizer region $0 \leqslant \widetilde{Z} \leqslant \widetilde{Z}_{fl}$, and

$$H = -\beta_{fl}\widetilde{Z}/\widetilde{Z}_{fl}, \tag{3.21}$$

with

$$\beta_{fl} = \beta_{fr} + \alpha/\mathcal{B} \tag{3.22}$$

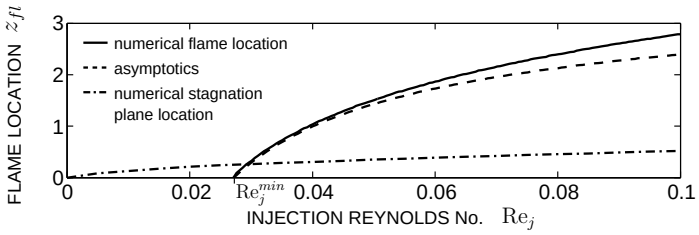

Figure 3.3: Numerical flame location z_{fl}, nondimensionalized with the mixing-layer thickness δ_M, and its asymptotic approximation (3.23) for $\mathrm{Pr} = 0.71$, and numerical stagnation plane location.

the heat-loss coefficient (2.52) based on equilibrium conditions. Figure 3.2 shows that β_{fl} decreases with increasing values of Re_j for sub-adiabatic disk temperatures, with $\beta \to Z_{st}(T_\infty - T_S)$ for $\mathrm{Re}_j \gg 1$. The value $H_{fl} = -\beta_{fl}$ corresponds to the excess enthalpy in the diffusion flame.

To leading order, the flame location in the $\widetilde{Z}$ coordinate corresponds to the stoichiometric coordinate $\widetilde{Z} = \widetilde{Z}_{fl}$. The dimensionless spatial flame location z_{fl} is obtained numerically by using the inverse of the transformation (2.35). For $\mathrm{Re}_j \ll 1$, z_{fl} is expected to be small, so that $\int_{z_{fl}}^{\infty} \exp[\int_0^{\xi} \mathrm{Pr}\phi dz]d\xi \sim \mathcal{B}/\mathrm{Re}_j\mathrm{Pr} - z_{fl}$, and the asymptotic approximation

$$\begin{aligned} z_{fl} &\sim [\mathrm{Pr}(1+\alpha)]^{-1}[-\alpha/\mathrm{Re}_j + \mathcal{B}_0 \\ &+ \mathcal{B}_1\mathrm{Re}_j + O(\mathrm{Re}_j^2)] \end{aligned} \tag{3.23}$$

is obtained, where $\mathcal{B}_0$ and $\mathcal{B}_1$ successive approximations of the mass-transfer number given by (2.39) and (2.40). Equation (3.23) is compared with the numerical integration of (2.35) in figure 3.2. Note that the flame is beyond the stagnation plane for $\mathrm{Re}_j > 0.029$. The Burke-Schumann solution (3.17)-(3.19) must satisfy the solvability condition $0 < Z_{st} \leqslant Z_S$, or alternatively $\widetilde{Z}_{fl} \leqslant 1$ for the flame to stand off the disk surface, which gives the minimum mass-transfer number

$$\mathcal{B}_{min} = \alpha \quad \text{for} \quad \widetilde{Z}_{fl} = 1. \tag{3.24}$$

The asymptotic expansion (2.38) yields the minimum injection Reynolds number

$$\mathrm{Re}_j^{min} \sim \frac{\alpha}{\mathcal{B}_1} \sim 0.027. \tag{3.25}$$

Values $\widetilde{Z}_{fl} > 1$, or equivalently $\mathrm{Re}_j < \mathrm{Re}_j^{min}$, represent the flame located somewhere inside the disk, a problem that is not addressed here. The minimum injection rate Re_j^{min} is not representative of flame extinction, but of the valid range of the space of solutions in the

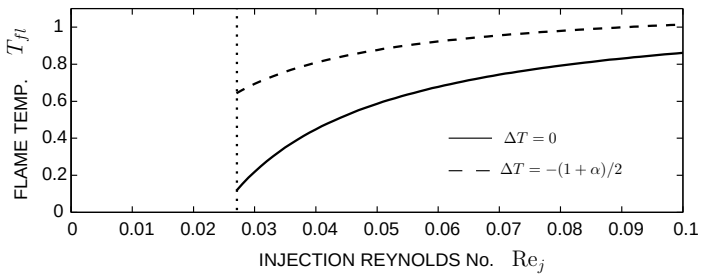

Figure 3.4: Dimensionless non-adiabatic Burke-Schumann temperature for $T_\infty = 300$ K.

Burke-Schumann regime. As detailed in Section 3.3, flame extinction occurs well before the minimum injection rate is reached, since nonequilibrium effects induced by finite-rate chemistry and low wall temperatures become of paramount importance as Re_j becomes small.

In the flame-sheet region, the equilibrium temperature is the non-adiabatic Burke-Schumann temperature

$$T_{fl} = T_\infty + 1 - \beta_{fl}, \tag{3.26}$$

which decreases with decreasing Reynolds numbers of injection as seen in figure 3.2. For $\mathrm{Re}_j = \mathrm{Re}_j^{min}$, this model predicts the unrealistic result that the flame temperature is equal to the disk temperature, $T_{fl} = T_S$, although flame extinction due to finite-rate chemistry effects occurs before this limit is actually achieved.

At sufficiently large $\mathrm{Re_j}$, the influences of the disk surface are negligible and the adiabatic flame temperature

$$T_{fl}^\infty = 1 + T_\infty - Z_{st}(T_\infty - T_S), \tag{3.27}$$

is recovered in (3.26). In this limit, the excess enthalpy distribution is solely produced by feed-stream enthalpy differences,

$$H = -Z(T_\infty - T_S), \tag{3.28}$$

which holds for both frozen and Burke-Schumann regimes.

3.3 Diffusion-flame extinction

The nonequilibrium effects associated with finite-rate chemistry and finite Damkhöhler numbers are expected to cause flame extinction well before the minimum-injection limit is

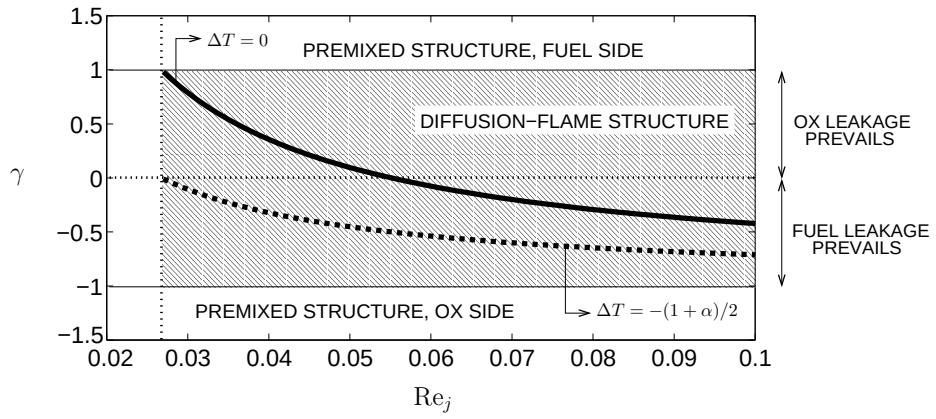

Figure 3.5: Variations of the leakage parameter γ (3.36) with respect to the injection Reynolds number.

reached. In particular, effects associated with the decrease in Da to cause flame-temperature variations in fractional amounts of order ϵ are now carried out following Liñán [23].

To $O(\epsilon)$, both reactants diffuse into a flame region of thickness of $O(\epsilon\Delta^{-1/3})$, in which temperature variations are of the same order with respect to the equilibrium flame temperature T_{fl},

$$T = T_{fl} - \Delta_0^{-1/3}\left[\epsilon\beta_1 + \epsilon\gamma\eta + O(\epsilon^2)\right], \tag{3.29}$$

where Δ_0 is a reduced Damkhöler number given by the first term of the expansion

$$\frac{4\mathrm{Pr}\widetilde{Z}_{fl}^2(T^2/T_a)^3}{\widetilde{\chi}_{fl}(1+\alpha)^2}\mathrm{Da}e^{-T_a/T} = \Delta_0 + \epsilon\Delta_1 + O(\epsilon^2), \tag{3.30}$$

so that

$$\Delta_0 = \frac{4\mathrm{Pr}\widetilde{Z}_{fl}^2(T_{fl}^2/T_a)^3}{\widetilde{\chi}_{fl}(1+\alpha)^2}\mathrm{Da}e^{-T_a/T_{fl}}, \tag{3.31}$$

to leading order. In this formulation, η is an inner variable in the flame region,

$$\eta = \frac{\Delta_0^{1/3}(1+\alpha)}{2\epsilon\widetilde{Z}_{fl}}(\widetilde{Z} - \widetilde{Z}_{fl}). \tag{3.32}$$

Thus, the diffusion-flame thickness becomes

$$\delta_{fl} \sim \epsilon\Delta^{-1/3}. \tag{3.33}$$

Upon substituting expansion (3.29) into (3.6), the following equation

$$\frac{d^2\beta_1}{d\eta^2} = (\beta_1 - \eta)(\beta_1 + \eta)\exp[-\Delta_0^{-1/3}(\beta_1 + \gamma\eta)], \tag{3.34}$$

is obtained, subject to $d\beta_1/d\eta \to \pm 1$ at $\eta \to \pm\infty$, which represents the inner (canonical) structure of a diffusion flame in the diffusion-flame regime and was found in earlier work by Liñán [23] for counterflow diffusion flames. In the present analysis, the excess enthalpy in the flame $-\beta_{fl}$ differs from that of [23] since it is affected by the fuel injection rate and the non-adiabatic disk surface. Nonetheless, for a given heat-loss coefficient β_{fl}, the solutions of the inner flame structure of [23] are valid for the extinction of the uniform diffusion flame on the rotating porous-disk burner. The fuel and oxidizer concentrations in the flame region are

$$Y_F = \epsilon\Delta_0^{-1/3}(\beta_1 + \eta), \quad \text{and} \quad Y_{O_2} = \epsilon\Delta_0^{-1/3}(\beta_1 - \eta) \quad \text{at} \quad \widetilde{Z} \sim \widetilde{Z}_{fl}. \tag{3.35}$$

In this formulation, γ is a leakage parameter given by

$$\gamma = -1 + 2(\alpha + \beta_{fl})/(1 + \alpha), \tag{3.36}$$

with $1 - \gamma$ twice the ratio between the heat lost from the flame toward the oxidizer region to the total chemical heat released in the flame. Since β_{fl} is a function of the boundary temperature difference and the injection mass flow, γ also assumes different values depending on those variables, as depicted in figures 3.2 and 3.5. Extinction occurs only in the region $|\gamma| < 1$ and for boundary temperature differences $-(1+\alpha) \le \Delta T \le (1+\alpha)/\alpha$, in the sense that no solution exists for Δ_0 below the extinction Damkhöler number Δ_{0E}. Outside this range of temperatures, no abrupt extinction event exists. For $0 < \gamma < 1$, the temperature gradient is steeper on the fuel side, which in turn freezes the chemical reaction on that side and enhances oxidizer leakage through the flame, with $\gamma \to 1$ reaching a premixed structure with $O(1)$ oxidizer leakage and $O(\epsilon)$ fuel leakage. For $-1 < \gamma < 0$ the temperature gradient is steeper on the oxidizer side and fuel leakage prevails, with $\gamma \to -1$ reaching a premixed structure with $O(1)$ fuel leakage and $O(\epsilon)$ oxidizer leakage. Therefore as $|\gamma| \to 1$ the flame region shows a premixed structure, with $O(1)$ leakage of one reactant, and the diffusion-flame regime looses accuracy. These considerations are shown in figure 3.5.

Conventional AEA analysis of nonpremixed counterflow combustion [23] predicts values of γ close to unity and strong fuel leakage when applied to hydrocarbon-air flames, for which Z_{st} is typically small. Since β and γ strongly depend on the fuel injection mass flow Re_j for the rotating-burner problem, fuel leakage is inhibited for sufficiently small mass flows for which $\gamma = 0$, a condition identified by the superscript *, and the experimental flame is close enough to the disk surface to produce a steeper temperature gradient on the fuel

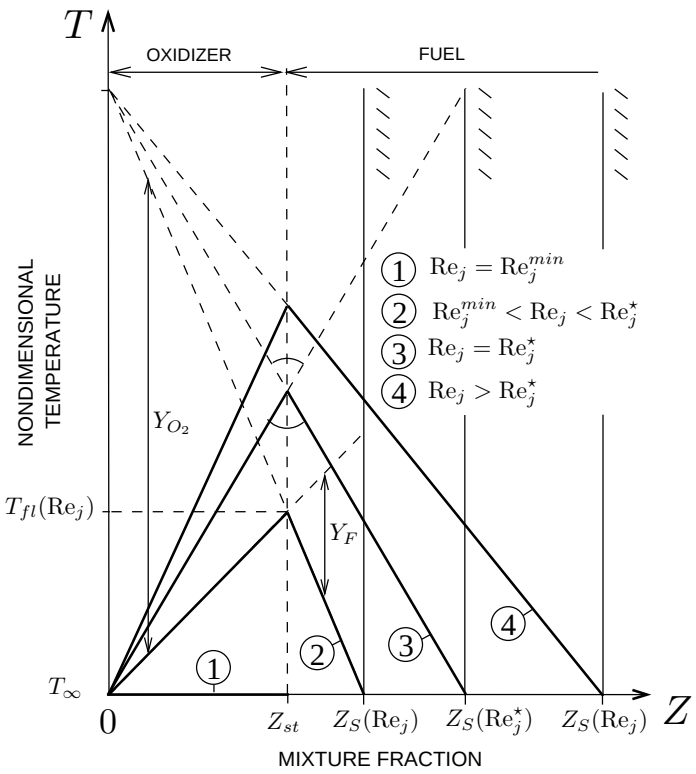

Figure 3.6: Asymptotic temperature and reactant mass fractions distributions in the diffusion-flame regime for different ranges of fuel injection mass flows and $T_\infty = T_S$.

side than the oxidizer side. The value of Re_j for which $\gamma = 0$ is given by

$$\mathcal{B}^\star(\mathrm{Re}_j^\star) = \frac{2\alpha[1 + \Delta T/(1+\alpha)]}{1 - \alpha - 2\alpha\Delta T/(1+\alpha)}, \tag{3.37}$$

where use has been made of (3.22) and (3.36). For $\mathrm{Re}_j < \mathrm{Re}_j^\star$, then $\gamma > 0$ and oxidizer leakage is favored. The occurrence of dominant oxidizer leakage when $\mathrm{Re}_j < \mathrm{Re}_j^\star$ is found only for $\Delta T \geqslant -(1+\alpha)/2$. These considerations are shown in figure 3.6 for the particular case $\Delta T = 0$.

The analysis [23] shows that equation (3.35) has a turning point at the reduced Damköhler number at extinction, namely for

$$\Delta_{0E} \backsimeq \mathrm{e}[(1 - |\gamma|) - (1 - |\gamma|)^2 + 0.26(1 - |\gamma|)^3 + 0.055(1 - |\gamma|)^4], \tag{3.38}$$

within 1% for $|\gamma| < 1$. Notice that the canonical equation (3.34) is symmetric in γ, since the change of variables $\gamma^* = -\gamma$ and $\eta = -\eta$ yields the same differential problem. Therefore the solution for positive and negative values of γ are trivially related, so that the reduced Damköhler number at extinction is a function solely of $|\gamma|$. The expansions (3.29) and

(3.38) fails near premixed conditions, $|\gamma| \sim 1$, where (3.38) erroneously predicts an infinite flame strength at the minimum injection rate Re_j^{min}. Nonetheless, extinction of the uniform diffusion flame in the rotating porous-disk burner is associated to larger values of Re_j in the range $0.07 < \mathrm{Re}_j < 0.09$ where Δ_{0E}, as it will be seen in Chapter 5 in figure 5.1(b).

Substituting expression (3.38) into (3.31) and making use of (2.28), (2.35), (2.37), (3.15), (3.22) and (3.26), the formula for the extinction Damköhler number

$$\mathrm{Da}_E(\mathrm{Re}_j) = \frac{\Delta_{0E}\mathrm{Re}_j^2\mathrm{Pr}(1+\alpha)^2 e^{T_a/T_{fl}}}{4\mathcal{B}^2\widetilde{Z}_{fl}^2[T_{fl}^2/T_a]^3}\exp\left[2\int_0^{z_{fl}}\mathrm{Pr}\phi(z)dz\right], \tag{3.39}$$

is found, which defines the extinction conditions in terms of the fuel mass flow rate and the angular velocity for the present experiments. In this formula, Δ_{0E}, $\mathcal{B}$, $\widetilde{Z}_{fl}$ and T_{fl}, as well as z_{fl} and the function $\phi(z)$, depend on Re_j, so that Da_E varies with Re_j. The comparison of the values obtained from the extinction formula (3.39) with experimental data is delayed until Chapter 5, figure 5.1(b), where the experiments are analyzed.

Chapter 4

Propagation dynamics of spiral edge flames

4.1 Frenet-frame formulation

The advancing edge region of the flame is a zone of finite thickness δ_f. Nevertheless, an edge location can be defined in a precise manner, for example, as the locus of the inflection points of the temperature profile, or, for large activation energies, as a discontinuity in a much larger scale, when the edge reaction zone is very thin compared with the hydrodynamic length scale of the flow, $\delta_f/\delta_M \ll 1$. An orthogonal, right-handed Frenet frame $\{n, s, b\}$ is defined attached to the moving curvilinear edge as depicted in figure 2.1. The Frenet trihedron is defined by the unit tangent vector $\mathbf{e_s}$ to the edge resulting from the intersection of the osculating and rectifying planes, the unit normal vector $\mathbf{e_n}$ to the edge resulting from the intersection of the osculating and binormal planes, and the unit binormal vector $\mathbf{e_b}$ to the edge resulting from the intersection of the binormal and rectifying planes. The normal vector $\mathbf{e_n}$ is defined as positive when pointing towards the burnt side of the edge, so that the front curvature $\mathcal{K}_s$ is then positive for fronts concave towards the flame sheet to satisfy by construction the first Frenet-Serret formula $d\mathbf{e_s}/ds = \mathcal{K}_s\mathbf{e_n}$ [37]. Additionally, the edge is assumed to have zero torsion, so that the third Frenet-Serret formula yields $d\mathbf{e_b}/ds = 0$, with $\mathbf{e_b} = \mathbf{e_z}$. Therefore, the equation of the osculating plane of the trailing flame is simply given by $z = z(\widetilde{Z}_{fl})$ in (2.35), with the edge-flame propagating along lines of stoichiometric mixture.

The edge may mathematically be described by the scalar $G(x, y, t) = G_0$, with

$G < G_0$ and $G > G_0$ for the burned and unburned states respectively. If the surface is smooth and continuous, the previously defined unit vector normal to the edge is then given by

$$\mathbf{e_n} = -\nabla G/|\nabla G|. \tag{4.1}$$

Every Lagrangian edge element may be considered to move with a velocity $\mathbf{U_{LF}}$ with respect to the laboratory frame, and since each such element remains on the edge, the relation

$$\frac{dG}{dt} = \frac{\partial G}{\partial t} + \mathbf{U_{LF}} \cdot \nabla G = 0 \tag{4.2}$$

serves to maintain the value of G equal to G_0 on the edge at future times. Although the previously defined nondimensionalization for lengths, times and velocities are applied here, the symbols also could be considered to represent dimensional quantities in (4.2), and different, appropriately revised nondimensionalizations will be introduced later. The relationship (4.2), which lies at the basis of the level-set methods, is to be used here for edge-tracking purposes.

Daou and Liñán [8] have shown that the ratio of a characteristic flame thickness $\delta_L^0 = D_T/\mathrm{S}_{L,st}^0$ of a laminar planar premixed flame to the radius of curvature of the premixed wings $\epsilon\delta_M$, namely

$$\Gamma = \frac{\delta_L^0}{\epsilon\delta_M}, \tag{4.3}$$

is of paramount importance for characterizing the structure and propagation dynamics of a triple flame. An edge flame represents the limit structure of a very slender triple flame propagating in large mixture-fraction gradients, $\Gamma \to \infty$. In this formulation, $\mathrm{S}_{L,st}^0 = (4\epsilon^3 A D_T Y_{O_2,st} \mathrm{e}^{-T_a/T_f})^{1/2}$ is the burning rate of a planar laminar premixed flame in stoichiometric proportions when the reaction rate is given by (2.27), T_f is a characteristic nondimensional edge temperature, and ϵ is the inverse of a Zel'dovich number given by

$$\epsilon = T_f^2/T_a \ll 1, \tag{4.4}$$

which is usually a small parameter in combustion applications because of the large overall activation energies involved in typical combustion processes. The propagation parameter Γ is related to a reduced Damköhler number Δ_f of the edge based on the temperature of the edge,

$$\Delta_f = \left(\frac{\delta_M}{\delta_L^0}\right)^2 = 4\mathrm{Pr}\epsilon^3 \mathrm{Da}\mathrm{e}^{-T_a/T_f} = \left(\frac{\mathrm{S}_{L,st}^0}{\mathrm{Pr}\delta_M\Omega}\right)^2 = \frac{1}{\Gamma^2\epsilon^2}, \tag{4.5}$$

which represents the ratio of the diffusion time through the mixing layer to the flame transit time over the front thickness. The reduced Damköhler number is also related to the Karlovitz number Ka or dimensionless strain rate, $\Delta_f = 1/\mathrm{Ka}$.

For large activation energies, $\epsilon \ll 1$, and low tangential curvatures, the length scale of variations in the normal direction to the front is much smaller than along its tangential direction. Thus, the edge-flame temperature and excess enthalpy have a weak dependence -of $O(\epsilon)$ at most- on the s coordinate in the first approximation, and solutions of (2.44) and (2.45) are sought for which contours n =constant are level curves of temperature and excess enthalpy. Additionally, if the edge is not deforming too rapidly, the time derivative in the Frenet frame can be neglected and translation-invariant solutions can be obtained; this occurs for a slowly meandering and slowly varying edge flame in which the time scale of variation in the moving frame is much larger that $1/\Omega$. When the radius of curvature of the premixed wings $\epsilon\delta_M$ is used as the unit length of the normal coordinate n, the planar premixed flame velocity $\mathrm{S}^0_{L,st}$ is used as the unit velocity scale, and the mixture fraction coordinate is stretched about the diffusion-flame height as $\widetilde{Z}^\star = (\widetilde{Z} - \widetilde{Z}_{fl})/\epsilon$, equations (2.44)-(2.49) become

$$\left[\mathrm{U_n} + \Gamma\epsilon\mathcal{K}_s + \mathrm{v_{n,rel}}(\widetilde{Z}^\star)\right]\frac{\partial H}{\partial n} = \Gamma\frac{\partial^2 H}{\partial n^2} + \Gamma\widetilde{\chi}(\widetilde{Z}^\star)\frac{\partial^2 H}{\partial \widetilde{Z}^{\star 2}}, \tag{4.6}$$

$$\left[\mathrm{U_n} + \Gamma\epsilon\mathcal{K}_s + \mathrm{v_{n,rel}}(\widetilde{Z}^\star)\right]\frac{\partial T}{\partial n} = \Gamma\frac{\partial^2 T}{\partial n^2} + \Gamma\widetilde{\chi}(\widetilde{Z}^\star)\frac{\partial^2 T}{\partial \widetilde{Z}^{\star 2}}, + \frac{\hat{Y}_F\hat{Y}_{O_2}}{4\Gamma\epsilon^3}\exp\left[-\frac{1}{\epsilon}\frac{(T_f - T)}{T/T_f}\right], \tag{4.7}$$

and

$$\hat{Y}_F = H + \epsilon\widetilde{Z}^\star/\widetilde{Z}_{fl} + 1 + T_\infty - T, \tag{4.8}$$

$$\hat{Y}_{O_2} = 1 - \alpha\epsilon\widetilde{Z}^\star/\widetilde{Z}_{fl} + H + T_\infty - T, \tag{4.9}$$

subject to

$$\epsilon(H + \Delta T) + \frac{1}{\mathcal{B}}\left(\frac{\partial H}{\partial \widetilde{Z}^\star} - \frac{\partial T}{\partial \widetilde{Z}^\star}\right) = 0, \qquad T = T_S, \tag{4.10}$$

at $\widetilde{Z}^\star = (1 - \widetilde{Z}_{fl})/\epsilon$, and

$$H \to 0, \qquad T \to T_\infty. \tag{4.11}$$

at $\widetilde{Z}^\star = -\widetilde{Z}_{fl}/\epsilon$. In this formulation,

$$\mathrm{U_n} = (\mathbf{v}_\perp|_{\widetilde{Z}=\widetilde{Z}_{fl}} - \mathbf{U_{LF}}) \cdot \mathbf{e_n} \tag{4.12}$$

is the front propagation velocity or burning-rate eigenvalue (in general dependent on the tangential curvature of the edge), and

$$\mathcal{K}_s = -\nabla \cdot \mathrm{e_n} = \frac{\nabla^2 G + \mathbf{e_n} \cdot \nabla(\mathbf{e_n} \cdot \nabla G)}{|\nabla G|} \tag{4.13}$$

is the edge tangential curvature measured in the hydrodynamic scale $1/\delta_M$. Equations (4.6) and (4.7) implicitly assume small curvatures, $\mathcal{K}_s \ll \mathrm{U_n}/\Gamma\epsilon$, such that the tangential variations of the temperature and excess enthalpy are $\leqslant O(\epsilon)$. This limit corresponds to a "nearly straight" edge flame, in which the tangential variations of the propagation velocity $\mathrm{U_n}$ with respect to its planar counterpart, $\mathrm{U_n^0}$, are much smaller than unity. For $\mathcal{K}_s \geqslant O(\mathrm{U_n}/\Gamma\epsilon)$, equations (4.6) and (4.7) loose accuracy since the tangential heat losses become important.

Equations (4.6) and (4.7) also contain the quantity $\mathrm{v_{n,rel}} = (\mathbf{v}_\perp - \mathbf{v}_\perp|_{\widetilde{Z}=\widetilde{Z}_{fl}}) \cdot \mathbf{e_n}$, which represents the relative flow advection with respect to the edge.

Upstream from the edge, $n \to -\infty$, the temperature and excess-enthalpy profiles correspond to the frozen profiles, (3.11) and (3.12). Downstream from the edge, $n \to +\infty$, the temperature and excess-enthalpy profiles can correspond either to the equilibrium profiles, (3.17), (3.19) and (3.21), or to the frozen profiles, (3.11) and (3.12), depending on the value of the mass transfer number $\mathcal{B}$ as detailed further below.

4.2 Influences of heat losses to the burner surface on the propagation of edge flames

4.2.1 Order-of-magnitude analysis of the conservation equations

Order-of-magnitude analyses can be performed in equations (4.6)-(4.11) as follows. The propagation velocity $\mathrm{U_n^0}$, nondimensionalized with $\mathrm{S_{L,st}^0}$, is of $O(1)$ as observed from a convective-diffusive balance in the preheat region, which has a thickness[1] of $O(\Gamma\epsilon)$. In this region, both streamwise convection and diffusion terms are of $O(1/\Gamma)$ in (4.6) and (4.7), whereas the transverse diffusion and reaction terms are of $O(\Gamma\epsilon^2)$ and $O(\mathrm{e}^{-1/\epsilon})$, respectively, the former follows from changes in $\widetilde{Z}$ being of $O(1)$ and the latter from $T_f - T$ being of $O(1)$. The nondimensional reaction-layer thickness δ_f in the edge region, where variations in temperature and composition are of $O(\epsilon)$, is obtained by a balance between the streamwise diffusion and reaction terms in (4.6) and (4.7), $\delta_f \sim \Gamma\epsilon^2$. Thus, the streamwise

[1] Characteristic thicknesses in this discussion are normalized with the mixing-layer thickness δ_M.

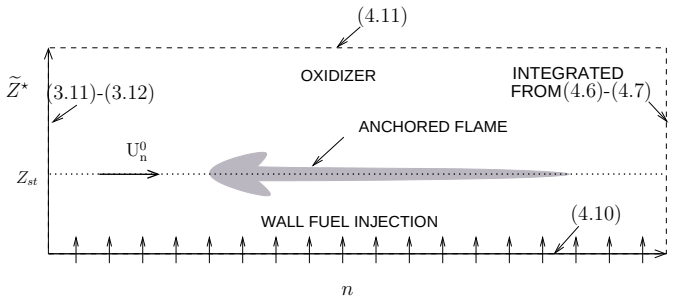

Figure 4.1: The computational model problem used to study the influences of the cold porous wall on the propagation of straight edge flames. The boundary conditions indicated refer to equations in the main text.

diffusion and reaction terms in the edge reaction-layer region are of $O(1/\Gamma\epsilon)$, whereas the streamwise convection transport is of $O(1/\Gamma)$ and the transversal diffusion term is of $O(\Gamma\epsilon)$, since variations of temperature of $O(\epsilon)$ occur in transversal distances of $O(\epsilon)$, which are of the same order as the radius of curvature ϵ of the triple-flame wings. The thickness of the trailing diffusion flame δ_{fl}, where variations in temperature and composition are of order $\epsilon\Delta_{fl}^{-1/3}$, is obtained by a balance between the transversal diffusion and reaction terms, $\delta_{fl} \sim \epsilon\Delta_{fl}^{-1/3}$. Finally, if $\Delta_{fl} \sim \Delta_f$, the diffusion-flame Damköhler number can be related to the propagation parameter Γ by using (4.5). However, both Damköhler numbers can differ by large amounts, as detailed below. These estimates are used in what follows to obtain the characteristic dimensions of triple flames propagating in strained mixing layers in both adiabatic and non-adiabatic modes.

Numerical computations were performed to analyze and isolate the effects of the cold porous wall on the propagation of a nearly straight edge flames. For that purpose, equations (4.6)-(4.11) were integrated numerically without streamwise hydrodynamic flow effects, $\mathrm{v_{n,rel}} = 0$ (a better approximation for small values of Γ), subject to (4.10) on the disk surface and to the frozen profiles (3.11)-(3.14) far upstream from the edge and in the oxidizer stream far from the surface. The effect of the von Kármán flow that was retained is its influences on the mixture-fraction field, through the scalar dissipation rate (2.42), which appears in (4.6) and (4.7). The boundary conditions far downstream were calculated from the conservation equations in each iteration. A schematic diagram of the computational model is shown in figure 4.1. The numerical calculations for the adiabatic case (large-$\mathcal{B}$ limit) used a Zel'dovich number $1/\epsilon = 8$ and a stoichiometric mixture fraction $Z_{st} = 1/2$, with a single-step chemical reaction of pure Arrhenius type and zero feed-stream temperature difference $T_\infty = T_S$ as in [8]. The numerical calculations for the non-adiabatic case (small-

$\mathcal{B}$ limit) used the same Zel'dovich number and a CH_4-air stoichiometric mixture fraction $Z_{st} = 0.056$, with zero feed-stream temperature difference $T_\infty = T_S$, and variable activation energy and heat release as in [33] to avoid unrealistic super-adiabatic flame speeds on the fuel side that are artifacts of hydrocarbon single-step reactions with constant activation energy [33].

Both cases were calculated using a centered, second-order finite-difference method with an explicit predictor-corrector time-relaxation numerical scheme, and with 42,000 mesh points for the adiabatic case and 72,000 mesh points for the non-adiabatic case. Numerical convergence was established by obtaining a constant propagation velocity and time-invariant excess enthalpy and temperature distributions with a tolerance of 10^{-8}. The method for anchoring the flame within the computational domain and for obtaining the burning-rate eigenvalue closely followed earlier work [38]. First, the computation was performed in the laboratory frame with a localized ignition of the mixture far downstream from the anchoring point, and the resulting propagation velocity was observed. Next, the front was fixed in a moving frame by specifying the temperature at an arbitrary anchoring point (which in the calculations was set to $n = 0$ and $Z = Z_{st}$), and the previously observed velocity was used as a first approximation in an iterative process. Finally, the convective velocity in the moving frame until convergence of the steady-flow problem was achieved.

4.2.2 Adiabatic triple-flame propagation regimes

For $\mathrm{Re}_j \geqslant O(1)$ the mass-transfer number is $\mathcal{B} \geqslant O(1)$ according to (2.37), the flame is far from the wall and the heat-loss term involving $\mathcal{B}$ in (4.10) is negligible. The edge, trailing diffusion flame, and adiabatic flame temperatures are expected to be nearly equal, $T_f \sim T_{fl} \sim T_{fl}^\infty$. In these regimes, the Damköhler numbers of the edge and trailing diffusion flame are of the same order of magnitude, $\Delta_f \sim \Delta_{fl}$, and the flame is isenthalpic if the feed-stream temperatures are equal.

Figure 4.2(a-d) shows the asymptotic propagation regimes found by using the scaling analyses outlined above for particular orderings of Γ, in the limit of large $\mathcal{B}$ and without streamwise hydrodynamic flow effects. The ordering of the reaction-zone shape (the shaded region) is different for the edge and for the trailing diffusion flame, and those orderings, following from [8], depend on the ordering of Γ. The transverse extent of the edge reaction zone is of $O(\epsilon)$ in all regimes, but the ordering of its longitudinal extent increases with increasing ordering of Γ, as does the ordering of the transverse extent of the reaction zone of the trailing diffusion flame. Advancing edges occur for small enough curvatures of the triple-

flame wings. At larger ordering of Γ, just prior to the complete diffusion-flame extinction, all edges retreat.

Figure (4.2)(e,f) shows an example of a triple flame structure obtained by the numerical integration of a similar set of equations to (4.6)-(4.11) as in [8], which corresponds to a two-dimensional steady triple flame in a counterflow mixing layer. This configuration is expected to be qualitatively similar to the large-$\mathcal{B}$ limit in the present analysis, and the similarity of the results helps to validate the numerical code utilized here. The premixed front and the trailing diffusion flame burn more intensely as the stratification in the mixing layer is reduced. Extinction of the trailing diffusion flame is not observed in any of the advancing-edge regimes. The dynamics of triple flames in these regimes has been studied extensively in the past [3-8,39].

4.2.3 Non-adiabatic triple-flame propagation regimes

For $\mathrm{Re}_j \ll 1$ the mass-transfer number is $\mathcal{B} \ll 1$ according to (2.37), and the heat-loss term in (4.10) is non-negligible. In this regime, the flame is non-insenthalpic even in the case of equal feed-stream temperatures. The temperature of the edge T_f and the trailing diffusion-flame temperature T_{fl} given by (3.26) are not necessarily the same because of the heat losses to the disk surface. Similarly, $T_{fl} < T_{fl}^{\infty}$ in view of (3.15), (3.22), (3.26) and (3.27). Small differences between T_f and T_{fl} lead to the expression

$$\begin{aligned} \frac{\Delta_f}{\Delta_{fl}} &\sim \exp\left[-\frac{1}{\epsilon}\left(\frac{T_{fl}-T_f}{T_{fl}/T_f}\right)\right] \\ &= \exp\left[\frac{1}{\epsilon}\left(\frac{H_f+\beta_{fl}}{1-(H_f+\beta_{fl})/T_f}\right)\right], \end{aligned} \tag{4.14}$$

where $H_f = -\beta_{fl} + T_f - T_{fl}$ is a characteristic excess enthalpy in the edge region. In particular, if $T_f - T_{fl} = O(\epsilon^n)$ with $0 < n < 1$, then the excess enthalpy of the edge is larger than the excess enthalpy in the diffusion flame $H_f > -\beta_{fl}$ by amounts of order ϵ^n, and $\Delta_f/\Delta_{fl} = O(\mathrm{e}^{\epsilon^{-|1-n|}}) \gg 1$. Similarly, if $T_f - T_{fl} = O(\epsilon^n \ln\epsilon)$ with $0 \leqslant n \leqslant 1$, then $H_f > -\beta_{fl}$ as well and $\Delta_f/\Delta_{fl} \sim \mathrm{e}^{\epsilon^{-|1-n|}/(1-n)} \gg 1$. These estimates show that, in the limit of large activation energy, small differences between the edge reaction-zone and trailing diffusion-flame temperatures can lead to triple flames with large or order-unity front Damköhler numbers and small diffusion-flame Damköhler numbers, which are representative of propagating edges of diffusion flames that are close to extinction or have already undergone complete extinction. These edges propagate nearly adiabatically with an excess enthalpy distribution that, in the first approximation, is uniform in the $n-$ direction

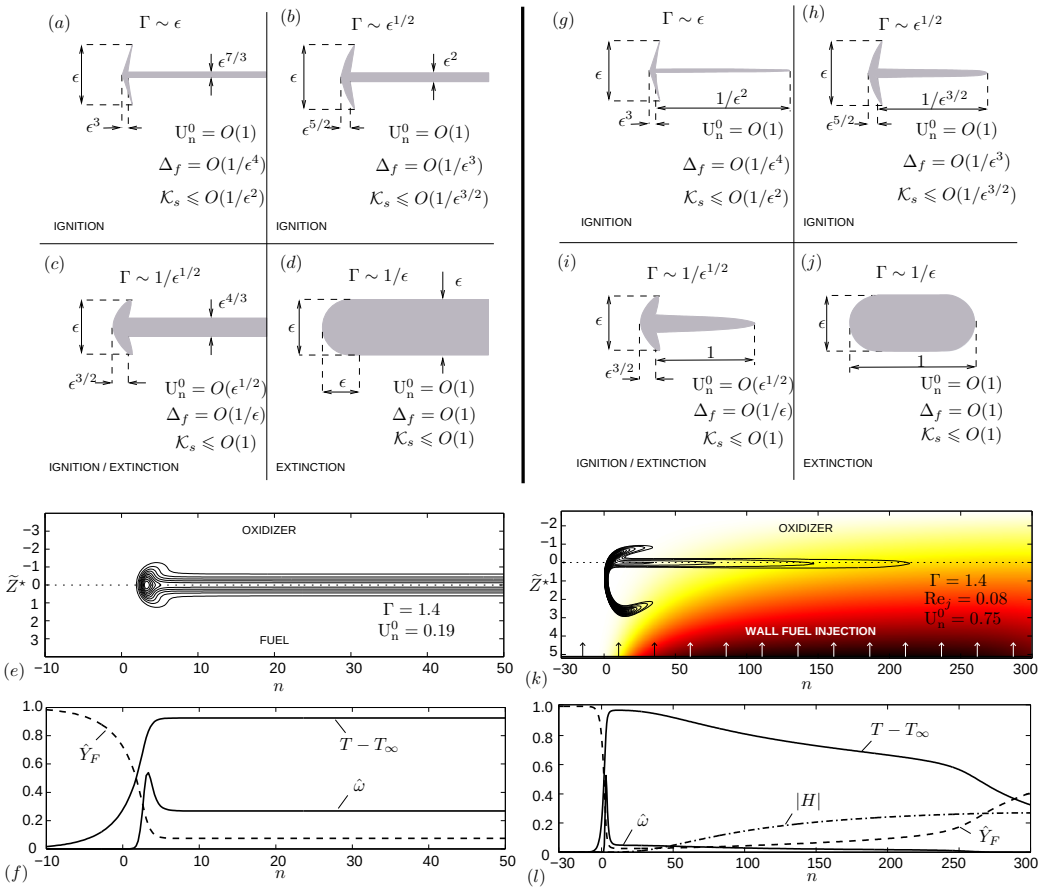

Figure 4.2: Asymptotic propagation regimes for small (a-b,g-h) and large (c-d,i-j) mixture-fraction gradients for adiabatic (left column) and non-adiabatic (right column) triple flames. Shaded areas represent reaction-zone thicknesses. Thicknesses are nondimensionalized with the hydrodynamic scale δ_M. The propagation velocity is nondimensionalized with the planar laminar premixed-flame velocity. The curvature value shown is the maximum curvature in hydrodynamic scales above which the curvature term in (4.6) and (4.7) has an order-unity effect on the planar propagation velocity and tangential heat loss terms should be retained; for smaller curvatures, the correction to the planar propagation velocity is expected to be small and simply linear as in $\mathrm{U_n} = \mathrm{U_n^0} - \Gamma\epsilon\mathcal{K}_s$, which is consistent with the overall convective velocity (or eigenvalue) that multiplies the streamwise convection terms (4.6) and (4.7) for $\mathrm{v_{n,rel}} = 0$. (e) Reaction-rate contours of the numerical solution for a freely propagating triple flame with $\Gamma = 1.4$ in a counterflow mixing layer as in [8], and (f) associated temperature, reaction-rate and fuel-mass fraction profiles along the stoichiometric line. (k) Excess-enthalpy color contours ranging from $H = -0.85$ (dark-red color, online version; dark-grey color, printed version) to $H = 0$ (white color), and reaction-rate contours of the numerical solution for a triple flame with $\Gamma = 1.4$ and $\mathrm{Re}_j = 0.08$ propagating near the disk wall in a von Kármán boundary layer, and (l) associated temperature, reaction-rate, excess-enthalpy and fuel-mass fraction profiles along the stoichiometric line.

and is given by (3.28); however phenomenologically different, such highly diffusive behavior of the excess enthalpy H is somewhat reminiscent of the "Fife limit" encountered in earlier treatments of some of the chemical patterns of table 1.1, in which the controller variable is found to diffuse much more rapidly than the propagator variable [40].

Figure 4.2(g-j) shows the asymptotic propagation regimes found by varying Γ in (4.6) and (4.7) for negligible tangential curvature and without effects of the normal hydrodynamic flow to the front. The nearly adiabatic propagation of the edge is justified by the fact that, i) for $\Gamma \ll 1/\epsilon$, the transverse heat diffusion term $\Gamma\widetilde{\chi}\partial^2 T/\partial\widetilde{Z}^{\star 2}$ in the preheat region, which is of $O(\Gamma\epsilon^2)$, is much smaller than the heat streamwisely convected to ignite the frozen mixture ahead, $\mathrm{U}_\mathrm{n}^0\partial T/\partial n = O(1/\Gamma)$, which is balanced with the streamwise heat diffusion $\Gamma\partial^2 T/\partial n^2 = O(1/\Gamma)$ there, and ii) for $\Gamma \ll 1/\epsilon$, the transverse heat diffusion in the edge reaction-layer region, $\Gamma\widetilde{\chi}\partial^2 T/\partial\widetilde{Z}^{\star 2}$, is of $O(\Gamma\epsilon)$ and much smaller than the streamwise diffusion $\Gamma\partial^2 T/\partial n^2 = O(1/\Gamma\epsilon)$, which is is balanced with the chemical reaction $O(1/\Gamma\epsilon)$ there. Therefore the front propagates in a transversally adiabatic mode in the first approximation for a range of Γ, either in advancing or in very weak retreating modes, $\Gamma \ll 1/\epsilon$.

For propagation regimes in which $\Delta_f/\Delta_{fl} \gg 1$, extinction of the trailing diffusion flame exists when $\Delta_{fl} \lesssim \Delta_E$ and a balance between the transverse diffusion and strain rate has been established downstream of the edge. This qualitative difference from figure 4.2(a-d) is illustrated in figure 4.2(g-j). The diffusion-flame extinction occurs at dimensional distances from the edge of order $\mathrm{U}_\mathrm{n}^0\delta_M^2/D_T$ (with U_n^0 dimensional), which is obtained by a balance between transverse diffusion and streamwise convection, and in the present nondimensional notation corresponds to $n_E \sim \mathrm{U}_\mathrm{n}^0/\Gamma\epsilon^2$ in scales $\epsilon\delta_M$. Over distances of order n_E, the frozen profiles (3.11)-(3.14) are recovered. The dimensional time for extinction of the diffusion flame is therefore

$$t_E \sim \delta_M^2/D_T, \tag{4.15}$$

which increases with decreasing Ω.

These aspects of non-adiabatic triple-flame regimes can be observed in figure 4.2(k,l), which shows the results of the numerical integration for small $\mathcal{B}$ mentioned previously. The values employed for the computation in the model illustrated in figure 1.5, namely $\Gamma = 1.4$ and $\mathrm{Re}_j = 0.08$, are beyond the static quenching point of the diffusion flame, as verified by a separate calculation of the extinction of the diffusion flame after dropping the streamwise transport terms in (4.6) and (4.7). The computation, which corresponds to a condition between that of figure 4.2(h) and figure 4.2(i), clearly exhibits a triple-flame type

of structure for the propagating reaction layer, although some broadening in the preheat region is expected.

It is worth mentioning that diffusion-flame edges behind which diffusion flames cannot exist have been characterized previously within the context of non-equidiffusive non-premixed combustion [41], for which a non-zero excess enthalpy distribution is enhanced by non-unity Lewis-number effects. It is well known that, since the adiabatic temperature is a thermodynamic property that is independent of the diffusive properties of the mixture, the Lewis number affects the diffusion-flame temperature but does not influence the premixed-flame temperature [1]. Therefore, extinction of the trailing diffusion flame can be induced by increasing the average Lewis number of the mixture and thereby reducing the diffusion of reactants into the reaction zone, which decreases the diffusion-flame temperature while maintaining the same front temperature, in this way producing what have been termed "edges of flames that do not exist" [41]. The present situation is different in that the excess enthalpy is responsible for the extinction of the diffusion flame, this negative excess coming from the heat losses to the disk surface, which are larger in the presence of the diffusion flame than in the preheat and edge reaction-layer regions of the propagating edge flame.

4.3 Edge dynamics

4.3.1 The G-equation

When the kinematic relation (4.12) is substituted into the edge equation (4.2), the expression

$$\frac{\partial G}{\partial t} + \mathbf{v}_{\perp}|_{\widetilde{Z}=\widetilde{Z}_{fl}} \cdot \nabla G = \mathrm{U_n}|\nabla G|, \tag{4.16}$$

for the scalar G is obtained, which has been termed the "G-equation" in turbulent-combustion literature [1, 2]. In this section, spatial coordinates and velocities are nondimensionalzed with δ_M and $\delta_M\Omega$, as in the original hydrodynamic formulation. A linear Markstein-type correction model for the effects of curvature on the propagation velocity $\mathrm{U_n}$ [43] is used in this study to account for heat losses from the curved edge,

$$\mathrm{U_n} = \mathrm{U_n^0} - \frac{\mathrm{Ma}}{\mathrm{Pr}}\mathcal{K}_s. \tag{4.17}$$

Here Ma, a Markstein number that in general would depend on the edge-flame structure, is set equal to unity to be consistent with the previous simplified formulation, which results in an equivalent Markstein length $\mathcal{L} = D_T/\mathrm{U_n^0}$, of the same order as the preheat thickness of the edge. The resulting approximation is expected to be reasonable for equidiffusional

flames in analogy to wrinkled premixed flames [44], but to be limited to small differences $(\mathrm{U}_\mathrm{n}^0 - \mathrm{U}_\mathrm{n})/\mathrm{U}_\mathrm{n}^0$. Upon substituting (4.17) into (4.16), the G-equation reduces to

$$\frac{\partial G}{\partial t} + \mathbf{v}_\perp|_{\widetilde{Z}=\widetilde{Z}_{fl}} \cdot \nabla G + \frac{\mathcal{K}_s|\nabla G|}{\mathrm{Pr}} = \mathrm{U}_\mathrm{n}^0|\nabla G|. \tag{4.18}$$

Expression (4.18) represents a Hamilton-Jacobi equation with a parabolic second-order differential operator in the curvature term. The first term on the left-hand side of (4.18) represents the local time variation of the edge shape, the second term accounts for the advection of the edge by the underlying swirling flow, the third term is a diffusive contribution that results from curvature effects on the propagation velocity, and the first term on the right-hand side is a source that accounts for the front self-propagating motion normal to itself because of the heat transfer from the planar edge to the frozen mixture upstream.

The scalar field G is a assumed to be of the form $G(r,\theta,t) = F(r,t) - \theta$, with $\partial F/\partial\theta = 0$, although it can be shown that the solution for G is independent of this ansatz [2]. The normal vector to the front is then

$$\mathbf{e_n} = -\left[\left(r\frac{\partial F}{\partial r}\right)\mathbf{e_r} - \mathbf{e}_\theta\right] \Bigg/ \sqrt{\left(r\frac{\partial F}{\partial r}\right)^2 + 1}, \tag{4.19}$$

where use has been made of (4.1). Thus, the tangential curvature (4.13) can be expressed as

$$\mathcal{K}_s = \left[r^2\left(\frac{\partial F}{\partial r}\right)^3 + 2\frac{\partial F}{\partial r} + r\frac{\partial^2 F}{\partial r^2}\right] \Bigg/ \left[r^2\left(\frac{\partial F}{\partial r}\right)^2 + 1\right]^{3/2}. \tag{4.20}$$

In view of (2.8), substituting (4.19) and (4.20) into (4.18), the equation

$$\begin{aligned} \frac{r\dfrac{\partial F}{\partial t}}{\sqrt{\left(r\dfrac{\partial F}{\partial r}\right)^2 + 1}} \;-\; & \frac{\dfrac{|\phi'_{fl}|r^2}{2}\dfrac{\partial F}{\partial r} - rV_{fl}}{\sqrt{\left(r\dfrac{\partial F}{\partial r}\right)^2 + 1}} \\ = \; & -\frac{r^2\left(\dfrac{\partial F}{\partial r}\right)^3 + 2\dfrac{\partial F}{\partial r} + r\dfrac{\partial^2 F}{\partial r^2}}{\mathrm{Pr}\left[r^2\left(\dfrac{\partial F}{\partial r}\right)^2 + 1\right]^{3/2}} + \mathrm{U}_\mathrm{n}^0 \end{aligned} \tag{4.21}$$

is obtained for the evolution of $F(r,t)$. In this formulation, $|\phi'_{fl}|/2$ and V_{fl} represent the self-similar radial and azimuth hydrodynamic velocity gradients in the radial direction evaluated at the flame height $\widetilde{Z} = \widetilde{Z}_{fl}$. Similar equations have been encountered in earlier studies [16, 17, 45] of spiral-wave propagation in pure reactive-diffusive systems; the results obtained in this section thereby represent a generalization by including swirling flow advection.

4.3.2 The tangential structure of a steadily rotating spiral

For the case of steadily rotating spirals, the front moves in a solid-rotation mode in the laboratory frame, describable as

$$\mathbf{U_{LF}} = -\omega r \mathbf{e}_\theta, \tag{4.22}$$

and the functional form

$$F(r,t) = f(r) + \omega t, \tag{4.23}$$

can be substituted in (4.21), where ω is the rotating burning rate eigenvalue nondimensionalized with the disk angular velocity Ω. An additional change of variables, $\varphi = r(df/dr) = \tan\gamma$, where γ is the slope angle between the edge and the radial unit vector, is performed here to facilitate calculations.

The experimental findings to be outlined in Chapter 5 suggest that the spirals rotate about a hole of finite radius, denoted dimensionally here by $r^\bigstar$, which is observed to be much larger than a representative radius of curvature $\mathcal{L}$ in the vicinity of the tip. This limit is referred to as the "large core" limit in what follows in analogy to earlier works on spirals in reactive-diffusive systems [16]. As will be seen later in figure 5.1, the spiral flames spin in solid rotation motion for sufficiently small Re_j and Da, and the radius $r^\bigstar$ decreases with decreasing Re_j and increasing Da. This is also true to some extent for slightly meandering spirals, for which the tip meanders about the disk center in an epicycloidal trajectory of an average radius that could be treated as $r^\bigstar$ (see Chapter 5, figure 5.2). However, the quasi-steady decomposition (4.23) is not generally valid for meandering spirals, since the unsteady effects would be important in that case. The inner region $r - r^\bigstar = O(\mathcal{L})$ represents the region where effects of reactant and heat diffusion cause a non-negligible contribution to the front propagation velocity through the flame tangential curvature.

Spatial dimensions are renormalized in equation (4.21) for convenience as $\tilde{r} = r/\ell$, with the outer scale ℓ defined as

$$\ell = \frac{2\mathrm{U}_n^0}{\Omega|\phi'_{fl}|}, \tag{4.24}$$

which corresponds to the radial length at which the radial velocity induced by the disk, $|\phi'_{fl}|\Omega\ell/2$, is equal to the dimensional planar front propagation velocity U_n^0. In this revised scale, the curvature (4.20) becomes

$$\widetilde{\mathcal{K}}_s = \frac{1}{\tilde{r}}\frac{\varphi}{(1+\varphi^2)^{1/2}} + \frac{d\varphi/d\tilde{r}}{(1+\varphi^2)^{3/2}}, \tag{4.25}$$

which is related to the propagation velocity by the Markstein formula (4.17), which becomes $\mathrm{U_n} = \mathrm{U_n^0}(1-\lambda\widetilde{\mathcal{K}}_s)$ in these variables. Similarly, the transport equation (4.21) is transformed into

$$\begin{aligned}\lambda\Big[\tilde{r}\frac{d\varphi'}{d\tilde{r}} &+ (1+\varphi^2)\varphi\Big] \\ &= (1+\varphi^2)\left[\tilde{r}(1+\varphi^2)^{1/2} - \tilde{r}^2(\mathcal{S}-\varphi)\right],\end{aligned} \tag{4.26}$$

where λ is a dimensionless Markstein diffusivity that represents the ratio of the characteristic radius of curvature to the outer spatial scale,

$$\lambda = \frac{\mathcal{L}}{\ell} = \frac{|\phi'_{fl}|}{2\mathrm{Pr}}\left(\frac{\delta_M\Omega}{\mathrm{U_n^0}}\right)^2 \ll 1, \tag{4.27}$$

which is experimentally observed to be a small parameter, and where

$$\mathcal{S} = 2(V_{fl}+\omega)/|\phi'_{fl}| \tag{4.28}$$

is a swirl number that represents the ratio of the effective swirl in the Frenet frame to the radial velocity component at any radial distance.

Figure 4.3 shows the variations of the swirl number $\mathcal{S}$ with the injection Reynolds number, calculated from (4.28) by using solutions of the von Kármán swirling flow with fuel injection, evaluated at the distance from the porous disk at which $Z = Z_{st} = 0.056$, the stoichiometric surface. The non-monotonicity of the dependence of $\mathcal{S}$ on Re_j for $\omega > 0$, is a reflection of the non-monotonicity of the radial velocity illustrated in figure 2.2(a). For small Re_j, near Re_j^{min}, as the injection velocity is decreased the stoichiometric surface approaches the surface of the disk, and $\mathcal{S}$ becomes infinite because the radial velocity reaches zero when it is at the disk; on the other hand, for large Re_j the stoichiometric surface moves farther into the air, where the radial velocity is smaller, as the injection rate is increased.

An expression for the dimensionless core radius, which represents the lift-off radius at which the tip is anchored by the radial convection, can be obtained, in the approximation (4.17) of a linear dependence of the propagation velocity on curvature, by rearranging (4.26), which gives

$$\tilde{r}^{\bigstar} = \left(1-\lambda\widetilde{\mathcal{K}}_s^{\bigstar}\right)\frac{\sqrt{1+\varphi^{\bigstar 2}}}{S-\varphi^{\bigstar}}, \tag{4.29}$$

where the superindex $^{\bigstar}$ represents quantities evaluated at the tip. The ratio $\ell/\delta_M = O(\Delta_f^{1/2}) \gg 1$ is a large number for having igniting fronts according to Figure 4.2 and equation (4.5), which indicates that the typical core size is much larger than the mixing layer thickness as observed in the experiments. The Markstein length is smaller than the mixing-layer thickness for having preheat thicknesses smaller than δ_M, so that $\mathcal{L} \ll \delta_M \ll r^{\bigstar} \leqslant \ell$,

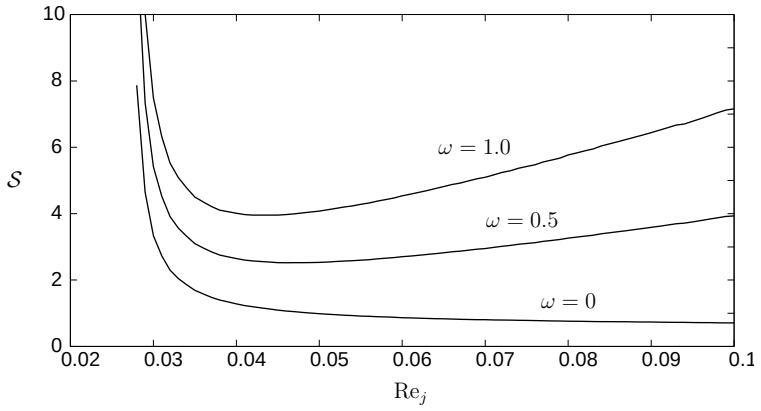

Figure 4.3: Swirl number as a function of the injection Reynolds number.

which is achieved when $\Gamma \ll 1/\epsilon$. In this limit, the spiral tip is anchored in a region of large radial and azimuth hydrodynamic velocities, which are of order $\ell\Omega$, whereas the normal fluid velocity to the disk is much smaller there, of order $\delta_M\Omega$.

The outer region

For $\tilde{r} \gg 1$ and $\lambda \ll 1$, the outer solution of (4.26) is

$$\varphi = \frac{\tilde{r}^2\mathcal{S} - \sqrt{\tilde{r}^2(1+\mathcal{S}^2)-1}}{\tilde{r}^2-1}, \tag{4.30}$$

to leading order in λ, which represents the equation of an edge flame propagating with a velocity that is unaffected by curvature.

Substituting (4.30) into (4.29) for $\lambda = 0$, the core radius

$$\tilde{r}_0^{\bigstar} = 1/\sqrt{1+\mathcal{S}^2} \tag{4.31}$$

is obtained, which corresponds to the radius at which the modulus of the incoming fluid velocity in the Frenet reference frame equals the planar propagation velocity, $\mathrm{U}_\mathrm{n}^0 = ||\mathbf{v}_\perp|_{\widetilde{Z}=\widetilde{Z}_{fl}} - \mathbf{U_{LF}}||$, so that the edge arrives at the tip normal to the incoming relative flow. For $\tilde{r} < \tilde{r}_0^{\bigstar}$, since $||\mathbf{v}_\perp|_{\widetilde{Z}=\widetilde{Z}_{fl}} - \mathbf{U_{LF}}|| < \mathrm{U}_n^0$, the normal component of the relative swirling flow $(\mathbf{v}_\perp|_{\widetilde{Z}=\widetilde{Z}_{fl}} - \mathbf{U_{LF}}) \cdot \mathbf{e_n}$ is smaller than the propagation velocity U_n^0, so that the spiral must end at $\tilde{r}_0^{\bigstar}$ in the first approximation $\lambda = 0$.

For $\tilde{r} \to \infty$, the outer solution asymptotes to

$$\varphi \sim \mathcal{S} - \frac{\sqrt{1+\mathcal{S}^2}}{\tilde{r}} + \frac{\mathcal{S}}{\tilde{r}^2} + O\left(\frac{1}{\tilde{r}^3}\right). \tag{4.32}$$

It is worth mentioning that the reactive-diffusive systems of figure 1.2(b-e) display Archimedean spiral patterns far from the core, $r \sim \theta$, whereas in the present analysis Bernoulli spirals are obtained in the far field in the first approximation, $\tilde{r} \sim \mathrm{e}^{\theta/\mathcal{S}}$, which coincide with the streamlines of the two-dimensional flow field relative to the flame. The spiral growth in geometric progression found in the experiments suggests that this is in fact the case for the spiral flames, which explains the few spiral turns observed and the rapid growth due to advection effects, which departs from the linear Archimedean growth of the reactive-diffusive spirals shown in figure 1.2 (b-e).

For $\tilde{r} \sim \tilde{r}_0^{\bigstar}$ the outer solution (4.30) asymptotes to

$$\varphi \sim -\frac{1}{\mathcal{S}} + \frac{\sqrt{2}}{\mathcal{S}^2}(1+\mathcal{S}^2)^{5/4}\left(\tilde{r}-\tilde{r}_0^{\bigstar}\right)^{1/2} + O\left(\tilde{r}-\tilde{r}_0^{\bigstar}\right). \tag{4.33}$$

Figure 4.4 shows the edges obtained by making use of (4.30) for different values of the swirl number. Large values of $\mathcal{S}$ are associated with highly curved spirals, whereas straight edges occur for small $\mathcal{S}$. According to figure 4.3, for the same value of $\mathcal{S}$, with $\mathcal{S} > 0$, there is an infinite set of counter-rotating spirals, as well as an infinite set of co-rotating spirals at much lower values of Re_j (less than its value for $\omega = 0$) that share the same edge geometry (since $\mathcal{S}$ is the same) and correspond to advancing fronts, $\mathrm{U}_\mathrm{n}^0 > 0$. In addition, at fixed Re_j, achievable, for instance, by fixing Ω and the fuel-injection rate, there are correspondingly infinite sets of spirals with different shapes, each with a different $\mathrm{U}_\mathrm{n}^0 > 0$.

The second term in the expansion (4.33) is not differentiable at the spiral tip, and the curvature (4.25) becomes infinite there for $\mathcal{S} > 0$, which renders the solution (4.30) non-uniform in the limit $\lambda \to 0^+$. For $\mathcal{S} = 0$, a straight edge that is stationary in the incoming fluid reference frame ($\mathrm{U}_\mathrm{n}^0 = 0$) is obtained, and it co-rotates with the local azimuth flow in the laboratory frame for all Re_j with an angular velocity ΩV_{fl} and a core radius $r^{\bigstar} = \ell$ to every order in λ. However, single steady co-rotating edges have been experimentally observed only in multiple-spiral dynamics, a problem that is not addressed here. Additionally, the tip calculated by the outer solution (4.30) is found to be quasi-statically unstable to spatial perturbations, as detailed in Section 4.3.3.

The inner region

The non-uniformity of the outer solution at the tip leads to the existence of an inner region, $\tilde{r} - \tilde{r}^{\bigstar} = O(\lambda)$, where the curvature term is non-negligible. According to equation (4.31), so long as $\mathcal{S}$ is not large, $\mathcal{S} \ll 1/\lambda$, the core radius $r^{\bigstar}$ is larger than the Markstein length $\mathcal{L}$, and $\lambda/\tilde{r}^{\bigstar}$ can be regarded as a small parameter as well, which represents the

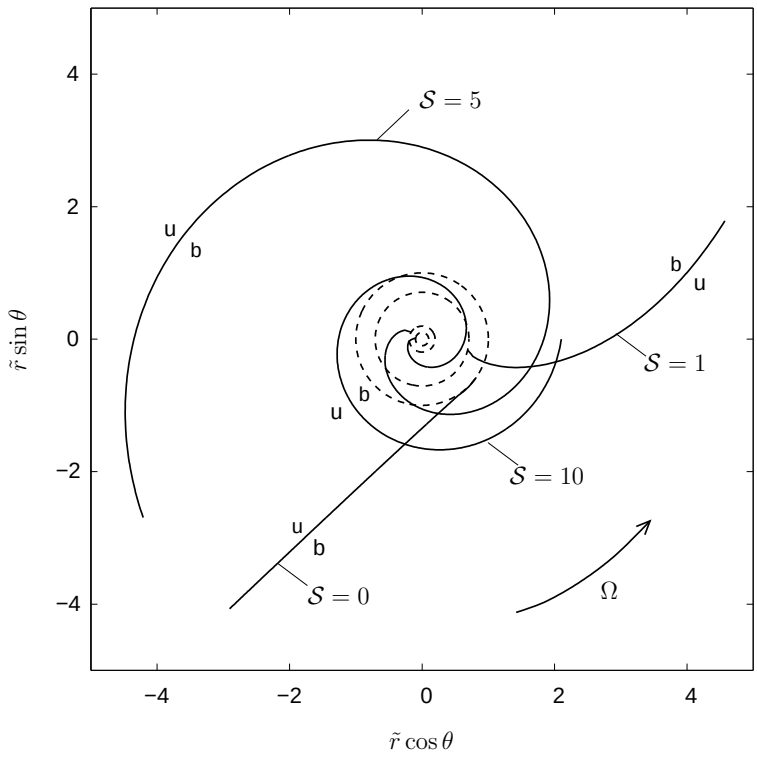

Figure 4.4: Spiral edges obtained by using the outer solution (4.30). The letters u and b denote the unburnt and burnt sides of the edge respectively, and the arrow indicates the swirling direction of the hydrodynamic flow.

large-core limit. In this limit, the inner-region equation

$$\frac{d\varphi}{d\xi} = (1+\varphi^2)^{3/2} - \tilde{r}^{\bigstar}(1+\varphi^2)(\mathcal{S}-\varphi), \tag{4.34}$$

is obtained to leading order in $\lambda/\tilde{r}^{\bigstar}$, where

$$\xi = \frac{\tilde{r}-\tilde{r}^{\bigstar}}{\lambda}, \tag{4.35}$$

is the inner variable. For $\xi \to +\infty$, the solution of (4.34) is asymptotic to $\varphi = -1/\mathcal{S} + \Psi$, where Ψ is a $O(\lambda)$ correction with respect to the outer leading-order value that satisfies the nonlinear equation $d\Psi/d\xi = \mathcal{S}\tilde{r}^{\bigstar}\Psi^2/2$ subject to $\Psi \to 0$ as $\xi \to +\infty$, which gives

$$\varphi \sim -\frac{1}{\mathcal{S}}\left(1+\frac{2}{\tilde{r}^{\bigstar}\xi}\right), \qquad \xi \to +\infty. \tag{4.36}$$

For $\xi \to 0$, the inner equation (4.34) reduces to $d\varphi/d\xi \sim (\tilde{r}^{\bigstar}-1)\varphi^3$ subject to $\varphi \to -\infty$ as $\xi \to 0$, which gives

$$\varphi \sim -\frac{1}{\mathcal{S}}\left(1+\frac{2}{\tilde{r}^{\bigstar}\xi}\right), \qquad \xi \to +\infty. \tag{4.37}$$

Upon substituting (**??**) into (4.25), the curvature value at the tip is found to be

$$\widetilde{\mathcal{K}}_s^{\bigstar} \sim \frac{1-\tilde{r}^{\bigstar}}{\lambda}, \tag{4.38}$$

which represents the maximum curvature of the edge. Therefore, the propagation velocity at the spiral tip is

$$\frac{\mathrm{U_n}^{\bigstar}}{\mathrm{U_n^0}} \sim \tilde{r}^{\bigstar}, \tag{4.39}$$

consistent with formulation based on (4.17).

Equation (4.39) can be read in dimensional variables as $\mathrm{U_n}^{\bigstar} = \Omega|\phi'_{fl}|r^{\bigstar}/2$, which represents a balance between the edge propagation velocity (with curvature correction included) and the radial convection at $r^{\bigstar}$. For $\lambda > 0$, with $\lambda \ll 1$, the edge in the tip region is normal to the radially advected mixture and advances towards it.

Figure 4.5 shows examples of spiral tips obtained by the numerical integration of (4.26) subject to $\varphi \to \mathcal{S}$ at $\tilde{r} \to \infty$. All the spirals with $\lambda \neq 0$ arrive perpendicularly to a radial vector, so that the circular motion of the spiral is locally irrelevant at the core radius. As the dimensionless Markstein diffusivity λ increases, the tip moves closer to the center of rotation, and it asymptotically passes through the center for a particular critical value $\lambda_C(\mathcal{S})$ that needs to be calculated numerically, and for which the edge goes from burning in an advancing mode, $\mathrm{U_n}^{\bigstar} > 0$, to being locally stationary, $\mathrm{U_n}^{\bigstar} = 0$. For $\lambda > \lambda_C$, there is an inner portion of the edge that propagates in a retreating mode, $\mathrm{U_n}^{\bigstar} < 0$, locally similar to a laboratory-stationary flame isola in a counterflow burner, while the outer portion still propagates in an advancing mode, as represented in figure 4.5 by the $\lambda = 1.0$ spiral. These last behaviors, however, are unlikely to occur within the range of validity of the linear relationship (4.17), and they are not seen in any of the experiments. The consideration of fixed λ and variable $\mathcal{S}$ produce similar dynamics to those outlined above.

The intermediate region

The asymptotic expansions (4.33) and (4.37) do not match to second order. An intermediate region exists, of thickness $O(\lambda^{3/2})$, that extends from the tip to the segment of the edge that is parallel to the radial unit vector, and the edge is purely azimuthally advected at that point. The intermediate asymptotic expansion

$$\varphi = -\frac{1}{\mathcal{S}} + \frac{\lambda^{1/3}(1+\mathcal{S}^2)^2}{\mathcal{S}^3}\psi + \ldots, \tag{4.40}$$

may be defined, with the intermediate variable

$$\sigma = \frac{\tilde{r} - \tilde{r}^{\bigstar}}{\lambda^{2/3}}. \tag{4.41}$$

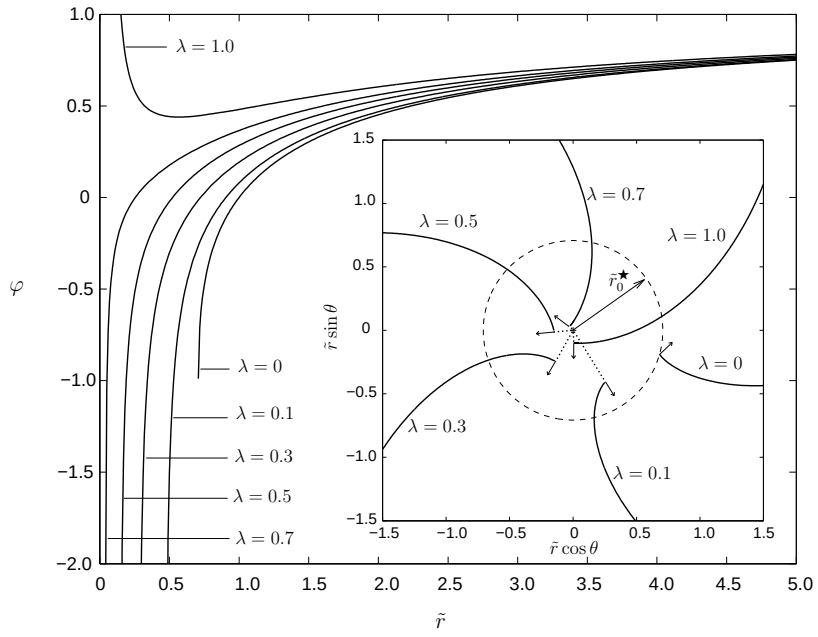

Figure 4.5: Spiral edges obtained by the numerical integration of (4.26) for $\mathcal{S} = 1$.

Substituting (4.40) and (4.41) into (4.26) and retaining terms of $O(\lambda^{2/3})$, the equation

$$\frac{d\psi}{d\sigma} - q\psi^2 + \sigma + p = 0, \tag{4.42}$$

is obtained in the distinguished limit $\tilde{r}^\star - \tilde{r}_0^\star = O(\lambda^{2/3})$. In this formulation, p and q are two order-unity constants given by

$$p = \frac{\tilde{r}^\star - \tilde{r}_0^\star}{\lambda^{2/3}}, \tag{4.43}$$

and

$$q = \frac{(1+\mathcal{S}^2)^{3/2}}{2\mathcal{S}^2}. \tag{4.44}$$

Equation (4.42) is a Ricatti equation, which can be cast into an Airy equation by changing the independent variable to $E = q^{1/3}(\sigma+p)$ and defining M such that $\psi = -(1/q^{2/3}M)dM/dE$ [46]. In these variables, (4.42) becomes

$$\frac{d^2M}{dE^2} = ME, \tag{4.45}$$

which solution is a linear combination of Airy functions $\mathrm{Ai}(E)$ and $\mathrm{Bi}(E)$. Matching of (4.40) with (4.33) requires M to be bounded for $E > 0$, so that $M = C\mathrm{Ai}(E)$, where C is an integration constant. Therefore

$$\psi = -\frac{1}{q}\frac{d\ln \mathrm{Ai}(\sigma)}{d\sigma} \tag{4.46}$$

represents the intermediate solution.

For $E \to +\infty$, $M \sim C\exp(-2E^{3/2}/3)/(2E^{1/4}\pi^{1/2})$ and $\psi \sim (\sigma/q)^{1/2}$; the substitution of this upper limit for ψ in (4.40) exactly reproduces the second term of the expansion (4.33) of φ in the upper overlapping region. For ξ large, the intermediate expansion of (4.37) reads $\varphi \sim -1/\mathcal{S} - (1+\mathcal{S}^2)^2/\mathcal{S}^3 q\sigma$. Since $\mathrm{Ai}(E) \sim E - c_1$ near the first zero $c_1 = -2.3381$ of Ai on the negative real axis, then $\psi \sim -q^{-2/3}[q^{1/3}(\sigma+p) - c_1]^{-1}$ for $E \sim c_1$, or equivalently, for $\sigma \to 0$. Therefore, asymptotic matching between the intermediate solution (4.40) and the inner solution (4.37) in the lower overlapping region requires that $pq^{1/3} = c_1$. This matching relation results in the second-order expansion

$$\tilde{r}_1^{\bigstar} = \tilde{r}_0^{\bigstar}\left(1 + 2^{1/3} c_1 \mathcal{S}^{2/3} \lambda^{2/3}\right), \tag{4.47}$$

which shows that the tip radius undergoes reductions of order $\lambda^{2/3}$ with respect to its leading order value when small curvature effects of $O(\lambda)$ on the edge propagation are considered.

Substituting the relation (4.47) into the equations (4.38) and (4.39) obtained from the inner region, the expansions

$$\widetilde{\mathcal{K}}_s^{\bigstar} \sim \frac{1 - \tilde{r}_0^{\bigstar}}{\lambda} - \frac{2^{1/3} c_1 \mathcal{S}^{2/3} \tilde{r}_0^{\bigstar}}{\lambda^{1/3}}, \tag{4.48}$$

and

$$\frac{\mathrm{U_n}^{\bigstar}}{\mathrm{U_n^0}} \sim \tilde{r}_0^{\bigstar}\left(1 + 2^{1/3} c_1 \mathcal{S}^{2/3} \lambda^{2/3}\right) \tag{4.49}$$

are obtained.

Equations (4.31) and (4.47) yield successive approximations of the spiral rotational velocity ω as a function of the rest of the parameters and of the tip curvature when the definitions (4.24), (4.27), (4.28) and (4.38) are used.

4.3.3 Spiral-flame anchoring and quasi-static stability

The rate of variation Υ of the relative normal velocity component in the normal direction to the edge with respect to the propagation velocity variation may be defined as

$$\begin{aligned} \Upsilon &= \frac{1}{\mathrm{U_n^0}}\left[\mathbf{e_n}\cdot\nabla(\mathbf{v}_\perp|_{\widetilde{Z}=\widetilde{Z}_{fl}} - \mathbf{U_{LF}})\cdot\mathbf{e_n} - \frac{\partial \mathrm{U_n}}{\partial n}\right] \\ &= -\frac{\varphi}{\sqrt{1+\varphi^2}}\left[\frac{(\mathcal{S}-\varphi)}{\sqrt{1+\varphi^2}} + \lambda\frac{d\widetilde{\mathcal{K}}_s}{dr}\right]. \end{aligned} \tag{4.50}$$

In particular, Υ represents a physical indicator of the stability of the front with respect to quasi-static infinitesimal perturbations in the normal direction. If $\Upsilon < 0$, when the edge

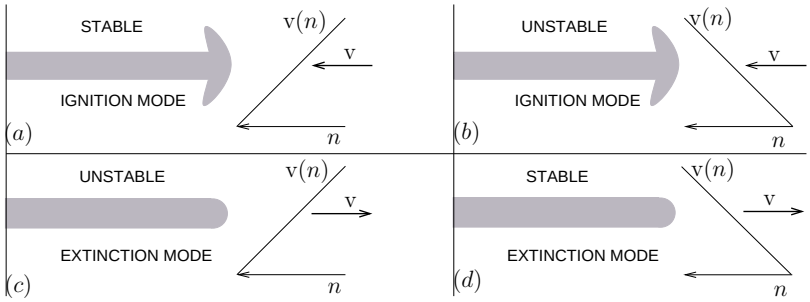

Figure 4.6: Stability schematics of straight edge flames in the presence of normal convective velocity gradients.

position is perturbed toward the propagation direction, the edge encounters a larger normal convective flow velocity component that returns it to its original position, as depicted in figure 4.6(a,d). If $\Upsilon = 0$ somewhere, that portion of the edge is in a neutrally stable state. If $\Upsilon > 0$, when the edge position is perturbed toward the propagation direction, the edge encounters a smaller normal flow velocity component that cannot balance the propagation velocity; under these conditions the edge is unstable and is blown off from its original position towards or away from the disk center, as depicted in figure 4.6(b,c).

Edge-flame instabilities have been encountered in flame holes and flame disks in counterflow burners [3, 26], which correspond respectively to cases (b) and (c) in figure 4.6. Stationary flame holes and flame disks in the laboratory frame are found to heal or expand when perturbed in uniformly strained mixing layers close to the burner axis, and curvature variations of the edges with respect to their radial position produce propagation-velocity variations that contribute to further increase the value of Υ and enhance the instability process. Therefore, these structures can only be observed experimentally in stationary mode when they propagate to distances larger than the injector radius, where the radial velocity decays with the radial distance [47], as in figure 4.6(a,d). However, in this analysis the curvature term $\partial \mathrm{U_n}/\partial n = -\lambda \partial \widetilde{\mathcal{K}}_s/\partial n$ in (4.50) is found to benefit the stability of the spiral flames, since the curvature acts as a heat loss in the range of interest. In this range, the tip region behaves as a flame hole with the opposite curvature sign; the curvature perturbation of the displaced tip contributes to increase the propagation velocity in figure 4.6(b) for perturbations towards the burnt side, and to decrease the propagation velocity for perturbations towards the unburnt side.

Figure 4.7(a) shows the calculated dependence of Υ on $\tilde{r}$ for $\lambda = 0$. For $\tilde{r} > 1/\mathcal{S}$ with $\mathcal{S} > 0$, the edge is stable as in figure 4.6(a), and for $\tilde{r}^{\bigstar} < \tilde{r} < 1/\mathcal{S}$, the inner portion of the edge and the spiral tip are unstable as in figure 4.6(b). The point $\tilde{r} = 1/\mathcal{S}$ is neutrally

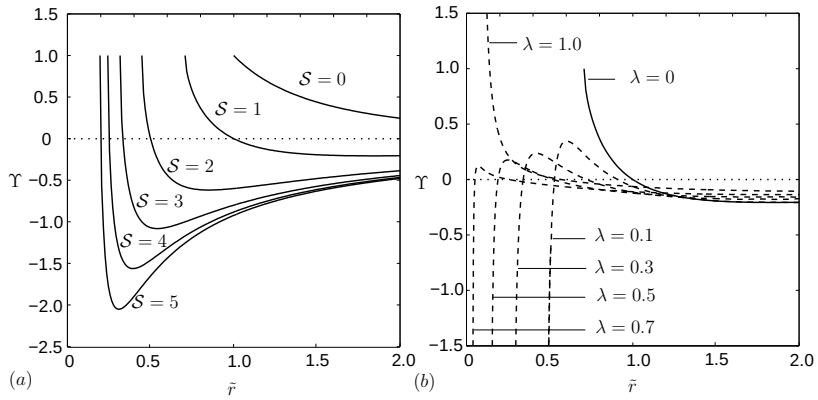

Figure 4.7: (a) Quasi-static stability of spiral edges for $\lambda = 0$. (b) Quasi-static stability of spiral edges for $\mathcal{S} = 1$.

stable since the normal variations are in the azimuth direction there, and the convective velocity modulus remains invariant in that direction. Edges with $\mathcal{S} = 0$, which correspond to stationary fronts in the incoming fluid frame, are unstable for all $\tilde{r}$. Advancing edges propagating at a constant velocity thus are stable at large radii, become neutrally stable when the edge becomes tangent to the radial direction, and are unstable at smaller radii.

Figure 4.7(b) shows the calculation of Υ for $\mathcal{S} = 1$ and $0 \leqslant \lambda \leqslant 1$. The consideration of fixed λ and variable $\mathcal{S}$ produces similar dynamics. Nondimensional Markstein diffusivities in the range $0 < \lambda < \lambda_C$ stabilize the tip region by compensating the decrease in the radial convection with decreasing radius by increasing the tip curvature, thus decreasing the tip propagation velocity. However, sufficiently large values of λ or $\mathcal{S}$ produce a tip that propagates in a retreating mode, as shown in figure 4.5 for the case $\lambda = 1.0$, which leads to an unstable tip as in figure 4.6(c). As shown in the following section, spiral meandering is associated with large values of $\mathcal{S}$ that may enhance such loss of tip stabilization. In this linear quasi-static analysis, there is no combination of values of $\mathcal{S}$ and λ for which $\Upsilon < 0$ for all $\tilde{r}$, and there is always a small part of the edge that is unstable, which is close to the tip in hydrodynamic scales but far from it in scales of order $\mathcal{L}$.

Since the spirals observed in the experiments are stable, the above reasoning indicates that, according to this model, the cuvature found in experiments must be large enough to produce departures from the linear Markstein formula (4.17) for the propagation velocity, such that the stabilizing term $\partial \mathrm{U_n}/\partial n$ may actually be larger than $-\lambda \partial \widetilde{\mathcal{K}}_s/\partial n$. It seems likely that, in analogy with the effects of heat loss on laminar burning velocities [48, 1], there is a critical finite value of the curvature at which the edge flame is extinguished, as illustrated schematically in figure 4.8. The non-linear effects beyond the range of the Mark-

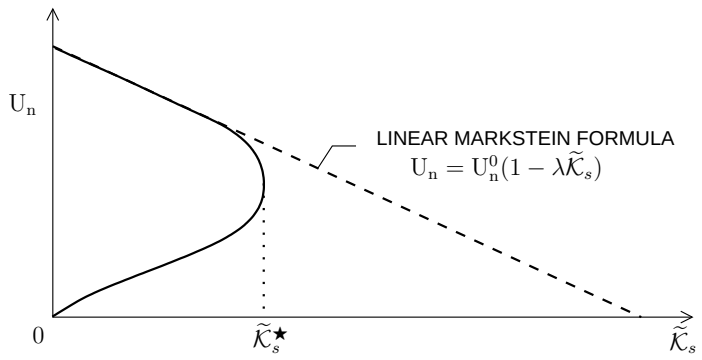

Figure 4.8: Sketch of the front propagation velocity as a function of the front tangential curvature.

stein expansion may then stabilize the spiral up until the maximum curvature is reached, at which point the edge flame is extinguished. This condition would correspond to the tip of the spiral, where its curvature is maximum, and its location is at the minimum radius for spirals that rotate steadily.

More involved analyses could be performed by generalizing earlier works on the time-dependent stability of reactive-diffusive spiral waves [49] to include the crucial effects of the hydrodynamic field, but this is beyond the scope of the present study.

Chapter 5

Experimental data analysis

Experiments were conducted in the spinning, water-cooled, sintered, bronze porous-disk burner, depicted in figure 1.4 and described at the end of Chapter 1. The experimental arrangement is shown in figure 1.4. The burner assembly was mounted on a water-cooled copper back-plate and a cup-shaped housing chamber which also serves as the plenum for the injected fuel gas. The fuel gas and the cooling water are supplied through concentric tubes located along the axis of this assembly. The concentric supply tubes are connected to external feed tubes through o-ring seals so that the entire burner assembly can be rotated around its axis with a stepper motor.

During an experiment, the burner is placed horizontally, with the exposed porous surface facing downwards to suppress buoyant instabilities, and it is then spun at a desired rotational speed with the cooling water supply turned on. Fuel gas is fed to the burner from a compressed-gas bottle through a programmable mass-flow controller at a specified flow rate and ignited by a propane torch. The entire experimental set up is enclosed in a large plexiglass box to prevent draft. All the flames observed in this study were blue and clearly visible to the naked eye. Flame images were captured using a 45° mirror with a high-speed intensified-array video camera at 250 frames per second. Video images were digitalized using a frame grabber and then analyzed frame by frame using image-analysis routines. Although several dynamic flame patterns were observed in the experiments, as indicated in figure 5.1, results are presented only for the spiral flames. Table 5.1 summarizes the findings obtained from six different experimental data sets that best represent the steady-rotation regime and that were selected for further detailed analysis to compare with the present theory.

Figure 5.1 shows the experimental map in the spiral-flame region [12, 13] obtained by varying the disk rotational speed and the fuel flow rate, nondimensionalized in terms

of the Reynolds number of injection (2.7) and the reduced Damköhler number (4.5). The values for Re_j and Δ were calculated by using $\mathrm{S}^0_{\mathrm{L,st}} = 40$ cm/s as a flame speed reference for CH_4-air mixtures and the following physical properties that correspond to air at normal conditions: $\rho = 1.19\mathrm{kg/m}^3$ for the density, $\nu = 1.57 \cdot 10^{-5}\mathrm{m}^2/\mathrm{s}$ for the kinematic viscosity, $D_T = 2.21 \cdot 10^{-5}\mathrm{m}^2/\mathrm{s}$ for the thermal diffusivity, and $\mathrm{Pr} = 0.71$ for the Prandtl number; the same physical properties are used throughout this Chapter. A line of maximum rotational speed of the bulk of the spiral is seen in figure 5.1 to separate the meandering and solid-rotation regimes. The rotational speed decays on of both sides of that line.

Flame extinction analysis

Figure 5.1b shows the calculated extinction Damköhler number (3.39) superimposed on the dimensionless experimental data. Even though the order of magnitude of Da_E does not vary appreciably when the rest of parameters the are changed, the best fit with the experimental curve of transition to the diffusion flame-hole regime occurs for an activation temperature of $T_a \sim 18,000\mathrm{K}$ if the disk is kept at the ambient temperature $T_\infty = T_S = 300\mathrm{K}$ by water cooling, so that $\Delta T = 0$; this activation temperature is somewhat higher than the activation temperature at stoichiometry ($15,900\mathrm{K}$) in [33], but instead it corresponds, in a variable-activation energy framework, to that at a mixture fraction of $Z = 0.076$, which would lie in the inner region for the values of ϵ encountered here. In that analysis it is shown that an increase of activation energy with the mixture fraction is needed in order to favor oxidizer leakage, which is consistent with the present results.

The threshold value $\mathrm{Re}_j^\star$ given by (3.37) below which oxidizer leakage prevails is found to be $\mathrm{Re}_j^\star \sim 0.055$, which as seen in figure 5.1(b) is smaller than typical fuel flow rates found in the transition region, so that according to AEA analysis moderate fuel leakage prevails there, rather than the physically correct oxygen leakage, with extinction occurring in the diffusion-flame regime. These observations indicate that it would be of interest to extend the Liñán [23] analysis to allow for variations of T_a in the inner region, to see whether this yields better agreement with experiments.

For constant angular velocity extinction is expected to occur if a minimum threshold of fuel injection is achieved. The system trajectories for Ω =const. would be represented by vertical lines Da =const. in figure 5.1(b). As $\dot{m}''$ decreases, the equilibrium temperature decreases producing longer chemical times in the flame, with the combustion process having to take place closer to the disk surface according to figure 3.3. Since the disk surface is kept at a moderate temperature $T_S \sim T_\infty$ by water cooling, flame extinction occurs because of

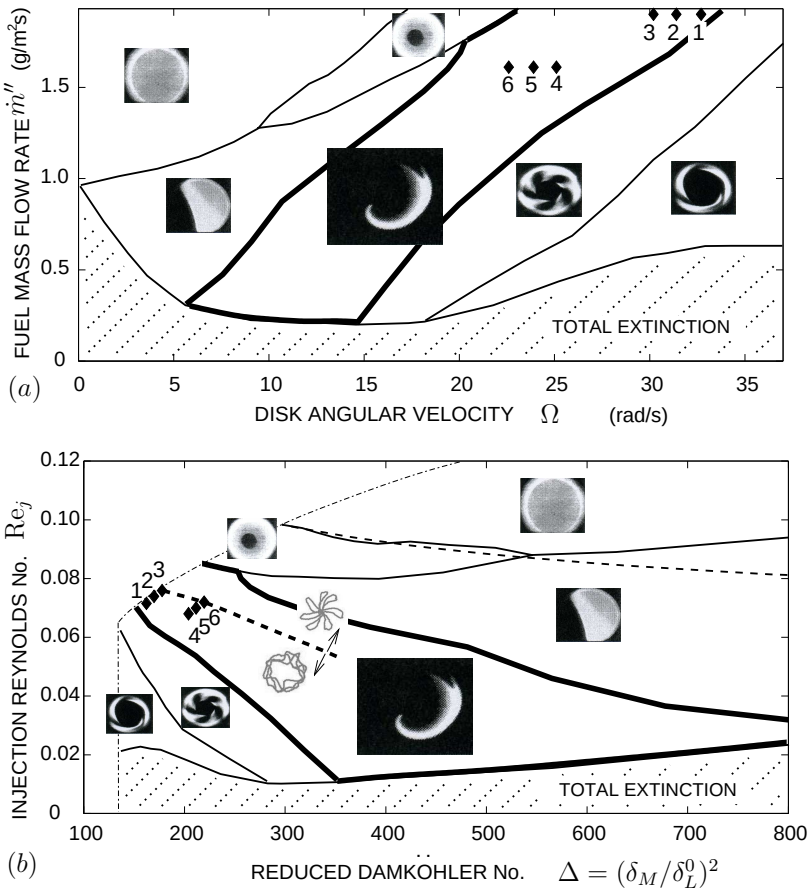

Figure 5.1: (a) Dimensional and (b) nondimensional experimental pattern map focused on the spiral-flame region. The dashed-line in (b) represents the line of maximum spiral rotational speed. The diamond-shaped points 1-6 correspond, respectively, to the experimental data sets 1-6 in table 5.1.

the decreasing amount of fuel and the proximity of the disk cold wall.

For constant fuel flow rates, extinction is expected to occur if a maximum threshold of angular velocity is achieved. The system trajectories for $\dot{m}''$ =const. would be represented by parabolas $\mathrm{Re}_j \propto \mathrm{Da}^{1/2}$ in figure 5.1(b). As Ω increases, the mixing thickness δ_M decreases, producing larger scalar dissipation rates χ_{fl} and shorter diffusion times across the flame t_d or flame-transit times. Extinction occurs when the chemical time t_c, which increases as Ω increases, becomes of the same order as the diffusion time t_d.

Solid rotation and meandering motions of spiral flames

A line of maximum rotational speed of the bulk of the spiral separates the meandering and solid-rotation regimes. The rotational speed decays on of both sides of that

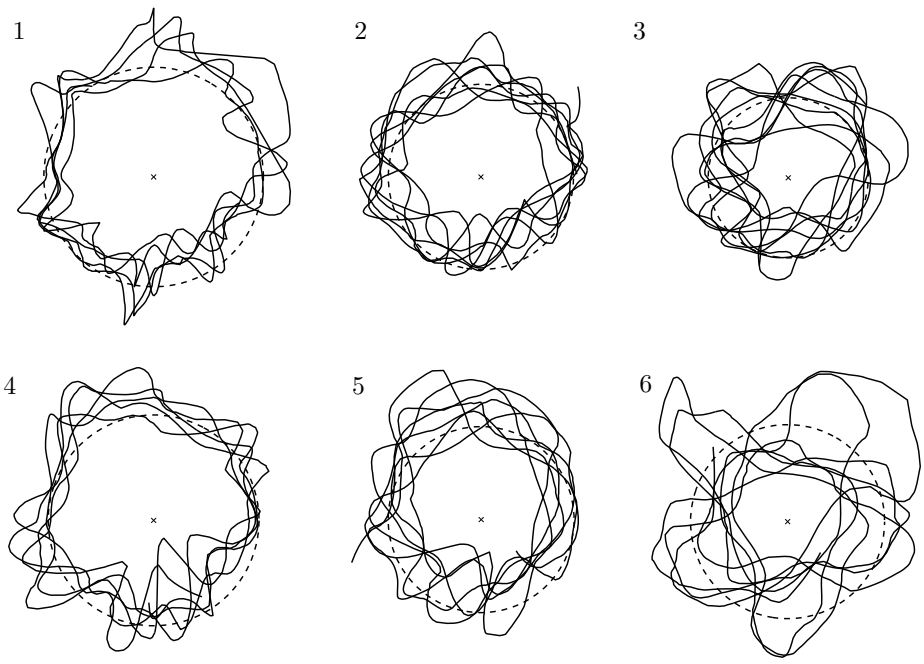

Figure 5.2: Tip trajectories (solid line) and average core radius (dashed line) corresponding to the series of experiments (1-6) in table 5.1.

line.

In particular, in the meandering regime the tip undergoes an epicycloidal motion that is composed at least of two orbital motions and therefore two rotational frequencies. Such motion shares common characteristics with the meandering of reactive-diffusive spirals found in earlier works [16, 17, 45]; it is not well understood but believed to be influenced by system hysteresis. In the present experiments, tip meandering is associated with large swirl numbers, small radial advection and large spiral rotational velocities, as well as with increasing flame stand-off distances and decreasing strain rates and heat losses, which eventually produce transition from spiral flames to straight propagating edges and flame holes, as indicated in figure 5.1. The analysis of the meandering motion is beyond the scope of the present study.

In the solid-rotation regime, the entire spiral structure undergoes a nearly circular motion of frequency ω and is anchored at a point of minimum radius $r^{\bigstar}$ where the radial advection balances the normal edge propagation, as detailed in Section 4.3. In this regime, the rotational velocity decreases and the core radius increases approximately linearly with increasing disk velocities for a fixed fuel flow rate. As observed in figure 5.1, too large disk velocities or small fuel flow rates produce transition from this regime to the multiple-spiral

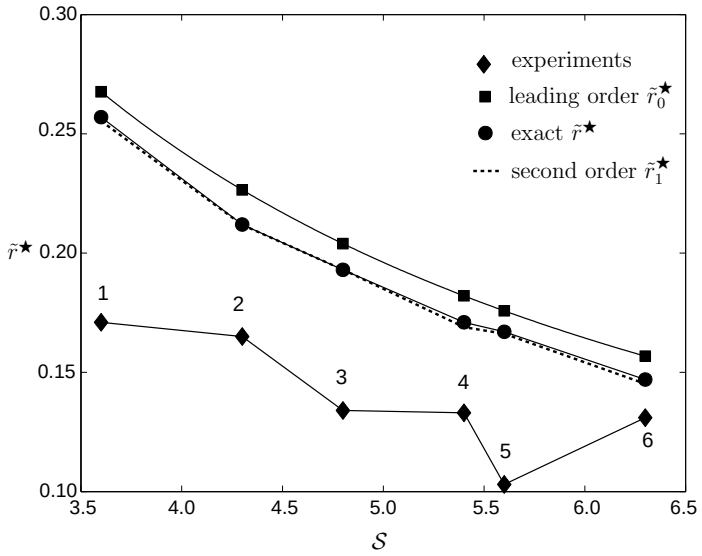

Figure 5.3: Experimental and analytical values of the dimensionless core radius corresponding to the set of experiments (1-6) in table 5.1.

regime, in which a number of spirals co-rotate with the flow.

Figure 5.2 shows the tip trajectories obtained from the six data sets, details of which are given in table 5.1. Slight meandering appears in cases 3 and 6, where the disk velocity is minimum within the range, and the spiral velocity is near its maximum. While not exactly circular, most tip trajectories are close to that.

The core radius

Figure 5.3 shows the resulting experimental nondimensional mean core radius $\tilde{r}^\star$ as a function of the swirl number. The theoretical results are also plotted in this figure for purposes of comparison. Farthest from the data is the leading-order result (4.31). The second-order result (4.47), which is almost identical to the exact value (4.29), is somewhat closer to the data. The theoretical and experimental dependencies on $\mathcal{S}$ are noticeably similar, and the fact that the theoretical values lie above the observation is consistent with the nonlinearity of the curve in figure 4.8, which becomes important as the extinction condition at the tip is approached, since the theoretical calculations do not include this effect.

Spiral-edge shapes

Planar propagation velocities, calculated using expression (4.12) far from the disk center (at a distance about 3/4 of the disk radius, sufficiently large but away from disk-edge effects), are found to increase with increasing Γ, which is inversely proportional to the Damköhler number. These velocities are seen to be comparable with or somewhat less than the laminar burning velocity of a methane-air planar stoichiometric flame, $S^0_{L,st} \approx 40$ cm/s, and as may be expected, they are smaller at smaller fuel injection rates. These values are used in (4.24) to calculate ℓ. The propagation parameter Γ is found to decrease with increasing disk rotational velocities, since the mixing layer becomes thinner and the diffusion time through its thickness smaller. The values for Γ obtained in table 5.1 represent edge flames propagating somewhere between the regimes (h) and (i) in figure 4.2, with a propagation velocity close to its adiabatic counterpart, supporting the results of Section 4.2.

Figure 5.3 shows the resulting experimental nondimensional mean core radius $\tilde{r}^{\bigstar}$ as a function of the swirl number. The theoretical results are also plotted in this figure for purposes of comparison. Farthest from the data is the leading-order result (4.31). The second-order result (4.47), which is almost identical to the exact value (4.29), is somewhat closer to the data. The theoretical and experimental dependencies on $\mathcal{S}$ are noticeably similar, and the fact that the theoretical values lie above the observation is consistent with the nonlinearity of the curve in figure 4.8, which becomes important as the extinction condition at the tip is approached, since the theoretical calculations do not include this effect.

Figure 5.4 shows a comparison between the analytical front shapes, obtained by integrating (4.26) and the experimental results from table 5.1. A good agreement is found for the overall trend, although the profiles seem to be somewhat inaccurate in the tip region, as expected. It is worth mentioning that, although the Markstein diffusivity and its ratio to the dimensionless core radius are found experimentally to be small, which support the theory proposed in Section 4.3, the typical propagation velocities in the neighborhood of the anchoring point are of order $r^{\bigstar}|\phi'_{fl}|\Omega/2$, which, after numerical evaluation, represent an order-unity reduction with respect to the planar propagation velocity U^0_n. This further indicates that $\lambda\tilde{\mathcal{K}}_s = O(1)$, and the Markstein linear correction (4.17) becomes innacurate for these large curvatures. The tip curvature $\tilde{\mathcal{K}}^{\bigstar}_s$, the tangential curvature for extinction of an edge flame, yet needs to be calculated numerically, although perhaps it could be approximated by the curvature for extinction of a positively curved two-dimensional premixed

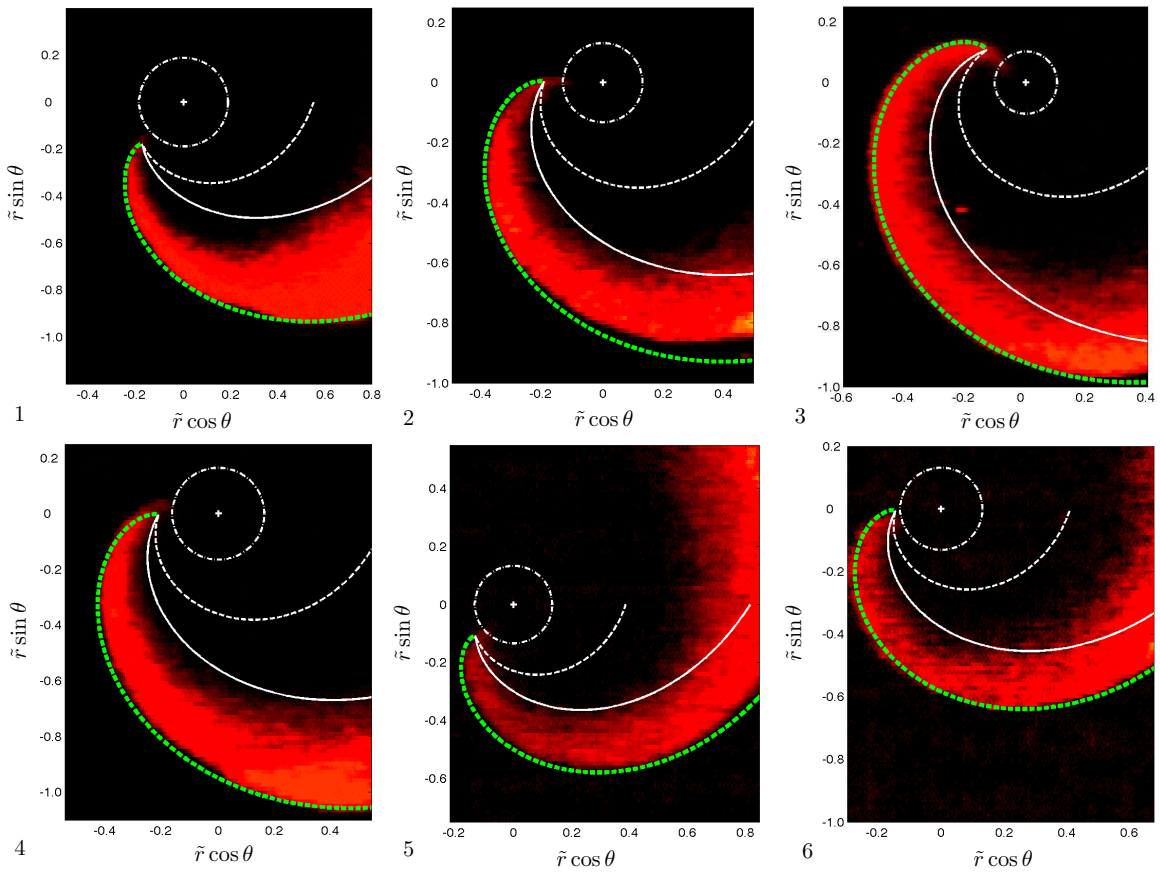

Figure 5.4: Comparison between the experimental images, corresponding to the data sets (1-6) from table 5.1, and the analytical front shapes (green solid line) calculated by integrating (4.26), together with the Frenet-frame (white dashed line) and laboratory-frame (white solid line) streamlines passing through the tip. The mean core radius is represented by the dot-dashed line.

front [1].

The cooling tail

The streamlines passing through the tip, both in the Frenet, $\tilde{r} = \tilde{r}^{\bigstar} \exp\left[(\theta - \theta^{\bigstar})/\mathcal{S}\right]$, and in the laboratory reference frames, $\tilde{r} = \tilde{r}^{\bigstar} \exp\left[(\theta - \theta^{\bigstar})/(\mathcal{S} - 2\omega/\Omega|\phi'_{fl}|)\right]$, are also plotted in figure 5.4. The Frenet-frame streamline passing through the tip clearly fails to describe the tail of the spiral, and since all the laboratory-frame streamlines have larger slopes than the former, the fluid particles in the stoichiometric coordinate must undergo extinction after being ignited. It may be considered that all fluid elements are required to have the same time for extinction, which is determined by heat losses to the disk as outlined in Section 4.2. With this idea, cases 1 and 3 of table 5.1 were used to obtain the tail

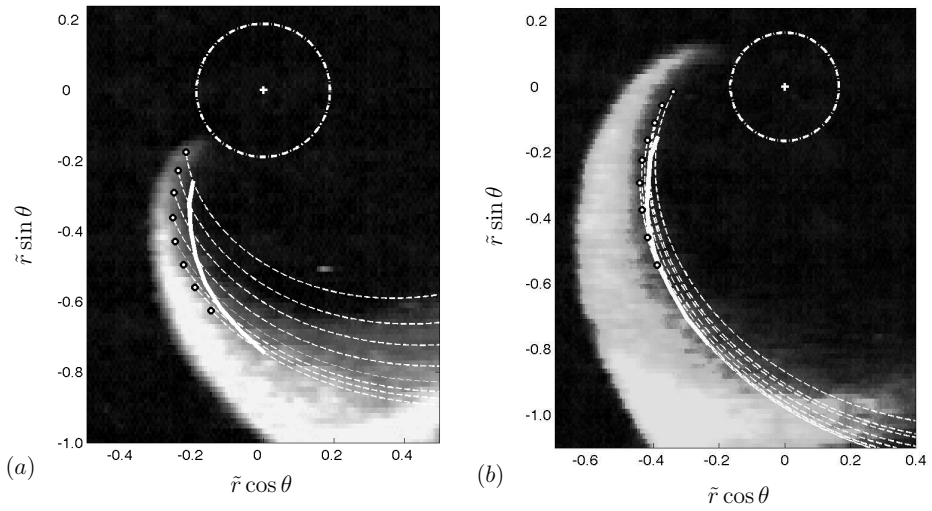

Figure 5.5: Comparison between the experimental images at $t = t_E$ and the analytical tail shapes (white solid line) calculated by the theory of equal times of extinction, together with the laboratory-frame streamlines (white dashed line) emerging from the spiral front at $t = 0$ along the stoichiometric plane. The points denote the fluid particles located on the front at $t = 0$. Figure (a) corresponds to case 1 of table 5.1, which gives a $t_E \sim 40$ms, and figure (b) corresponds to case 3 of table 5.1, which gives a $t_E \sim 68$ms.

shape, as shown in figure 5.5. An array of fluid particles at the front at $t = 0$ was tracked along the laboratory-frame streamlines on the stoichiometric coordinate, and all particles extinguished after a time $t = t_E$, which increases with the Damköhler number, giving a good approximation of the tail shape; this calculation is justified as long as the entrainment remains small compared with the two planar velocity components, which appears to be a reasonable approximation along the flame radial positions encountered in this study.

Table 5.1: Experimental values obtained for different combinations of the disk speed Ω (rad/s) and the fuel flow rate $\dot{m}''$ (g/sm^2). The spiral rotational speed ω (rad/s) and the core radius $r^\bigstar$ (cm) were obtained by time averaging. The planar propagation velocity U_n^0 (cm/s) was obtained by time averaging (4.12) far from the disk center, using the von Kármán solution (2.8) for the underlying hydrodynamic field. The mixing-layer thickness δ_M (mm), outer scale ℓ (cm), Markstein length $\mathcal{L}$ (mm), Markstein diffusivity λ (-), swirl number $\mathcal{S}$ (-), propagation parameter Γ (-), azimuth velocity gradient V_{fl} (-), radial velocity gradient $|\phi'_{fl}|$ (-) and injection Reynolds number Re_j (-) were calculated by using the definitions given in the main text.

Case	Ω	$\dot{m}''$	ω	δ_M	$r^\bigstar$	U_n^0	$\mathcal{L}$	ℓ	Re_j	$\lvert\phi'_{fl}\rvert$	V_{fl}	Γ	$\mathcal{S}$	λ	$\lambda/\tilde{r}^\bigstar$
1	32.7	1.93	7.5	0.69	1.8	38.8	0.057	10.5	0.071	0.226	0.181	0.65	3.6	0.00054	0.0031
2	31.4	1.93	11.3	0.71	1.5	39.1	0.056	11.2	0.073	0.222	0.176	0.63	4.8	0.00051	0.0038
3	30.2	1.93	13.2	0.72	1.3	40.2	0.055	12.3	0.074	0.217	0.170	0.61	5.6	0.00045	0.0043
4	25.1	1.61	8.2	0.79	1.6	29.4	0.075	9.8	0.068	0.239	0.194	0.56	4.3	0.00076	0.0046
5	23.9	1.61	10.7	0.81	1.4	29.5	0.075	10.6	0.070	0.233	0.183	0.55	5.4	0.00071	0.0053
6	22.6	1.61	11.9	0.83	1.5	29.9	0.074	11.7	0.072	0.226	0.182	0.53	6.3	0.00063	0.0048

Chapter 6

Conclusions

The propagation dynamics of spiral edge flames in von Kármán swirling flows was analyzed in this study. A formulation of the conservation equations was presented in the thermodiffusive and equidiffusive limits and within the framework of large overall activation energies. The formulation was written in terms of two main nondimensional parameters: the injection Reynolds number Re_j and the Damköhler number Δ; these two numbers contained nondimensional combinations of the two experimentally controlled variables, the disk rotational velocity and the fuel flow rate, in addition to the chemical parameters. The resulting equations represented a non-adiabatic system with an induced non-zero excess enthalpy distribution, in which heat losses occurred because of the nearby cold disk surface. The Burke-Schumann and frozen regimes were summarized, and the diffusion-flame temperature was found to depend on the injection rate. The uniform diffusion flame is extinguished when $\Delta < \Delta_E$, with Δ_E a function of Re_j. Extinction occurs in the diffusion-flame regime with a moderately small fuel leakage if activation energy asymptotics is used, because of the nearby cold wall which enhances oxidizer leakage through the flame.

A formulation in the Frenet frame, written in terms of the curvilinear intrinsic coordinates, was introduced to analyze propagating fronts that connect the burning and frozen regions. Asymptotic propagation regimes were obtained by scaling analyses of the conservation equations, and a two-dimensional numerical simulation of the conservation equations of a nearly straight edge flame near a cold porous wall, embedded in a von Kármán boundary layer, showed that there exist regimes, below the static quenching Damköhler number Δ_E of the diffusion flame, for which a propagating front burns vigorously near the wall but the trailing diffusion flame is extinguished because of heat losses to the disk. That these regimes are possible is justified by noticing that the transverse heat diffusion

in the edge reaction-layer and preheat regions is negligible compared to the streamwise balances of reaction-diffusion and convective-diffusion, respectively, in each region. As a result, the temperature along the stoichiometric line increases at the edge and gradually decays through the transition zone until the balance of strain and reaction is reached in the diffusion-flame region, the point at which the reaction shuts off and the trailing flame is extinguished. The characteristic distance for extinction of the diffusion flame was found to be proportional to the propagation velocity and to increase with the Damköhler number of the edge. This defines a characteristic time t_E for extinction of the diffusion flame, which increases with increasing flow times.

The steady dynamics of the spiral-edge propagation in the von Kármán hydrodynamic swirling field was analyzed by integrating the G-equation of the edge transport and using a Markstein-like expression for the tangential curvature correction of the propagation velocity. The dimensionless Markstein diffusivity λ becomes a singular perturbation parameter in the G-equation. The asymptotic structure of the edge was obtained by using asymptotic matching for $\lambda \ll 1$ in the large core limit, in which the radial distance of the tip from the center is small compared with the Markstein length, and solutions were found for spiral fronts that depended on the Markstein diffusivity and on the magnitude of the swirl number $\mathcal{S}$, which measures the ratio of the net swirl in the Frenet frame to the radial advection. Large values of $\mathcal{S}$ corresponded to highly curved spirals. Expressions were derived for the core radius as a function of $\mathcal{S}$ and λ, which in turn determines a relationship between the spiral rotational velocity and the core radius. In the absence of the decrease in propagation velocity produced by the Markstein diffusivity, the spirals were shown to become unstable at radii less than that at which the edge is tangent to the radial advection, but the increasing curvature stabilizes the edge propagation. This stabilization persists until the curvature reaches a critical maximum value at which edge-flame extinction occurs. This critical curvature for extinction determines the core radius and thereby the spiral rotational velocity. At the core radius, the edge is perpendicular to the radial direction, and its propagation velocity equals the radial gas velocity at the stoichiometric surface for steadily rotating spirals.

Experiments performed in the porous-disk burner were analyzed and theoretical predictions were tested. The spiral tip can undergo either a solid rotation motion for sufficiently large disk rotational velocities and small fuel flow rates, or epicycloidal motions for smaller disk rotational velocities and larger fuel flow rates. In the studied data range, the angular velocity of the spiral was found to decrease linearly with the disk rotational

velocity for a given fuel flow rate. Meandering spirals are associated with rapidly rotating flames, large swirl numbers, moderately large injection Reynolds numbers, large Damköhler numbers, and decreasing heat losses and strain rates, which promote transition to the regimes of straight propagating edges and flame holes. Solid rotation is associated with the opposite behavior, which promotes transition to the multiple-spiral regime. Core radii were measured and agreed reasonably with the theoretical model, which predicts a reduction of the core radius with increasing values of $\mathcal{S}$. Spiral shapes obtained by the analytical model are in reasonable agreement with the experimental images. These results show that non-unity Lewis numbers are not necessary for having spiral-shaped edges and cooling tails in these experiments, contrary to suggestions made in earlier works [50-52].

The analyses performed in this study may be relevant for characterizing the dynamics of tangentially curved sheets of triple flames and their transport in fluid flows near non-adiabatic walls. Although much research has been performed on triple flame dynamics, there appears to be a large number of unknowns regarding the linear and non-linear effects of the tangential curvature and strain on the velocity of propagation of triple flames and their extinction. Finally, the meandering motion of the spiral flames reported in this study seems to emerge from an instability at the anchoring point of the tip, which may be worth investigating for having potential applications on the understanding of triple-flame anchoring processes in turbulent flows and on flame flickering. Meandering is the next theoretical problem to be addressed for spiral edges of diffusion flames in von Kármán swirling flows.

Chapters 1 to 5, in part, have been published in in the *Proceedings of the Combustion Institute*, "Diffusion-flame extinction on a rotating porous-disk burner," by J. Urzay, V. Nayagam and F. A. Williams (2008) **32**, 1119-1126, and have been submitted for publication in *Combustion and Flame*, "Theory of the propagation dynamics of spiral edges of diffusion flames in von Kármán swirling flows," by J. Urzay, V. Nayagam and F. A. Williams (2010). The thesis author is the primary investigator in these publications.

Experiments in Part I were performed by Dr. V. Nayagam at the National Center for Space and Exploration Research, NASA Glenn Research Center, Cleveland (OH). This investigation was partially funded by the NASA Microgravity Combustion Science Program.

References

[1] Williams, F. A. (1965) *Combustion Theory*, Addison-Wesley.

[2] Peters, N. (2000) *Turbulent Combustion*, Cambridge University Press.

[3] Buckmaster, J. (2002) Edge-flames. *Prog. Energ. Combust.* **28** 435–475.

[4] Phillips, H. (1965) Flame in a buoyant methane layer *Proc. Combust. Inst.* **10** 1277–1283.

[5] Dold, J. W. (1989) Flame propagation in a non-uniform mixture: analysis of a slowly varying triple flame. *Combust. Flame* **76** 71–88.

[6] Kioni, P. N., Rogg, B., Bray, K. N. C., Liñán, A. (1993) Flame spread in mixing layers: the triple flame. *Combust. Flame* **95** 276–290.

[7] Ruetsch, G. R., Vervisch, L., Liñán, A. (1995) Effects of heat release on triple flames. *Phys. Fluids* **7** 1147–1454.

[8] Daou, J., Liñán, A. (1998) The role of unequal diffusivities in ignition and extinction fronts in strained mixing layers *Combust. Theor. Model.* **2** 449–477.

[9] Kim, N. I., Seo, J. I., Guahk, Y. T., Shin, H. D. (2006) The propagation of tribrachial flames in a confined channel. *Combust. Flame* **146** 168–179.

[10] Yetter, R., Glassman, I., Gabler, H. C. (2000) Asymmetric whirl combustion: a new low NOx approach. *Proc. Combust. Inst.* **28** 1265–1272.

[11] Nayagam, V. (2006) *Pattern Formation in Diffusion Flames Embedded in Von Kármán Swirling Flows*, Tech. Rep. NASA/CR–2006-214057, National Aeronautics and Space Administration.

[12] Nayagam, V., Williams, F. A. (2006) *Dynamics of spiral flames in von Kármán swirling Flows.* 31st International Symposium in Combustion (Poster).

[13] Urzay, J., Nayagam, V., Williams, F. A. (2009) Diffusion-flame dynamics in a rotating porous-disk burner. *Proc. Combust. Inst.* **32** 1219–1226.

[14] Hossain, K. N., Jackson, T. L., Buckmaster, J. (2009) Numerical simulations of flame patterns supported by a spinning burner. *Proc. Combust. Inst.* **32** 1209–1217.

[15] P. Grindrod *The Theory and Applications of Reaction-Diffusion Equations: Patterns and Waves*, Clarendon Press, Oxford (1996).

[16] Tyson, J. J., Keener, J. P. (1988) Singular perturbation theory of travelling waves in excitable media. *Physica D* **32** (1988) 327–361.

[17] Keener, J., Sneyd, J. *Mathematical Physiology*, Springer (2004).

[18] Nayagam, V., Williams, F. A. (2000) Rotating spiral edge flames in von Kármán swirling flows *Phy. Rev. Lett.* **84** 479–482.

[19] Plesser, T., Muller, S., Hess, B. (1990) Spiral wave dynamics as a function of proton concentration in the ferroin-catalyzed Belousov-Zhabotinskii reaction *J. Phys. Chem.* **94** 7501–7507.

[20] Bär, M., Nettesheim, S., Rotermund, H., Eiswirth, M., Ertl, G. (1995) Transition between fronts and spiral waves in a bistable surface reaction. *Phys. Rev. Lett.* **74** 1246–1254.

[21] Siegert, F., Weijer, C. (1995) Spiral and concentric waves organize multicellular Dictyostelium mounds. *Curr. Biol.* **5** 937–943.

[22] Clapham, D. E. (1995) Calcium signaling. *Cell* **80** 259–258.

[23] Liñán, A. (1974) The asymptotic structure of counterflow diffusion flames for large activation energies. *Acta Astronaut.* **1** 1007–1039.

[24] Zel'dovich, Y., Frank-Kamenetskii, D. A. (1938) A theory of thermal propagation of flame. *Acta Physicochim. URSS* **9** 341–350.

[25] Kolmogorov, A., Petrovskii, I., Piskounov, N. (1937) Study of the diffusion equation with growth of the quantity of matter and its application to a biology problem. *Bulletin of the State University of Moscow* **1** 1–25.

[26] Nayagam, V., Balasubramaniam, R., Ronney, P. D. (1999) Diffusion flame-holes. *Combust. Theor. Model.* **3** 727–742.

[27] Nayagam, V., Williams, F. A. (2001) Diffusion-flame dynamics in Von Karman boundary layers. *Combust. Flame* **125** 974–981.

[28] Pantano, C., Pullin, D. I. (2003) On the dynamics of the collapse of a diffusion-flame hole *J. Fluid Mech.* **480** 311–333.

[29] Buckmaster, J. (1996) Edge-flames. *J. Eng. Math.* **31** 269–284.

[30] Matkowsky, B. J., Sivashinsky, G. I. (1979) An asymptotic derivation of two models in flame theory associated with the constant density approximation. *SIAM J. Appl. Math.* **37** 686–99.

[31] Smooke, M., Bilger, R. W. (1991) *Reduced kinetic mechanisms and asymptotic approximations for methane-air flames: a topical volume.* Springer-Verlag.

[32] von Kármán, T. (1921) Uber laminare und turbulente Reibung. *Z. Angew. Math. Mech.* **1** 233–52.

[33] Fernández-Tarrazo, E., Sánchez, A. L., Liñán, A., Williams, F. A. (2006) A simple one-step chemistry model for partially premixed hydrocarbon combustion. *Combust. Flame* **147** 32–38.

[34] Law, C. K. (2006) *Combustion Physics*, Cambridge University Press.

[35] Seshadri, K., Peters, N. (1988) Asymptotic structure and extinction of methane air diffusion flames. *Combust. Flame* **73** 23–44.

[36] Urzay, J., Nayagam, V., Williams, F. A. (2007) Diffusion-flame extinction in rotating porous-disk burners. *Proc. Combust. Inst.* **32** 1119–1126.

[37] Weatherburn, C. E. (1961) *Differential Geometry of Three Dimensions,* Cambridge University Press.

[38] Kurdyumov, V., Fernández-Tarrazo, E., (2002) Lewis number effect on the propagation of premixed laminar flames in narrow open ducts. *Combust. Flame* **128** 382–394.

[39] Fernández-Tarrazo, E., Vera, M., Liñán, A. (2006) Liftoff and blowoff of a diffusion flame between parallel streams of fuel and air. *Combust. Flame* **144** 261–276.

[40] Bernoff, A. J. (1991) Spiral wave solutions for reaction-diffusion equations in a fast reaction/slow diffusion limit *Physica D* **53** 125–150.

[41] Thatcher, R. W., Dold, J. W. (2000) Edges of flames that do not exist: flame-edge dynamics in a non-premixed counterflow. *Combust. Theor. Model.* **4** 435–457.

[42] Thatcher, R. W., Omon-Arancibia, A. A. (2005) Multiple speeds of flame edge propagation for Lewis numbers above one. *Combust. Theor. Model.* **9** 647–658.

[43] Markstein, G. H., (1951) Experimental and theoretical studies of flame-front stability. *J. Aero. Sci.* **18** 199–209.

[44] Clavin, P., Williams, F. A. (1982) Effects of molecular diffusion and of thermal expansion on the structure and dynamics of premixed flames in turbulent flows of large scale and low intensity. *J. Fluid Mech.* **116** 251–282.

[45] Hakim, V., Karma, A. (1999) Theory of spiral wave dynamics in weakly excitable media: Asymptotic reduction to a kinematic model and applications*Phys. Rev. E* **60** 5073–5105.

[46] C. M. Bender, S. A. Orszag, *Advanced Mathematical Methods for Scientists and Engineers*, Springer (1999).

[47] Santoro, V. S., Liñán, A., Gomez, A. (2000) Propagation of edge flames in counterflow mixing layers: experiments and theory *Proc. Combust. Instit.* **28** 2039–2046.

[48] Joulin, G., Clavin, P. (1976) Analyse asymptotique des conditions d'extinction des flammes laminaires. *Acta Astronaut.* **3** 223–240.

[49] Pelce, P., Sung, J. (1999) Stability of spiral waves in large-hole-radius limit. *Phys. Rev. A* **44** 7906–7909.

[50] Williams, F. A. (2004) Spiral diffusion flames. In: Higuera, F. J., Jiménez, J., Vega, J. M., Editors, *Simplicity, Rigor and Relevance in Fluid Mechanics: A volume in honor of Amable Liñán,* CIMNE, Barcelona, 61–74.

[51] Nayagam, V., Williams, F. A. (2002) Lewis-number efects on edge-flame propagation. *J. Fluid Mech.* **458** 219–228.

[52] Nayagam, V., Williams, F. A. (2004) Curvature effects on edge-flame propagation in the premixed-flame regime *Combust. Sci. Tech.* **176** 2125–2142.

Part II

The Elastohydrodynamic Gliding Motion and Adhesion of a Solid Particle to Soft and Sticky Substrates at Low Reynolds Numbers

NOMENCLATURE

a	Particle radius (m)
A_{sfw}	Hamaker coefficient (J)
β	Azimuth angle of rotation (rad)
c	Speed of sound waves in the substrate (m/s)
c_i	Ionic concentration (M)
c_i^{∇}	Critical coagulation concentration (M)
Δ^{vdW}	Van der Waals compliance (-)
Δ^{el}	Electric compliance (-)
D_i	Ionic diffusion coefficient (m^2/s)
δ	Gap clearance (m)
δ^{∇}	Minimum clearance for adhesion (m)
e	Protonic charge (C)
E	Young modulus (Pa)
ϵ	Dimensionless gap clearance (-)
ϵ_0	Permittivity of vacuum (F/m)
ϵ_f	Fluid dielectric constant (-)
ϵ_s	Particle dielectric constant (-)
ϵ_w	Substrate dielectric constant (-)
η	Hydrodynamic compliance, elastoviscous number (-)
η_C	Critical compliance for irreversible adhesion (-)
η_L	Lift-off compliance (-)
F_x	Drag force (N)
F_y	Drift force (N)
F_z	Lift force (N)
γ	Pressure-velocity phase angle (rad)
γ_L	Lift-off shear rate (1/s)
h	Dimensionless gap profile (-)
H	Dimensionless surface deformation (-)
H_c	Characteristic surface deflection (m)
k	Boltzmann constant (J/K)
κ	Debye-Hückel parameter (-)

$\kappa^{\triangledown}$	Debye-Hückel parameter for adhesion (-)
ℓ	Elastic layer thickness (m)
ℓ_D	Debye length (m)
λ	Exponential prefactor (-)
μ	Fluid dynamic viscosity (Pa· s)
$\boldsymbol{n}$	Normal unit vector to the substrate surface (-)
N_A	Avogadro's number (molec/mol)
ν	Poisson coefficient (-)
ω	kinematic parameter (-)
Ω	Particle angular velocity (rad/s)
P	Dimensionless hydrodynamic pressure (-)
$P^{\bigstar}$	Dimensionless hydromolecular pressure (-)
Pe_i	Ionic Péclet number (-)
Π^{el}	Dimensionless electric disjoining pressure (-)
Π^{vdW}	Dimensionless Van der Waals disjoining pressure (-)
Ψ_s^d	Dimensionless Stern potential of the particle (-)
Ψ_w^d	Dimensionless Stern potential of the substrate (-)
Re	Reynolds number (-)
r	Dimensionless radial coordinate (-)
ρ	Fluid density (kg/m^3)
$\boldsymbol{\sigma}$	Solid stress tensor (Pa)
τ	Dimensionless shear stresses (-)
θ	Polar angle (rad)
$\boldsymbol{u}$	Elastic displacements (m)
Υ	Ratio of the Van der Waals to hydrodynamic stresses (-)
$\boldsymbol{v}$	Dimensionless hydrodynamic velocity (-)
$\mathcal{V}$	Dimensionless characteristic velocity (-)
φ	Reduced azimuth angle (rad)
$\dot{W}$	Particle gliding power (W)
Ξ	Ratio of the Van der Waals to hydrodynamic stresses (-)
ζ	Dimensionless elastic-layer thickness (-)
z_i	Ionic valency (-)

Chapter 7

Introduction

Soft materials can be deformed by the action of external forces [1, 2]. Nearby substrate deformations produced by hydrodynamic and intermolecular forces induce nonlinearities on the otherwise linear equations of viscous fluid motion at low Reynolds numbers, and produce forces on submerged moving particles and swimmers that may serve as representative sources of lateral motility at small scales and may also suppress adhesion. However, such deformations may as well enhance adhesion if the internal restoring force of the substrate is not sufficiently large to outweigh the resulting hydrodynamic and intermolecular traction stresses on its surface.

The study of the intermolecular and viscous hydrodynamic interactions between solids and soft substrates may be of some interest from a biological perspective [3]. Motivated by the practical importance of the control and suppression of biofilm growth on surfaces, adhesion of motile bacteria to rigid substrates has been previously analyzed by accounting for electric and van der Waals forces [4]. The study of the distinguished balance between these two interactions is the subject of the celebrated Derjaguin-Landau Verwey-Overbeek (DLVO) theory [5, 6], which is regarded as the fundamental theory of the stabilization and adhesion of lyophobic particles, although this theory may need to be modified to account for hydrodynamic effects and to describe accurately the phenomena of bacterial adhesion [4, 7]. Earlier work [4] identified reversible (short residence times and lateral motility) and irreversible (long residence times and sessility) adhesion modes, which depended on the ionic strength in the solvent. The reversible adhesion mode exemplifies a gliding motion along the surface in which the bacteria is momentarily entrapped in an accessible potential minimum, whereas the irreversible mode is experimentally observed as a "sudden death" of the bacteria when it falls into the primary minimum, a region dominated by Born repul-

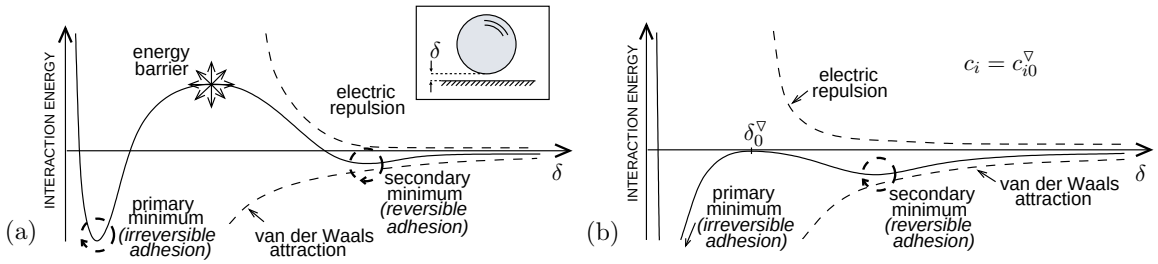

Figure 7.1: Sketch of typical particle-surface interaction-energy curves in the DLVO theory, adapted from [20], for (a) low and (b) high (critical coagulation) concentration of electrolyte in the solvent.

sion and steric forces, once the energy barrier becomes small at sufficiently large electrolyte concentrations, as shown in figure 7.1. Effects of surface chemical heterogeneities have been previously proposed as precursors of lateral immobilization and irreversible adhesion [8]. The near-contact motion of microorganisms close to soft living tissues may be inevitably influenced by a number of complex biochemical, intermolecular and hydrodynamic interactions and surface deformations upon adhesion, but the study of simplified analytical models may still be warranted for shedding some modest amount of light into these intricacies.

In a more general situation, the presence of a nearby soft interface has been proved to produce kinematically-irreversible forces on swimming bodies and moving particles at low Reynolds numbers [9-14], which may modify their adhesion behavior; the velocity scaling of these forces departs from the linear, kinematically-reversible Stokesian velocity scaling of the hydrodynamic forces in viscous flows bounded by rigid surfaces, in that it produces direction-invariant forces under velocity-direction reversals. The effect of a nearby non-slip rigid wall on the motion of micro-swimmers has been found to be important [15]. The reversibility properties of the Stokes equations yield a zero lift force F_z on a sphere steadily translating and rotating near a wall. This can be demonstrated by observing that the imaginary problem of a sphere near a wall steadily translating with the reversed translational velocity $-U$ and at the reversed angular velocity $-\Omega$ turns out to be the same as the original one if the change of variables in velocity $\boldsymbol{v}' = -\boldsymbol{v}$ and pressure $P' = -P$ is performed in the equations of fluid motion. This implies that $F_z' = -F_z$, from which it follows that the lift force must be zero by symmetry [11]. Some nonlinear mechanisms that break the symmetry of the Stokes equations have been proposed and tested experimentally, such as fluid inertia [16, 17], electrokinetics [18], elastohydrodynamics [9, 11] and non-Newtonian effects [19].

From a general engineering standpoint, electric and van der Waals intermolecular forces are inherently present in the near-contact dynamics of liquid and solid interfaces, and

are perhaps the most important contribution to the forces involved in the coagulation of colloids, bubble and droplet coalescence, physical adsorption and adhesion of particles to substrates [20, 21]. Although the van der Waals forces between two atoms or molecules decrease with the seventh power of the separation distance, the forces between large molecular assemblies, such as spheres or plates, decrease with the second or third power of the separation distance, so that the effects of these interactions between macroscopic bodies prove to be still appreciable at a moderately long range (0.1 μm or more) [20, 21]. Dispersion and coagulation of a suspension of particles may occur depending on the relative intensity of the electric double-layer and van der Waals forces, the balance of which is mainly modulated by the ionic strength in the solvent [5, 6]. Similarly, sheared concentrated suspensions of dense polymer microgel pastes display a slip behavior beyond a critical sliding stress that is thought of being produced by a combination of elastohydrodynamic and intermolecular effects [22, 23].

Earlier pioneering works on the viscous motion of a cylinder near soft and non-sticky surfaces by Skotheim and Mahadevan [11], and the near-contact dynamics of a sphere near a rigid wall by Goldman et al. [24], O'Neill and Stewartson [25] and Cooley and O'Neill [26], are generalized in this investigation by addressing the canonical problem of the forces exerted on a small spherical particle undergoing slow translation and rotation in a perfect liquid near a soft substrate, subject to electric and van der Waals intermolecular forces. Forces produced by the triple interaction of hydrodynamic, intermolecular and substrate-deformation effects are derived, and novel limiting conditions for adhesion, based on critical substrate-mechanical properties, gliding velocities and electrolyte concentrations, are obtained in this analysis by making use of asymptotic analyses and numerical methods.

This part is organized into three additional chapters. Chapter 8 is dedicated to a general formulation of the problem within the framework of a hydrodynamic lubrication model. Chapter 9 summarizes the main characteristics of the leading-order solution for rigid substrates, and addresses the effects of substrate deformability on the dynamics of the particle. Finally, conclusions are drawn in Chapter 10.

Chapter 8

Formulation

8.1 Hydrodynamic equations

A rigid spherical particle of radius a and dielectric constant ε_s, translates at constant velocity U along the x axis, and rotates at constant angular velocity Ω about an axis orientated at an arbitrary azimuth angle β with respect to the translation axis, with both axes parallel to the unperturbed wall surface as depicted in figure 8.1, in this way representing a general drift motion on the horizontal plane. The sphere is immersed in a Newtonian incompressible fluid, which corresponds to an aqueous symmetric electrolyte of density ρ, equal to that of the sphere, viscosity μ, ionic valency z_i, ionic diffusion coefficient D_i and dielectric constant ε_f. The clearance or minimum gap distance between the sphere and the unperturbed wall surface is $\delta = \epsilon a$, with $\epsilon \ll 1$ a small parameter. The ionic concentration in the bulk electrolyte far from the sphere is denoted by c_i. The soft substrate is comprised of an elastic layer of thickness ℓ, dielectric constant ε_w, Young modulus E and Poisson coefficient ν, and is bonded to a rigid motionless substrate. The ratio of the characteristic surface deflection H_c, produced by the hydrodynamic stress, to the minimum clearance δ is defined as the softness parameter, elastoviscous number or hydrodynamic compliance $\eta = H_c/\delta$. The motion can be considered steady in the reference frame shown in figure 8.1 as long as the time scale of the sphere motion, δ/U, is much longer than the viscous time scale, δ^2/ν, which is also much longer than the substrate response time scale, δ/c, where c is the speed of sound in the substrate. Then the Reynolds numbers of translation and rotation are small, $Re_U = \rho U a/\mu \ll 1$ and $Re_\Omega = \omega Re_U \ll 1$, so that the flow can be described by the Stokes equations to leading order. In this formulation, $\omega = \Omega a/U$ is a kinematic parameter that measures the ratio of the rotational to the translational (peripheral) velocities.

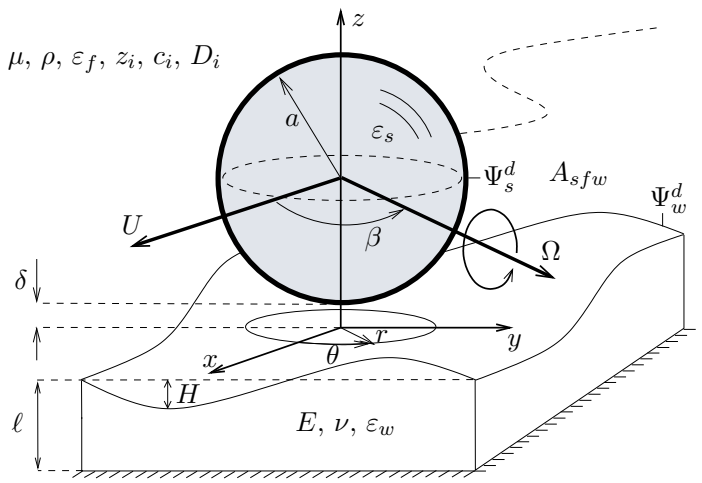

Figure 8.1: The model problem. The soft substrate is deformed by the hydrodynamic, electric and van der Waals intermolecular forces between the sphere and wall surfaces. Cases $\beta = 0$ and $\beta = \pi/2$ represent corkscrew and purely rolling motions respectively.

The conservation equations are nondimensionalized with a the unit of length, H_c the unit of surface deflection, $U\mathcal{V}(\omega,\beta)$ the unit of velocity, and $\mu U\mathcal{V}(\omega,\beta)/a$ the unit of pressure, where

$$\mathcal{V}(\omega,\beta) = |\boldsymbol{e_x} - \boldsymbol{\omega} \times \boldsymbol{e_z}| = \sqrt{1+\omega^2+2\omega\sin\beta}, \tag{8.1}$$

is a characteristic nondimensional velocity in the clearance, with $\boldsymbol{e_i}$ unit vectors, and $\boldsymbol{\omega} = \boldsymbol{\Omega}a/U$. Thus, the velocity $U\mathcal{V}(\omega,\beta)$ is referred to as the "gliding velocity" in what follows. In these variables, and in an inertial reference frame translating with the sphere, the mass and momentum conservation equations for the velocity $\boldsymbol{v}$ and hydrodynamic pressure P become

$$\begin{aligned} \boldsymbol{\nabla}\cdot\boldsymbol{v} &= 0, \\ -\boldsymbol{\nabla}P + \nabla^2\boldsymbol{v} &= 0, \end{aligned} \tag{8.2}$$

subject to non-slip boundary conditions on the sphere and substrate surfaces, where the velocities are

$$\boldsymbol{v} = \frac{\omega(z-1-\epsilon)\sin\beta}{\mathcal{V}(\omega,\beta)}\boldsymbol{e_x} - \frac{\omega(z-1-\epsilon)\cos\beta}{\mathcal{V}(\omega,\beta)}\boldsymbol{e_y} + \frac{\omega(y\cos\beta - x\sin\beta)}{\mathcal{V}(\omega,\beta)}\boldsymbol{e_z}, \tag{8.3}$$

and

$$\boldsymbol{v} = -\frac{\boldsymbol{e_x}}{\mathcal{V}(\omega,\beta)} + \frac{\eta\epsilon(\boldsymbol{\nabla}_\perp H\cdot\boldsymbol{e_x})}{\mathcal{V}(\omega,\beta)}\boldsymbol{e_z} \tag{8.4}$$

respectively. In this formulation, $\boldsymbol{\nabla}_\perp$ is the two-dimensional gradient operator in x and y. The second term on the right-hand side of (8.4) represents the vertical fluid entrainment induced by the surface-deformation field, which remains stationary in this reference frame.

A lubrication approximation can be obtained for $\epsilon \ll 1$ by defining the inner velocities $v_r' = v_r$, $v_\varphi' = v_\varphi$ and $v_z' = v_z\epsilon^{-1/2}$, the inner hydrodynamic pressure $P' = P\epsilon^{3/2}$ and the inner coordinates $z' = z/\epsilon$ and $r' = r/\epsilon^{1/2}$. The surface of the sphere in the gap region is given by (dropping primes)

$$h_0(r) = 1 + r^2/2 + O(\epsilon). \tag{8.5}$$

In these variables, a regular expansion in powers of ϵ yields, to leading order, the conservation equations

$$\begin{aligned} &\frac{1}{r}\frac{\partial}{\partial r}(rv_r) + \frac{1}{r}\frac{\partial v_\varphi}{\partial \varphi} + \frac{\partial v_z}{\partial z} = 0, \\ &\frac{\partial P}{\partial r} = \frac{\partial^2 v_r}{\partial z^2}, \quad \frac{1}{r}\frac{\partial P}{\partial \varphi} = \frac{\partial^2 v_\varphi}{\partial z^2}, \quad \frac{\partial P}{\partial z} = 0, \end{aligned} \tag{8.6}$$

subject to

$$v_r = -\cos\varphi + \frac{\cos(\varphi-\gamma)}{\mathcal{V}(\omega,\beta)}, \quad v_\varphi = \sin\varphi - \frac{\sin(\varphi-\gamma)}{\mathcal{V}(\omega,\beta)}, \quad v_z = -r\cos\varphi + \frac{r\cos(\varphi-\gamma)}{\mathcal{V}(\omega,\beta)}, \tag{8.7}$$

on the sphere surface $z = h_0(r)$, and

$$v_r = -\frac{\cos(\varphi-\gamma)}{\mathcal{V}(\omega,\beta)}, \quad v_\varphi = \frac{\sin(\varphi-\gamma)}{\mathcal{V}(\omega,\beta)}, \quad v_z = \frac{\eta \boldsymbol{\nabla}_\perp H \cdot \boldsymbol{e_x}}{\mathcal{V}(\omega,\beta)}, \tag{8.8}$$

on the wall surface $z = -\eta H$. In this formulation, θ is the physical azimuth angle (measured from the $x-$axis as shown in figure 8.1), and

$$\varphi = \theta + \gamma \tag{8.9}$$

is a reduced angle, with $\gamma(\omega,\beta)$ is a phase angle of the gap pressure distribution given by

$$\gamma(\omega,\beta) = \arctan\left(\frac{\omega\cos\beta}{1+\omega\sin\beta}\right), \tag{8.10}$$

with $-\pi/2 \le \gamma \le \pi/2$. For purely rolling motion, $\beta = \pi/2$ and $\gamma = 0$, so that $\varphi = \theta$ and the pressure distribution is dominated by the entrainment of fluid taking place along the $\theta = 0$ axis. For corkscrew motion, $\beta \to 0$ and $\gamma \sim \arctan\omega$, so that as ω increases the peak pressures are expected to be increasingly dominated by the lateral fluid entrainment enhanced by the rotational motion, shifting the pressure peaks towards the line $\theta = -\gamma$. The rotated system of coordinates (r, φ, z) is shown in figure 8.2, and constitutes a valuable asset for the simplification of the analytical and numerical integration of the problem as further detailed below.

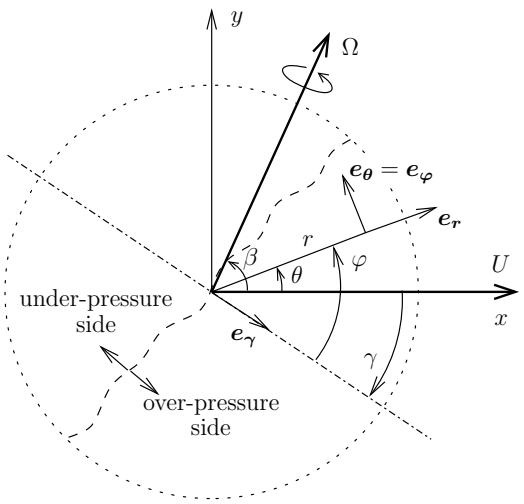

Figure 8.2: Top view of the gap region showing the spatial orientation of the polar azimuth angle θ, phase angle γ and reduced angle φ.

The surface location and the vertical velocity there render the problem (8.6)-(8.8) nonlinear. The continuity equation may still be used to eliminate the velocities after integrating the momentum equations, which yields the Reynolds equation

$$\frac{\partial}{\partial r}\Big(r\frac{\partial P}{\partial r}h^3 + 6rh\cos\varphi\Big) + \frac{1}{r}\frac{\partial}{\partial \varphi}\Big(\frac{\partial P}{\partial \varphi}h^3 - 6rh\sin\varphi\Big) = 0, \tag{8.11}$$

with $h = h_0(r) + \eta H$ the gap profile. Equation (8.11) is subject to the boundedness and periodicity conditions

$$|P| < \infty \quad \text{at} \quad r = 0, \quad P \to 0 \quad \text{at} \quad r \to \infty, \quad P|_{\varphi=0} = P|_{\varphi=2\pi}, \quad \frac{\partial P}{\partial \varphi}\Big|_{\varphi=0} = \frac{\partial P}{\partial \varphi}\Big|_{\varphi=2\pi}. \tag{8.12}$$

It is noteworthy to mention that the velocity scaling and azimuth angle redefinition given by (8.1) and (8.9) renders the nonlinear partial differential problem (8.11)-(8.12) independent of ω and β, so that pressure solutions $P(r, \varphi)$ obtained by integration of (8.11)-(8.12) are valid for any rotation rate ω and rotation azimuthal orientation β, thus reducing the space of solutions by two dimensions.

The radial and azimuth velocity fields in the gap correspond to a combination of

Couette and Poiseuille flows,

$$\begin{aligned} v_r &= \frac{1}{2}\frac{\partial P}{\partial r}\left\{z^2 - z\left[h_0(r) - \eta H\right] - \eta H h_0(r)\right\} \\ - &\left[\cos\varphi - \frac{2\cos(\varphi-\gamma)}{\mathcal{V}(\omega,\beta)}\right]\left[\frac{z+\eta H}{h_0(r)+\eta H}\right] - \frac{\cos(\varphi-\gamma)}{\mathcal{V}(\omega,\beta)}, \\ v_\varphi &= \frac{1}{2r}\frac{\partial P}{\partial \varphi}\left\{z^2 - z\left[h_0(r) - \eta H\right] - \eta H h_0(r)\right\} \\ + &\left[\sin\varphi - \frac{2\sin(\varphi-\gamma)}{\mathcal{V}(\omega,\beta)}\right]\left[\frac{z+\eta H}{h_0(r)+\eta H}\right] + \frac{\sin(\varphi-\gamma)}{\mathcal{V}(\omega,\beta)}, \end{aligned} \tag{8.13}$$

and the vertical velocity is obtained by integrating the mass conservation equation,

$$v_z = \int_z^{h_0(r)} \left[\frac{1}{r}\frac{\partial}{\partial r}(r v_r) + \frac{1}{r}\frac{\partial v_\varphi}{\partial \varphi}\right] dz + v_z\Big|_{z=h_0(r)}, \tag{8.14}$$

with the three velocity components expressed in the (r, φ, z) system of coordinates.

8.2 The electric double-layer and van der Waals pressures.

Van der Waals forces arise from the interaction between permanent polar molecules (Keesom orientation force), permanent polar and polarizable molecules (Debye induction force) and non-polar but polarizable molecules (London dispersion force). In contrast to other type of forces that may be present depending on the particular properties of the molecules, the London dispersion interactions are always present because of quantum-mechanical effects between fluctuating electron clouds, and they are not easily screened by polar solvents. Using the Derjaguin approximation [27], the effect of this interaction is assumed to result in a nonretarded disjoining pressure or intermolecular compression stress Π^{vdW}, that represents the excess pressure in the gap compared to that of the bulk flow P. The disjoining pressure acts as an additional compression stress on both the sphere and wall surfaces, and its nondimensional magnitude is

$$\Pi^{vdW} = -\frac{\Upsilon}{h^3}, \tag{8.15}$$

with

$$\Upsilon = \frac{A_{sfw}}{6\pi\mu U \mathcal{V}(\omega,\beta) a^{1/2}\delta^{3/2}} \tag{8.16}$$

the ratio of the van der Waals to hydrodynamic characteristic stresses. In this formulation, A_{sfw} is the Hamaker coefficient, which depends on the particle, fluid and wall dielectric constants and absorption spectra, and typically ranges from 1 to 100 times the thermal energy kT, with k the Boltzmann constant and T the temperature [20, 21]. The sign of the

the Hamaker coefficient is the same as the sign of the product of the excess polarizabilities $\varepsilon_s - \varepsilon_f$ and $\varepsilon_w - \varepsilon_f$ [28]. If the dielectric constant of the liquid ϵ_f is intermediate between ϵ_w and ϵ_s, the van der Waals force is repulsive, and attractive otherwise. The van der Waals interactions are commonly attractive due to the high dielectric constant of usual solvents.

The van der Waals forces alone do not usually determine the total intermolecular interaction, except in vacuum or deionized solvents. In aqueous electrolyte solutions, electroneutral solid surfaces may become spontaneously charged even under no externally applied electric field. Specific ions are preferentially adsorpted by the surface due to non-electrical affinity interactions with its molecules, while others form an atmosphere of ions in rapid thermal motion in a thin cloud of thickness of $O(\ell_D)$ close to the surface, where ℓ_D is the Debye length, in such a way that the charged cloud and surface charge form an electroneutral system. Associated to this spontaneous formation of the double layer is a decrease of the Gibbs free energy, that ultimately leads to a combination of an osmotic overpressure and Maxwell stresses in the gap, with their total contribution classically represented by a disjoining pressure or electric compression stress Π^{el} given by [27]

$$\Pi^{el} = \Xi \mathrm{e}^{-\kappa(h-1)}, \tag{8.17}$$

with

$$\Xi = \frac{64\delta^{3/2} c_i N_A kT}{\mu U \mathcal{V}(\omega,\beta) a^{1/2}} \lambda(\Psi_w^d, \Psi_s^d) \mathrm{e}^{-\kappa} \tag{8.18}$$

the ratio of the electric to hydrodynamic characteristic stresses, and

$$\kappa = \frac{\delta}{\ell_D} = \sqrt{\frac{2(z_i e \delta)^2 c_i N_A}{\varepsilon_0 \varepsilon_f kT}} \tag{8.19}$$

is the Debye-Hückel parameter. The function $\lambda(\Psi_w^d, \Psi_s^d)$ is given by [21]

$$\lambda(\Psi_w^d, \Psi_s^d) = \tanh\left(z_i \Psi_w^d/4\right) \tanh\left(z_i \Psi_s^d/4\right). \tag{8.20}$$

Equation (8.17) represents the nondimensional electric pressure for the interaction of two double layers of a symmetric electrolyte solution of concentration c_i. In this model, Ψ_s^d and Ψ_w^d are the nondimensional Stern potentials (which are approximately similar to the zeta potentials) of the sphere and substrate surfaces respectively, which are assumed to be constant and are nondimensionalized with the thermal voltage $kT/e \sim 25$ mV. Additionally, in this formulation e is the protonic charge, ε_0 is the permittivity of vacuum and N_A is the Avogadro's number. At constant and symmetric zeta potentials, the double-layer interaction results in a repulsive force, since, as the particle approaches the wall, ions must be driven off

the substrate to decrease the surface charge, which in turn is proportional to the gradient of the electric potential on the surface. This forced discharge results in an increase of Gibbs free energy. More involved models of electric double-layer pressures could be used here, which may include important effects such as charge regulation due to surface chemical equilibrium constraints [20, 21], or surface permeability to ionic fluxes, which is believed to influence bacterial adhesion by ion-channelling effects in bacterial walls [29]. Nonetheless, equation (8.17) represents a logical starting point for the present investigation.

Earlier work by [18] found that the pressure gradient in the gap between a sliding sphere and a planar wall may distort the electric double-layer equilibrium configuration described above, producing an electroosmotic flow of ions near both surfaces and a streaming potential in the gap, that in turn generate an electrokinetic lift on the particle. Electrokinetic interactions are found to be comparable to intermolecular forces only for highly viscous, low-conductivity solutions such as 95% glycerol-water mixtures [30], for which the ionic Péclet number $Pe_i = U\mathcal{V}\delta/D_i$ is of order unity or larger, with D_i the ionic diffusion coefficient. In this investigation, electrokinetic forces produced by pressure gradients are neglected since the characteristic diffusion time of the ions in the gap, δ^2/D_i, is assumed to be much smaller than the characteristic time of translational or rotational motion, $\delta/U\mathcal{V}$, so that $Pe_i \ll 1$ and the perturbation of the equilibrium electric double-layer produced by the convective transport of ions can be neglected in the first approximation. This simplification leads to a Boltzmann distribution of ionic concentration in the gap, from which the electric pressure (8.17) is derived by solving the corresponding Poisson-Boltzmann equation [21]. The condition $Pe_i \ll 1$ is easily satisfied by typical highly conductive physiological solutions (mostly containing Na^+, K^+, Cl^-, Ca^{2+} and Mg^{2+}), for which the ionic diffusion dominates and the electrokinetic lift on the sphere is at least three to four orders of magnitude smaller than the elastohydromolecular forces resulting from the present analysis.

For convenience, the hydromolecular pressure $P^\bigstar$

$$P^\bigstar = P + \Pi^{vdW} + \Pi^{el}, \tag{8.21}$$

is defined, which represents the net compression normal stress (hydrodynamic and intermolecular) acting on the sphere and substrate surfaces. The hydromolecular pressure $P^\bigstar$ is in general a function of the intermolecular and kimematic parameters, the fluid and wall mechanical properties and the spatial coordinates.

Equations (8.11)-(8.12), (8.15) and (8.17) need to be supplied with an appropriate substrate mechanical model. The substrate mechanics is analyzed in Section 8.3.

8.2.1 The DLVO critical ionic concentration for adhesion

In the framework of the classical DLVO theory, sufficiently large electrolyte concentrations c_i may lead to a double-layer compression effect, by which the Debye thickness ℓ_D decreases with increasing c_i and the particle can approach to a shorter distance before any repulsion is felt. Further approach produces a large attracting van der Waals force on the particle able to outweigh any repulsion. This leads to rapid coagulation if the energy barrier to the irreversible adhesion minimum becomes smaller than the energy associated to Brownian perturbations of the gap distance. The critical concentration for the rapid coagulation of a sphere on a flat rigid substrate is given by the system of equations

$$F_z(\delta^\nabla) = 0 \quad \text{and} \quad \int_{\delta^\nabla}^{\infty} F_z(\delta) d\delta \approx bkT, \tag{8.22}$$

where F_z is the net intermolecular force on the sphere and b is a constant, which is conventionally set to $b = 0$ for a small energy barrier [6]. Equations (8.22) represent the coagulation event or irreversible adhesion at the primary minimum as sketched in figure 7.1, and they give the critical conditions for which the force on the particle is zero while the work produced by a random perturbation of the gap distance against the normal force is roughly a multiple of the thermal energy of the surrounding molecules. When F_z is obtained by the classic DLVO theory, these expressions yield the critical coagulation concentration [21]

$$c_{i0}^\nabla = 73728\pi^2 \mathrm{e}^{-2} \frac{(\varepsilon_0\varepsilon_f)^3 (kT)^5 \lambda^2 (\Psi_w^d, \Psi_s^d)}{(z_i e)^6 A_{sfw}^2 N_A}. \tag{8.23}$$

The minimum clearance for coagulation, δ_0^∇, measured with respect to the Debye layer thickness based on c_{i0}, is given by $\kappa_0^\nabla = \delta_0^\nabla / \ell_{D0}^\nabla = 1$.

As shown further below, F_z is also influenced by hydrodynamic and substrate compliance effects, so that equation (8.23) needs to be correspondingly modified. Additionally, local substrate deformations produced by elastic instabilities of hydromolecular origin are found in this analysis to induce irreversible adhesion, an effect that is obliterated by simply using the criterion (8.22)-(8.23).

8.3 Substrate mechanics

In this analysis, the substrate is modelled by a compliant layer of thickness ℓ coating a rigid foundation as depicted in figure 8.1. The material of the layer is assumed to be isotropic and characterized by its Young modulus E and Poisson coefficient ν, with $0 < \nu < 1/2$ for compressible materials such as gels, and $\nu \sim 1/2$ for incompressible materials such

as elastomers, for which the Poisson effect becomes primarily important. The solid stress tensor $\boldsymbol{\sigma}$ satisfies the internal equilibrium equation

$$\boldsymbol{\nabla} \cdot \boldsymbol{\sigma} = 0 \tag{8.24}$$

in the absence of volumetric forces in the thin layer, and is related to the displacement vector $\boldsymbol{u}$ by the linear constitutive equation

$$\boldsymbol{\sigma} = \frac{E(\boldsymbol{\nabla u} + \boldsymbol{\nabla u^T})}{2(1+\nu)} + \frac{\nu E(\boldsymbol{\nabla} \cdot \boldsymbol{u})\boldsymbol{I}}{(1+\nu)(1-2\nu)}, \tag{8.25}$$

subject to boundary conditions of solid-liquid interface equilibrium and compatibility of deformations with the rigid foundation,

$$\boldsymbol{\sigma} \cdot \boldsymbol{n^T} = \boldsymbol{\sigma^\bigstar} \cdot \boldsymbol{n^T} \quad \text{at} \quad z = -H, \quad \text{and} \quad \boldsymbol{u} = 0 \quad \text{at} \quad z = -\ell, \tag{8.26}$$

where $\boldsymbol{\sigma^\bigstar} = -P^\bigstar \boldsymbol{I} + \mu(\boldsymbol{\nabla v} + \boldsymbol{\nabla v^T})$ is the hydromolecular stress tensor, which is composed of the sum of the isotropic hydromolecular pressure tensor and the deviatoric viscous stress tensor. In this formulation, $\boldsymbol{n} = (-\partial u_z/\partial r|_{z=0}, -r^{-1}\partial u_z/\partial \varphi|_{z=0}, 1) + O(\epsilon)$ is a unit vector normal to the substrate surface. Equations (8.24), (8.25) and (8.26) are generally coupled to the lubrication problem (8.11)-(8.12) in a rather cumbersome way for arbitrary layer thickness ℓ. Asymptotic analysis of this complicated problem can be performed by assuming that the ratio of the layer thickness ℓ to the characteristic lubrication region dimension $\delta/\epsilon^{1/2}$ is a small parameter,

$$\zeta = \frac{\epsilon^{1/2}\ell}{\delta} \ll 1, \tag{8.27}$$

so that the layer thickness ℓ may well be much larger than the minimum gap distance δ since $\ell/\delta \ll 1/\epsilon^{1/2}$ and $\epsilon \ll 1$, but is still small compared with the particle radius, $\ell/a \ll \epsilon^{1/2}$. The purpose of this section is to obtain the surface deformation, by solving asymptotically (8.24)-(8.26), as a function of $P^\bigstar$ and the hydrodynamic compliance η, for $\eta = O(1)$ and $\zeta \ll 1$.

The qualitative asymptotic behavior of the solution can be readily extracted from an order of magnitude analysis of (8.24)-(8.26). Surface loads of order unity applied on the thin layer are expected to produce a compression normal stress $\sigma_{zz} = O(1)$ and a vertical deformation $u_z = O(\zeta)$. The Poisson effect produces radial and azimuthal normal stresses $\sigma_{rr} = O(1)$ and $\sigma_{\varphi\varphi} = O(1)$, and displacements $u_r = O(\zeta^2)$ and $u_\varphi = O(\zeta^2)$. For nearly incompressible materials, $\nu \sim 1/2$, the stresses become independent of the material properties in the first approximation, and the vertical displacement becomes $u_z = O(\zeta^3)$ to satisfy the vanishing cubical dilatation constraint $\nabla \cdot \boldsymbol{u} = 0$ in the incompressible limit [1].

Equations (8.24)-(8.26) are nondimensionalized with ℓ the unit of vertical coordinate, $\delta/\epsilon^{1/2}$ the unit of radial coordinate, δ the unit of vector displacement, and $E(1-\nu)\delta/[\ell(1+\nu)(1-2\nu)]$ the unit of stress tensor. In these variables, (8.24) and (8.25) become

$$\begin{aligned}
\frac{\partial\sigma_{rz}}{\partial z}+\zeta\left[\frac{1}{r}\frac{\partial}{\partial r}(r\sigma_{rr})+\frac{1}{r}\frac{\partial\sigma_{r\varphi}}{\partial\varphi}-\frac{\sigma_{\varphi\varphi}}{r}\right]&=0,\\
\frac{\partial\sigma_{\varphi z}}{\partial z}+\zeta\left[\frac{1}{r}\frac{\partial}{\partial r}(r\sigma_{r\varphi})+\frac{1}{r}\frac{\partial\sigma_{\varphi\varphi}}{\partial\varphi}+\frac{\sigma_{r\varphi}}{r}\right]&=0,\\
\frac{\partial\sigma_{zz}}{\partial z}+\zeta\left[\frac{1}{r}\frac{\partial}{\partial r}(r\sigma_{rz})+\frac{1}{r}\frac{\partial\sigma_{z\varphi}}{\partial\varphi}\right]&=0,
\end{aligned}\tag{8.28}$$

and

$$\begin{aligned}
\sigma_{rr} &= \frac{\nu}{1-\nu}\frac{\partial u_r}{\partial z}+\left[\frac{\partial u_r}{\partial r}+\frac{\nu}{1-\nu}\left(\frac{u_r}{r}+\frac{1}{r}\frac{\partial u_\varphi}{\partial\varphi}\right)\right]\zeta,\\
\sigma_{r\varphi} &= \frac{1-2\nu}{2(1-\nu)}\left[r\frac{\partial}{\partial r}\left(\frac{u_\varphi}{r}\right)+\frac{1}{r}\frac{\partial u_r}{\partial\varphi}\right]\zeta,\\
\sigma_{rz} &= \frac{1-2\nu}{2(1-\nu)}\left(\frac{\partial u_r}{\partial z}+\zeta\frac{\partial u_z}{\partial r}\right),\\
\sigma_{\varphi\varphi} &= \frac{1-2\nu}{1-\nu}\left(\frac{1}{r}\frac{\partial u_\varphi}{\partial\varphi}+\frac{u_r}{r}\right)\zeta\\
&+ \frac{\nu}{1-\nu}\left[\frac{\partial u_z}{\partial z}+\zeta\left(\frac{1}{r}\frac{\partial}{\partial r}(ru_r)+\frac{1}{r}\frac{\partial u_\varphi}{\partial\varphi}\right)\right],\\
\sigma_{\varphi z} &= \frac{1-2\nu}{2(1-\nu)}\left(\frac{\partial u_\varphi}{\partial z}+\frac{\zeta}{r}\frac{\partial u_z}{\partial\varphi}\right),\\
\sigma_{zz} &= \frac{\partial u_z}{\partial z}+\frac{\nu}{1-\nu}\left[\frac{1}{r}\frac{\partial}{\partial r}(ru_r)+\frac{1}{r}\frac{\partial u_\varphi}{\partial\varphi}\right]\zeta.
\end{aligned}\tag{8.29}$$

The regular asymptotic expansions

$$\begin{aligned}
\boldsymbol{\sigma}&=\boldsymbol{\sigma_0}+\zeta\boldsymbol{\sigma_1}+\zeta^2\boldsymbol{\sigma_2}+O(\zeta^3)\\
\boldsymbol{u}&=\boldsymbol{u_0}+\zeta\boldsymbol{u_1}+\zeta^2\boldsymbol{u_2}+O(\zeta^3),
\end{aligned}\tag{8.30}$$

are substituted into (8.28) and (8.29). The hydrodynamic compliance η defined in Section 8.1 is found in what follows to be described by an asymptotic expansion of the form

$$\eta=\hat{\eta}_0+\zeta^2\hat{\eta}_2+O(\zeta^4),\tag{8.31}$$

where $\hat{\eta}_i=\eta_i/\zeta^i$. To leading order in ζ, equations (8.28) and (8.29) reduce to

$$\frac{\partial^2 u_{r0}}{\partial z^2}=\frac{\partial^2 u_{\varphi 0}}{\partial z^2}=\frac{\partial^2 u_{z0}}{\partial z^2}=0,\tag{8.32}$$

subject to $u_{r0}=u_{\varphi 0}=u_{z0}=0$ on $z=-1$ and $\partial u_{z0}/\partial z=-\eta_0 P^{\bigstar}$ at $z=0$. In this formulation, the hydrodynamic compliance η_0 is given by

$$\eta_0=\frac{\mu U\mathcal{V}(\omega,\beta)\ell a^{1/2}(1+\nu)(1-2\nu)}{E(1-\nu)\delta^{5/2}}.\tag{8.33}$$

The leading-order stresses and deformations are given by

$$\sigma_{rr0} = \sigma_{\varphi\varphi 0} = -\frac{\nu\eta_0 P^\bigstar}{1-\nu}, \quad \sigma_{zz0} = -\eta_0 P^\bigstar, \quad \sigma_{r\varphi 0} = \sigma_{rz0} = \sigma_{\varphi z0} = 0,$$

and

$$u_{r0} = u_{\varphi 0} = 0, \quad u_{z0} = -\eta_0 P^\bigstar (1+z), \tag{8.34}$$

which resemble the classic rigid foundation model [2], in which the wall deflection is proportional to the net normal stress (intermolecular and hydrodynamic stress). If the Poisson effect is negligible, the leading-order radial and azimuthal normal stresses vanish in the first approximation due to the large material compressibility. If the Poisson effect is important, $\nu \sim 1/2$, the hydrodynamic compliance η_0 and elastic displacements vanish in this approximation, giving no useful information of the deformation field, for which higher-order terms must be retained. It is worth mentioning that, for large hydrodynamic compliances, $\eta_0 = O(\epsilon^{-1/2}) \gg 1$, the boundary condition $\partial u_{z0}/\partial z = -\eta_0 P^\bigstar$ at $z = 0$ becomes inaccurate in this approximation, since the curvature of the surface may produce non-negligible viscous shear forces, thereby producing non-negligible contributions by the non-diagonal terms of the hydromolecular stress tensor to the surface deformation field.

To second order in ζ, (8.28) and (8.29) become

$$\frac{\partial^2 u_{r1}}{\partial z^2} = \frac{\eta_0}{1-2\nu}\frac{\partial P^\bigstar}{\partial r}, \quad \frac{\partial^2 u_{\varphi 1}}{\partial z^2} = \left(\frac{\eta_0}{1-2\nu}\right)\frac{1}{r}\frac{\partial P^\bigstar}{\partial \varphi}, \quad \frac{\partial^2 u_{z1}}{\partial z^2} = 0, \tag{8.35}$$

subject to $u_{r1} = u_{\varphi 1} = u_{z1} = 0$ at $z = -1$ and $\partial u_{r1}/\partial z = \partial u_{\varphi 1}/\partial z = \partial u_{z1}/\partial z = 0$ at $z = 0$, which solutions yield the second-order stresses and deformations

$$\sigma_{rr1} = \sigma_{\varphi\varphi 1} = \sigma_{zz1} = \sigma_{r\varphi 1} = 0, \quad \sigma_{r\varphi 1} = \left(\frac{\nu\eta_0 z}{1-\nu}\right)\frac{\partial P^\bigstar}{\partial r}, \quad \sigma_{\varphi z1} = \left(\frac{\nu\eta_0 z}{1-\nu}\right)\frac{1}{r}\frac{\partial P^\bigstar}{\partial \varphi},$$

and

$$u_{r1} = \frac{\eta_0(z^2-1)}{2(1-2\nu)}\frac{\partial P^\bigstar}{\partial r}, \quad u_{\varphi 1} = \frac{\eta_0(z^2-1)}{2(1-2\nu)}\frac{1}{r}\frac{\partial P^\bigstar}{\partial \varphi}, \quad u_{z1} = 0, \tag{8.36}$$

so that the second-order correction to the vertical displacement is zero.

Finally, to third order in ζ, (8.28) and (8.29) become

$$\frac{\partial^2 u_{r2}}{\partial z^2} = \frac{\partial^2 u_{\varphi 2}}{\partial z^2} = 0, \quad \frac{\partial^2 u_{z2}}{\partial z^2} = -\frac{2\nu\eta_0 z}{1-2\nu}\nabla_\perp^2 P^\bigstar, \tag{8.37}$$

subject to $u_{r2} = u_{\varphi 2} = u_{z2} = 0$ at $z = -1$, and

$$\frac{\partial u_{r2}}{\partial z} = \frac{\partial u_{\varphi 2}}{\partial z} = 0, \quad \frac{\partial u_{z2}}{\partial z} = \frac{\nu\eta_0\nabla_\perp^2 P^\bigstar}{2(1-\nu)(1-2\nu)}, \tag{8.38}$$

at $z = 0$, which solutions give the displacement field

$$\begin{aligned} u_{r2} &= u_{\varphi 2} = 0, \\ u_{z2} &= \frac{\nu\eta_0\nabla_\perp^2 P^\bigstar}{1-2\nu}\left[-\frac{z^3}{3} + \frac{z}{2(1-\nu)} + \frac{1+2\nu}{6(1-\nu)}\right]. \end{aligned} \tag{8.39}$$

The asymptotic deformation field given by (8.34), (8.36) and (8.39) yields zero cubical dilatation $\nabla \cdot \boldsymbol{u} = 0$ to $O(\zeta^3)$ in the incompressible limit $\nu \sim 1/2$.

According to (8.34), (8.36) and (8.39), the substrate deflection

$$u_z = -\eta_0 P^\bigstar + \eta_2 \nabla_\perp^2 P^\bigstar + O(\zeta^3) \quad \text{at} \quad z = 0, \tag{8.40}$$

is found, with the higher-order hydrodynamic compliance η_2 given by

$$\eta_2 = \frac{\mu U \mathcal{V}(\omega,\beta)\ell^3}{E a^{1/2}\delta^{7/2}}. \tag{8.41}$$

Note that neither η_2 nor u_{z3} vanish in the incompressible limit $\nu \sim 1/2$.

For compressible materials, the rigid-foundation model

$$H = P^\bigstar = P - \frac{\Upsilon}{[h_0(r) + \eta_0 H]^3} + \Xi \mathrm{e}^{-\kappa[h_0(r)+\eta_0 H - 1]} \tag{8.42}$$

represents the first approximation of the substrate deformation, with the hydrodynamic compliance appearing implicitly in the Reynolds equation (8.11) given by (8.33). For incompressible materials $\nu \sim 1/2$, the vertical displacement becomes $O(\zeta^3)$ and (8.40) yields

$$H = -\nabla_\perp^2 P^\bigstar = -\nabla_\perp^2 P + \nabla_\perp^2 \left\{ \frac{\Upsilon}{[h_0(r) + \eta_2 H]^3} - \Xi \mathrm{e}^{-\kappa[h_0(r)+\eta_2 H - 1]} \right\} \tag{8.43}$$

as an approximation valid to $O(\zeta^3)$, with η_2 given by (8.41). Expression (8.43) represents a much simpler approximation than usual solutions of the deformation field of incompressible layers based on Hankel transforms [1, 2], and allows the calculation of asymptotic solutions to the lubrication problem (8.11)-(8.12) for $\eta_2 \ll 1$.

In the asymptotic limit of very thick elastic substrates, $\zeta \to \infty$, the surface displacement can be obtained by the method of Green's functions as detailed in classic texts of elasticity theory [1, 2]. In the present notation, the surface deformation becomes

$$H = \int_0^{2\pi}\int_0^\infty \frac{P^\bigstar(r',\varphi')r'dr'd\varphi'}{\sqrt{r'^2 + r^2 - 2rr'\cos(\varphi - \varphi')}}, \tag{8.44}$$

with

$$\eta_\infty = \frac{\mu U \mathcal{V}(\omega,\beta) a(1-\nu^2)}{\pi E \delta^2}, \tag{8.45}$$

the hydrodynamic compliance for semi-infinite (compressible or incompressible) elastic substrates.

Quantities similar to those represented by the hydrodynamic compliances (8.33), (8.41) and (8.45), can be obtained to describe the substrate compliance due to the action of the intermolecular stresses. The van der Waals and electric compliances are defined as

$$\Delta_0^{vdW} = \eta_0 \Upsilon = \frac{A_{sfw}\ell(1+\nu)(1-2\nu)}{6\pi E(1-\nu)\delta^4} \tag{8.46}$$

and

$$\Delta_0^{el} = \eta_0 \Xi = \frac{64(1+\nu)(1-2\nu)\ell c_i N_A kT}{E(1-\nu)\delta}\lambda(\Psi_w^d, \Psi_s^d)\mathrm{e}^{-\kappa} \tag{8.47}$$

for thin compressible elastic layers,

$$\Delta_2^{vdW} = \eta_2 \Upsilon = \frac{A_{sfw}\ell^3}{6\pi a E\delta^5} \tag{8.48}$$

and

$$\Delta_2^{el} = \eta_2 \Xi = \frac{64\ell^3 c_i N_A kT}{Ea\delta^2}\lambda(\Psi_w^d, \Psi_s^d)\mathrm{e}^{-\kappa} \tag{8.49}$$

for thin incompressible elastic layers, and

$$\Delta_\infty^{vdW} = \eta_\infty \Upsilon = \frac{A_{sfw}a^{1/2}(1-\nu^2)}{6\pi^2 E\delta^{7/2}} \tag{8.50}$$

and

$$\Delta_\infty^{el} = \eta_\infty \Xi = \frac{64(1-\nu^2)a^{1/2}c_i N_A kT}{\pi E\delta^{1/2}}\lambda(\Psi_w^d, \Psi_s^d)\mathrm{e}^{-\kappa}, \tag{8.51}$$

for semi-infinite elastic substrates.

The lubrication problem (8.11)-(8.12) is closed by either (8.42), (8.43) or (8.44). The semi-infinite elastic substrate equation (8.44) yields a three-dimensional non-linear partial integro-differential equation when coupled with the lubrication problem (8.11)-(8.12) that represents quite an analytical challenge, since the hydromolecular pressure is generally a two-dimensional field. In this analysis, emphasis is mainly made on the more analytically tractable thin-layer configurations (8.42) and (8.43), since a thorough physical understanding of these cases, which could be extended to more involved situations, can be achieved by deriving exact solutions and using asymptotic methods. Chapter 9 briefly addresses the influences of material incompressibility and layer thickness.

8.4 Nearly-rigid-wall asymptotics (NRWA) and summary of main nondimensional parameters

In this model, the characteristic area of the lubrication region is δ^2/ϵ, which, by the chordal theorem, is also roughly the area of the circular zone centered at a distance $-\delta$ inside the sphere. This area is of the same order of magnitude as the effective interaction area of the van der Waals forces, and it is larger than the typical interaction area $\delta^2/\epsilon\kappa$ of the electric double-layer forces [20], since these decay exponentially in the radial direction with a slope proportional to κ, with $\kappa \geqslant O(1)$. It must be emphasized that, in this analysis, surface deformations are restrained to occur in the lubrication region. This assumption proves to be accurate if the characteristic deformation H_c is much smaller than the lubrication region size $\delta/\epsilon^{1/2}$, or equivalently, if the hydrodynamic compliance satisfies $\eta \ll 1/\epsilon^{1/2}$. Analyses for larger values of η may produce appreciable surface deformations outside the inner lubrication region, so that η may have to be incorporated in the inner scaling of the lubrication zone and an asymptotic matching may have to be performed with the outer viscous region as similarly performed in earlier works [25, 26] for the rigid-wall case.

The regular asymptotic expansions

$$\begin{aligned} P^{\bigstar} &= P_0^{\bigstar} + \eta P_1^{\bigstar} + O(\eta^2), \\ h &= h_0(r) + \eta[H_0 + \eta H_1 + O(\eta^2)], \\ \boldsymbol{v} &= \boldsymbol{v_0} + \eta \boldsymbol{v_1} + O(\eta^2), \end{aligned} \tag{8.52}$$

are defined for slightly soft surfaces $\eta \ll 1$. The corresponding expansions of the van der Waals (8.15) and electric pressures (8.17) yield

$$\Pi^{vdW} = \Pi_0^{vdW} + \eta\Pi_1^{vdW} + O(\eta^2) = -\Upsilon/h_0^3(r) + 3\Upsilon H_0\eta/h_0^4(r) + O(\eta^2), \tag{8.53}$$

and

$$\Pi^{el} = \Pi_0^{el} + \eta\Pi_1^{el} + O(\eta^2) = \Xi \mathrm{e}^{-\kappa[h_0(r)-1]} - \kappa\Xi\eta H_0 \mathrm{e}^{-\kappa[h_0(r)-1]} + O(\eta^2). \tag{8.54}$$

The van der Waals and electric compliances are defined as

$$\Delta^{vdW} = \eta\Upsilon, \qquad \text{and} \qquad \Delta^{el} = \eta\Xi, \tag{8.55}$$

and they represent the ratio of the intermolecular to the elastic characteristic stresses. The method for the calculation of Δ^{el}, Δ^{vdW} and η as a function of the dimensional parameters is detailed in Section 8.3, and they are given by the expressions (8.46)-(8.51).

Table 8.1: Fundamental nondimensional parameters and their definition, their asymptotic ordering (Ord.) in the NRWA limit and numerical estimates (Est.), which are based on a particle of radius $a = 50$ μm gliding at $U\mathcal{V} = 50$ μm/s. The parameters of the substrate are $E = 1$ kPa, $\ell = 0.5$ μm (when finite), $\nu = 0$ (when compressible), $\nu = 0.5$ (when incompressible), $\delta = 0.1$ μm. The solvent is a symmetric monovalent aqueous electrolyte of $c_i = 1$ mM NaCl, $z_i = 1$, $\rho = 1000$ kg/m^3, $\mu = 1$ mPa·s, $\epsilon_f = 80$, $\Psi_s^d = \Psi_w^d = -2$ and $D_i = 10^{-9}$ m^2/s. The Hamaker coefficient is $A_{sfw} = 1.5kT$, with $T = 300$ K. Typical values of the dimensional intermolecular parameters are obtained from [20] and [21].

Parameter	Substrate	Definition	Ord.	Est.
hydrodynamic compliances:				
η_0	thin layer compressible	$\dfrac{\mu U\mathcal{V}(\omega,\beta)\ell a^{1/2}(1+\nu)(1-2\nu)}{E(1-\nu)\delta^{5/2}}$	$\ll 1$	0.05
η_2	thin layer incompressible	$\dfrac{\mu U\mathcal{V}(\omega,\beta)\ell^3}{Ea^{1/2}\delta^{7/2}}$	$\ll 1$	0.002
η_∞	semi-infinite medium	$\dfrac{\mu U\mathcal{V}(\omega,\beta)a(1-\nu^2)}{\pi E\delta^2}$	$\ll 1$	0.08
van der Waals compliances:				
Δ_0^{vdW}	thin layer compressible	$\dfrac{A_{sfw}\ell(1+\nu)(1-2\nu)}{6\pi E(1-\nu)\delta^4}$	$\ll 1$	0.001
Δ_2^{vdW}	thin layer incompressible	$\dfrac{A_{sfw}\ell^3}{6\pi aE\delta^5}$	$\ll 1$	0.00008
Δ_∞^{vdW}	semi-infinite medium	$\dfrac{A_{sfw}a^{1/2}(1-\nu^2)}{6\pi^2 E\delta^{7/2}}$	$\ll 1$	0.002
electric compliances:				
Δ_0^{el}	thin layer compressible	$\dfrac{64(1+\nu)(1-2\nu)\ell c_i N_A kT}{E(1-\nu)\delta}\lambda \mathrm{e}^{-\kappa}$	$\ll 1$	0.005
Δ_2^{el}	thin layer incompressible	$\dfrac{64\ell^3 c_i N_A kT}{Ea\delta^2}\lambda \mathrm{e}^{-\kappa}$	$\ll 1$	0.0002
Δ_∞^{el}	semi-infinite medium	$\dfrac{64a^{1/2}c_i N_A kT(1-\nu^2)}{\pi E\delta^{1/2}}\lambda \mathrm{e}^{-\kappa}$	$\ll 1$	0.008
intermolecular-hydrodynamic stress ratios:				
Υ	—	$\dfrac{A_{sfw}}{6\pi\mu U\mathcal{V}(\omega,\beta)a^{1/2}\delta^{3/2}}$	$\ll 1/\eta$	0.03
Ξ	—	$\dfrac{64\delta^{3/2}c_i N_A kT}{\mu U\mathcal{V}(\omega,\beta)a^{1/2}}\lambda \mathrm{e}^{-\kappa}$	$\ll 1/\eta$	0.1
Debye-Hückel parameter:				
κ	—	$\sqrt{\dfrac{2(z_i e\delta)^2 c_i N_A}{\varepsilon_0\varepsilon_f kT}}$	$\geqslant O(1)$	10.3

In what follows, asymptotic solutions of (8.11)-(8.12) are sought in the nearly-rigid-wall asymptotic (NRWA) limit: $\eta \ll 1$, $\Delta^{vdW} \ll 1$, $\Delta^{el} \ll 1$ and $\kappa \geqslant O(1)$. In this asymptotic limit, the elastic stress dominates over the intermolecular and hydrodynamic stresses on the substrate, which produce small surface deformations, with no clear limitation in the ratios of hydrodynamic to intermolecular stresses as long as they are sufficiently small so that the expansions (8.53) and (8.54) are asymptotic, $\Upsilon \ll 1/\eta$ and $\Xi \ll 1/\eta$.

It is worth emphasizing that the NRWA limit may represent realistic physical conditions that may well be found in the hydrodynamics of small particles over soft materials. Table 8.1 summarizes the nondimensional parameters introduced in the preceding sections and compares the asymptotic ordering required in the NRWA limit with typical values extracted from earlier studies in particle adhesion assuming a moderately soft material as a substrate. Nonetheless, the substrate compliances are highly non-linear in the gap distance and inversely proportional to the substrate compliance, so that they are expected to rapidly attain $O(1)$ values upon adhesion and for softer materials.

Chapter 9

Particle Dynamics

9.1 Dynamics near rigid substrates: hydrodynamic and intermolecular forces

To leading order in η, the substrate corresponds to a perfectly rigid surface, and the intermolecular forces are decoupled from the hydrodynamic forces since there is no surface deformation. In this Section, earlier results [24, 25, 26] are summarized and generalized to account for general azimuth rotation angles, and remarks about the leading-order pressure distribution are made in preparation for Sections 9.3 and 9.4, where the effects of substrate deformability are analyzed.

Integrating the electric and van der Waals pressures (8.15) and (8.17) over the vertical projection of the inner element of sphere surface $\mathbf{d}\boldsymbol{S}_{\boldsymbol{z}} = -a^2\epsilon r\mathrm{d}r\mathrm{d}\varphi\boldsymbol{e}_{\boldsymbol{z}}$ yields

$$F_{z0}^{vdW} = -\frac{\mu U\mathcal{V}(\omega,\beta)a}{\epsilon^{1/2}}\int_0^{2\pi}\int_0^{\infty}\Pi_0^{vdW}r\mathrm{d}r\mathrm{d}\varphi = -\frac{\pi\mu U\mathcal{V}(\omega,\beta)a\Upsilon}{\epsilon^{1/2}} = -\frac{A_{sfw}a}{6\delta^2},$$

and

$$\begin{aligned} F_{z0}^{el} &= \frac{\mu U\mathcal{V}(\omega,\beta)a}{\epsilon^{1/2}}\int_0^{2\pi}\int_0^{\infty}\Pi_0^{el}r\mathrm{d}r\mathrm{d}\varphi \\ &= \frac{2\pi\mu U\mathcal{V}(\omega,\beta)a\Xi}{\epsilon^{1/2}\kappa} = 128\pi a\ell_D c_i^{\infty}N_AkT\lambda(\Psi_w^d,\Psi_s^d)\mathrm{e}^{-\delta/\ell_D}, \end{aligned} \tag{9.1}$$

that correspond to well-known formulas of intermolecular forces [31, 27], which are independent of the hydrodynamic field or gliding kinematics.

To leading order in η, the Reynolds equation (8.11) becomes

$$r^2\frac{\partial^2 P_0}{\partial r^2} + \left[r + \frac{3r^3}{h_0(r)}\right]\frac{\partial P_0}{\partial r} + \frac{\partial^2 P_0}{\partial\varphi^2} = -\frac{6r^3}{h_0^3(r)}\cos\varphi, \tag{9.2}$$

where P_0 is the leading term of a regular asymptotic expansion of the hydrodynamic pressure in powers of η. Equation (9.2) is subject to boundary conditions (8.12) particularized for the leading-order hydrodynamic pressure. The exact solution

$$P_0 = \left[\frac{\mu U a^{1/2}(1+\omega^2+2\omega\sin\beta)^{1/2}}{\delta^{3/2}}\right]\frac{6r\cos[\theta+\gamma(\omega,\beta)]}{5(1+r^2/2)^2}, \tag{9.3}$$

can be obtained in terms of the dimensional hydrodynamic pressure. The contours of (9.3), nondimensionalized with $\mu U a^{1/2}/\delta^{3/2}$, are shown in figure 9.1. It is worth mentioning that once the cosine term in (9.3) is expanded, the pressure scaling with the velocity results to be linear in both U and ω, with the total pressure the sum of the pressures induced by each motion mode. The leading-order velocity components can be calculated by using (9.3) and retaining the first term of the expansion in powers of η of (8.13) and (8.14), which yields

$$\begin{aligned}
v_{r0} &= \left\{\frac{3z^2(2-3r^2)}{10h_0^3(r)} - \frac{z}{h_0(r)}\left[\frac{3(2-3r^2)}{10h_0(r)}+1\right]\right\}\cos\varphi + \left[\frac{2z}{h_0(r)}-1\right]\frac{\cos(\varphi-\gamma)}{\mathcal{V}(\omega,\beta)},\\
v_{\varphi 0} &= -\left[\frac{3z^2}{5h_0^2(r)} - \frac{8z}{5h_0(r)}\right]\sin\varphi - \left[\frac{2z}{h_0(r)}-1\right]\frac{\sin(\varphi-\gamma)}{\mathcal{V}(\omega,\beta)},\\
v_{z0} &= \left[\frac{2z^3(4r-r^3)}{5h_0^4(r)} - \frac{z^2r(r^2+26)}{10h_0^3(r)}\right]\cos\varphi + \frac{z^2r\cos(\varphi-\gamma)}{h_0^2(r)\mathcal{V}(\omega,\beta)}.
\end{aligned} \tag{9.4}$$

Expressions (9.3) and (9.4) reduce to the corresponding pressure and velocity fields in the gap region for the cases of purely translational and rotational motions near a rigid wall [24, 25, 26].

The calculation of the hydrodynamic drag forces and torques is a singular perturbation problem in the small parameter ϵ, in that it requires asymptotic matching with the outer non-lubrication viscous region. As $\epsilon \to 0^+$ the pressure and velocity gradient become singular because of the vanishing thickness of the lubrication layer. Following earlier work [24, 25, 26], the leading-order forces and torques become

$$F_{x0}^h = 6\pi\mu U a\left[\left(\frac{8}{15}-\frac{2}{15}\omega\sin\beta\right)\ln\epsilon - 0.95429 - 0.25725\omega\sin\beta + o(1)\right], \tag{9.5}$$

$$F_{y0}^h = 6\pi\mu\Omega a\cos\beta\left[\frac{2}{15}\ln\epsilon + 0.25725 + o(1)\right], \tag{9.6}$$

$$F_{z0}^h = 0, \tag{9.7}$$

$$T_{x0}^h = 8\pi\mu\Omega a^2\cos\beta\left[\frac{2}{5}\ln\epsilon - 0.37085 + o(1)\right], \tag{9.8}$$

$$T_{y0}^h = 8\pi\mu U a^2\left[\left(\frac{2}{5}\omega\sin\beta-\frac{1}{10}\right)\ln\epsilon - 0.19296 - 0.37085\omega\sin\beta + o(1)\right], \tag{9.9}$$

$$T_{z0}^h = 0, \tag{9.10}$$

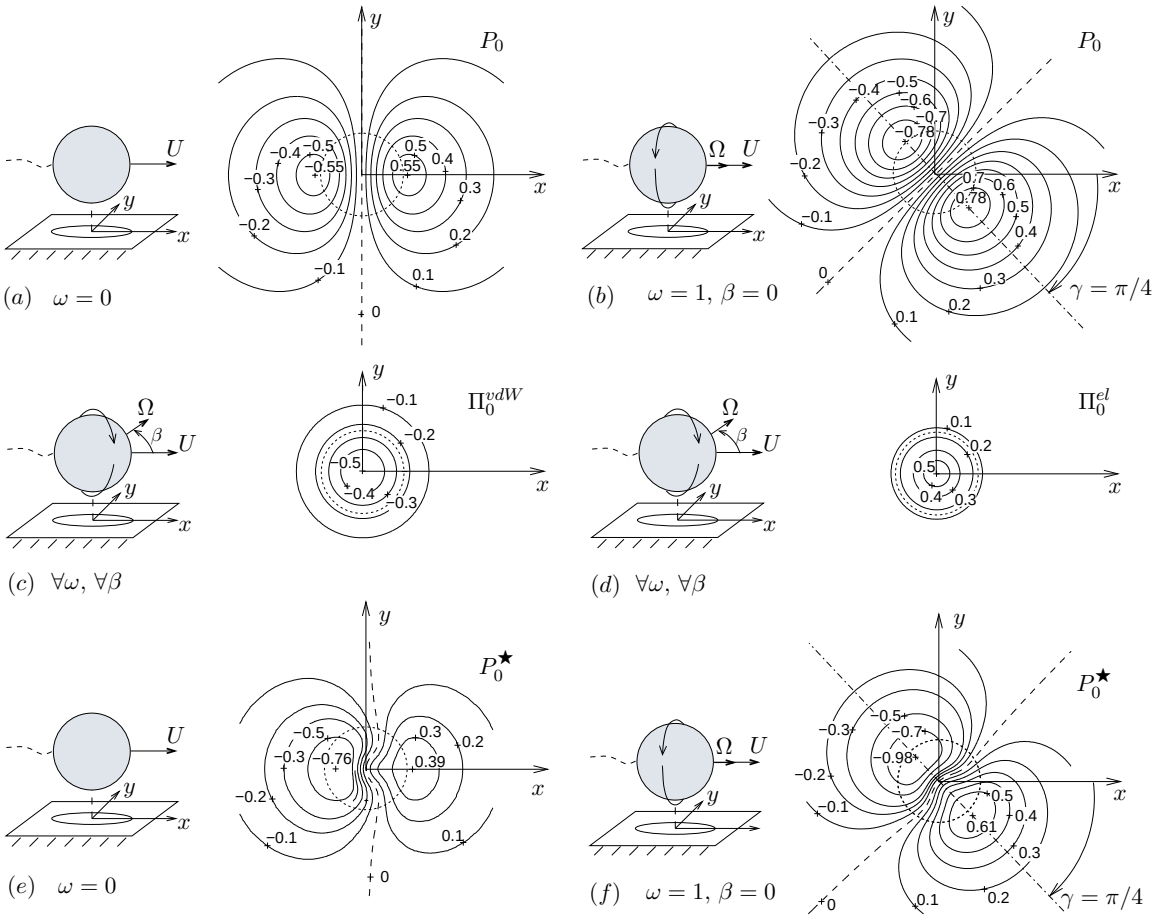

Figure 9.1: Leading-order (rigid-wall) pressure and stress contours. (a) Hydrodynamic pressure contours for purely translational motion, (b) hydrodynamic pressure contours for corkscrew motion, (c) van der Waals stress contours (independent of rotation), (d) electric stress contours (independent of rotation), (e) hydromolecular pressure contours for purely translational motion, and (f) hydromolecular pressure contours for corkscrew motion. Positive contour labels represent compression stresses on the substrate, whereas negative ones represent traction stresses. In this figure, $\Upsilon = \Xi = 0.5$, and the dotted line represents a circle of spatial unit radius.

which have been conveniently modified in the present investigation to account for an arbitrary azimuth angle of rotation β.

It is worth mentioning that, since the problem (8.11)-(8.12) is linear to leading order in η, the hydrodynamic forces (9.5)-(9.10) produced by the rotational and translational motions are decoupled. Since, according to the classical Stokesian scaling, these forces scale linearly with the velocities U and Ω, they are kinematically reversible, in that if the rotation and translation velocity vectors are reversed at once, the forces and torques moduli remain invariant but their directions become reversed. As a result of this kinematically-reversible

effect, no hydrodynamic lift force is exerted on the sphere to leading order in η, and the intermolecular forces (9.1) and (9.1) are the only forces acting along the normal axis to the substrate. The classic DLVO theory therefore holds in the first approximation, and the particle can only be made to adhere to the substrate if the electrolyte concentration is larger than its critical coagulation value $c_{i0}^{\triangledown}$ given by (8.23).

Additionally, the decoupling between rotation and translation causes the leading-order drag force (9.5) to remain invariant if rotation about an axis parallel to the translation axis is enabled, $\beta = 0$. This effect is shown in figure 9.1(a,b) and can be explained in terms of the antisymmetry of the leading-order hydrodynamic pressure with respect to the axis $\theta = \pi/2 - \gamma$ or $\varphi = \pi/2$, for any value of γ, which cancels the effects of the rotational motion on the pressure along the $x-$axis.

Similarly, a hydrodynamic drift force (9.6) is also exerted on the sphere perpendicularly to its translation axis for $\beta \neq \pi/2$, which solely depends on the rotational velocity. This force can be of paramount importance in the study of the near-contact trajectories of particles and microorganisms. In particular, the hydrodynamic effect of the drift force in the case of corkscrew motion, $\beta = 0$, was found in earlier work by [15], to be responsible, when coupled to the corresponding drift force exerted on its flagella, for the circular swimming-path dynamics of *E. Coli* bacteria when they are close to a rigid boundary.

As shown further below, effects produced by the presence of a nearby deformable sticky substrate modify the conclusions derived from the rigid-wall case in that i) a lift force is induced as a result of a combined elastohydromolecular effect, ii) the forces no longer scale linearly with the velocities, iii) the drift force becomes dependent on the translational velocity as well, iv) the drag force does not remain invariant if corkscrew motion is enabled, and v) the limiting conditions for the onset of adhesion are not generally determined solely by the critical coagulation concentration.

9.2 Statics near deformable substrates: elastomolecular forces

In this Section, the much simpler problem of a stationary sphere standing off at some distance δ from the wall surface, which represents an effective zero-Reynolds number regime, is analyzed and used to exemplify the interaction of substrate-deformation effects with the intermolecular forces. Since there is no particle motion, $U = 0$ and $\Omega = 0$, the hydrodynamic pressure is zero in the gap region (i.e. the difference between the ambient

pressure and the absolute hydrodynamic pressure in the gap is zero). The van der Waals and electric forces, (9.1) and (9.1), need to be corrected to account for the substrate elasticity.

9.2.1 Elastomolecular force

The balance of electric and van der Waals forces upon the axisymmetric pseudo-hertzian static indentation of a sphere to an elastic infinite half-space, in the absence of fluid flow, is the subject of study of classical theories [35, 36]. For simplicity, fluid-drainage viscous effects during particle capture are neglected in this section. Thorough studies on the dynamics of two colliding soft spheres can be found elsewhere [37, 38], where use was also made of infinite half-space formulation and numerical solutions were sought. In this section, the analysis is restrained to a simple description of the quasi-static stability of the flat elastic layer, which leads to estimates of the parametric ranges for which the problem (8.11)-(8.12), subject to (8.42), may have a static solution under no fluid flow, and the reasoning serves to interpret the physical meaning of the elastohydromolecular lift components of its asymptotic series calculated in Subection 9.3.1 for the gliding sphere.

In the absence of fluid motion, the wall constitutive equation (8.42) becomes

$$H = \Delta_0^{el} \mathrm{e}^{-\kappa[h_0(r)+H-1]} - \frac{\Delta_0^{vdW}}{[h_0(r)+H]^3}. \tag{9.11}$$

In this section, H represents the wall surface deformation nondimensionalized with the minimum gap clearance δ. Equation (9.11) represents the equilibrium balance between the elastic, electric and van der Waals stresses on the substrate surface.

To unveil the influences of the substrate compliance effects, the asymptotic expansion of the surface deformation $H = H_0 + \Delta_0^{vdW} H_1 + \Delta_0^{vdW^2} H_2 + O(\Delta_0^{vdW^3})$, for $\Delta_0^{vdW} \ll 1$, is introduced in (9.11) by keeping the ratio of electric and van der Waals characteristic stresses $\Delta_0^{el}/\Delta_0^{vdW}$ as an order-unity parameter, which yields the elastomolecular force

$$\begin{aligned} F_z &= -\Delta_0^{vdW} + \frac{2\Delta_0^{el}}{\kappa} - \left(\Delta_0^{vdW} - \Delta_0^{el}\right)^2 - 3\Delta_0^{vdW^3} + \Delta_0^{vdW^2}\Delta_0^{el}(\kappa+6) \\ &- \Delta_0^{vdW^2}\Delta_0^{el^2}(2\kappa+3) + \kappa\Delta_0^{el^3} + O\left(\Delta_0^{vdW^4}, \Delta_0^{el^4}\right). \end{aligned} \tag{9.12}$$

In this formulation, F_z is nondimensionalized with the characteristic elastic force $\pi E(1-\nu)\delta^2 a/\ell(1+\nu)(1-2\nu)$. The first two terms in (9.12) represent the well-known van der Waals and electric double-layer forces (9.1) and (9.2) on a sphere near a rigid wall. The remaining are correction terms that correspond to perturbations introduced by the substrate elasticity, which show that the electric and van der Waals components of the intermolecular force are

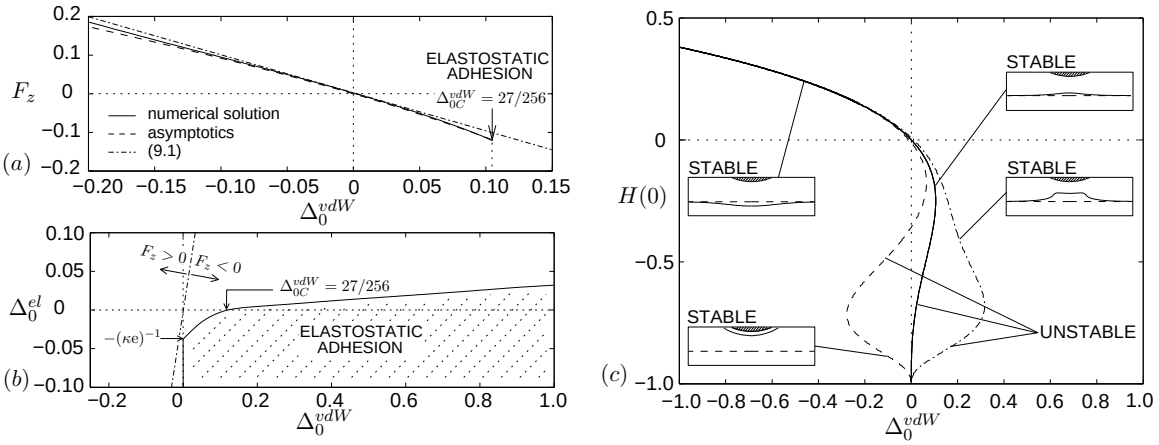

Figure 9.2: (a) Nondimensional static normal force on the sphere as a function of the van der Waals compliance for deionized solvents. (b) Map of static solutions, for a stationary sphere, in terms of the electric compliance Δ_0^{el} and the van der Waals compliance Δ_0^{vdW}; the hatched area denotes the occurrence of elastostatic adhesion or non-existence of a static solution, which represents an elastic instability produced by the unbounded attracting van der Waals or electric stresses, and is bounded by the critical compliance Δ_{0C}^{vdW} (solid line). The dot-dashed line denotes the compliance Δ_{0L}^{vdW} for $F_z = 0$. (c) Centerline elastic displacement of the substrate as a function of the van der Waals compliance for deionized solvents (solid line), repulsive (dot-dashed line) and attractive (dashed line) electric forces. Insets show typical radial deformation profiles in each branch. Calculations were performed here for $\kappa = 10$.

not generally additive when acting on a deformable wall. The asymptotic expression (9.12) is compared in figure 9.2(a) with the numerical solution of (9.11), for deionized solvents. It is noteworthy to mention that, according to (9.12), the first perturbation introduced by the deformable wall is to enhance the attracting effect in the case of attractive intermolecular forces ($\Delta_0^{vdW} > 0$ or $\Delta_0^{el} < 0$) due to an effective reduction on the gap size, and to suppress the effect of repulsion in the case of repulsive intermolecular forces ($\Delta_0^{vdW} < 0$ or $\Delta_0^{el} > 0$) due to an effective increase on the gap size. For $\Delta_{0L}^{vdW} \sim 2\Delta_0^{el}/\kappa$, the force on the sphere is zero in the first approximation. For $\Delta_0^{vdW} < \Delta_{0L}^{vdW}$, the force on the sphere is repulsive, and the opposite occurs for $\Delta_0^{vdW} > \Delta_{0L}^{vdW}$.

9.2.2 Surface bifurcations in the substrate: elastostatic adhesion

Further examination of (9.11) shows the existence of bifurcations in the solution of the displacement field. Particularizing (9.11) for attracting van der Waals forces $\Delta_0^{vdW} > 0$ and repulsive electric forces $\Delta_0^{el} > 0$, which may correspond to the most usual physical

configuration [20, 29, 21], shows that, as Δ_0^{vdW} increases, the elastic deformation towards the sphere side increases, reaching a turning point, at which the wall surface develops an unstable sharp cusp along the axis $r = 0$ that is representative of elastostatic adhesion or capture of the stationary particle by the elastic substrate for a minimum compliance $\Delta_{0C}^{vdW} = \Delta_{0C}^{vdW}(\Delta_0^{el}, \kappa)$, in the sense that no equilibrium solution of (9.11) exists for $\Delta_0^{vdW} > \Delta_{0C}^{vdW}$, as shown in figure 9.2(c). In this regime, the critical compliance Δ_{0C}^{vdW} increases with the electric-elastic stress ratio Δ_0^{el}, as observed in figure 9.2(b), and decreases with increasing κ, with $\Delta_{0C}^{vdW} = 27/256$ for deionized solvents $\Delta_0^{el} = 0$. For $\Delta_0^{vdW} < \Delta_{0C}^{vdW}$ with $\Delta_0^{vdW} > 0$, two equilibrium solutions of (9.11) may exist for the same value of Δ_0^{vdW}, with the low-strain solution being the stable solution. The high-strain solution is unstable, in that a small perturbation on the surface deformation towards the sphere side produces a steeper increment of the intermolecular traction stress compared with the corresponding increments undergone by the electric and internal restoring elastic stresses in the layer, so that the wall surface departs from static equilibrium and adhesion occurs with $H = -h_0(r)$. A similar description holds for the case of attractive van der Waals and electric forces, $\Delta_0^{vdW} > 0$ and $\Delta_0^{el} < 0$.

In the absence of van der Waals forces, $\Delta_0^{vdW} = 0$, elastostatic adhesion occurs for sufficiently attractive electric forces $\Delta_0^{el} < \Delta_{0C}^{el} = -1/\kappa\mathrm{e}$. For repulsive electric and van der Waals forces, $\Delta_0^{vdW} < 0$ and $\Delta_0^{el} > 0$, the elastic layer is always stable and a single equilibrium solution is obtained. For repulsive van der Waals forces and attractive electric forces, $\Delta_0^{vdW} < 0$ and $\Delta_0^{el} < 0$, three solutions may be obtained for the same value of Δ_0^{vdW} resembling a S-curve, with a stable low-strain branch in which repulsion dominates, an unstable middle-branch, and a stable high-strain solution in which there is a balance between attraction, repulsion and the elastic restoring force that places the flat layer at a short equilibrium distance from the sphere surface. Notice that complete elastostatic adhesion (i.e. mechanical disequilibrium of the substrate) is not possible in this configuration due to the strong singularity of the van der Waals repulsive stresses.

The intermolecular force asymptotic expansion (9.12) corresponds to the low-strained stable solutions of (9.11). It is noteworthy to mention that a particle free to move will not experience elastostatic adhesion for $\Delta_0^{vdW} < \Delta_{0L}^{vdW}$ since the net intermolecular force would be repulsive. For $\Delta_0^{vdW} > \Delta_{0L}^{vdW}$, the net intermolecular force on the particle is attractive, but it is not until the gap distance δ becomes sufficiently small, with $\Delta_0^{vdW} > \Delta_{0C}^{vdW}$, that the elastostatic adhesive mechanism sets in.

If the DLVO criterion (8.22) is used, adhesion by random perturbations of the

gap distance can occur if the electrolyte concentration is sufficiently large such that the energy barrier is small, as detailed in Section 8.2.1 and shown in figure 7.1. The critical ionic concentration for rapid coagulation of the sphere on the deformable substrate can be obtained by combining (8.22) and (9.12), which yields the system of equations

$$\begin{aligned} 1 \;-\; & \left(\frac{c_{i0}^{\nabla}}{c_i^{\nabla}}\right)^{1/2} (\kappa^{\nabla})^2 \mathrm{e}^{-(\kappa^{\nabla}-1)} + \Delta_{0\nabla}^{vdW}\left[\frac{1}{(\kappa^{\nabla})^4}\left(\frac{c_i^{\nabla}}{c_{i0}^{\nabla}}\right)^2 + \left(\frac{c_i^{\nabla}}{4c_{i0}^{\nabla}}\right)(\kappa^{\nabla})^2 \mathrm{e}^{-2(\kappa^{\nabla}-1)}\right. \\ & \left. - \left(\frac{c_i^{\nabla}}{c_{i0}^{\nabla}}\right)^{3/2} \frac{\mathrm{e}^{-(\kappa^{\nabla}-1)}}{\kappa^{\nabla}}\right] = O(\Delta_{0\nabla}^{vdw^2}), \\ 1 \;-\; & \left(\frac{c_{i0}^{\nabla}}{c_i^{\nabla}}\right)^{1/2} \kappa^{\nabla} \mathrm{e}^{-(\kappa^{\nabla}-1)} + \Delta_{0\nabla}^{vdW}\left[\frac{1}{5(\kappa^{\nabla})^4}\left(\frac{c_i^{\nabla}}{c_{i0}^{\nabla}}\right)^2 + \left(\frac{c_i^{\nabla}}{8c_{i0}^{\nabla}}\right)(\kappa^{\nabla}) \mathrm{e}^{-2(\kappa^{\nabla}-1)}\right. \\ & \left. - \left(\frac{c_i^{\nabla}}{c_{i0}^{\nabla}}\right)^{3/2} \frac{\mathrm{e}^{-(\kappa^{\nabla}-1)}}{\kappa^{\nabla}} m(\kappa)\right] = O(\Delta_{0\nabla}^{vdw^2}), \end{aligned} \tag{9.13}$$

where c_{i0}^{∇} is given by (8.23), and

$$m(\kappa) = -\frac{\kappa^2}{2}\mathrm{e}^{\kappa}\mathrm{Ei}(-\kappa) + \frac{1-\kappa}{2}, \tag{9.14}$$

with Ei the Exponential Integral function. In this formulation, $\Delta_{0\nabla}^{vdW}$ is based on $\delta = \delta_0^{\nabla}$. It can be shown that the expansions

$$\frac{c_i^{\nabla}}{c_{i0}^{\nabla}} = 1 - 0.053\Delta_{0\nabla}^{vdW} + O(\Delta_{0\nabla}^{vdw^2}), \tag{9.15}$$

$$\kappa^{\nabla} = 1 + 0.223\Delta_{0\nabla}^{vdW} + O(\Delta_{0\nabla}^{vdw^2}), \tag{9.16}$$

are asymptotic solutions of (9.13) for $\Delta_{0\nabla}^{vdw} \ll 1$. In particular, (9.15) represents the perturbation of the critical coagulation concentration (8.23) due to the substrate elasticity, and it shows that adhesion by electrolyte addition would occur at a lower concentration level in the hypothetical case that elastic instabilities are negligible, which represents a good approximation in the range of validity of (9.15), $\Delta_0^{vdW} \ll \Delta_{0\nabla}^{vdW} \ll 1$, and if $\Delta_{0\nabla}^{vdW} < \Delta_{0C\nabla}^{vdW}$. The value $\Delta_{0C\nabla}^{vdW}$ represents the van der Waals compliance for elastostatic adhesion evaluated at the DLVO critical coagulation conditions (8.22), and it can be obtained numerically by use of (9.11) and noticing that, in the first approximation, $\Delta_{0\nabla}^{vdW} = \Delta_{0\nabla}^{el}$ when $c_i^{\nabla} = c_{i0}^{\nabla}$ and $\kappa^{\nabla} = \kappa_0^{\nabla}$, from which $\Delta_{0C\nabla}^{vdW} = 0.452$. However, if $\Delta_{0\nabla}^{vdW} > \Delta_{0C\nabla}^{vdW}$ elastostatic adhesion occurs before the particle has surpassed the small energy barrier, and the corrected DLVO criterion (9.15) losses accuracy. Equation (9.15) is consistent with the fact that substrate-deformation effects increase the effective value of the attractive forces and decrease that of the repulsive forces.

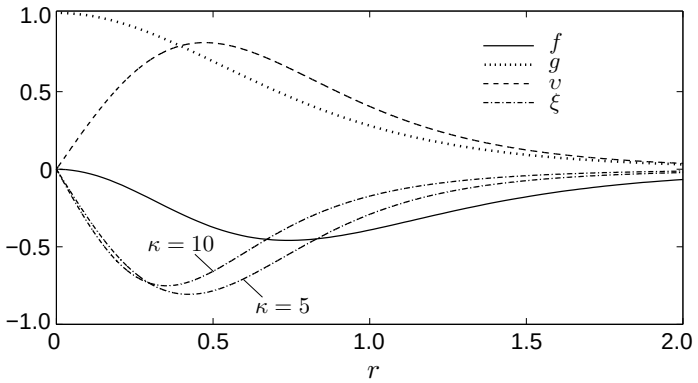

Figure 9.3: Functions f, g, υ and ξ obtained from the numerical integration of (9.21)-(9.24).

The onset of fluid flow by rotational or translational motion of the sphere produces a nonzero hydrodynamic pressure in the clearance, which alters the adhesion dynamics exposed in this section. These hydrodynamic effects are addressed in Section 9.4.

9.3 Dynamics near deformable substrates: elastohydromolecular forces

The compliance of the substrate couples the hydrodynamic field described by the Reynolds equation (8.11) with the substrate responses (8.42), (8.43) or (8.44), and with the intermolecular stress distributions (8.15) and (8.17). Such a coupling effect breaks the intrinsic symmetry of the Stokes equations (8.2)-(8.4), and renders the problems (8.2)-(8.4) and (8.11)-(8.12) nonlinear.

To second order in η, equation (8.11) becomes

$$r^2\frac{\partial^2 P_1}{\partial r^2}+\left[r+\frac{3r^3}{h_0(r)}\right]\frac{\partial P_1}{\partial r} \quad + \quad \frac{\partial^2 P_1}{\partial \varphi^2}=\frac{18}{5}\frac{r^3(6+r^2)}{h_0^5(r)}H_0\cos\varphi$$
$$+ \quad \frac{48}{5}\frac{r}{h_0^3(r)}\frac{\partial H_0}{\partial \varphi}\sin\varphi+\frac{12}{5}\frac{r^2(r^2-4)}{h_0^4(r)}\frac{\partial H_0}{\partial r}\cos\varphi. \quad (9.17)$$

Equation (9.17) is subject to boundary conditions (8.12). The case of a thin compressible layer (8.42) is addressed in detail in this section.

To leading order in η, equation (8.42) yields the normal surface deformation

$$H_0=P_0+\Pi_0^{vdW}+\Pi_0^{el}=\frac{6r\cos\varphi}{5h_0^2(r)}-\frac{\Upsilon}{h_0^3(r)}+\Xi \mathrm{e}^{-\kappa[h_0(r)-1]}. \quad (9.18)$$

Substituting this expression into the second-order balance Reynolds equation (9.17), the

equation

$$r^2\frac{\partial^2 P_1}{\partial r^2}+\left[r+\frac{3r^3}{h_0(r)}\right]\frac{\partial P_1}{\partial r}+\frac{\partial^2 P_1}{\partial \varphi^2}=\frac{72}{25}\frac{r^4(20+r^2)}{h_0^7(r)}\cos^2\varphi+\left\{\frac{18}{5}\frac{\Upsilon r^3(r^2-14)}{h_0^8(r)}\right.$$
$$\left.+\frac{12}{5}\frac{\Xi\kappa r^3(4-r^2)\mathrm{e}^{-\kappa[h_0(r)-1]}}{h_0^4(r)}+\frac{18}{5}\frac{\Xi r^3(6+r^2)\mathrm{e}^{-\kappa[h_0(r)-1]}}{h_0^5(r)}\right\}\cos\varphi-\frac{288}{25}\frac{r^2}{h_0^5(r)}, \tag{9.19}$$

is obtained. A particular integral of the form

$$P_1=f(r)\cos^2\varphi+[\Upsilon\upsilon(r)+\Xi\xi(r,\kappa)]\cos\varphi+g(r), \tag{9.20}$$

is substituted into (9.19), which yields the linear system of ordinary differential equations

$$\mathcal{L}_2 f = \frac{72}{25}\frac{r^4(20+r^2)}{h_0^7(r)}, \tag{9.21}$$

$$\mathcal{L}_1\upsilon = \frac{18}{5}\frac{r^3(r^2-14)}{h_0^8(r)}, \tag{9.22}$$

$$\mathcal{L}_1\xi = \frac{12}{5}\frac{\kappa r^3(4-r^2)\mathrm{e}^{-\kappa[h_0(r)-1]}}{h_0^4(r)}+\frac{18}{5}\frac{r^3(6+r^2)\mathrm{e}^{-\kappa[h_0(r)-1]}}{h_0^5(r)}, \tag{9.23}$$

$$\mathcal{L}_0 g+2f = -\frac{288}{25}\frac{r^2}{h_0^5(r)}, \tag{9.24}$$

with $\mathcal{L}_n$ a differential operator given by

$$\mathcal{L}_n=r^2\frac{d^2}{dr^2}+\left[r+\frac{3r^3}{h_0(r)}\right]\frac{d}{dr}-n^2,\quad \text{with}\quad n=0,1,2. \tag{9.25}$$

For $r\ll 1$, $f=O(r^2)$, $g=O(1)$, $\upsilon=O(r)$ and $\xi=O(r)$. Similarly, for $r\gg 1$, $f=O(r^{-8})$, $g=O(r^{-8})$, $\upsilon=O(r^{-11})$ and $\xi=O(\mathrm{e}^{-\kappa r^2}/r^3)$. Therefore, the boundary conditions of (9.21)-(9.24) are $f=\upsilon=\xi=0$ and $g'=0$ for $r=0$, and vanishing values of f, g, υ and ξ for large r. Figure 9.3 shows the solutions to (9.21)-(9.24), which need to be obtained numerically. Nonetheless, for later use, the auxiliary function $\sigma=2g+f$ is defined by combining equations (9.21) and (9.24). It can be shown that the resulting differential equation has the exact solution

$$\sigma=2g+f=\frac{18}{125}\frac{(14-5r^2)}{h_0^5(r)},\quad \text{with}\quad \int_0^\infty \sigma r dr=\frac{48}{125}. \tag{9.26}$$

The dimensionless hydromolecular pressure perturbation is given by

$$\begin{aligned}P_1^\bigstar &= P_1+\Pi_1^{vdW}+\Pi_1^{el}\\ &= f(r)\cos^2\varphi+\left\{\Upsilon\left[\upsilon(r)+\frac{18r}{5h_0^6(r)}\right]+\Xi\left[\xi(r,\kappa)-\frac{6r\kappa\mathrm{e}^{-\kappa[h_0(r)-1]}}{5h_0^2(r)}\right]\right\}\cos\varphi\\ &+ g(r)-\frac{3\Upsilon^2}{h_0^7(r)}-\kappa\Xi^2\mathrm{e}^{-2\kappa[h_0(r)-1]}+\Xi\Upsilon\left\{\frac{\mathrm{e}^{-\kappa[h_0(r)-1]}}{h_0^3(r)}\left[\frac{3}{h_0(r)}+\kappa\right]\right\},\end{aligned} \tag{9.27}$$

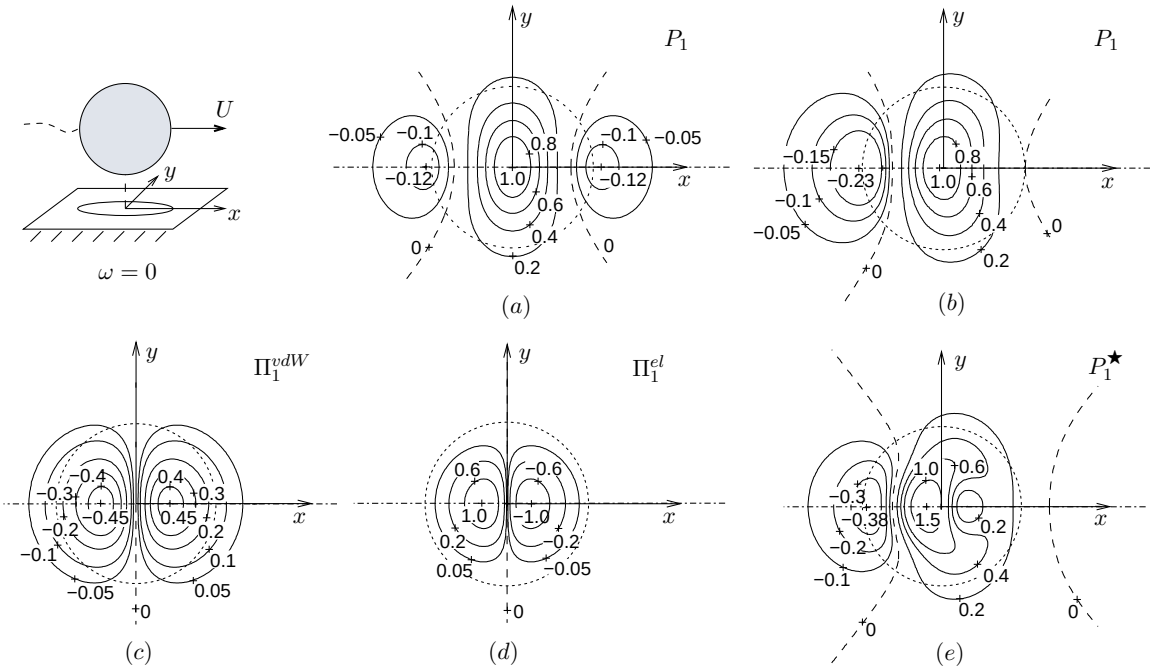

Figure 9.4: Second-order pressure and stress contours for purely translational motion. The figure shows (a) the hydrodynamic pressure disturbance in the absence of intermolecular effects, $\Xi = \Upsilon = 0$, and the influences of intermolecular effects, with $\Xi = \Upsilon = 0.5$, on (b) the hydrodynamic pressure, (c) van der Waals stress, (d) electric stress and (e) hydromolecular pressure perturbations. The dotted line represents a circle of spatial unit radius.

where use has been made of (8.53), (8.54), (9.18) and (9.20). Since $P_1^{\bigstar}$ decays sufficiently rapidly for large r, the calculation of the force and torque perturbations thereby is not a singular perturbation problem, in that the required indefinite integrals of the hydromolecular pressure perturbation are convergent for large r.

Figures 9.4 and 9.5 show the contours of the first perturbations of the hydrodynamic pressure (9.20), the hydromolecular pressure (9.27), and of the intermolecular stresses (8.53) and (8.54), nondimensionalized with $\mu U a^{1/2}/\delta^{3/2}$ to illustrate the rotational effects. The substrate compliance decreases and increases the hydrodynamic overpressure and underpressure levels respectively, which breaks the antisymmetry of the leading-order hydrodynamic pressure contours and induces a lift force, and drag-force and drift-force perturbations. It is noteworthy to mention that the corkscrew rotation actively affects the pressure component of the drag force, as observed by comparing the projection along the x-axis of the contours in figures 9.4 and 9.5 and superposing them onto those shown in figure 9.1.

The shear-stress perturbations can be obtained by differentiating the second term

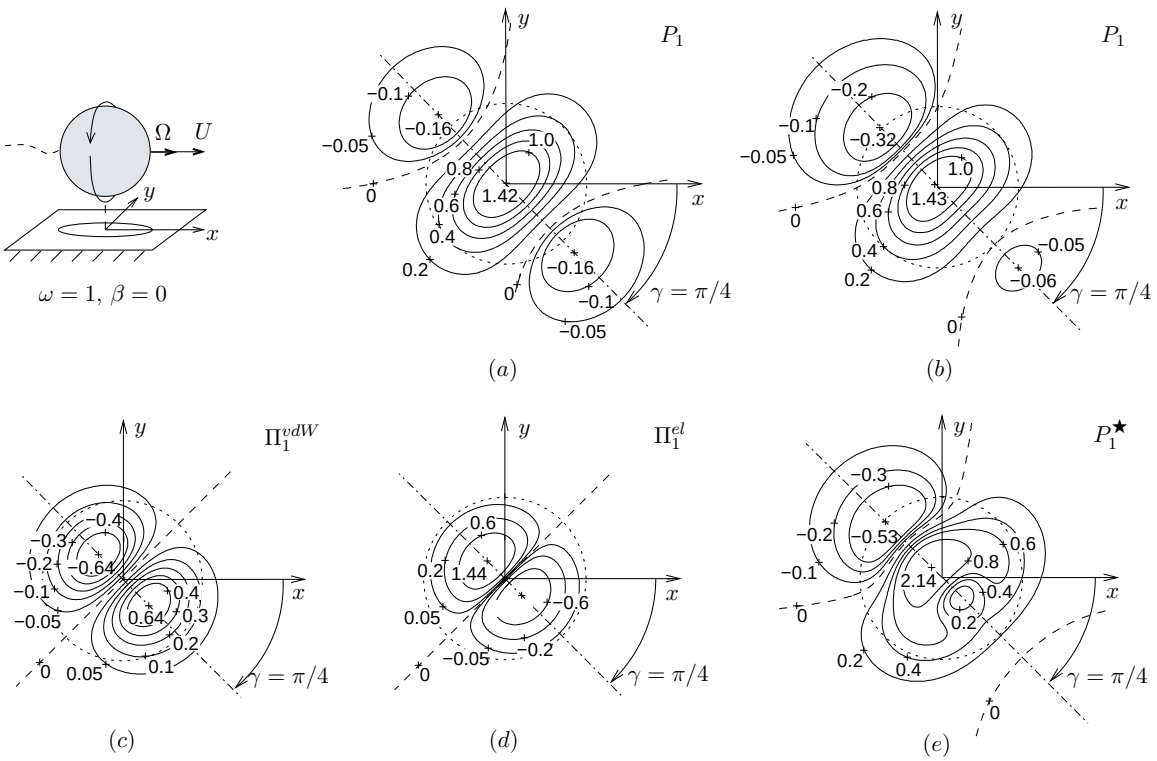

Figure 9.5: Second-order pressure and stress contours for corkscrew motion. The figure shows (a) the hydrodynamic pressure disturbance in the the absence of intermolecular effects, $\Xi = \Upsilon = 0$, and the influences of intermolecular effects, with $\Xi = \Upsilon = 0.5$, on (b) the hydrodynamic pressure, (c) van der Waals stress, (d) electric stress and (e) hydromolecular pressure perturbations. The dotted line represents a circle of spatial unit radius.

of the expansion of (8.13) and (8.14) in powers of η_0, which yields

$$\begin{aligned}
\tau_{rz1} &= \frac{\partial v_{r1}}{\partial z}\Big|_{z=h_0(r)} = \left[\frac{12r(4-r^2)}{25h_0^5(r)} + \frac{h_0(r)}{2}\frac{df(r)}{dr}\right]\cos^2\varphi \\
&+ \left\{\frac{\Upsilon}{h_0^5(r)} - \frac{\Xi \mathrm{e}^{-\kappa[h_0(r)-1]}}{h_0^2(r)}\right\}\frac{2\cos(\varphi-\gamma)}{\mathcal{V}(\omega,\beta)} + \left\{\frac{2\Xi(4-r^2)\mathrm{e}^{-\kappa[h_0(r)-1]}}{5h_0^3(r)} + \frac{2\Upsilon(r^2-4)}{5h_0^6(r)}\right. \\
&+ \left.\frac{h_0(r)}{2}\left[\Upsilon\frac{dv(r)}{dr} + \Xi\frac{\partial\xi(r,\kappa)}{\partial r}\right]\right\}\cos\varphi - \frac{12r\cos\varphi\cos(\varphi-\gamma)}{5h_0^4(r)\mathcal{V}(\omega,\beta)} + \frac{h_0(r)}{2}\frac{dg(r)}{dr},
\end{aligned} \tag{9.28}$$

and

$$\begin{aligned}
\tau_{\varphi z1} &= \frac{\partial v_{\theta 1}}{\partial z}\Big|_{z=h_0(r)} = -\left[\frac{48r}{25h_0^4(r)} + \frac{h_0(r)f(r)}{r}\right]\sin\varphi\cos\varphi \\
&+ \left\{\frac{8\Upsilon}{5h_0^5(r)} - \frac{8\Xi\mathrm{e}^{-\kappa[h_0(r)-1]}}{5h_0^2(r)} - \frac{[\Upsilon v(r) + \Xi\xi(r,\kappa)]h_0(r)}{2r}\right\}\sin\varphi \\
&+ \left[\frac{\Xi\mathrm{e}^{-\kappa[h_0(r)-1]}}{h_0^2(r)} - \frac{\Upsilon}{h_0^5(r)}\right]\frac{2\sin(\varphi-\gamma)}{\mathcal{V}(\omega,\beta)} + \frac{12r\cos\varphi\sin(\varphi-\gamma)}{5h_0^4(r)\mathcal{V}(\omega,\beta)},
\end{aligned} \tag{9.29}$$

where use has been made of (9.18) and (9.20).

The values of the forces obtained from the analytical integration of (9.27)-(9.29) are compared in what follows to the numerical solution of the problem (8.11)-(8.12) and (8.42), which was integrated by using a second-order finite-differences numerical scheme. In this investigation, torques are not calculated since they are found to be of $O(\epsilon\eta_0)$, which correspond to higher-order effects that are not considered here.

9.3.1 Lift force

Integrating the asymptotic expansion of the hydromolecular pressure (9.27) over the vertical projection of the inner element of the surface of the sphere in cylindrical coordinates, $\mathbf{d}\boldsymbol{S}_z = -a^2\epsilon r dr \mathrm{d}\varphi \boldsymbol{e_z}$, and using expressions (9.26), the elastohydromolecular lift force

$$\begin{aligned} F_z &= \frac{\mu U \mathcal{V}(\omega,\beta) a}{\epsilon^{1/2}} \int_0^{\infty}\int_0^{2\pi} P_1^{\bigstar} r dr d\varphi \\ &= \frac{\pi\mu U \mathcal{V}(\omega,\beta) a}{\epsilon^{1/2}} \Bigg\{ -\Upsilon + \frac{2\Xi}{\kappa} + \eta_0 \left[\frac{48}{125} - (\Upsilon - \Xi)^2 \right] \\ &+ O(\eta_0^3, \eta_0^3\Upsilon^2, \eta_0^3\Xi^2, \eta_0^3\Upsilon\Xi, \eta_0^3\Upsilon^2\Xi^2, \eta_0^3\Upsilon\Xi^3, \eta_0^3\Upsilon^3\Xi) \Bigg\} \end{aligned} \tag{9.30}$$

is obtained. It can be shown that the contribution of the viscous shear stresses to the lift force is of order $\epsilon\eta_0 \ll \eta_0$ [13], which is neglected in this analysis. The lift force (9.30) is composed of two leading-order terms that represent the values (9.1) and (9.1) of the intermolecular forces on a small sphere near a rigid wall. These are the two fundamental forces acting in the DLVO theory. The lift force also includes a term $48\eta_0/125$, that corresponds to the positive elastohydrodynamic lift force [12, 13]. The squared bracketed term $-(\Upsilon - \Xi)^2$ represents a negative elastomolecular lift force that is a nonlinear superposition of intermolecular effects; this force corresponds to the disturbance of the intermolecular force on a stationary sphere induced by the soft substrate, as shown in Section 9.2 by the second-order term of (9.12). Higher-order terms result from a full elastohydromolecular coupling and involve combinations of the hydrodynamic and intermolecular compliances, such that the resulting dimensionless groups are proportional to even powers of the velocity; the expansion of the lift force remains kinematically irreversible to every order, in that its direction is independent of the direction of rotation and translation.

To leading order in η_0, only the DLVO force, which origin is purely related to the intermolecular stresses and not hydrodynamically enhanced, acts on the particle along the $z-$axis; this force is kinematically irreversible, although the flow is still Stokesian in a linear

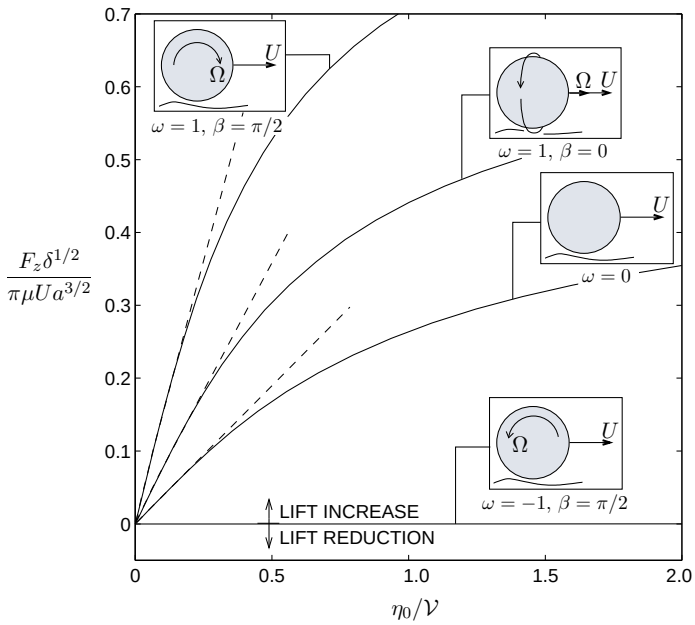

Figure 9.6: Influences of rotation ω and azimuth angle of rotation β on the lift force (9.30) in the absence of intermolecular forces, $\Xi = \Upsilon = 0$. The numerical and asymptotic solutions are shown in solid and dashed lines respectively.

sense. For non-zero η_0, the existence of a kinematically-irreversible lift force of elastohydromolecular origin is explained in terms of the nonlinearity induced by the substrate compliance and intermolecular effects. Nonlinear effects in Stokes-type flows can be produced by small convective disturbances in the flow [16, 17], non-Newtonian fluid behaviors [19] or electrokinetic effects [18], all of which induce kinematically-irreversible forces on submerged particles and are important in certain range of rheological applications. In this model, the elastohydromolecular lift force is produced by the combined action of the intermolecular and hydrodynamic stresses on the substrate, which ultimately modify the compliant gap geometry and the hydrodynamic flow through that region as shown by the contours of the pressure and stress disturbances in figures 9.4 and 9.5.

Influences of rotation and of rotation-axis orientation on the lift force

Rotational motions distort the magnitude and orientation of the pressure distribution in the gap and also modify the gap geometry, as observed in figure 9.5. To isolate the rotational effects, the lift force (9.30) is nondimensionalized independently of the velocity scale $\mathcal{V}(\omega, \beta)$, and expressed as a function of the translational hydrodynamic compliance $\eta_0/\mathcal{V}(\omega, \beta)$ as shown in figure 9.6, where intermolecular effects have been neglected for il-

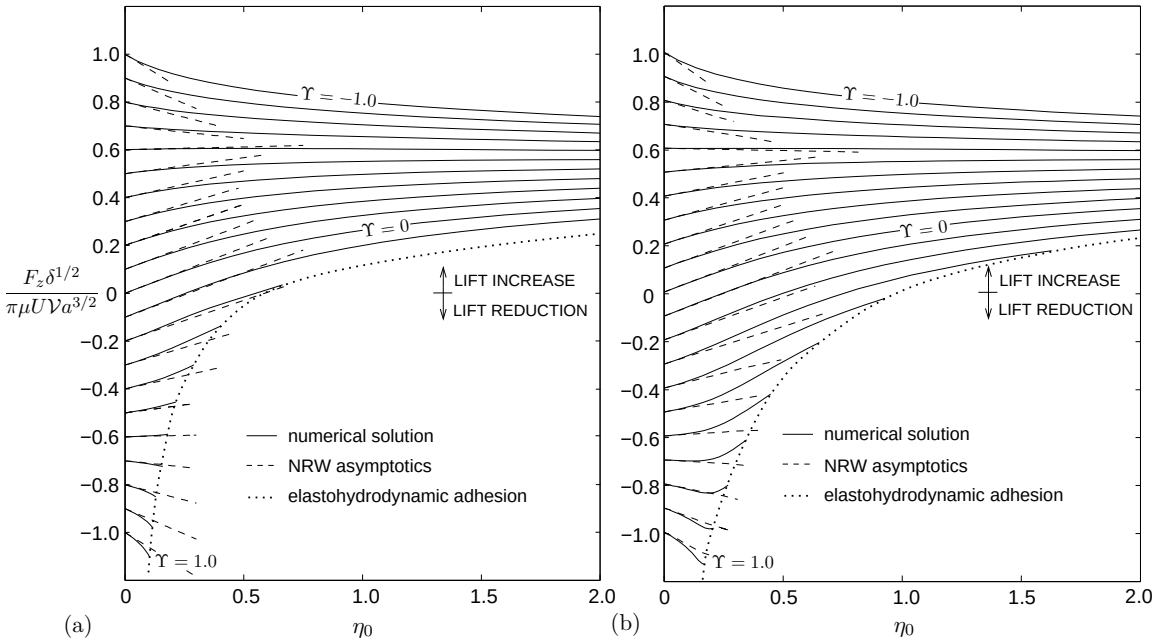

Figure 9.7: Dimensionless elastohydromolecular lift force on the sphere, for any rotation rate and rotation axis orientation, as a function of the hydrodynamic compliance η_0 for $-1 \leq \Upsilon \leq 1$, with an interval step $\Delta\Upsilon = 0.1$ between lines, for (a) deionized solvents, $\Xi = 0$, and (b) ionized solvents with $\Xi = 0.035$ (electric repulsion) and $\kappa = 10$. The dotted envelope line represents the values for elastohydrodynamic adhesion, beyond which no solution of (8.11)-(8.12) and (8.42) was found because of a loss of static mechanical equilibrium on the substrate surface.

lustrative purposes. As advanced in a previous study [13], the inverse purely rolling motion ($\omega = -1$, $\beta = \pi/2$) completely suppresses the production of elastohydrodynamic lift force, since a local Couette flow is induced in the gap, and the hydrodynamic pressure becomes zero to every order of η_0. That is not the case when the intermolecular forces are not negligible, since both the leading-order intermolecular and second-order elastomolecular contributions to the lift force are present in (9.30). Similarly, the present formulation reveals that, for the same translational velocity, particle dimensions and substrate mechanical properties, the purely rolling motion ($\omega = 1$, $\beta = \pi/2$) produces a larger lift force than the corkscrew ($\omega = 1$, $\beta = 0$) and translational ($\omega = 0$) motions; during the rolling motion, the fluid entrainment of the combined rotation and translation are aligned along the $\theta = 0$ axis and both effects more strongly synergize causing a larger positive overpressure peak in the gap and therefore larger substrate deformations. In this model, no negative values of the elastohydrodynamic lift force were found for any combination of rotation and translation.

Influences of intermolecular effects on the lift force

Figure 9.5 shows that the intermolecular stresses produced by the electric and van der Waals forces disturb the compliant wall and modify the net normal stress acting on the sphere. The influences of these intermolecular effects on the lift force are shown in figure 9.7, which value is independent of ω and β. For negative and order-unity values of Υ, or more precisely $\Upsilon \lesssim -(48/125)^{1/2}$, which correspond to order-unity and repulsive van der Waals forces, the lift force decreases with increasing η_0 due to the gap-distance-augmentation effect outlined in Section 9.2, by which the repulsion decreases because of the increase of the substrate compliance and the effective clearance, which dominates the elastohydrodynamic force that typically increases with increasing η_0. For smaller but still repulsive van der Waals forces, $-(48/125)^{1/2} \lesssim \Upsilon < 0$, the lift force is positive and increases with η_0. Slightly attractive van der Waals forces produce negative lift forces on the sphere up to a resuspension or lift-off hydrodynamic compliance η_{0L}, beyond which the elastohydrodynamic effect dominates and a positive lift force occurs. This increase proceeds up to a critical hydrodynamic compliance η_{0C} for the occurrence of irreversible elastohydrodynamic adhesion, in that no solution of the problem (8.11)-(8.12) and (8.42) is found beyond η_{0C} at constant Υ because of a loss of static mechanical equilibrium on the substrate surface. Positive and order-unity values of Υ, which correspond to large and attractive van der Waals forces, enhance earlier irreversible elastohydrodynamic adhesion. The lift-off and elastohydrodynamic adhesion processes are addressed in detail in Section 9.4, and a similar but simpler adhesion phenomenon is exemplified in Section 9.2 for a stationary sphere. Solvent ionization and electric repulsion augment the lift force, decrease the magnitude of the lift-off hydrodynamic compliance, and extend the irreversible elastohydrodynamic adhesion boundary to larger η_{0C} by electrically stabilizing the substrate surface.

9.3.2 Drag-force and drift-force first-order perturbations

The perturbations of the drag and drift forces on the sphere are calculated as

$$\begin{aligned} F_{x1} &= -\mu U \mathcal{V} a \eta_0 \int_0^{2\pi} \int_0^{\infty} \left[P_1^{\bigstar} r^2 \cos(\varphi - \gamma) + \tau_{rz1} r \cos(\varphi - \gamma) - \tau_{\varphi z1} r \sin(\varphi - \gamma) \right] dr d\varphi \\ &= \pi \mu U a \eta_0 \Big\{ \Xi \left[\mathcal{E}(\kappa) + \mathcal{J}(\kappa) \omega \sin\beta \right] - \Upsilon \left[\mathcal{F} - \mathcal{G} \omega \sin\beta \right] + O(\eta_0^2, \eta_0 \Upsilon^2, \eta_0 \Xi^2, \eta_0 \Xi \Upsilon) \Big\}, \end{aligned} \tag{9.31}$$

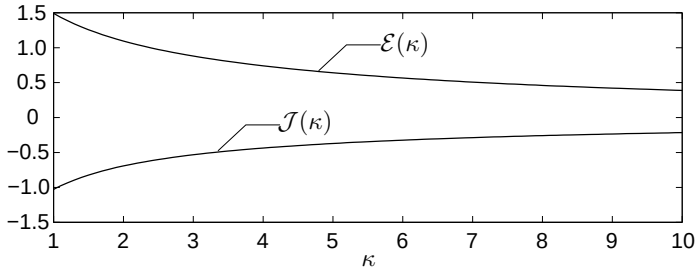

Figure 9.8: Drag and drift coefficients (9.33) of the electric force.

and

$$\begin{aligned} F_{y1} &= -\mu U\mathcal{V}a\eta_0\int_0^{2\pi}\int_0^{\infty}\Big[P_1^{\bigstar}r^2\sin(\varphi-\gamma)+\tau_{rz1}r\sin(\varphi-\gamma)+\tau_{\varphi z1}r\cos(\varphi-\gamma)\Big]\,dr d\varphi \\ &= -\pi\mu U a\eta_0\Big\{\omega\cos\beta\,[\Upsilon\mathcal{G}+\Xi\mathcal{J}(\kappa)]+O(\eta_0^2,\eta_0\Upsilon^2,\eta_0\Xi^2,\eta_0\Xi\Upsilon)\Big\}, \end{aligned} \tag{9.32}$$

where the electric force coefficients $\mathcal{E}(\kappa)$ and $\mathcal{J}(\kappa)$ are given by

$$\begin{aligned} \mathcal{E}(\kappa) &= 2-\frac{6\kappa}{5}+(6\kappa-4)\,\frac{\kappa}{5}\mathrm{e}^{\kappa}\mathrm{Ei}(-\kappa)-\frac{1}{2}\int_0^{\infty}\xi(r,\kappa)r^2\mathrm{d}r, \\ \mathcal{J}(\kappa) &= -2-\frac{6\kappa}{5}-\frac{\kappa}{5}(6\kappa+16)\mathrm{e}^{\kappa}\mathrm{Ei}(-\kappa)+\frac{1}{2}\int_0^{\infty}\xi(r,\kappa)r^2\mathrm{d}r, \end{aligned} \tag{9.33}$$

which are shown in figure 9.8, and with the van der Waals force coefficients $\mathcal{F}$ and $\mathcal{G}$ given by

$$\mathcal{F}=\frac{17}{25}+\frac{1}{2}\int_0^{\infty}\upsilon(r)r^2dr=0.9905,\quad\text{and}\quad\mathcal{G}=\frac{8}{25}-\frac{1}{2}\int_0^{\infty}\upsilon(r)r^2dr=0.0095. \tag{9.34}$$

The drag-force and drift-force perturbations are composed of two terms of $O(\eta_0\Upsilon)$ and $O(\eta_0\Xi)$: the the van der Waals and electric drag/drift forces. These are representative of the forces induced by mixed elastohydromolecular effects. Higher-order terms involve combinations of the hydrodynamic and intermolecular compliances, such that the resulting dimensionless groups are proportional to odd powers of the velocity; the expansions of the drag and drift force remain kinematically reversible to every order, in that their direction changes under gliding direction reversal. It is noteworthy to mention that, if the intermolecular effects are negligible, $\Upsilon=\Xi=0$, the substrate-deformation effects on the drag and drift forces become of $O(\eta_0^2)$ for $\eta_0\ll 1$, which cannot be analytically captured by solely retaining the order $O(\eta_0)$ terms in the expansions (9.31) and (9.32).

Influences of rotation and of rotation-axis orientation on the drag-force disturbance

Figure 9.9 shows the effects of the rotation ω and the azimuthal orientation β of the rotation axis on the disturbance of the drag force, obtained by numerical integration of (8.11)-(8.12) and (8.42), in the absence of intermolecular forces, $\Upsilon = \Xi = 0$. The substrate compliance reduces the leading-order drag force (9.5) because of a decrease in the hydromolecular pressure and viscous shear stresses in the deformed gap region. The inverse purely rolling motion ($\omega = -1$, $\beta = \pi/2$) completely suppresses the elastohydrodynamic drag force disturbance, since no deformation is produced in this case. For the same translational velocity, particle dimensions and substrate mechanical properties, the purely rolling motion ($\omega = 1$, $\beta = \pi/2$) produces a larger drag force reduction than the corkscrew ($\omega = 1$, $\beta = 0$) and translational ($\omega = 0$) motions. For $\eta_0 = O(1)$, the elastohydrodynamic drag force disturbance produced by surface-deformation effects is approximately $6\ln(1/\epsilon)$ times smaller than the leading-order force (9.5), which, as a maximum, represents a 5 to 10% drag reduction for $\epsilon = 0.1$. It must be emphasized that the rotational and translational motions are nonlinearly coupled as in the corkscrew motion, for which rotation about an axis parallel to the translation axis induces an additional drag reduction; this nonlinear effect departs from the decoupled behaviour of the rotational and translational motions observed in the leading-order drag force (9.5), which is typical of linear viscous flows. In this model, no negative values of the elastohydrodynamic drag-force disturbance were found for any combination of rotation and translation.

Influences of the intermolecular effects on the drag-force disturbance

The influences of the intermolecular effects on the drag force disturbance on the sphere are shown in figure 9.10. For negative values of Υ, which correspond to repulsive van der Waals forces, the drag-force disturbance increases with η_0, which results in an additional drag reduction to that solely produced by substrate-deformation effects. Slightly attractive van der Waals forces, $\Upsilon \ll 1$, produce a drag increase on the sphere up to a critical compliance, beyond which the elastohydrodynamic effect dominates and a drag reduction occurs. Positive and order-unity values of Υ, which correspond to large and attractive van der Waals forces enhance irreversible elastohydrodynamic adhesion. Electric repulsion augments the drag-reduction trend, and extend the elastohydrodynamic adhesion boundary to larger η_0.

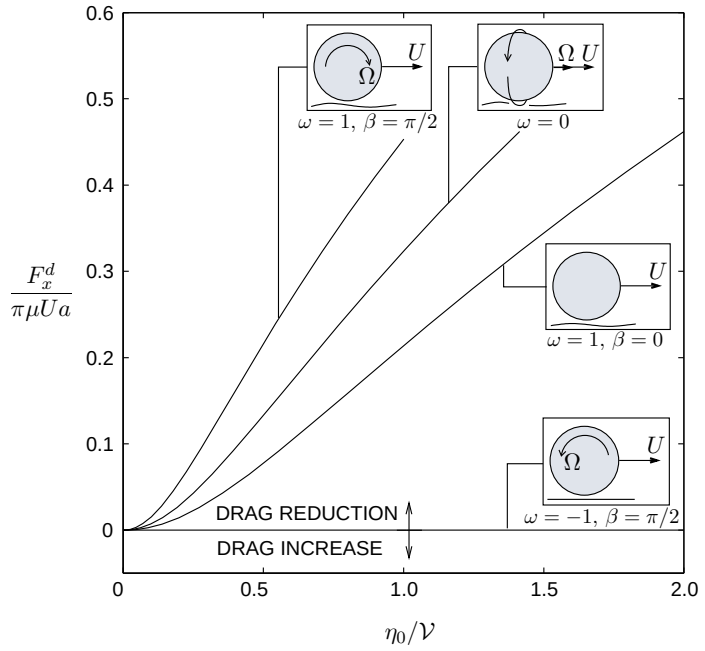

Figure 9.9: Influences of rotation ω and azimuth angle of rotation β on the drag force disturbance, obtained by numerical integration of (8.11)-(8.12) and (8.42), in the absence of intermolecular forces, $\Upsilon = \Xi = 0$.

Influences of the intermolecular effects on the drift-force disturbance

Substrate-deformation effects are found to play a very weak role on the drift force. For a stationary rotating sphere near a soft substrate, $\omega \to \infty$, $U \to 0$, this can be explained in terms of the mutual cancellation of the two following effects: a hydrodynamic overpressure decrease in the gap region, which increases the drift, and the loss of traction due to the viscous shear-stress decrease in the same region, which reduces the drift force; both effects are found to be of the same magnitude in the range of hydrodynamic compliances η_0 studied in this analysis, which yields a negligibly small drift disturbances with respect to the leading-order force (9.6). Nonetheless, the formula (9.32) predicts a drift reduction and increase due to electric repulsion and van der Waals forces respectively, both of which actively modify the shear stress distribution in the gap and the viscous-traction efficiency.

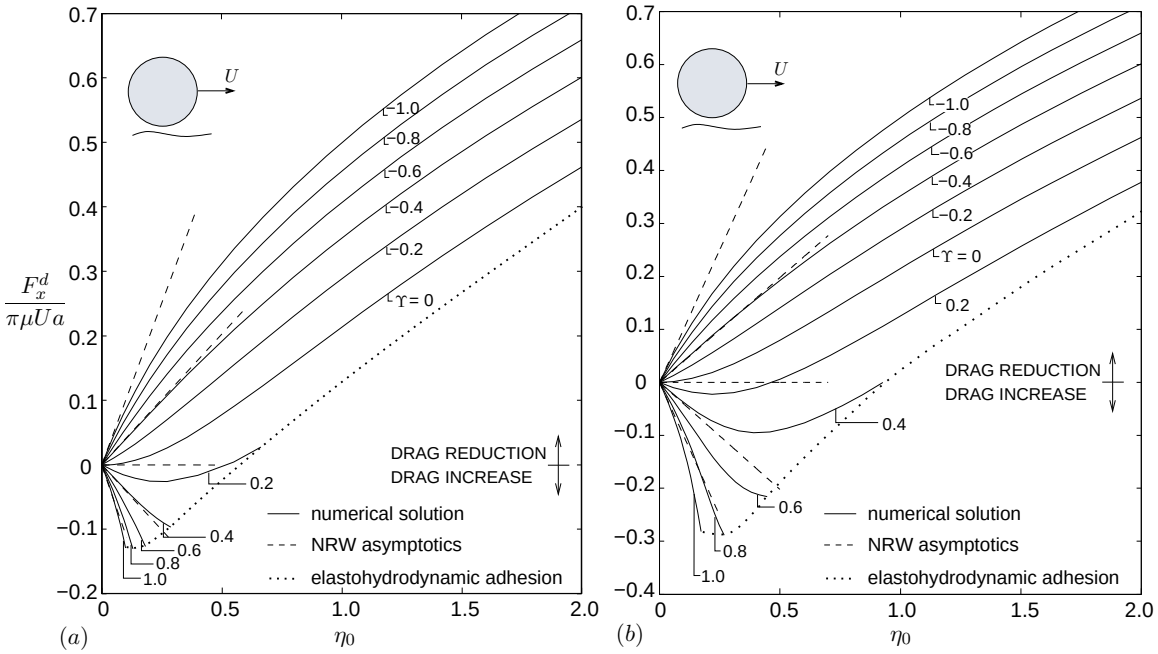

Figure 9.10: Dimensionless elastohydromolecular drag force disturbance on a translating sphere as a function of the hydrodynamic compliance η_0 for $-1 \leq \Upsilon \leq 1$, for (a) deionized solvents, $\Xi = 0$, and (b) ionized solvents with $\Xi = 0.035$ (electric repulsion) and $\kappa = 10$. The dotted envelope line represents the values for hydrodynamic adhesion, beyond which no numerical solution of (8.11)-(8.12) and (8.42) was found because of a loss of static mechanical equilibrium on the substrate surface.

9.4 Elastohydrodynamic adhesion and lift-off

A characteristic lift-off compliance, η_{0L}, can be defined as the value for which the lift force becomes zero,

$$\eta_{0L} \approx \left\{ \frac{125}{48} \left[\Delta_0^{vdW} - \frac{2\Delta_0^{el}}{\kappa} + \left(\Delta_0^{vdW} - \Delta_0^{el} \right)^2 \right] \right\}^{1/2}, \tag{9.35}$$

which is representative of reversible adhesion on the substrate; for $\eta_0 = \eta_{0L}$ the particle can undergo lateral motions along the substrate surface. For a given set of intermolecular parameters and particle dimensions, the lift-off hydrodynamic compliance can be achieved by sufficiently large gliding velocities or substrate compliances.

For $\eta_0 < \eta_{0L}$, the lift force on the particle is negative, and irreversible elastohydrodynamic adhesion occurs for sufficiently large Δ_0^{vdW}. This adhesion mechanism is due to surface instabilities on the substrate, and however qualitatively similar to the elastostatic adhesion mechanism for a stationary sphere presented in Section 9.2, here the hydrodynamic pressure plays an important role on the stabilization of the surface. The limiting values for

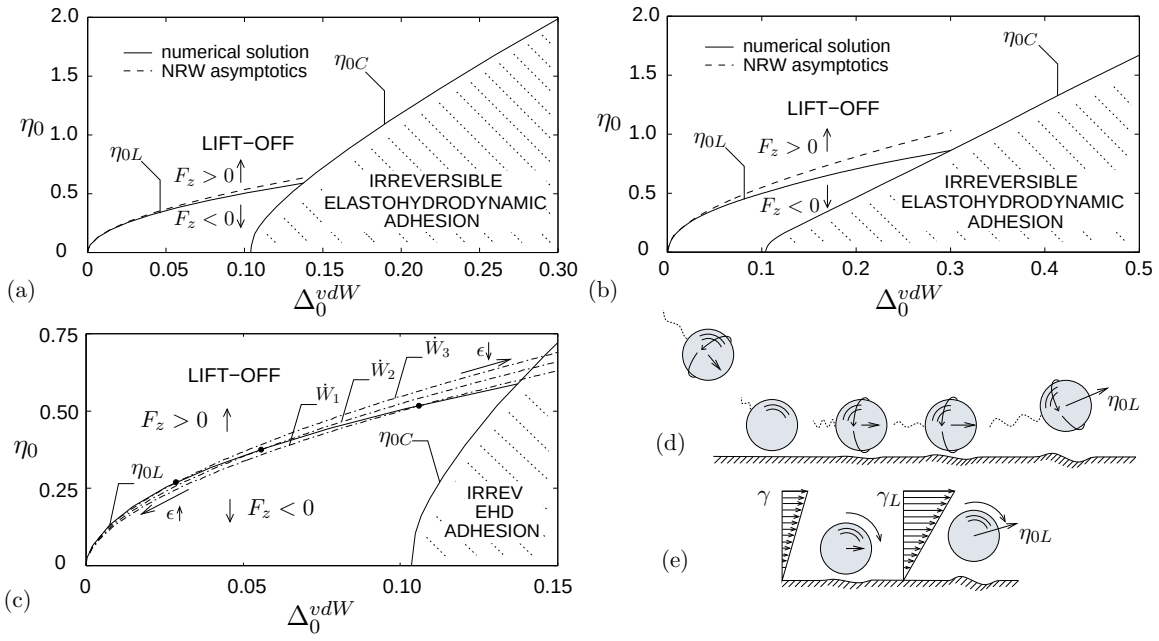

Figure 9.11: Lift-off and critical hydrodynamic compliances for elastohydrodynamic adhesion as a function of the van der Waals compliance, for (a) deionized solvents, $\Xi = 0$, and (b) ionized solvents with $\Xi = 0.035$ (electric repulsion) and $\kappa = 10$. (c) Gliding-power $\dot{W}$ isolines (dot-dashed lines) in deionized solvents, with $\dot{W}_1 < \dot{W}_2 < \dot{W}_3$. The figure also shows two examples of migration mechanisms on a soft and sticky substrate: (d) Swimming-induced migration: a slow swimmer gets entrapped in an accessible potential minimum as it approaches the substrate surface, from where it escapes when the lift-off velocity η_L is achieved. (e) Shear-induced migration: a particle close to the substrate migrates under the action of sufficiently high shear rates γ_L.

irreversible elastohydrodynamic adhesion are given by the critical hydrodynamic compliance η_{0C}, which needs to be calculated numerically, and which depends on the intermolecular compliances as shown in figure 9.11(a,b). For $\eta_0 > \eta_{0L}$, the lift force is positive, but irreversible elastohydrodynamic adhesion is not fully prevented since the substrate becomes softer and more unstable as η_0 increases.

That adhesion can occur for positive lift forces may seem a counter-intuitive result, especially if comparison to the stationary-sphere case in Section 9.2 is made, since elastostatic adhesion always occurs there for net attractive intermolecular forces. This concept can be explained by use of figure 9.7 where, by holding Υ and Ξ constant and varying η_0, effects induced solely by the substrate softness can be extracted: irreversible elastohydrodynamic adhesion events for $F_z > 0$ observed in figure 9.7 show that sufficiently large compliances destabilize the substrate surface for a given gliding velocity, particle dimensions, gap distance and intermolecular intensity, and promote adhesion by decreasing the

strength of the restoring elastic stress. Similarly, effects induced solely by the gliding velocity can be extracted by keeping Δ_0^{vdW} constant in figure 9.11(a,b) and varying η_0 along a vertical line: sufficiently small gliding velocities enhance elastohydrodynamic adhesion by hydrodynamically destabilizing the substrate surface for a given substrate compliance, gap distance, particle dimensions and intermolecular intensity. An increase in the repulsive electric force decreases the extent of the hydrodynamic adhesion region, as shown in figure 9.11(b), by exerting a stabilizing compressive stress on the substrate surface. The irreversible elastohydrodynamic adhesion mechanism can occur in ionized and deionized solvents. In deionized solvents there is no spontaneous electrical interaction; therefore elastohydrodynamic adhesion cannot be described by the classic DLVO theory.

It is worth emphasizing that the reversible elastohydrodynamic regime $\eta_0 = \eta_{0L}$ corresponds to a stable regime in a dynamic lift-off process at constant gliding power $\dot{W}$ under small quasi-static perturbations of the gap distance. An iso-power gliding trajectory $\dot{W} = F_{x0}U$ =const., on a $\{\eta_0, \Delta_0^{vdW}\}$ plane, is given by

$$\eta_0 \sim C_1 \Delta_0^{vdW^{5/8}} [\ln(\Delta_0^{vdW^{1/4}}/C_2)]^{-1/2} \tag{9.36}$$

for deionized solvents, where $C_1 = f(\dot{W}) = O(1)$ and $C_2 = O(\epsilon \Delta_0^{vdW^{1/4}}) = O(\Delta_{0a}^{vdW^{1/4}}) \ll 1$ are two constants, with $\Delta_{0a}^{vdW^{1/4}}$ the van der Waals compliance based on a gap distance of $O(a)$. A necessary requirement for (9.36) to be accurate is that $\Delta_0^{vdW^{1/4}} \gg C_2$, since $\epsilon = O(1)$ when $\Delta_0^{vdW^{1/4}} = O(C_2)$. As shown in figure 9.11(c), a small decrease of the minimum gap clearance δ below its lift-off value induces a positive lift force, which returns the particle to its initial vertical position above the substrate. However, a sufficiently large perturbation of the particle position towards the substrate can induce irreversible elastohydrodynamic adhesion. Similarly, an increase of the minimum gap clearance above its lift-off value induces a positive lift force, which returns the particle to its initial vertical position above the substrate. This stable equilibrium is similar to that found for ionized solvents in the DLVO secondary minimum, from which particles and microorganisms are believed to be able to escape from the potential well due to van der Waals retardation effects at large gap distances [20, 21]. Similar dynamics are found for constant-force trajectories. Based on these results, a reversible adhesion regime and resuspension may be envisioned for a constant-power micro-swimmer as that depicted in figure 9.11(d). The lift-off and lateral motility of the swimmer are entirely elastohydrodynamically enhanced, such that these effects cease once the gliding motion stops.

Similar phenomena have been observed in the slip and flow of dense polymer mi-

crogel pastes in earlier works [22, 23], where experiments, scaling and numerical analyses of elastohydrodynamic models found a slip regime of sheared pastes over surfaces beyond a critical sliding yield stress. Below the sliding yield stress, the paste seems to adhere to the surface. The transition point is qualitatively reminiscent of the onset of the irreversible elastohydrodynamic adhesion regime described in this section.

A ball park example of the applicability of these results may be the estimation of the lift-off shear rate for a spherical particle near a deformable and sticky substrate, as sketched in figure 9.11(e). Earlier works [32, 33] have shown that the viscous drag force and torque on a neutrally buoyant sphere, in a slow linear shear flow near a rigid wall, are $F_x = 1.7005 \cdot 6\pi\mu\gamma a^2$ and $T_y = 0.4719 \cdot 8\pi\mu\gamma a^3$, where γ is the undisturbed shear rate. Equating these two results to the leading-order force and torque (9.5) and (9.9), and neglecting $O(\eta_0\Upsilon, \eta_0\Xi)$ terms in the drag force, the nondimensional rotational velocity of the sphere induced by the shear flow becomes $\omega = 0.567$ to maintain dynamical equilibrium, with $\beta = \pi/2$. The lift-off shear rate is found to be

$$\gamma_L \approx \left[\frac{2.403 + \ln(a/\delta)}{2.451}\right] \sqrt{\frac{(A_{sfw} - 768 c_i N_A k T \lambda \ell_D \delta^2 \pi \mathrm{e}^{-\delta/\ell_D}) E (1-\nu)\delta}{\pi\mu^2 \ell a^3 (1+\nu)(1-2\nu)}}, \tag{9.37}$$

which increases with the substrate stiffness and intermolecular attraction. The shear rate can be increased up to the critical shear rate for irreversible elastohydrodynamic adhesion, for which $\eta_{0L} = \eta_{0C}$, which value depends on the particular relative intensity of the intermolecular parameters.

9.4.1 Elastohydrodynamic corrections to the DLVO theory

If the DLVO criterion (8.22) is used, the critical ionic concentration c_i^∇ for adhesion can be obtained by solving the system of equations

$$\begin{aligned}
1 \;-\; & \left(\frac{c_{i0}^\nabla}{c_i^\nabla}\right)^{1/2} (\kappa^\nabla)^2 \mathrm{e}^{-(\kappa^\nabla - 1)} + \eta_{0\nabla} \left\{ \Upsilon_\nabla \left[\frac{1}{(\kappa^\nabla)^4} \left(\frac{c_i^\nabla}{c_{i0}^\nabla}\right)^2 + \left(\frac{c_i^\nabla}{4 c_{i0}^\nabla}\right) (\kappa^\nabla)^2 \mathrm{e}^{-2(\kappa^\nabla - 1)} \right.\right. \\
& \left.\left. - \left(\frac{c_i^\nabla}{c_{i0}^\nabla}\right)^{3/2} \frac{\mathrm{e}^{-(\kappa^\nabla - 1)}}{\kappa^\nabla} \right] - \frac{48}{125 \Upsilon_\nabla \kappa^\nabla} \left(\frac{c_i^\nabla}{c_{i0}^\nabla}\right)^{1/2} \right\} = O(\eta_{0\nabla}^2), \\
1 \;-\; & \left(\frac{c_{i0}^\nabla}{c_i^\nabla}\right)^{1/2} \kappa^\nabla \mathrm{e}^{-(\kappa^\nabla - 1)} + \eta_{0\nabla} \left\{ \Upsilon_\nabla \left[\frac{1}{5(\kappa^\nabla)^4} \left(\frac{c_i^\nabla}{c_{i0}^\nabla}\right)^2 + \left(\frac{c_i^\nabla}{8 c_{i0}^\nabla}\right) (\kappa^\nabla) \mathrm{e}^{-2(\kappa^\nabla - 1)} \right.\right. \\
& \left.\left. - \left(\frac{c_i^\nabla}{c_{i0}^\nabla}\right)^{3/2} \frac{\mathrm{e}^{-(\kappa^\nabla - 1)}}{\kappa^\nabla} m(\kappa) \right] - \frac{24}{125 \Upsilon_\nabla \kappa^\nabla} \left(\frac{c_i^\nabla}{c_{i0}^\nabla}\right)^{1/2} \right\} = O(\eta_{0\nabla}^2),
\end{aligned} \tag{9.38}$$

where use has been made of (9.30). In this formulation, $\eta_{0\nabla}$ and Υ_∇ are based on $\delta_{0\nabla}$, and $m(\kappa)$ is given by (9.14). It can be shown that the expansions

$$\frac{c_i^\nabla}{c_{i0}^\nabla} = 1 - \eta_{0\nabla}\left(0.053\Upsilon_\nabla - \frac{48}{125\Upsilon_\nabla}\right) + \ldots, \tag{9.39}$$

$$\kappa^\nabla = 1 + \eta_{0\nabla}\left(0.223\Upsilon_\nabla - \frac{24}{125\Upsilon_\nabla}\right) + \ldots, \tag{9.40}$$

are asymptotic solutions of (9.38) for $\eta_{0\nabla} \ll 1$. In particular, equation (9.39) represents the elastohydrodynamic correction to the critical coagulation concentration, and it shows i) that the perturbation of the critical concentration is kinematically irreversible in that it does not depend on the velocity direction, and ii) that the critical concentration decreases with increasing $\eta_{0\nabla}$ if the van der Waals force is strong enough to outweigh the elastohydrodynamic repulsion, $\Upsilon_\nabla > 2.691$, and increases with increasing $\eta_{0\nabla}$ if the van der Waals force is small enough such that the repulsive elastohydrodynamic effect prevails, $\Upsilon_\nabla < 2.691$. The elastostatic result (9.15) recovered in the limit of small nondimensional velocities $\Upsilon_\nabla \gg 2.691$. Therefore, sufficiently large nondimensional velocities $\Upsilon_\nabla < 2.691$ contribute to suppress adhesion by electrolyte addition. Note that $\Upsilon = (\delta_0^\nabla/\delta)^{3/2}\Upsilon_\nabla < \Upsilon_\nabla$ and $\eta_0 = (\delta_0^\nabla/\delta)^{5/2}\eta_{0\nabla} < \eta_{0\nabla}$, so that the expansion (9.39) is valid for quite small values of η_0 since $\eta_0 < \eta_{0\nabla} \ll 1$, for which the elastohydrodynamic barrier is small, thereby enhancing adhesion for sufficiently reduced electric repulsion. Equation (9.39) models adhesion in the the hypothetical case that elastic instabilities are negligible in the range $\delta_0^\nabla < \delta \ll a$, which represents a good approximation for $\eta_0 < \eta_{0\nabla} \ll 1$, and if $\eta_{0\nabla}\Upsilon_\nabla < \Delta_{0C\nabla}^{vdW}$. In this formulation, $\Delta_{0C\nabla}^{vdW}$ represents the critical van der Waals compliance for irreversible elastohydrodynamic adhesion evaluated at $\eta_{0\nabla}$, $\Delta_{0\nabla}^{el}$ and κ^∇, which, to leading order in $\eta_{0\nabla}$, is given by $\Delta_{0C\nabla}^{vdW} = 0.451$ as detailed in Section 9.2. If these conditions are not satisfied, the particle undergoes irreversible elastohydrodynamic adhesion before surpassing the energy barrier, and the corrected DLVO criterion (9.39) losses accuracy to describe adhesion. Similarly, if the solvent is deionized, (9.39) cannot describe adhesion.

9.5 General influences of the substrate thickness and material incompressibility

If the substrate material is incompressible, $\nu = 1/2$, all the results presented in the previous sections, such as the lift force, drag and drift-force perturbations, lift-off and hydrodynamic adhesion compliances, lift-off shear rate and corrections to the critical con-

centration, become zero; the substrate behaves as a rigid wall to leading order in the nondimensional layer thickness ζ, as noticed in Section 8.3. To obtain the influences of the incompressibility effects, higher-order terms in the ζ asymptotic expansion of the surface deformation must be retained. If use of (8.43) is made, it can be shown that a substrate composed of a thin layer of incompressible material develops the same type of elastic instability for sufficiently large van der Waals compliances as the one presented in Section 9.2, and that, in the absence of electric forces, the critical van der Waals compliance for elastostatic adhesion is $\Delta_{2C}^{vdW} = 0.013$. Using (8.43) and following the same procedures as in Section 9.3, the lift force on a gliding particle near an incompressible substrate

$$F_z = \frac{\pi\mu U\mathcal{V}(\omega,\beta)a}{\epsilon^{1/2}}\left\{ -\Upsilon + \frac{2\Xi}{\kappa} + \eta_2\left[\frac{1296}{875} - \kappa\Xi^2 \right.\right.$$
$$\left.\left. -\frac{18\Upsilon^2}{7} + \Upsilon\Xi\kappa\left[2\kappa^3 e^{\kappa}\mathrm{Ei}(-\kappa) + 2\kappa^2 - 2\kappa + 4\right]\right] + \ldots\right\} \tag{9.41}$$

is obtained, where η_2 is given by (8.41). Similar to the lift force (9.30) for the case of a compressible layer, the sum of the mixed terms of $O(\eta_2\Upsilon^2, \eta_2\Xi^2, \eta_2\Upsilon\Xi)$ in (9.41) always has a negative sign independent of the values of Υ and Ξ, which induces a non-additivity in the intermolecular forces, and represents the perturbation of the intermolecular force on a stationary sphere near an incompressible deformable substrate. The lift-off hydrodynamic compliance is given by

$$\eta_{2L} \approx \left\{ \frac{875}{1296}\left[\Delta_2^{vdW} - \frac{2\Delta_2^{el}}{\kappa} + \kappa\Delta_2^{el^2} + \frac{18}{7}\Delta_2^{vdW^2} \right.\right.$$
$$\left.\left. -\Delta_2^{vdW}\Delta_2^{el}\kappa\left[2\kappa^3 e^{\kappa}\mathrm{Ei}(-\kappa) + 2\kappa^2 - 2\kappa + 4\right]\right]\right\}^{1/2}, \tag{9.42}$$

where Δ_2^{vdW} and Δ_2^{el} are given by (8.48) and (8.49) respectively. Since $\eta_2^{vdW}/\eta_0 = O(\zeta^2) \ll 1$, $\Delta_2^{vdW}/\Delta_0^{vdW} = O(\zeta^2) \ll 1$ and $\Delta_{el}^{vdW}/\Delta_0^{el} = O(\zeta^2) \ll 1$, the compliance of an incompressible layer under a stress load of intermolecular or hydrodynamic origin, is much less than that of a compressible layer under the same load, because of confinement effects produced by the rigid substrate, so that the material incompressibility tends to suppress the elastohydrodynamic adhesion of the particle to the substrate and reduce the elastohydromolecular effects on the forces.

In this investigation, expressions have not been derived for the lift force and lift-off compliances for the case of a semi-infinite elastic substrate. Nonetheless, the perturbation of the lift force on a particle gliding over a semi-infinite elastic medium can be assumed

to scale with η_∞, which is given by (8.45), such that the hydrodynamic lift-off compliance becomes

$$\eta_{\infty L} \approx \left\{ C_3 \left[\Delta_\infty^{vdW} - \frac{2\Delta_\infty^{el}}{\kappa} + O(\Delta_\infty^{vdW^2}, \Delta_\infty^{el^2}) \right] \right\}^{1/2}, \tag{9.43}$$

where Δ_∞^{vdW} and Δ_∞^{el} are given by (8.50) and (8.51) respectively, and C_3 is an order-unity constant. The correction term of $O(\Delta_\infty^{vdW^2}, \Delta_\infty^{el^2})$ represents the perturbation of the intermolecular force on a stationary sphere near a semi-infinite elastic substrate. Since $\eta_\infty/\eta_0 = O(1/\zeta) \gg 1$, $\Delta_\infty^{vdW}/\Delta_0^{vdW} = O(1/\zeta) \gg 1$ and $\Delta_\infty^{el}/\Delta_0^{el} = O(1/\zeta) \gg 1$, the compliance of a semi-infinite elastic layer under a stress load, of intermolecular or hydrodynamic origin, is much larger than that of a thin compressible layer under the same load, so that the layer thickness tends to enhance the elastohydrodynamic adhesion of the particle to the substrate and increase the elastohydromolecular effects on the forces.

Chapter 10

Conclusions

Substrate compliance and intermolecular effects on the slow translational and rotational motions of a small solid spherical particle were analytically and numerically investigated in this study by making use of a hydrodynamic lubrication approximation. Electric double-layer and van der Waals stresses were formulated to model the intermolecular influences in the gap region by using the Derjaguin approximation. The hydrodynamic compliance, η, and intermolecular compliances, Δ^{vdW} and Δ^{el}, were found to be the relevant nondimensional parameters that characterize the relative intensity of the hydrodynamic and intermolecular stresses with respect to the restoring elastic stresses on the surface. Influences of a general particle drift motion were analyzed by introducing in the formulation the rotational to translational velocity ratio ω, and the azimuth angle of orientation of the rotation axis β relative to the translation axis. A characteristic velocity $U\sqrt{1+\omega^2+2\omega\sin\beta}$ was defined as the gliding velocity for the general case of drift motion, where U is the translational velocity without drift. The formulation was applied to a substrate composed of a thin compressible elastic layer coating a rigid foundation, and special emphasis was made on the influences of attracting van der Waals forces and repulsive electric forces. Asymptotic formulas were derived in the nearly rigid-wall asymptotic limit (NRWA), $\eta \ll 1$, and they were compared to numerical computations for fully deformable substrates, for which $\eta \leqslant O(1)$.

The combination of elastohydromolecular effects was found to induce irreversible and reversible elastohydrodynamic regimes, a lift force, and drag-force and drift-force disturbances, all of which appear to be new. For $\eta = \eta_L$ a reversible elastohydrodynamic regime is found. For $\eta < \eta_L$, an irreversible elastohydrodynamic regime occurs with negative lift forces. For $\eta > \eta_L$, an irreversible elastohydrodynamic regime occurs with positive

lift forces. The limiting values of elastohydrodynamic adhesion and expressions of the forces were derived in the NRWA limit and compared to numerical solutions.

The lift force, which scales with even powers of the gliding velocity, is negative for large and attracting van der Waals forces, and is positive for repulsive van der Waals forces or for intermediate attracting van der Waals forces and sufficiently soft substrates. Electric intermolecular repulsion increases the magnitude of the lift force. For the same translational velocity, particle dimensions and substrate mechanical properties, the purely rolling motion ($\omega = 1$, $\beta = \pi/2$) produces a larger lift force than the corkscrew ($\omega = 1$, $\beta = 0$) and translational ($\omega = 0$) motions. In addition to the leading-order intermolecular forces, to second order in the substrate compliance, the lift force is composed of elasto-hydrodynamic and elastomolecular terms, the latter corresponding to the perturbation of the intermolecular force on a stationary sphere, which is always attractive and represents a non-additivity of intermolecular effects. The drag-force perturbation scales with odd powers of the velocity. Substrate compliance favors a drag-force reduction. The coupling between intermolecular and elasticity effects induces a van der Waals drag force and an electric drag force. In general, intermolecular attractive forces increase the drag on the sphere, and the contrary holds for repulsive forces. For the same translational velocity, particle dimensions and substrate mechanical properties, the pure rolling motion ($\omega = 1$, $\beta = \pi/2$) produces a larger drag force reduction than the corkscrew ($\omega = 1$, $\beta = 0$) and translational ($\omega = 0$) motions. Substrate-deformation effects are found to play a very weak role on the drift force. Attractive intermolecular forces produce small increments on the drift force due to a viscous-traction enhancement, and the contrary holds for repulsive forces.

A reversible elastohydrodynamic adhesion regime was found in both ionized and deionized solvents for a lift-off hydrodynamic compliance $\eta = \eta_L$, which value increases with Δ^{vdW} and decreases with increasing Δ^{el}. In this regime, particle lateral motion and lift-off from the wall can occur. The lift-off hydrodynamic compliance can be achieved by sufficiently large gliding velocities or substrate compliances. This regime ceases to exist if the gliding motion stops, and it is found to be stable against small-gap disturbances at constant gliding power.

In the region $\eta < \eta_L$, the particle is subject to a negative lift, and an irreversible elastohydrodynamic adhesion regime occurs for sufficiently large Δ^{vdW}. This irreversible adhesion mechanism is found in both ionized and deionized solvents, and is induced by elastic instabilities in the form of surface bifurcations in the substrate, which have been studied in §9.2 in its elastostatic version for a stationary sphere near a deformable substrate.

The limiting values for irreversible elastohydrodynamic adhesion are given by the critical hydrodynamic compliance $\eta = \eta_C$, which was numerically calculated. The compliance η_C was found to increase with Δ^{vdW} and decrease with increasing Δ^{el}.

In the region $\eta > \eta_L$, the particle is subject to a positive lift force, but an irreversible elastohydrodynamic adhesion regime can take place since the substrate becomes softer and more unstable as η_0 increases. In this regime, adhesion is enhanced by sufficiently large substrate compliances and gliding velocities.

An increase in the repulsive electric force tends to suppress elastohydrodynamic adhesion. However, elastohydrodynamic adhesion can occur and be suppressed in deionized solvents, where there is no electrical repulsion, and cannot be described by the classic Derjaguin-Landau Verwey-Overbeek (DLVO) theory of colloid stabilization.

Elastohydrodynamic corrections to the DLVO critical coagulation concentration, for which the energy barrier against Brownian perturbations of the gap distance is small, were obtained in the NRWA limit for very small η, when the elastohydrodynamic barrier was also small, which showed that the critical concentration decreases with increasing η because of an enhancement of the attractive van der Waals force; this trend continues up to a critical van der Waals to hydrodynamic stress ratio η/Δ^{vdW}, above which the elastohydrodynamic repulsion dominates and the critical coagulation concentration increases with η. The corrected DLVO critical concentration may be accurate to describe the adhesion process for sufficiently small compliances for which the elastic substrate remains in static mechanical equilibrium, but loses accuracy for low-midway compliances for which elastohydrodynamic adhesion occurs before the particle has surpassed the energy barrier, and it is not applicable when the solvent is deionized.

Material incompressibility in the substrate is found to suppress adhesion, and formulas for the lift force and lift-off hydrodynamic compliance have been derived for a fully incompressible substrate. A semi-infinite elastic substrate is shown to enhance adhesion and elastohydromolecular effects by having larger hydrodynamic and intermolecular compliances, which may represent an important feature to account for in future numerical work and laboratory experiments.

The results obtained in this study show that the mechanical and surface properties of the substrate and the gliding kinematic characteristics of the particle have important influences on the adhesive and migrating behaviors, and therefore potential benefits in practical applications, such as particle and cell manipulations in microfluidics systems, may be obtained by modifying those magnitudes to enhance or suppress dynamical phenomena

like lift-off from the surface and drag reduction.

Chapters 7 to 10, in part, have been published in *Physics of Fluids*, "The elasto-hydrodynamic force on a sphere near a soft wall," by J. Urzay, S. G. Llewellyn Smith and B. J. Glover (2007) **19** 103106 1-7, and in the *Journal of Fluid Mechanics*, "Asymptotic theory of the elastohydrodynamic adhesion and gliding motion of a solid particle over soft substrates at low Reynolds numbers," by J. Urzay (2010) (In Press). The thesis author is the primary investigator in these publications.

References

[1] Landau, L.D., Lifshitz, E.M. (1959) *Theory of Elasticity*. Pergamon Press, London.

[2] Johnson, K. L. (1985) *Contact Mechanics*. Cambridge University Press, Cambridge.

[3] Jin, Z. M. Dowson, D. (2005) Elastohydrodynamic lubrication in biological systems. *J. Eng. Tribology*, **219** 367-380, 2005.

[4] Vigeant, M. A. S., Ford, R. M. & Wagner, M. (2005) Reversible and irreversible adhesion of motile escherichia coli cells analyzed by total internal reflection aqueous fluorescence microscopy. *App. Environ. Microbiol.* **68**, 2794–2801.

[5] Derjaguin, B. V., Landau, L. (1941) Theory of the stability of strongly charged lyophobic sols and the adhesion of strongly charged particles in solutions of electrolytes. *Acta Physicochim. URSS* **14**, 633–662.

[6] Verwey, E. J. W., Overbeek, J. Th. G. (1948) *Theory of the stability of lyophobic colloids*. Elsevier, London.

[7] Berke, A. P., Turner, L., Berg, H. C., Lauga, E. (2008) Hydrodynamic attraction of swimming microorgansims by surfaces. *Phys. Rev. Lett.* **101** (038102).

[8] Busscher, H. J., Poortinga, A. T., Bos, R. (1998) Lateral and perpendicular interaction forces involved in mobile and immobile adhesion of microorganisms on model solid surfaces. *Curr. Microbiol.* **37**, 319–323.

[9] Purcell, E. M. (1977) Life at low Reynolds number. *Am. J. Phys.* **45**, 3–11.

[10] Berdan, C., Leal, G. (1981) Motion of a sphere in the presence of a deformable interface. i. perturbation of the interface from flat: The effects on drag and torque. *J. Colloid Interf. Sci.* **87**, 62–80.

[11] Skotheim, J. M., Mahadevan, L. (2005) Soft lubrication: The elastohydrodynamics of nonconforming and conforming contacts. *Phys. Fluids* **17**.

[12] Weekley, S. L., Waters, S. L. & Jensen, O. E. (2006) Transient elastohydrodynamic drag on a particle moving near a deformable wall. *Q. Jl Mech. Appl. Math.* **59**, 277–300.

[13] Urzay, J., Llewellyn-Smith, S. G., Glover, B. J. (2007) The elastohydrodynamic force on a sphere near a soft wall. *Phys. Fluids* **19**, 103106.

[14] Trouilloud, R., Yu, T. S., Hosoi, A. E., Lauga, E. (2008) Soft swimming: Exploiting deformable interfaces for low reynolds number locomotion. *Phys. Rev. Lett.* **101**, 048102.

[15] Lauga, E., DiLuzio, W. R., Whitesides, G. M., Stone, H. A. (2006) Swimming in circles: motion of bacteria near solid boundaries. *Biophys. J.* **90**, 400–412.

[16] Saffman, P. G. (1964) The lift on a small sphere in a slow shear flow. *J. Fluid Mech.* **22**, 385–400.

[17] Leighton, D. & Acrivos, A. (1985) The lift on a small sphere touching a plane in the presence of a simple shear flow. *Z. Angew. Math. Phys.* **36**, 174–178.

[18] Bike, S. G., Prieve, D. C. (1995) The electrokinetic lift of a sphere moving in a slow shear flow parallel to a wall. *J. of Colloid and Interf. Sci.* **175**, 422–434.

[19] Hu, H. H., Joseph, D. D. (1999) Lift on a sphere near a plane wall in a second order fluid. *J. non-Newtonian Fluid Mech.* **88**, 173–184.

[20] Israelachvili, J. N. (1985) *Intermolecular and surface forces*. Academic, London.

[21] Lyklema, J. (2005) *Fundamentals of interface and colloid science. Volume IV: Particulate colloids*. Elsevier, London.

[22] Meeker, S. P., Bonnecaze, R. T., Cloitre, M. (2004) Slip and flow in pastes of soft particles: Direct observation and rheology. *J. Rheol.* **48**, 1295–1320.

[23] Seth, J. R., Cloitre, M., Bonnecaze, R. T. (2008) Influence of short-range forces on wall-slip in microgel pastes. *J. Rheol.* **52**, 1241–1268.

[24] Goldman, A. J., Cox, R. G., Brenner, H. (1967) Slow motion of a sphere parallel to a plane wall: motion through a quiescent fluid. *Chem. Eng. Sci.* **22**, 637–51.

[25] O'Neill, M. E., Stewartson, K. (1967) On the slow motion of a sphere parallel to a nearby plane wall. *J. Fluid Mech.* **27**, 705–724.

[26] Cooley, M. D. A., O'Neill, M. E. (1968) On the slow rotation of a sphere about a diameter parallel to a nearby plane wall. *J. Inst. Math. Applics.* **4**, 163–173.

[27] Derjaguin, B. V. (1934) Analysis of friction and adhesion iv: The theory of the adhesion of small particles. *Kolloid Zeits.* **69**, 155–164.

[28] Lifshitz, E.M. (1956) The theory of molecular attractive forces between solids. *Sov. Phys. JETP-USSR* **2**, 73–83.

[29] Poortinga, A. T., Bos, R., Norde, W., Busscher, H. J. 2002 Electric double layer interactions in bacterial adhesion to surfaces. *Surf. Sci. Rep.* **47**, 1–32.

[30] Wu, X., Warszynksi, P. & van de Ven, T. G. M. (1995) Electrokinetic lift: observations and comparisons with theories. *J. Colloid Interf. Sci.* **180**, 61–9.

[31] Hamaker, H. C. (1937) The london-van der waals attraction between spherical particles. *Physica IV* **10**, 1058–72.

[32] Goldman, A. J., Cox, R. G., Brenner, H. (1967) Slow motion of a sphere parallel to a plane wall: Couette flow. *Chem. Eng. Sci.* **22**, 653–660.

[33] O'Neill, M. E. (1968) A sphere in contact with a plane wall in a slow linear shear flow. *Chem. Eng. Sci.* **23**, 1293–1298.

[34] Johnson, K. L., Kendall, K. & Roberts, A. D. (1971) Surface energy and contact of elastic solids. *Proc. R. Soc. London, Ser. A* **324**, 301–13.

[35] Johnson, K. L., Kendall, K. & Roberts, A. D. (1971) Surface energy and contact of elastic solids. *Proc. R. Soc. London, Ser. A* **324**, 301–13

[36] Derjaguin, B. V., Muller, V. M., Toporov, Y. P. (1975) Effect of contact deformations on adhesion of particles. *J. Colloid Interf. Sci.* **53**, 314–326..

[37] Davis, R. H., Serayssol, J. M., Hinch, E. J. (1986) The elastohydrodynamic collision of two spheres. *J. Fluid Mech.* **163**, 479–497.

[38] Serayssol, J. M., Davis, R. H. (1986) The influence of surface interactions on the elastohydrodynamic collision of two spheres. *J. Colloid Interf. Sci.* **114**, 54–65.

Part III

Aerodynamics and Aeroelasticity of Wind Pollination

NOMENCLATURE

A_e	Effective frontal area (m^2)
C_{De}	Effective drag coefficient (-)
d	Filament diameter (m)
D	Pollen grain diameter (m)
E	Filament Young modulus (Pa)
ϵ	Stokes-Reynolds number (-)
E_u	Power spectrum of the wind-velocity fluctuations (m^2/s)
F	Instantaneous total force (N)
$\tilde{F}$	Dimensionless total force (-)
F_{ad}	Adhesion force (N)
$F_{ad}^{\star}$	Maximum adhesion force (-)
$\tilde{F}_{AM}$	Dimensionless added-mass force (-)
$\tilde{F}_B$	Dimensionless Basset force (-)
$\tilde{F}_D$	Dimensionless Stokes drag force (-)
F_D	Instantaneous Stokes drag force (N)
F_D^{∞}	Steady Stokes drag force (N)
H	Filament length (m)
ℓ	Integral length scale (m)
L	Anther chord length (m)
m_a	Anther mass (kg)
m_p	Pollen grain mass (kg)
m_s	Filament + anther mass (kg)
μ	Air dynamic viscosity (Pa· s)
n	Natural frequency (Hz)
ν	Air kinematic viscosity (m^2/s)
ω	Angular frequency (rad/s)
ω_n	Natural angular frequency (rad/s)
P	Probability of pollen-shedding (-)
Ψ	Pollen-shedding number (-)
Re_L	Reynolds number based on L (-)
ρ	Air density (kg/m^3)

s	Anther displacement (m)
$\ddot{s}_c$	Critical anther acceleration (m/s^2)
τ	Dimensionless time coordinate (-)
t_a	Aeroelastic time scale (s)
t_ν	Viscous time scale (s)
t_o	Wind-gust time scale (s)
T_u	Turbulent intensity (-)
$\tilde{U}$	Dimensionless wind velocity (-)
U_L	Instantaneous local wind velocity (m/s)
U_L^∞	Steady local wind velocity (m/s)
u'	Instantaneous wind-velocity fluctuation (m/s)
U_w	Instantaneous Wind velocity (m/s)
$\bar{U}_w$	Average wind velocity (m/s)
ξ	Damping ratio (-)

Chapter 11

Introduction

All land plants are descended from a single lineage that made the transition from water to land approximately 470 million years ago. This transition represented an enormous endeavor to the emergent land plants as their ancestors had no defense against the dehydrating terrestrial atmosphere. The earliest land plants were presented with a number of problems such as gaseous exchange -solved by the development of pores in their cuticles-, structural support -which induced the evolution of structural materials such as lignin-, nutrient accumulation -solved by the development of roots-, and transport -solved by the evolution of a vascular system-. However, the biggest challenge of adaptation to life on land was that of reproduction without the benefit of a surrounding aqueous environment for gamete dispersal. The gametes must have a thin outer cover in order to fuse with other gametes and form the zygotes, and they must disperse across long distances for cross fertilization to occur. In an aqueous environment, transport of gametes was warranted by water currents and presented no difficulties. Thus, early land plants were constrained to reproduce in aqueous environments, although their adult forms were already successful at surviving the dehydrating terrestrial environment. Examples of these early developments are fern and mosses, which release swimming sperm only in wet conditions.

It was not until the origins of the seed plants, around 300 million years ago, that plants freed themselves from the need for external water for reproduction. Seed-bearing plants consist of gymnosperms (like conifers) and angiosperms (like flowering plants). The seed plants solved the reproduction problem by means of desiccation-resistant pollen [1]. The male spore was retained within the tissues of the parent plant, and produced a male gametophyte -the pollen grain- that was adapted for dispersal and was encased in a dehydration-resistant coating. The pollen grain can therefore be thought of as a waterproof dispersal

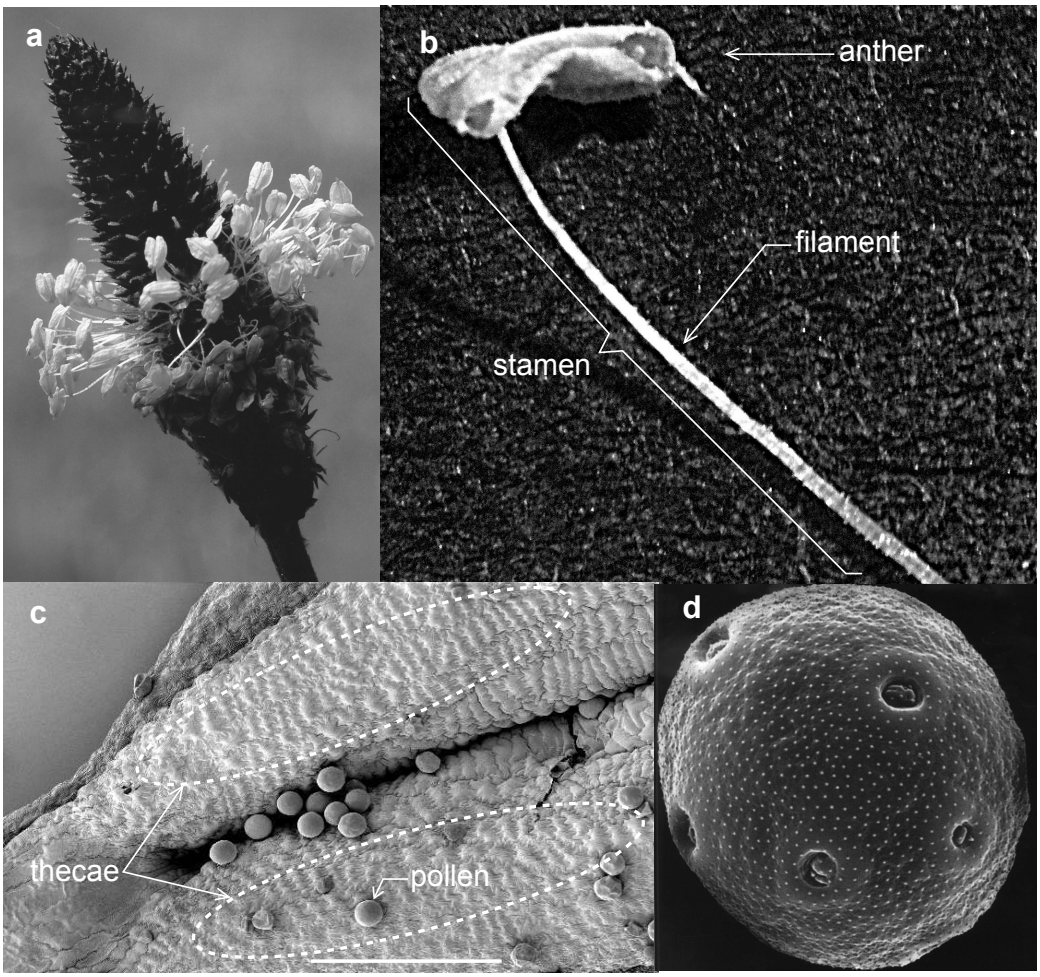

Figure 11.1: (a) *Plantago* inflorescence. (b) *Plantago* stamen. (c) *Plantago* anther showing the thecae and the exposed pollen grains during dehiscence (scale bar 200 μm). (d) *Plantago* pollen.

vehicle that contains the male gametes and associated cells. Finally, the pollen grain arrives to another diploid plant of the same specie where it germinates aided by rehydration [2].

The success of the land plants was dependent upon the effectiveness of these dispersal vehicles. The first seed plants were wind pollinated, and wind pollination has remained the norm for the majority of gymnosperm lineages, which dominate ecosystems such as the Arctic and Siberian tundra. The first angiosperms are believed to have been insect-pollinated [3], but a large proportion of angiosperm species (around 25,000, or 10% of the total) evolved wind pollination secondarily [1]. These species include the ecologically dominant grasses, whose pollen is responsible for many human allergic reactions, and whose successful pollination is essential to the production of cereal crops.

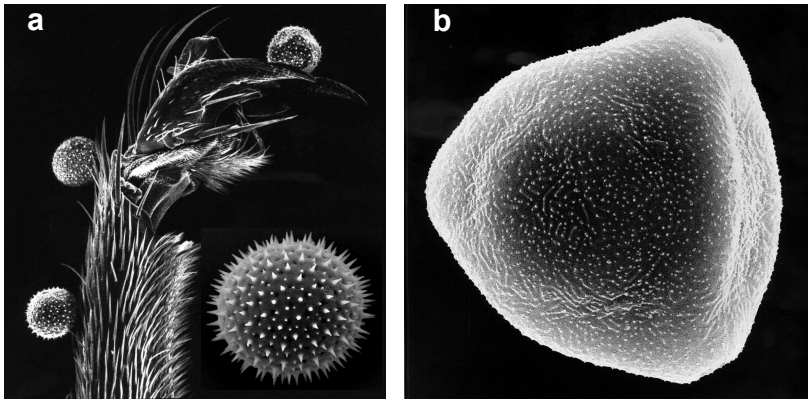

Figure 11.2: (a) Common Mallow pollen adhered to a bumble-bee leg. (b) Hazel pollen. Adapted from [4].

The importance of pollination was first recognized a long time ago in ancient civilizations. The pioneering work of Linnaeus [5] established the pollen grain as a scientifically well-defined identity participating in the plant sexuality. Although there are a great variety of pollen types, their main functionalities are similar in that they are designed to succeed in the same mission. Wind-pollinated species have smoother pollen coats than insect-pollinated species, but the exact influences of these shapes and coating properties on their adhesive behavior and aerodynamics remain still unknown. The outer layer of the pollen wall (exine) is composed of a highly stable biopolymer called sporopollenin, which consists of carbon, hydrogen and oxygen. The sporopollenin is a relatively stiff structure extraordinarily resistant to enzymic attacks. The pollen surface is usually dry in most wind pollinated species like oak, hazel and alder pollen, with a thin deposit of pollenkitt and a coat of lipids that collaborates in adhesion to the stigma [6]. Depending on the pollen type and its transport vector, the surface of the grain shows different patterns or sculptural elements. Some species, like Common Mallow (*Malva Sylvestris*) and Rhododendron exhibit a spinulate pattern that adheres to bumblebee legs as shown in figure 11.2. But most wind-pollinated pollens have a relatively smooth surface like plantago or hazel (*Corylus Avellana L.*). The normal density of a pollen grain is of the order of the density of the protoplasm that it contains, which is of the same order of magnitude as the density of water. Little is known about the electrostatic charge of pollen grains, although earlier studies [7, 8] showed a negative charge of the order of 10^{-15} C for airborne pollen grains. The electrostatic effect has been found to be important in deposition processes on stigmas [9-12]. The anther surface is composed of a layer of tapetal cells that before the dehiscence are the precursors of the production of sporopollenin and pollenkitt deposition. Typical wind pollinated anthers

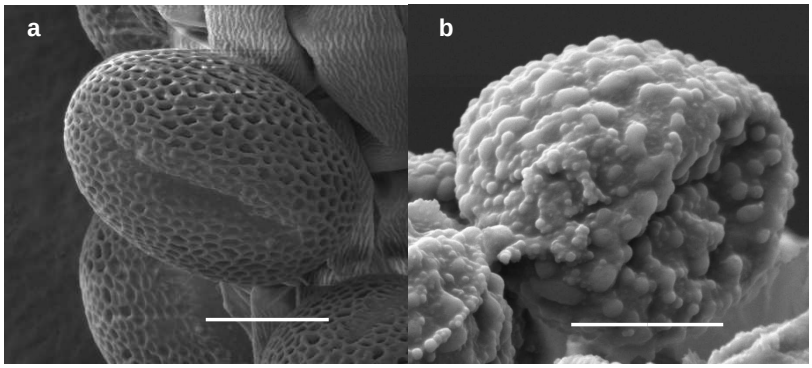

Figure 11.3: Genetic modifications performed at the University of Cambridge (UK), Department of Plant Sciences. (a) *Arabidopsis* pollen (scale bar 10 μm). (b) *Arabidopsis-KOM* mutant (scale bar 10 μm). The KOM mutant is unable to produce sufficient callose to build a normal exine, and sporopollenin surface deposition is also randomised.

are aerodynamically shaped in order to maintain mechanical integrity under wind loads. The anther and filament together form the stamen as shown in figure 11.1(b).

At pollen maturity, the thecae of the anthers dehydrate and split open as seen in figure 11.1(c), leaving the pollen grains exposed to the ambient air flow and subject to a set of environmental forces. This ultimately leads to the pollen's removal if the external forces overcome the threshold imposed by molecular adhesion. Accomplishing this loss without the aid of animals is no easy task for anemophilous pollen, which leads, by extension of the functionally similar process of fungal spore liberation [13-15], to the 'paradox of pollen liberation' [16], according to which the wind speed necessary to detach pollen and small fungal spores, as predicted by steady aerodynamic theory, is much larger than the threshold wind speed measured in the field.

Understanding of pollen shedding, dispersal and germination mechanisms is essential for tracking the evolution and adaptation of plant species [16, 17], for improvement of the cultivation of genetically engineered plants [18], and for the control of allergenic species and epidemics. In particular, the genetic modification of pollen properties is currently a cause of concern, not only because of the possible beneficial consequences of insect-resistant and herbicide-tolerant transgenic crops, which may decrease the use of environmentally harmful chemicals to control pests, but for the negative effects that biological invasion of genetically-engineered species have by gene introgression into food crops, including maize, wheat, rice, soybean, barley and cotton seed [18]. Figure 11.3 shows genetically modified pollen grains of *Arabidopsis thaliana*; such modifications can be readily performed to change morphological characteristics such as sizes, shapes, surface patternings and sporopollenin spatial

depositions [19], which in the near future may enable a thorough control over processes like shedding, dispersal and deposition of pollen, once the influences of those properties on these processes are fully understood from a mechanical standpoint.

The release, dispersal and deposition of pollen grains has been extensively reviewed [20, 21] but, contrary to the case of fungal-spore liberation [13-15], the fundamental problem of pollen liberation has not been resolved. In this investigation, scaling analyses are used to clarify the conditions under which classical spore-removal descriptions [13-15] are appropriate to describe pollen shedding, and then a simplified model is proposed, which explicitly takes into account both the turbulent nature of the micrometeorological conditions in the vicinity of the plant and the elastic and aerodynamic properties of the plant. The parametric models proposed in this study represent the first attempt to establish a quantitative relationship between morphological characteristics of pollen grains and their influences on the overall shedding process and its efficiency.

Chapter 12

Pollen shedding forces

12.1 Aerodynamic shedding forces

12.1.1 Steady aerodynamic forces

Earlier analyses of the physical processes involved in pollen and small fungal spore liberation are based on boundary-layer air flow models around a pollen grain on an anther [13-16,20,21], as depicted in figure 12.1. The pollen grain is assumed to be a spherical particle of equivalent diameter D and mass m_p. Wind-pollinated pollen grains are mostly of similar sizes, and tend to be round and smooth. Their exact shape can be shown to have only a small influence in the low-speed flow regimes encountered in the classic steady aerodynamic explanations of release since the drag force is mainly dominated by the skin (shear-stress) drag, and is of no importance in the stochastic aeroelastic mechanism proposed in section 12.2. A scaling analysis is developed here, supported by experimental measurements on typical wind-pollinated species (see table 12.1), to analyze the effect of aerodynamic forces experienced by the pollen grain on an anther. The relative importance of inertial and viscous forces in a fluid is expressed as a dimensionless number, the Reynolds number $\mathrm{Re}_L = UL/\nu$, where U is the fluid velocity, L is a characteristic length and $\nu = \mu/\rho$ is the kinematic viscosity, with μ and ρ respectively the dynamic viscosity and density of the fluid, which in the present analysis correspond to the viscosity and density of the air at standard conditions: $\mu = 1.85 \cdot 10^{-5}$ Pa·s, $\rho = 1.18$ kg/m^3 and $\nu = 1.57 \cdot 10^{-5}$ m^2/s.

The steady air flow around a typical anther of length $L \sim 0.6 - 4.3$ mm (see table 12.1) is a laminar boundary-layer flow, resulting in $\mathrm{Re}_L = U_w L/\nu \sim 36 - 271$ at ordinary wind speeds $U_w \sim 1$ m/s. Using boundary-layer scaling [22], a typical pollen grain of diam-

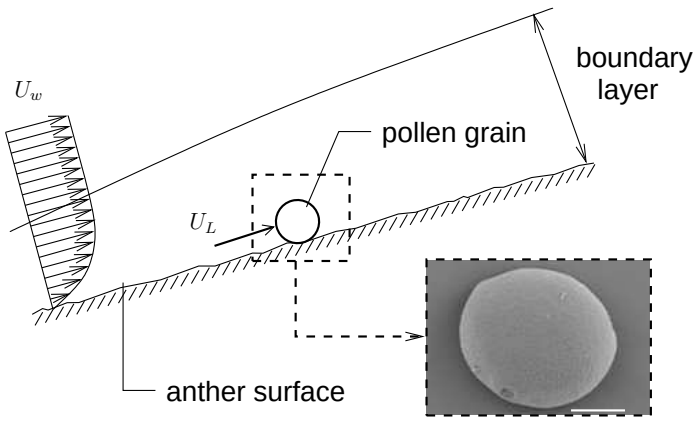

Figure 12.1: The boundary-layer model. The inset shows a *Betula albosinensis* pollen grain (scanning electron microscopy, scale bar 10 μm.)

eter $D \sim 16.7 - 95.3$ μm (see table 12.1) is affected by local wind speeds U_L^∞ of order

$$U_L^\infty \sim 0.166 U_w \mathrm{Re}_L^{1/2} D/L, \tag{12.1}$$

where the superindex $^\infty$ denotes its steady value. In this formulation, since the pollen grain is well embedded in the boundary layer, $D/2L \ll 1/\mathrm{Re}_L^{1/2}$, use has been made of the well-known boundary-layer theory result that the friction coefficient on the anther surface is given by $0.664/\mathrm{Re}_L^{1/2}$ [22], from which the local shear flow can be linearized and the local velocity is obtained as (12.1). The local velocity ranges in the interval $U_L^\infty \sim 18.0 - 40.7$ mm/s, resulting in local Reynolds numbers $\mathrm{Re}_D = U_L^\infty D/\nu \sim 0.03 - 0.13$: the flow is essentially fully viscous at scales of order D. The disparity between the free-stream wind speed, U_w, and that close to the anther, U_L, is inherent in boundary-layer flows because of viscosity, and is the reason why steady aerodynamic forces are not sufficient to remove small fungal spores under steady aerodynamic conditions for typical wind speeds [13, 14, 16, 15]. The steady Stokes drag force on a spherical particle of the same size as a pollen grain in contact with a planar wall [23] is

$$F_D^\infty = 1.7009 \cdot (3\pi\mu D U_L^\infty), \tag{12.2}$$

giving $F_D^\infty \sim 0.1 - 0.6$ nN for the species analyzed in Table 1 and $U_w = 1$ m/s, and $F_D^\infty = 3.9 - 19.7$ nN for $U_w = 10$ m/s. The exact value of the adhesion force F_{ad} is poorly known, but reported measurements range from $0.1 - 1$ nN for insect-pollinated species [24, 25] to 100 nN for fungal spores [13]. According to these estimates, the steady Stokes aerodynamic drag F_D^∞ may in fact be large enough to shed typical pollen grains during steady wind conditions, since anemophilous pollen-anther adhesion forces F_{ad} are expected

to be reasonably smaller than the upper-limit values of $0.1 - 1$ nN for insect-pollinated species [24, 25], which have a sticky layer of pollenkitt that is absent from the surface of anemophilous pollen grains.

12.1.2 Unsteady aerodynamic forces.

To solve a functionally similar paradox, that of fungal spores liberation from infected plant leaves, earlier work [13, 14] on conidia of *Helminthosporium maydis* (*Cochliobolus heterostrophus*; Southern corn leaf blight), 96 μm in length and 17 μm in diameter, 75 nN adhesion force, proposed the existence of gusts of wind with velocity fluctuations u' that take place over a small distance, which corresponds to the gust front thickness δ_o, so that at a fixed point on the leaf the velocity fluctuation u' is swept over that point in a time of order

$$t_o = \delta_o / u', \tag{12.3}$$

causing the removal of spores by unsteady aerodynamic forces. Typical magnitudes measured in earlier experimental works [13, 14] are $u' = 2.5$m/s, δ_o=1mm, $t_o = 0.4$ ms. The existence of wind gusts is consistent with subsequent analyses of canopy turbulence [15, 26, 27]: the turbulence in the canopy of trees or smaller plants displays striking differences to classical turbulent boundary layers in that a mixing-layer instability and the canopy-induced internal wakes may trigger severe intermittency and wind gusts in the canopy region.

Atmospheric conditions typical of instability are also found during pollen release [16]. However, when the same wind-gust explanation is applied to describe pollen shedding, the resulting unsteady forces exerted by the surrounding air on the pollen grain may not lead to pollen release, since the viscous time scale

$$t_\nu = D^2/\nu \sim 0.02 - 0.58 \text{ ms}, \tag{12.4}$$

is typically the smallest time scale of the problem as observed in table 12.1, where values of the viscous to wind-gust time scale ratio (i.e. the Stokes-Reynolds number)

$$\epsilon = t_\nu / t_o, \tag{12.5}$$

are listed for typical wind-pollinated species. Assuming (12.3) as a typical value of wind-gust time scale, ϵ is found to be a small parameter, $\epsilon \ll 1$, for most of the species listed in table 12.1. There may be exceptions to this rule, such as maize pollen, for which gravitational force may also play a role in pollen removal because of its heavy weight.

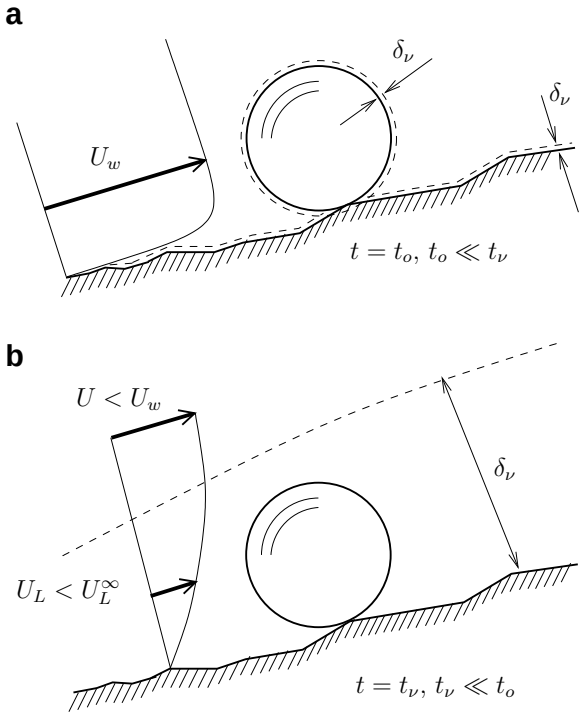

Figure 12.2: Sketches of the flow field around a pollen grain on an anther subject to a wind gust for (a) $\epsilon \gg 1$, and (b) $\epsilon \ll 1$.

It must be emphasized that, contrary to some fungal spores, which are liberated from conidiophores that extend higher into the boundary layer [13-15], pollen grains are mostly liberated directly from the anther surface, so that removal by wind gusts may not be so effective for them as detailed below.

Figure 12.2(a) shows a frozen sketch of the flow field around a pollen grain, after times of order t_o, for the hypothetical case of strongly accelerated wind gusts $\epsilon \gg 1$. In this regime, the inertial time-variation of the outer flow dominates over the viscous effects, which occur on a much longer time scale. Since the Reynolds number of the pollen grain $\mathrm{Re}_D = U_w D/\nu$ is not too large ($\mathrm{Re}_D \sim 1.1 - 6.1$ for $U_w = 1$ m/s), the drag force acting on the pollen grain may be calculated using the Stokes drag[1] $F_D = 3\pi\mu D U_w$ based on the free stream velocity, which yields a force range $F_D = 2.9U_w - 16.6U_w$ nN, where U_w is the wind velocity in m/s. The wind-gust explanation may then be appropriate to describe the release of relatively large pollen grains of diameters $D \gg (\nu t_o)^{1/2}$, for which $\epsilon \gg 1$, and adhesion forces in the range $2.9U_w - 16.6U_w$ nN, which corresponds to larger adhesion forces than those able to be overcame by steady wind conditions. Notice that, for the wind-gust time

[1]Anther surface effects, which are important in a thin layer of thickness $\delta_\nu \sim \sqrt{\nu t_o}$, are neglected in the $\epsilon \gg 1$ regime since the velocity profile is nearly uniform on scales of order $D \gg \delta_\nu$.

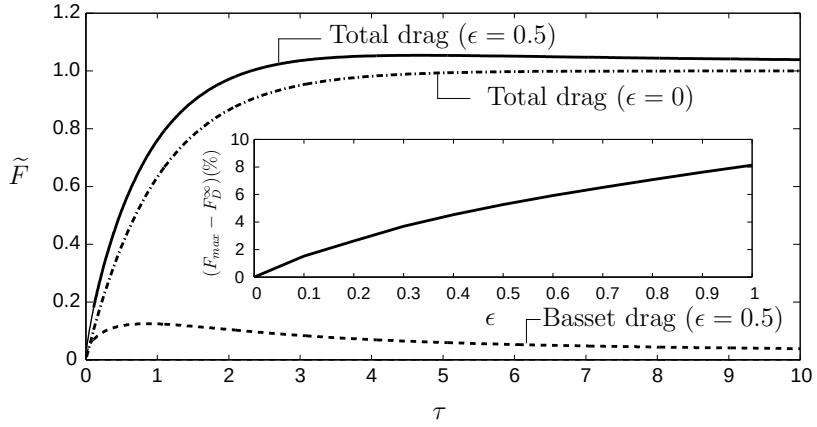

Figure 12.3: Total drag force and Basset forces for $\epsilon = 0$ and $\epsilon = 0.5$ calculated from (12.6). The added mass force is too small to distinguish at this scale. The inset shows the percentage variation of the maximum total drag force with respect to its steady value (12.2).

scale $t_o = 0.4$ ms [14], the critical diameter becomes $(\nu t_o)^{1/2} = 79.2$ μm, which is larger than the diameters listed in table 12.1 (with the exception of the maize pollen, which may be influenced by gravitational forces, as mentioned above).

Figure 12.2(b) shows a frozen sketch of the flow field around a pollen grain, after times of order t_ν, for the more realistic $\epsilon \ll 1$ case for pollen shedding. After times of order t_ν, the accelerating wind stream is not yet fully developed, and the boundary layer thickness has grown to be of the same size as the pollen grain diameter. The local velocity U_L is still smaller than its corresponding steady-state value (12.1), which is fully attained after times of order t_o. Time-dependent effects such as the added-mass and Basset forces [9] may still be considered important effects at this point of the analysis, since these forces may be larger than the steady Stokes drag (12.2) during the transient regime $0 < t < t_\nu$ [2]. To address this question more rigorously, a local velocity variation of the form $\widetilde{U} = 1 - \exp(-\tau)$ is considered, where $\widetilde{U}$ is the local velocity nondimensionalized with its steady-state value U_L^∞ given by (12.1) and τ is the time coordinate nondimensionalized with the gust time scale t_o. In this model, the boundary layer thickness grows progressively in time from an initial zero value.

Since the local Reynolds number based on the grain diameter $\mathrm{Re}_D = U_L^\infty D/\nu$ is

[2] It is worth noting that explanations of the effects produced by unsteady wind streams based on Rayleigh's problem (flat plate suddenly started from rest in a viscous fluid) used in earlier works on spore removal [13, 14], implicitly assume $t_o = 0$ (or $\epsilon \to \infty$) and are not appropriate in the $\epsilon \ll 1$ regime, since the time scale of acceleration is large compared with the viscous time scale.

small, the unsteady hydrodynamic force can be estimated as [9]

$$\begin{aligned} \widetilde{F} &= c_1\epsilon\frac{d\widetilde{U}}{d\tau} + c_2\epsilon^{1/2}\int_0^\tau \frac{d\widetilde{U}}{d\xi}\frac{d\xi}{\sqrt{\tau-\xi}} + \widetilde{U} \\ &= \widetilde{F}_{AM} + \widetilde{F}_B + \widetilde{F}_D, \end{aligned} \tag{12.6}$$

with $\widetilde{F}$ the hydrodynamic force nondimensionalized with the steady Stokes drag force (12.2), and $c_1 = 1/(36 \cdot 1.7009)$ and $c_2 = 1/(2 \cdot 1.7009\sqrt{\pi})$ are two geometric constants that result directly from such nondimensionalization. In this formulation, the three terms $\widetilde{F}_{AM}$, $\widetilde{F}_B$, and $\widetilde{F}_D$ denote the dimensionless added-mass, Basset, and Stokes drag forces respectively. It must be emphasized that equation (12.6) is an estimate of the unsteady force exerted on a sphere in a free stream: the effects of a nearby wall on the first two terms remain largely unknown. The relative values of each of the terms in (12.6) generally depend on time. In the asymptotic limit $\epsilon \ll 1$, three aerodynamic regimes of interest are found: $t \ll t_\nu \ll t_o$, $t \sim t_\nu \ll t_o$, and $t_\nu \ll t \sim t_o$, or equivalently, $\tau \ll \epsilon$, $\tau \sim \epsilon$ and $\tau \sim 1$.

For $\tau \ll \epsilon$ the flow around the pollen grain results in a nearly potential or irrotational flow [28], except in very thin Stokes layers which grow on the solid surfaces. The dominant force at this stage is the added mass force $\widetilde{F}_{AM} \sim \epsilon$, which is entirely produced by the inertia of the displaced fluid. The Basset force $\widetilde{F}_B \sim (\epsilon\tau)^{1/2}$ and the Stokes force $\widetilde{F}_D \sim \tau$ are in fact negligible at these short times, since $\widetilde{F}_B/\widetilde{F}_{AM} \sim (\tau/\epsilon)^{1/2} \ll 1$ and $\widetilde{F}_D/\widetilde{F}_{AM} \sim \tau/\epsilon \ll 1$. For $\tau \sim \epsilon$ the boundary layer thickness, which grows as $(\tau/\epsilon)^{1/2}$, has reached a size sufficiently large to engulf the pollen grain. Once the boundary layer has grown sufficiently around the grain, it will detach, generating a recirculating flow that will start around the rear stagnation point. For $\tau \sim \epsilon$, the three terms in (12.6) are of order ϵ. For $\tau \sim 4\epsilon$, the Basset and Stokes drag are equal in the first approximation. Finally, for $\tau \sim 1$ and larger the flow is steady and fully viscous at scales of order D. The dominant force is then the steady Stokes drag force $\widetilde{F}_D$ that asymptotically reaches its steady value (12.2), with the added-mass and Basset forces exponentially small.

Figure 12.3 shows an example of the numerical integration of (12.6) for $\epsilon = 0$ and $\epsilon = 0.5$, which shows that, in the more physically realistic $\epsilon \ll 1$ regime for pollen shedding, the transient dynamics do not cause any significant force overshoot. The inset of figure 12.3 shows the percentage variation of the maximum drag force with respect to (12.2) as a function of ϵ for $0 \leqslant \epsilon \leqslant 1$. As ϵ increases, the effects of the transient terms in (12.6) become more important, and transient forces slightly larger (within only a 10 % variation) than the Stokes drag F_D^∞ may occur. As ϵ increases, the wind-gust model used to calculate figure 12.3 misrepresents the magnitude of the velocity near the pollen grain,

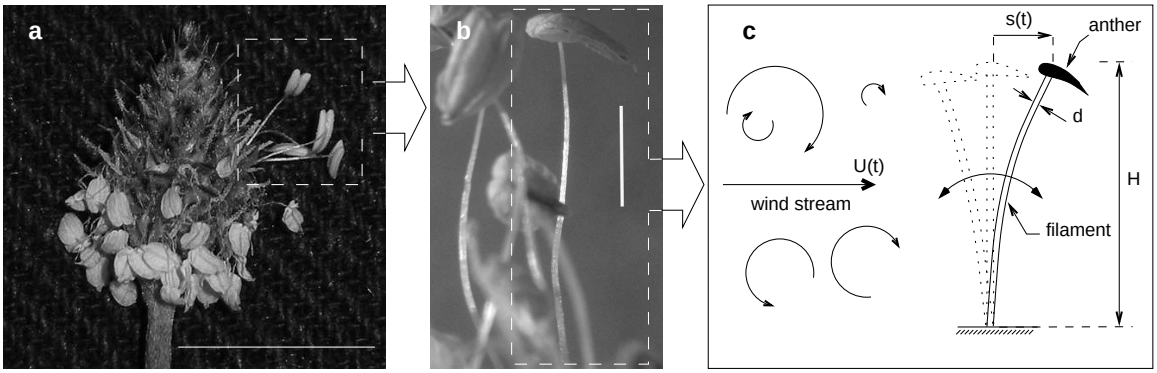

Figure 12.4: (a) *Plantago* inflorescence (scale bar 1 cm) and (b) anthers in scanning electron microscopy (scale bar 2 mm). Panel (c) shows the mathematical model and aeroelastic motion schematics of a wind-pollinated stamen immersed in a turbulent wind stream of instantaneous velocity $U(t)$.

which becomes closer to U_w for large ϵ as observed in figure 12.2(b). These calculations show that the unsteady forces produce only a small overshoot in the total drag force on the pollen grain of at most an order of magnitude smaller than the steady Stokes drag force, reducing the significance of time-dependent effects in the boundary layer around the anther upon pollen release.

12.2 Aeroelastic shedding forces

Atmospheric turbulence and its inherent unsteadiness may in fact play a notable role in pollen shedding, not in the sense of perturbing the viscous boundary layer near the anther surface as analyzed in Section 12.1.2 or previously conceptually proposed in earlier works [13-16,20,21], but by promoting a shaking motion of the stamen. In this study, the energy flow from the oncoming fluid kinetic energy to the viscous drag forces on the pollen grain examined earlier [13-16,20,21] is subtly modified, and thought of as an energy flow from the turbulent kinetic energy of the oncoming flow to the elastic energy of the stamen in the form of oscillating motion of the stamen, as depicted in figure 12.4. Finally, part of the kinetic energy is transferred to the pollen, which is ejected from the anther above a threshold mean wind speed. Aeroelasticity, the interaction between elastic structures and fluid flows [29, 30], is a broad subject and has been used to examine the drag on trees [27].

Since turbulence is inherently stochastic, it is appropriate to use a framework of mean displacements, velocities and accelerations, and fluctuations around these values. In particular, the longitudinal wind velocity is expressed as a sum of a mean velocity $\bar{U}_w$ and

the velocity fluctuations around the mean $u'(t)$. The wind longitudinal velocity fluctuations are described by the power spectrum $E_u(\omega)$ that satisfies

$$\overline{u'^2(t)} = \int_0^\infty E_u(\omega) d\omega, \tag{12.7}$$

with ω the angular frequency. The power spectrum of the force and stamen acceleration fluctuations can be defined in a similar way to (12.7) by simply substituting the mean square of the corresponding fluctuation in the left hand side.

In what follows, the shedding process is thus no longer a deterministic process but a stochastic one. Pollen shedding conditions are expected to be determined by statistically extreme events, in the sense that the unsteady fluctuations of the force around a mean, steady value, are the interactions that may promote grains to dislodge; this happens when the induced aeroelastic forces on the stamen are larger than the threshold imposed by the pollen-anther molecular adhesion forces.

12.2.1 The simplified stamen model

For simplicity we model the stamen as a linear isotropic elastic filament attached to a motionless substrate, with the center of pressure located in the anther as depicted in Fig. 12.4c. Elastic properties of the stamen can be obtained experimentally to yield the resonance frequency $\omega_n = (3EI/m_S H^3)^{1/2}$, where EI is the flexural rigidity, $m_S = m_a + m_f$ is the effective mass of the stamen and H is the filament length. The masses m_a and m_f denote the anther and filament mass respectively. For an elastic modulus $E \sim 100$ MPa, which corresponds to a typical stiffness of soft living vegetal tissues [27], values of table 12.1 yield a range $n = \omega_n/2\pi \sim 10.9 - 35.5$ Hz for the resonance frequency. Notice that these frequencies are much larger than characteristic natural frequencies of typical plant low-energy bulk motions, which are of the order of 1 Hz [31, 32].

The system depicted in figure 12.4c corresponds to a linear damped oscillator, with the anther displacement $s(t)$ described by the stochastic ordinary differential equation

$$\ddot{s}(t) + 2\xi\omega_n \dot{s}(t) + \omega_n^2 s(t) = F(t)/m_S, \tag{12.8}$$

where $F(t)$ is the stochastic force exerted on the filament windward surface, which can be expressed as the sum of a mean force $\bar{F}$ and force fluctuations around the mean $F'(t)$. In this formulation, ξ is the damping ratio caused by the viscous drag on the stamen during its motion relative to the mean flow and by structural dissipation in the plant material, and ω_n is the resonance frequency defined above. Typical values of ξ in plants and trees

are of order $\xi \sim 0.1$ [32, 27], which can be obtained by free oscillation tests [31, 32]. This coefficient may be much smaller for plant stamens because of the small dimensions and large resonance frequencies involved. An estimate of ξ can be obtained by assuming negligible structural dissipation in the plant material, so that only the hydrodynamic damping is present, with $\xi = \rho \bar{U}_w C_{De} A_e/(2\omega_n m_S)$ [30], where C_{De} and A_e are respectively the effective drag coefficient and frontal area of the stamen structure. Additionally, the Reynolds numbers $\mathrm{Re}_L = \bar{U}_w L/\nu$ and $\mathrm{Re}_d = \bar{U}_w d/\nu$ are sufficiently small so that the damping ratio can be computed from the viscous drag on the anther. This is taken to be the sum of the drag on the anther head, modelled as a sphere of diameter L, and the drag on the filament, which is modelled as a slender tapering cylinder [33]. The result is $\xi = \{4\pi\mu H/[\ln(2H/d) + 1/2] + 3\pi\mu L\}/\omega_n m_s$, which gives $\xi = 0.006 - 0.086$ for the species listed in table 12.1. These values correspond to an underdamped system with free exponentially-decaying oscillatory behavior.

If the turbulent intensity squared is a small number, $T_u^2 = \overline{u'^2}/\bar{U}_w^2 \ll 1$, the force fluctuations may be linearized in the velocity fluctuations to give

$$F'(t) = \rho C_{De} A_e \bar{U}_w u'(t), \tag{12.9}$$

and the power spectrum of the force can be easily obtained from the power spectrum of the velocity fluctuations $E_u(\omega)$ by using (12.9) as thoroughly detailed in classical fluid-structure interaction texts [29, 30]. Turbulence intensity measurements in maize crops [34], which give an average of $T_u \sim 0.2 - 0.6$ depending on the height above the canopy, show that (12.9) is a reasonable approximation.

By decomposing the anther acceleration $\ddot{s}(t)$ into the sum of a mean acceleration, which is of no interest because of its nonstochastic nature, and a fluctuation $\ddot{s}'(t)$, responsible for the stochastic inertial forces exerted on the pollen grain, a stochastic differential equation, similar to (12.8), can be obtained, which describes the time evolution of the fluctuation. The power spectrum of the acceleration fluctuations may be obtained from that of the longitudinal wind velocity fluctuations [29, 30]. The root-mean-square of the accelerations induced by the aeroelastic stamen motion on the pollen grain becomes $\sqrt{\overline{\ddot{s}'^2}} = \bar{U}_w/t_a$, where t_a is a characteristic aeroelastic time given by

$$t_a = \left(\frac{\bar{U}_w}{2\xi\omega_n}\right) \Big/ \left[\int_0^\infty \frac{\omega^4 E_u(\omega) d\omega}{|\mathcal{Z}(\omega)|^2}\right]^{1/2}, \tag{12.10}$$

where $|\mathcal{Z}(\omega)|^2 = (\omega_n^2 - \omega^2)^2 + 4\xi^2\omega^2\omega_n^2$ is the squared modulus of the impedance of the oscillatory system represented by equation (12.8). Non-unity aerodynamic admittance effects

have been neglected in (12.10). An estimate of the aeroelastic time t_a can be calculated by integrating (12.10) using a von Kármán turbulent spectrum for the longitudinal velocity fluctuations,

$$E_u(\omega) = \frac{4\overline{u'^2}\ell/\bar{U}_w}{\left[1 + 1.79\left(\frac{\omega\ell}{\bar{U}_w}\right)^2\right]^{5/6}}, \tag{12.11}$$

where ℓ is an integral length scale of the turbulent coarse vortices. The von Kármán spectrum has been widely used to analyze the turbulence-induced vibrations in man-made structures [29, 30] and plants [35]. Typical values $T_u = 0.5$ and $\ell = 1$ m for cereal crops [35] and estimates of ξ and ω_n mentioned above, based on table 12.1, are used to numerically integrate (12.10), which gives $t_a = 0.14 - 0.26$ s at $\bar{U}_w = 1$ m/s, $t_a = 0.08 - 0.15$ s at $\bar{U}_w = 5$ m/s, and $t_a = 0.07 - 0.12$ s at $\bar{U}_w = 10$ m/s.

The critical fluctuating acceleration for pollen dislodgement $\ddot{s}_c$ of a single pollen grain is given by the value for which the inertial aeroelastic forces are of the same order of magnitude as the adhesion force F_{ad}, so that $\ddot{s}_c = F_{ad}/m_p$.

12.2.2 Pollen-shedding number and probability

In this stochastic framework, the anther displacement fluctuation $s'(t)$ and its time-derivatives are described by an associated probability density function (PDF), obtained by solving the associated Fokker-Planck equation to equation (12.9). Since the dissipation ξ is relatively small in this system, the majority of the response of the stamen to the turbulent flow may occur in a narrow band of frequencies centered about the natural frequency ω_n. For simplicity, the probability density function is assumed to be a Rayleigh distribution in the first approximation, which represents a narrow-band Gaussian random process [30]. Such distribution yields the *probability of pollen shedding*,

$$P(\ddot{s}' > \ddot{s}'_c) = \mathrm{e}^{-\Psi^2/2}, \tag{12.12}$$

where

$$\Psi = \frac{\ddot{s}'_c}{\sqrt{\overline{\ddot{s}'^2}}} = \frac{F_{ad}t_a}{\bar{U}_w m_p}, \tag{12.13}$$

is a *pollen-shedding number*.

Equation (12.12) represents the probability of pollen shedding by aeroelastic forces $P(\Psi)$, as shown in Fig. 12.5, in terms of a single nondimensional parameter or shedding number Ψ given by equation (12.13), that may be thought of as a quantity proportional to the ratio of the adhesion force F_{ad} to the root-mean-square of the characteristic aeroelastic

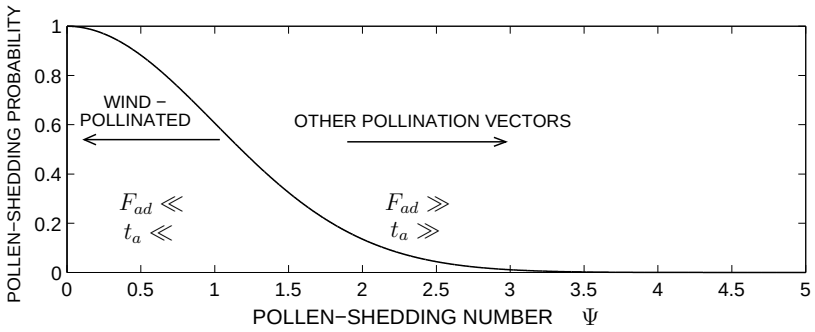

Figure 12.5: Pollen-shedding probability model (12.12) as a function of the shedding number Ψ.

force fluctuations exerted on the pollen grain $m_p\bar{U}_w/t_a$. Typical wind-pollinated species are then expected to release pollen grains over small aeroelastic time scales and to have small adhesion forces, with $\Psi \ll 1$ a small number. The opposite trend would hold for species pollinated by other vectors. Values of acceleration greater than six times the root-mean-square acceleration $\bar{U}_w/t_a$ are very unlikely to be observed in turbulence-induced vibrations that follow the cumulative probability distribution (12.12) [30]. Therefore, $\Psi \leqslant 6$, or equivalently, the force of adhesion F_{ad} may have to yield a value $F_{ad} \leqslant F^{\star}_{ad} = 6\bar{U}_w m_p/t_a$ for the aeroelastic mechanism to represent a suitable description of wind-pollination. Based on pollen mass values given in table 12.1 and estimates of t_a mentioned above, the range of values of the maximum allowed adhesion force are $F^{\star}_{ad} \sim 0.6$ nN at a wind velocity $\bar{U}_w = 1$ m/s, $F^{\star}_{ad} \sim 5$ nN at $\bar{U}_w = 5$ m/s, and $F^{\star}_{ad} \sim 13$ nN at $\bar{U}_w = 10$ m/s. According to the simplified stamen model analyzed in this investigation, the stamen acceleration produced by the aeroelastic forces is sufficiently large to dislodge the pollen grains if the pollen-anther adhesion force is smaller than $F^{\star}_{ad}$ at the corresponding wind velocity. It is worth noting that the values of $F^{\star}_{ad}$ are physically feasible in anemophilous species and comparable to the range of adhesion forces that are able to be overcame by purely steady aerodynamic forces. Nonetheless, more accurate evaluation of Ψ requires the experimental determination of F_{ad} and calculation of t_a, which requires accurate experimental determination of $C_{De}A_e$ or ξ, and E or ω_n for each species.

Table 12.1: Representative measurements of anthers, filaments and pollen from a range of wind or partially wind-pollinated species.

Species	Anther mass m_a (mg)	Anther length L (mm)	Filament+ anther mass m_S (mg)	Filament length H (mm)	Filament diameter d (mm)	Pollen mass m_p (ng)	Pollen diameter D (μm)	Stokes-Reynolds no. $\epsilon = t_\nu/t_o$
Betula coerula-grandis (birch)		0.83		0.51**	0.18**		25.30	0.10
Betula albosinensis Hergest (birch)		0.69					24.47	0.09
Briza sp. (grass)		2.99					23.45	0.08
Chionocloa bromoides (grass)		3.41[(1)]						
Pinus sylvestris (pine)						21.95[(5)]	59.00[(5)]	0.55
Plantago lanceolata (plantain)	0.08	2.11	0.11	7.2	0.06	14.40[(5)]	29.75	0.14
Plantago ovata (plantain)		0.60[(2)]						
*Salix caprea** (willow)	0.07	0.66	0.28	9.63	0.10	3.43[(5)]	16.68	0.04
Salix sepulcralis - - *var chrysocoma** (willow)	0.09	0.56	0.25	5.58	0.11		19.76	0.06
Schiedea sp. (Hawaiian shrub)		4.25[(3)]						
Thalictrum polycarpum (meadow rue)		1.74		3.05	0.10		23.37	0.08
Trictium aestivum (wheat)		2.85[(4)]					51.8[(6)]	0.42
Zea mays (maize)				3.92		219-380	95.29	1.44

*Members of the genus *Salix* are reported to be part-insect, part wind-pollinated.

**_Betula_ catkins contain shorter, wider anther filaments.

References: [(1)][36], [(2)][41], [(3)][38], [(4)][40], [(5)][16], [(6)][39].

Microscopy and measurements: Representative measurements were made for a range of wind-pollinated, or partially wind-pollinated, species for as many of the characteristics listed as possible. Supplementary data was taken from the literature where available. To measure pollen dimensions, and where anther filaments could not be measured without microscopy, fresh plant material was collected at the Cambridge University Botanic Gardens (Cambridge, UK) and immediately frozen in liquid nitrogen. Following freeze drying and sputter coating with gold, measurements were made (Scion Image; Scion Corp, Frederick, Maryland, USA) on digital images recorded using scanning electron microscopy (Oxford Instruments CT 1500; Abingdon, Oxfordshire, UK).

Chapter 13

Conclusions

Earlier attempts to solve the paradox of pollen liberation, based on wind-gust aerodynamic models of unsteady viscous forces exerted on a fungal spore attached to a motionless substrate in a boundary layer, are shown in this study to be inappropriate to describe pollen shedding. Steady Stokes drag forces are found to be capable of removing pollen from anemophilous anthers. Since viscous effects are found to be more important in typical anemophilous pollen than inertial accelerations of the outer wind stream, with the ratio ϵ of the viscous time scale t_ν to the wind-gust time scale t_o typically a small number, unsteady boundary-layer forces produced by wind gusts are found to be mostly ineffective. Nonetheless, removal of pollen by wind gusts may occur for sufficiently large pollen grains.

We have proposed a new turbulence-initiated, wind-pollination mechanism to explain the phenomenon in a complementary way. A straightforward scaling analysis, accounting for the level of turbulence near the ground and the elastic properties of the plant, gives a first approximation of the quantitative probabilistic measure of pollen shedding when the anthers are shaken by the stochastic action of the wind. The effectiveness of this mechanism depends on the shedding number $\Psi = F_{ad} t_a / m_p \bar{U}_w$, which is found to be an order-unity parameter when estimated from typical turbulent power spectra. Nonetheless, a more accurate evaluation of the shedding number needs an accurate determination of the pollen-anther adhesion force and aeroelastic times, two magnitudes that are difficult to define experimentally and therefore unexplored in the existing literature. Further analyses on more elaborated aeroelastic models, and their experimental validation, accounting for a wider range of biomechanical effects, such as a plant physical representation by a structure with multiple degrees of freedom and non-uniform mechanical properties, will allow a fuller understanding of the processes involved in the shedding of pollen.

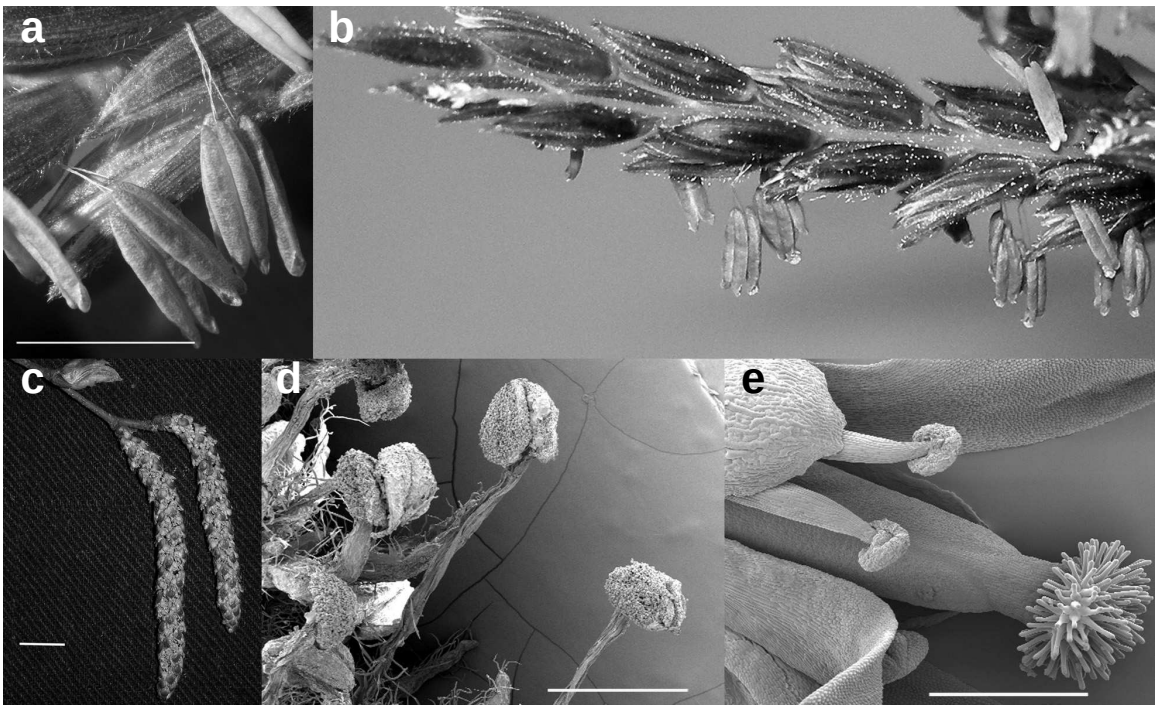

Figure 13.1: (a) *Zea mays* anthers (scale bar, 5 mm) and (b) inflorescence; (c) *Betula albosinensis* catkin (scale bar, 1 cm), (d) *Salix sepulchralis* anthers (scanning electron microscropy; scale bar, 1 mm); (e) In contrast, self-fertile *Arabidopsis thaliana* anthers have shorter, less mobile filaments (scanning electron microscropy; scale bar, 500 μm).

We note that not all wind-pollinated plants have such long anthers. However, where anther filaments are short or solid, it is invariably the case that wind-pollinated flowers are borne on mobile, flexible inflorescence stems (catkins; figure 13.1), or, in the case of gymnosperm anthers, the male cones are borne on long, flexible branches. These different mechanical solutions to the same problem represent independent evolutionary innovations, but all may operate within the simple model we describe here.

One of the most important features of a suitable long-range dispersal model of pollen grains or fungal spores is the characterization of the physical and biological processes that occur in the source and release of these small particles into the air. The extraordinary model sensitivity to these small-scale processes sets pollen-transport models apart from pure pollutant dispersal models, where the source is reasonably independent of the surrounding micrometeorology.

From the standpoint of the fluid dynamics science, the models used in this study are very basic, but they represent a novel treatment of the problem of pollen shedding and they establish a framework for plant biologists and future refinements. The fundamental question

of whether the wind-pollinated species are aerodynamically and aeroelastically optimized or not by having lower pollen adhesion forces and small aeroelastic times scales, has not been answered in this investigation; further experiments, to measure plant-structural properties and pollen adhesion forces of a wide range of wind-pollinated species, would be needed to answer that question, which is of practical interest for analyses of pollen dispersal, crop production, maintenance of biodiversity and management of genetically modified plants.

Chapters 11 to 13, in part, have been published in the *Journal of Theoretical Biology*, "Wind gusts and plant aeroelasticity effects on the aerodynamics of pollen shedding: a hypothetical turbulence-initiated wind-pollination mechanism," by J. Urzay, S. G. Llewellyn Smith, E. Thompson and B. J. Glover (2009) **259** 785-792. The thesis author is the primary investigator in this publication.

Experiments in Part III were performed by Dr. E. Thompson and Dr. B. J Glover at the Department of Plant Sciences in the University of Cambridge (UK). This investigation was funded by the Human Frontier Science Program, grant #RGY 0073/2005.

References

[1] Willis, K.J, McElwain, J.C. (2002) The Evolution of Plants (Oxford University Press, Oxford).

[2] Heslop-Harrison, J.H. (1979) An interpretation of the hydrodynamics of pollen. *American Journal of Botany* **66** (6) 737–743.

[3] Crane, P.E., Friis, E.M, Pedersen, K.R. (1995) The origin and early diversification of angiosperms. Nature **374** 23-33.

[4] Kessler, R., Harley, H. (2006) *Pollen: the hidden sexuality of flowers*. Firefly Books, New York.

[5] Linnaeus, C.V., (1751) *Philosophia Botanica*.

[6] Zinkl, G.M., Zwiebel, B.I., Grier, D.G., Preuss, D. (1999) Pollen-stigma adhesion in arabidopsis: a species-specific interaction mediated by lipophilic molecules in the pollen exine. *Development* **126** 5431–5440.

[7] Vercoulen, P.H.W., Roos, R.A., Marijinissen, J.C.M., Scarlet, B. (1992) Measuring electric charge on pollen. *J. of Aerosol Science.* **23** 377–380.

[8] Bowker, G., Crenshaw, H.C. (2003) The influence of fair weather electricity on the charging of wind-dispersed pollen. In *Proceedings of The International Commission on Atmospheric Electricity*.

[9] Erickson, E.H, Buchmann, S.L. (1983) Electrostatics and pollination. In *Handbook of experimental pollination biology.*. Scientific and Academic Editions.

[10] Bechar, A., Shmulevich, I. Eisikowitch, D., Vaknin, Y., Ronen, B. & Gan-Mor, S. (1999) Modeling and experiment analysis of electrostatic date pollination. *Transactions of the ASAE.* **42** 1511–1516.

[11] Vaknin, Y., Gan-Mor, S., Bechar, A., Ronen, B., Eisikowitch, D. (2000) Are flowers morphologically adapted to take advantage of electrostatic forces in pollination?. *New Phytologist.* **152**, 301–306.

[12] Vaknin, Y., Gran-Mor, S., Bechar, A., Ronen, B., Eisikowitch, D. (2000) The role of electrostatic forces in pollination. *Plant Syst. Evol.* **222** 133–142.

[13] Aylor, D.E., Parlange, J.Y. (1975) Ventilation required to entrain small particles from leaves. Plant Physiol. **56** 97-99.

[14] Aylor, D.E. (1985) Force required to detach conidia of *Helminthosporium maydis*. Plant Physiol. **55** 99-101.

[15] Aylor, D.E. (1999) The role of intermittent wind in the dispersal of fungal pathogens. Annu. Rev. Phytopat. **28** 73-92.

[16] Jackson, S.T., Lyford, M.E. (1999) Pollen dispersal models in quaternary plant ecology: assumptions, parameters and prescriptions. Botanical Rev. **65** 39-75.

[17] Culley, T.M., Weller, S.G., Sakai, A.K. (2002) The evolution of wind pollination in angiosperms. *Trends in Ecology and Evolution.* **17** 361–369.

[18] Wolfenbarger, L.L., Phifer, P.R. (2000) The ecological risks and benefits of genetically engineered plants. *Science.* **290** 2088–2093.

[19] Thompson, E. (2006) Private Communication. Department of Plant Sciences, University of Cambridge (UK).

[20] Niklas, K.J. (1985) Aerodynamics of wind pollination. Botanical Rev. **51** 328-386.

[21] Niklas, K.J. (1992) *Plant Biomechanics*. University of Chicago Press, Chicago.

[22] Schlichting, H. (1979) *Boundary layer theory*. McGraw-Hill, New York.

[23] O'Neill, M.E. (1968) A sphere in contact with a plane wall in a slow linear shear flow. *Chem. Eng. Sci.* **23** 1293-1298.

[24] King, M.J., Lengoc, L. (1993) Vibratory pollen collection dynamics. T. ASAE **36** 135-140.

[25] King, M.J., Buchmann, S.L. (1995) Bumble-bee initiated vibration release mechanism of *Rhododendron* pollen. Am. J. Bot. **82** 1407-1411.

[26] Finnigan, J. (2000) Turbulence in plant canopies. Annu. Rev. Fluid Mech. **32** 519-571.

[27] De Langre, E. (2008) Effects of wind on plants. Annu. Rev. Fluid Mech. **40** 141-168.

[28] Lamb, H. (1945) Hydrodynamics. Dover, New York.

[29] Simiu, E., Scanlan, R.H. (1996) Wind effects on structures. John Wiley, New York.

[30] Blevins, R.D. (1990) Flow-induced vibration. Van Nostrand Reinhold, New York.

[31] Flesch, T.K., Grant, R.H. (1992) Corn motion in the wind during senescence: effect of dynamic plant characteristics. Agron. J. **84** 742-747.

[32] Doaré, O., Moulia, B., De Langre, E. (2004) Effect of plant interaction on wind-induced crop motion. J. Biomech. Eng. **126** 146-151.

[33] Cox, R.G. (1970) The motion of slender bodies in a viscous fluid. Part 1: General theory. J. Fluid Mech. **44** 791-810.

[34] Shaw, R.H., Den Hartog, G., King, K.M., Thurtell, G.W. (1974) Measurements of mean wind flow and three-dimensional turbulence intensity within a mature corn canopy. Agricult. Meteor. **13** 419-425.

[35] Baker, C.J. (1995) The development of a theoretical model for the windthrow of plants. J. Theor. Biol. **175** 355-372.

[36] Connor, H.E. (1990) Breeding systems in New Zealand grasses. XI. Gynodioecism in *Chionochloa bromoides*. New Zealand J. Bot. *28* 59-65.

[37] Emberlin, J., Adams-Groom, B., Tidmarsh, J. (1999) A Report on the Dispersal of Maize Pollen. Commissioned by the Soil Association. Worcester University College, Worcester.

[38] Golonka, A.M., Sakai, A.K., Weller, S. G. (2005) Wind pollination, sexual dimorphism, and changes in floral traits of Schiedea *(Caryophyllaceae)*. Am. J. Bot. **92** 1492-1502.

[39] Hammer, K. (2005) Remarks to thebreeding systems of the *Triticeae* with special reference to the pollen to ovule ratios. Czech J. Genet. Plant Breed **41** 145-153.

[40] Komaki, M.K., Tsunewaki, K. (1981) Genetical studies on the difference of anther length among common wheat cultivars. Euphytica. **30** 45-53. 7.

[41] Sharma, N., Koul, P., Koul, A.K. (1992) Reproductive biology of *Plantago*: shift from cross- to self-pollination. Ann. Bot. **69** 7-11.